Electron optics in ballistic graphene studied by scanning gate microscopy

Marco Guerra

Université Grenoble Alpes

THÈSE

Pour obtenir le grade de

DOCTEUR DE L'UNIVERSITE GRENOBLE ALPES

Spécialité : Physique de la Matière Condensée et du Rayonnement

Arrêté ministériel : 25 mai 2016

Présentée par

Marco Guerra

Thèse dirigée par **Hermann Sellier**, Université Grenoble Alpes
préparée au sein de **l'Institut Néel, CNRS**
dans **l'École Doctorale de Physique**

Electron optics in ballistic graphene studied by scanning gate microscopy

Études d'optique électronique dans le graphène balistique par microscopie à grille locale

Thèse soutenue publiquement le **28 juin 2021**,
devant le jury composé de :

Stefan HEUN
Directeur de recherche, NEST, CNR, SNS, Pisa, Rapporteur
Walter ESCOFFIER
Maître de conférence, LNCMI, CNRS, INSA, Toulouse, Rapporteur
Benoît HACKENS
Professeur, IMCN, FNRS, UCL, Louvain-la-Neuve, Examinateur
Jean-Philippe POIZAT
Directeur de recherche, NEEL, CNRS, UGA, Président
Vincent RENARD
Maître de conférence, PHELIQS, CEA, UGA, Examinateur
Benjamin SACÉPÉ
Chargé de recherche, NEEL, CNRS, UGA, Co-Encadrant de thèse
Hermann SELLIER
Maître de conférence, NEEL, CNRS, UGA, Directeur de thèse

Dedico questo lavoro
ai miei genitori

To my parents

Abstract

In this thesis, I studied the electronic transport of relativistic Dirac fermions in ballistic graphene p-n junctions. These junctions consist of a graphene flake encapsulated between two flakes of hexagonal boron nitride, fabricated by the van-der-Waals pick-up technique. Two independent backgates, made from a highly-doped silicon substrate and a local graphite flake, control the carrier density in two regions of the graphene junction, which can operate both in unipolar (n-n' or p-p' junctions) and bipolar (n-p or p-n junctions) regimes. While in the unipolar regimes it is possible to characterize the influence of the interface on a ballistic stream of particles, in the bipolar regime electron waves in graphene experience negative refraction when passing rapidly from the conduction band to the valence band. The negative refraction produces a Veselago lensing phenomenon, with the formations of a focal point obeying to the Snell-Descartes law for Dirac fermions. The devices integrate a series of essential features to engineer electron-optics devices, such as pinhole collimators, reflection-less edges with electron absorbers, and a thin pristine graphite backgate for precise interface definition.

To image the current flow through these graphene p-n junctions, I employed a scanning gate microscope (SGM). It relies on a cryogenic atomic force microscope (AFM) with an electrically polarized tip, which scans at a fixed height above the device surface, inducing a local potential change. Electrical measurements during the scans give access to spatial information on electron transport. The local electrostatic perturbation of the SGM tip scatters the electron flow and generates spatial maps of transmitted current with a high contrast at the p-n interface. I observed signatures of Veselago focusing that agree quantitatively with the theory. The SGM maps of the reflected current show interesting features that could be attributed to Klein tunnelling promoted by the electrostatic action of the tip, and to the formation of scattering states close to the injection region. In order to reverse-engineer the effect of the tip potential on the electron trajectories, I developed ray-tracing simulations in a semi-classical context which are compared with the experimental data.

In a second part of the thesis, I performed a series of SGM experiments that provide spatial information on the backscattering process between chiral quantum Hall edge states in high-mobility graphene Hall bars. A local graphite backgate allows to characterize the electrostatic confinement of edge channels in space. I identified a series of concentric rings typical of single-charge transport through a localized state gated by the tip. The diamond-shaped stability diagram, recorded at finite source-drain bias in the proximity of these rings, demonstrates the key-role of Coulomb blockade in the percolation of quantum Hall edge channels through a disordered potential landscape.

Acknowledgment

The conclusion of a PhD is always a special moment, it represents the end of a personal journey of a few years, where a lot of effort and creativity are deployed for a better understanding of what is written in the great book of Nature. During this journey I had the unbelievable chance to work with many fabulous people, who helped me a lot in numerous ways.

I would like to thank first Hermann Sellier. Since the beginning of my M2 internship he taught me with care and dedication how to use the SGM setup and how to make quantum transport experiments. During the PhD he continued to wisely guide and support me with the great enthusiasm that distinguishes him, and probably with a good dose of patience. I am deeply grateful for all the inspiring conversations done together, it is incredible how much you can learn by talking to him.

I am grateful to my co-supervisor Benjamin Sacépé, who made this PhD possible by putting me in contact with Hermann. Thank you for your suggestions and constructive comments on my work. It was a pleasure and a honor to collaborate with you during these years.

Of course I want to thank the jury members who accepted to read and evaluate my manuscript and my thesis defense. Thanks to Stefan Heun and Walter Escoffier for writing the reports to my manuscript.

I want to express my thanks to Vincent Bouchiat for allowing me to carry out my industrial secondment in the MedTech company Grapheal. It was an invaluable learning experience.

A portion of my PhD was dedicated to the device fabrication. This part would not have been possible without the initial help of Louis Veyrat, who was always ready to give me a proper support. I enjoyed a lot the time together talking about science, life and music. I want to thank him for the great evening parties and for all the gorgeous cakes, he is a wonderful baker.

A big thank goes to the Néel Institute staff. I will start with the people that helped me in the cleanroom and allowed me to obtain the experimental results presented in the manuscript. Specifically, I want to acknowledge the important role of the nanofabrication team: Thierry Crozes, Gwénaëlle Julie, Bruno Fernandez, Latifa Abbassi and Jean-François Motte. I would like to thank Simon Le Denmat for his help in the AFM lab. For the administrative part, I express my gratitude to Florence Pois.

Like in any good journey with mysterious adventurers in time and space, there is always someone who stands out to be the villain of the story and another who is more the comic relief. While I was clearly the latter, the villain role was perfectly suited for Alexis Coissard. Jokes aside, I was very lucky to share the office with him. I want to thank him for his constant help throughout my entire PhD. I am especially grateful of his valuable suggestions with my scientific illustrations, he is a great master and I learned a lot from him.

Good friends are the one who can tell good stories, help when you have problems, and who can fill your empty glass with great wine. All these qualities, and many others, can be found in my colleague and friend Corentin Déprez. I want to thank him for all our scientific discussions and for the amazing evenings and outdoor activities. During the PhD he showed an incredible

strength and passion for research. He was a true source of inspiration for me.

A special thanks goes to Hadrien Vignaud for his help in the lab and for his moral support. It was a pleasure to talk with him about physics, technology, French traditions and culture.

It has been a great pleasure to supervise the M2 internship of Akash Patil. I particularly enjoyed doing nanofabrication and SGM experiments in the quantum Hall regime with him.

I also thank many people from the Hybrid team at Néel Institute, Riadh Othmen for his endless creativity and kindness, Pryiank Singh for our discussions on gym and unconventional physics, Enzo Kloss for his great personality and pizzas, Goutham Nayak for his friendship and the logistic help during the end of my PhD, and Guilliam Butseraen for his incredible humor and for the musical evenings around the piano.

A big thank you to all the permanents, students and post-docs of the quantum nanoelectronics and spectroscopy team: Jean-Yves Veuillen, Pierre Mallet, Clemens Winkelmann, Hervé Courtois, Efe Gumus, Danial Majidi, David Wander, David Perconte, Wenmin Yang, Bilal Kousar, etc. Whether directly or indirectly, you made my PhD experience much more enjoyable.

I would like to thank my flatmate Niccolò Castellani. I can tell, from my own personal experience, that a colocation lasting more than 3 years with the same people, doesn't happen frequently. Since the beginning, we managed to establish a wonderful equilibrium in the house. I really enjoyed our improvised reflections after dinner, talking about ancient history, music, lifestyles, figs, etc. Similarly to the characters of the Decameron, we admirably survived a real virus pandemic.

During my last year of PhD, Sara Baratto joined the colocation. With her characteristic sunny personality, we immediately became good friends. I am grateful for her incredible funny stories, she is an exceptional story teller.

Infine, vorrei ringraziare la mia famiglia ed in particolare i miei genitori. Grazie per il sostegno ed il grande aiuto che mi avete dato durante tutti questi anni.

Good luck my friends, I hope our paths will cross again.

Contents

Introduction

After the discovery of Maxwell's equations for the description of the electromagnetic waves, and their experimental validation provided by Hertz, the wave picture of light started to gain in prominence, slowly replacing the ancient corpuscular theory supported by Descartes, Fermat and Newton. However, at that time lenses manufacture processes for eye glasses and optical technology was already a well established reality, proving somehow the validity of the geometrical optic limit of the Maxwell's theory. The propagation of electrons has many interesting similarities with the propagation of light. A crucial stepping stone contributing towards the understanding of the wave nature of electrons was given by the electron diffraction experiment done in 1927 by C. Davisson and L. H. Germer [43].

Propagation of photons is described by the Maxwell theory, just as electrons are described by the Schrödinger equation. However, besides the formal theoretical differences between the two wave-like descriptions, still it is very challenging to discern wave-like behaviour of electrons in solid systems. Indeed, electrons in solids display an effective mass and a charge, making them very interactive with the surrounding electrostatic environment. The interactions with lattice phonons, as well as the presence of lattice defects contribute to the spoil of ideal wave-like behaviour. This is why the main requirement for the design of solid state platforms for electron optics, is the employment of mono crystalline materials at cryogenic temperatures.

First examples of electron optics in solids were made with high-mobility 2DEG in GaAs [131]. The possibility to employ semiconductors to realize experiments in a geometrical optic limit, turned out to be also an excellent gateway to visualize in space, with scanning probe techniques, the magneto-focusing of electron waves.

Under this perspective, graphene van der Waals heterostructures are suitable candidates for novel electro optical devices. The remarkable high-mobilities of graphene, joint with the low-energy electronic excitations, allows to realize devices with massless Dirac fermions having a linear dispersion relation like photons. Moreover, with external gate voltages, it is possible to design electronic lenses with graphene p-n interfaces, by combing together regions of electron and hole doping. The current transmission across these interfaces depends on the incidence angles of charge carriers and is described by an effective Snell-Descartes law for Dirac fermions. This evidence makes graphene the elective material for the 2D realization of common optical elements, such as Veselago lenses, beam splitters, collimators and waveguides. Quite recently a theoretical proposal for a 2D graphene scanning electron microscopy has been made as well [11].

The first goal of this thesis work is to use the scanning gate microscopy (SGM) technique on a graphene p-n junction, in order to extract spatially-resolved informations on the transmission and reflection processes of charge carriers at the potential interface.

In this PhD thesis, I have accomplished the SGM imaging of ballistic transport in three different graphene p-n junctions. I obtained signatures of transmission and reflection, which have been reverse engineered with a series of home made ray-tracing simulations in the semi-classical transport regime. In particular, our SGM images give strong indications of the Veselago

lens focusing effect, which has been an elusive phenomena for many years.

A second part of the thesis deals with graphene devices under high magnetic field, exhibiting an anomalous relativistic quantum Hall effect, with the appearance of quantum Hall conductance plateaus at $2e^2/h$, $6e^2/h$, $10e^2/h$, etc. The magnetic field allows to suppress the backscattering events inside chiral edge channels, leading to a perfect topological protection in wide devices, which avoid any dissipation. In addition, quantum Hall systems are suitable platforms for the study of interactions effects developing in compressible states of graphene devices. In mesoscopic devices with sub-micron size, charge impurities, which are responsible for the presence of localized states, promote the backscattering between counter-propagating edge channels via tunnelling effect.

The second part of the thesis is therefore dedicated to the SGM imaging of these backscattering events in different graphene Hall bars. SGM allows to characterize the Coulomb blockade charge dynamics inside localized states, in a similar way as performed in past experiments with GaAs heterostructures [114]. In the thesis, I successfully manage to image and characterize with SGM the backscattering events inside two different Hall bars. The electrically polarized tip of the microscope allowed local manipulation of edge states, promoting tunnelling of charge carriers between the counter-propagating modes, either directly or through localized quantum Hall islands. I identified a series of concentric arcs which are typical of charge resonances through a percolative state gated by the tip. The diamond-shaped stability diagrams allowed to demonstrate the key-role of Coulomb blockade in the backscattering process through a disordered potential landscape.

Chapter 1 introduces the electronic properties of graphene at zero magnetic field, as well as the transport properties of ballistic graphene p-n junctions within the gradient-index optics framework.

Chapter 2 is an instrumental chapter dedicated to the SGM microscope and the cryogenic scanning probe techniques employed during the experiments.

Chapter 3 starts with a review of the literature in which the semi-classical theory has been employed to understand and simulate the SGM signals in different electronic systems. The second part provides a description of the ray-tracing algorithm, developed during the thesis, in order to simulate the SGM transport signatures in graphene p-n junctions. Finally, the layout of a graphene p-n junction for electron optics is presented.

Chapter 4 presents the van der Waals pick-up technique for the fabrication of graphene heterostructures. This transfer method enables the encapsulation of graphene between hexagonal boron nitride flakes, preserving the quality of graphene during the lithographic steps for the fabrication of high-mobility devices.

Chapter 5 is the experimental chapter where are reported the major SGM results on three different graphene p-n junctions. I provide evidences of ballistic electron flows, negative refractions, back reflections and branching inside graphene p-n junctions. I present an analysis on the SGM imaging of electron caustics associated to Veselago lensing.

Chapter 6 is the last experimental chapter, dedicated to SGM in the quantum Hall effect. The chapter starts with a description of the quantum Hall effect in graphene and continues with a series of SGM experiments in two different graphene Hall bars, providing spatial informations on the backscattering processes. The last part of the chapter reports on the Coulomb blockade in the backscattering process through a disordered potential landscape.

Introduction - version en français

Après la découverte des équations de Maxwell décrivant l'électromagnétisme, et leur validation fournie par Hertz, l'interprétation ondulatoire de la lumière gagna en popularité, remplaçant l'ancienne théorie supportée par Descartes, Fermat et Newton. Toutefois, à ce moment là, les processus de fabrication des lentilles étaient une réalité bien établie, prouvant ainsi l'efficacité de la limite géométrique vers laquelle tend l'optique ondulatoire. La propagation des électrons présente de nombreuses similitudes avec la propagation de la lumière. En 1927, l'expérience de diffraction par C. Davisson et L.H. Germer marque un jalon très important dans la compréhension de la nature ondulatoire de l'électron [43].

La théorie de Maxwell décrit la propagations des photons, tout comme l'équation de Schrödinger décrit la propagation des électrons. Hélas, malgré les ressemblances formelles entre les deux descriptions ondulatoires, il est encore très difficile d'observer le comportement ondulatoire des électrons dans la matière condensée. Un électron dans un matériau est caractérisé par une masse effective et une charge, qui le rendent interagissant avec le paysage électrostatique qui l'entoure. Les interactions avec des phonons et la présence de défauts cristallins constituent des facteurs limitants pour l'observation d'un comportement ondulatoire idéal. Voilà pourquoi, afin de réaliser une expérience d'optique électronique dans un solide, il est impératif d'employer des matériaux monocristallins à basses températures.

Les premiers exemples d'optique électronique dans le solide ont été obtenus avec des hétérostructures à base de GaAs à haute mobilité [131]. La possibilité d'employer les semi-conducteurs pour des expériences d'optique électronique dans la limite géométrique, s'est révélée être aussi tremplin pour l'observation, avec un microscope à grille locale, de la magnéto-focalisation des ondes électroniques dans l'espace.

Dans cette perspective, les hétérostructures van der Waals sont des candidats parfaits pour la création de nouveaux dispositifs pour l'optique électronique. La haute mobilité du graphène, combinée avec les excitations électroniques à basses énergies, permet de réaliser des dispositifs avec des fermions de Dirac ayant une dispersion linéaire similaire aux photons.

En fonction des différentes tensions de grille, il est possible de créer des lentilles électroniques avec des interfaces p-n, mettant en contact des régions avec un dopage de type électron et trou. La transmission du courant électrique à travers ces interfaces est décrite par une loi effective de Snell-Descartes, et est fonction de l'angle d'incidence des porteurs de charge.

Cette évidence rend le graphène le matériau idéal pour la réalisation des éléments optiques 2D, comme des lentilles Veselago, des miroirs semi-réfléchissants, des collimateurs et guides d'ondes. Récemment il y a eu aussi une proposition pour la réalisation d'un microscope à balayage électronique 2D en graphène [11].

Le premier objectif de cette thèse est d'employer un microscope à grille locale (SGM) sur une jonction p-n en graphène, afin d'extraire des informations avec résolution spatiale concernant la transmission et la réflexion des porteurs de charge sur une interface électrostatique.

Au cours de cette thèse, j'ai réalisé avec succès l'imagerie SGM du transport balistique dans trois différentes jonctions p-n. J'ai obtenu des signatures de transmission et réflexion, qui

ont été interprétées avec une série de simulations en régime semi-classique. Les images SGM montrent des signes évidents de focalisation Veselago, qui a été un phénomène insaisissable depuis de nombreuses années.

La seconde partie de cette thèse est consacrée aux dispositifs de graphène soumis à un fort champ magnétique transverse, montrant des signatures d'effet Hall quantique relativiste, avec l'apparition des plateaux de conductance $2e^2/h$, $6e^2/h$, $10e^2/h$, etc. L'application d'un champ magnétique permet la suppression de la rétrodiffusion entre canaux de bords chiraux, permettant une protection topologique parfaite dans des dispositifs larges. Les systèmes électroniques sujet au régime Hall quantique, sont des plateformes intéressantes pour l'étude des effets d'interactions entre états compressibles. Les dispositifs mésoscopiques, de taille inférieure à 1 micron, peuvent présenter des impuretés donnant lieu à des états localisés, responsables de la présence de rétrodiffusion entre canaux de bords contre-propageant par effet tunnel.

La deuxième partie de cette thèse s'est focalisée sur l'imagerie des événements de rétrodiffusion dans diverses barres de Hall en graphène. La technique SGM permet de caractériser le comportement dynamique des électrons lié au blocage de Coulomb entre états localisés, de la même manière que les expériences antérieures dans des dispositifs en GaAs [114].

J'ai réalisé des mesures de rétrodiffusion à l'aide du microscope SGM dans deux barres de Hall. Avec une pointe de microscope à force atomique (AFM) chargée négativement, il est possible de manipuler dans l'espace les états de bord, favorisant l'effet tunnel entre les canaux, soit directement ou indirectement au travers des états localisés. J'ai pu identifier la présence d'arcs de résonance, caractérisant des phénomènes de percolation de charge entre états modifiés localement par la pointe du microscope. La mesure d'un diagramme de stabilité de charge avec des diamants de Coulomb, démontre le rôle clé joué par le blocage de Coulomb dans le processus de rétrodiffusion à travers d'un potentiel désordonné.

Chapter 1 introduit les propriétés électroniques du graphène, ainsi que les propriétés de transport des jonctions p-n dans le cadre de l'optique à gradient d'indice.

Chapter 2 est un chapitre instrumental dédié au microscope SGM employé durant les expériences.

Chapter 3 commence avec une revue de la littérature sur l'approche semi-classique pour la compréhension et la simulation du signal SGM dans des systèmes électroniques différents. La deuxième partie du chapitre, présente l'algorithme ray-tracing développé pendant la thèse, pour simuler les signatures de transport SGM dans les jonctions p-n en graphène. La fin du chapitre introduit les éléments constitutifs des jonctions p-n pour l'optique électronique.

Chapter 4 présente la technique de "pick-up" van der Waals pour la fabrication d'échantillons en graphène. Cette technique de transfert permet d'encapsuler un flocon de graphène entre deux fins cristaux de nitrure de bore hexagonal. L'encapsulation préserve la qualité du graphène durant toutes les étapes de lithographie pour la fabrication de dispositifs à haute mobilité.

Chapter 5 est le chapitre expérimental avec les résultats SGM principaux sur trois jonctions p-n en graphène. Je présente des évidences de transport électronique en régime balistique, réfraction négative, réflexion totale et branching dans les jonctions p-n. J'expose une analyse sur l'imagerie SGM d'une caustique d'électrons associée à l'effet Veselago.

Chapter 6 est le dernier chapitre expérimental, qui s'ouvre avec une description de l'effet Hall quantique dans le graphène et continue ensuite avec des expériences SGM sur la rétrodiffusion dans deux barres de Hall en graphène. La dernière partie du chapitre apporte une analyse sur la rétrodiffusion dominée par le blocage de Coulomb à travers un potentiel désordonné.

Chapter 1

Electron optics in graphene

Contents

This chapter focuses on the description of the transport properties that make graphene a suitable candidate for the realization of electron optical lenses, which can refract electron waves similarly to left-handed metamaterials in optical systems. Via the ambipolar field effect of electrostatic gates on a graphene plane, it is possible to combine together regions of electron and hole doping. The current transmission across these interfaces is described by an effective Snell-Descartes law for Dirac fermions, which allows the realization of planar and circular Veselago lenses, where charge carriers trajectories experience negative refraction processes. Example of current trajectories through different lenses are reported inside the chapter, illustrated within a semi-classical gradient-index optics framework.

In the end of the chapter, I report experiments from the literature, providing the indirect observation of Veselago lensing in graphene p-n junctions.

1.1 Band structure of graphene

Graphene is a single layer graphite, an allotrope of carbon in the form of a two-dimensional honeycomb lattice. Its peculiar properties come from its characteristic band structure predicted by P.R. Wallace in 1947 [146].

The quest toward the isolation of graphene accumulated a significant delay. In the 1960s, superconductivity was observed in graphite planes with the intercalation of potassium atoms [63], but despite this first attempt to play with graphite layers, the idea to isolate a single graphene crystal remained unpursued. Although there were the thoughts of Landau and Peierls in the 1940s that 2D materials couldn't exist [120, 85], surprisingly in 2004 Novoselov et al managed successfully to make graphene a laboratory reality [111]. In the following chapter I give a brief description on the ultra-relativistic electronic properties of graphene.

1.1.1 Honeycomb lattice

The atoms of carbon composing a graphene single-crystal exhibit a characteristic sp^2 hybridization. Each atom presents three $2s2p$ orbitals involved in a series of strong σ-bonds

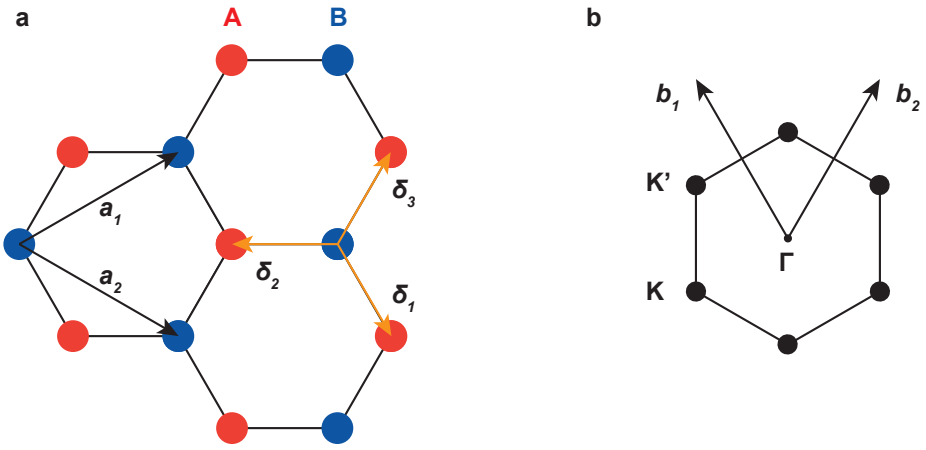

Figure 1.1: (a) Graphene honeycomb lattice in the real space. $\mathbf{a}_1$ and $\mathbf{a}_2$ represent the primitive vectors, while δ_1, δ_2 and δ_3 are the nearest neighbour hopping vectors. (b) Irreducible Brillouin zone of the hexagonal lattice. The basis vectors $\mathbf{b}_1$ and $\mathbf{b}_2$ are centred around the $\mathbf{\Gamma}$ point. $\mathbf{K}$ and $\mathbf{K}'$ are the inequivalent corners of the Brillouin zone. Pictures inspired from [26].

in the xy plane. The remaining $2p_z$ orbital overlaps with the others out-of-plane carbon orbitals distributed over the graphene honeycomb lattice. The resulting carbon-carbon distance is $a_0 = 1.42$ Å. The overalp between the out-of-plane orbitals generates a cloud of delocalized π electrons. Which are mainly responsible for the electron properties of graphene. More precisely, the overlap gives birth to the π and π^* bands characterizing the energy eigenvalues for charge carriers.

The honeycomb lattice (see Fig.1.1.a) can be visualized as a particular triangular Bravais lattice having two atom basis, usually called A and B. The B lattice is generated by the primitive vectors $\mathbf{a}_1$ and $\mathbf{a}_2$, directly connected to the A lattice via the nearest neighbour hopping vectors δ_1, δ_2, δ_3. Just like the original lattice, the reciprocal lattice displays always a hexagonal structure, rotated by $\pi/2$ in comparison with the real space lattice, and it is described by the primitive translation vectors $\mathbf{b}_1$ and $\mathbf{b}_2$ centered around the $\mathbf{\Gamma}$ point. The relation between the real and reciprocal primitive vectors is $\mathbf{a}_\mathrm{i} \cdot \mathbf{b}_\mathrm{i} = 2\pi\delta_\mathrm{ij}$. The boundaries of the irreducible first Brillouin zone are the lines normal to the reciprocal lattice vectors at their midpoints. Among the six corners of the Brillouin zone, only two are inequivalent and are indicated as the $\mathbf{K}$ and $\mathbf{K}'$ points.

1.1.2 Dispersion relation

Let us imagine, as a Gedankenexperiment, to build a hexagonal graphene lattice by bringing the various carbon atoms close to each other. When the interatomic spacing starts to be comparable with the space extension of the $2p_z$ orbital, the physical proximity induces orbital overlaps, and electrons in one orbital starts to "feel" the neighbouring atoms. In the tight-binding approximation, the overlap between the atomic wavefunctions requires the presence of a correction factor from the single-atom model, and the final result consists on the building up of a series of Bloch wave functions. In the case of graphene, the Bloch wave function is written as a linear sum of Bloch waves centred around the A and B atoms. If we denote with $\phi(\mathbf{r})$ the atomic wave function of a p_z-orbital, we can rewrite the previous combination in the following manner:

$$\psi_\mathbf{k}(\mathbf{r}) = \frac{1}{\sqrt{N}} \sum_\mathbf{R} e^{i\mathbf{k}\cdot\mathbf{R}} \left(f_{\mathbf{k},\mathrm{A}}\phi(\mathbf{r} - \mathbf{R} - \delta_3) + f_{\mathbf{k},\mathrm{B}}\phi(\mathbf{r} - \mathbf{R}) \right), \tag{1.1}$$

where $f_{\mathbf{k},\mathrm{A}}$ and $f_{\mathbf{k},\mathrm{B}}$ are the complex coefficients of the linear combination, $\mathbf{R}$ is the lattice vector and N the quantity of lattice sites.

The solution of the Schrödinger equation $H\psi_\mathbf{k}(\mathbf{r}) = E_\mathbf{k}\psi_\mathbf{k}(\mathbf{r})$, within the tight-binding model, gives the energy dispersion of graphene. In order to simplify the analytical calculation of the spectrum $E_\mathbf{k}$, the overlap among the A and B-type orbital wave functions can be neglected by imposing the orthogonality relation $\langle\phi(\mathbf{r})|\phi(\mathbf{r} - \delta_3)\rangle = 0$. Considering that an electron can hop between the nearest-neighbour (nn) and next-nearest-neighbour (nnn) atoms, the energy dispersion takes the form:

$$E_\pm(\mathbf{k}) = \pm t\sqrt{3 + f(\mathbf{k})} - t' f(\mathbf{k}), \tag{1.2}$$

with $f(\mathbf{k}) = 2\cos(\sqrt{3}k_\mathrm{x}a_0) + 4\cos(\frac{\sqrt{3}}{2}k_\mathrm{x}a_0)\cos(\frac{3}{2}k_\mathrm{y}a_0)$. t and t' are respectively the nearest-neighbour and the next-nearest-neighbour hopping energies. This last term is responsible for the π and π^* bands broken symmetry. In Fig.1.2 we show the full band structure, with a zoom in the vicinity of the Dirac point at the K point of the Brillouin zone.

In the hypothesis of low excitation energies governing the free quasi particles in graphene, the dispersion relation can be linearised in the close vicinity of the Dirac point by calculating

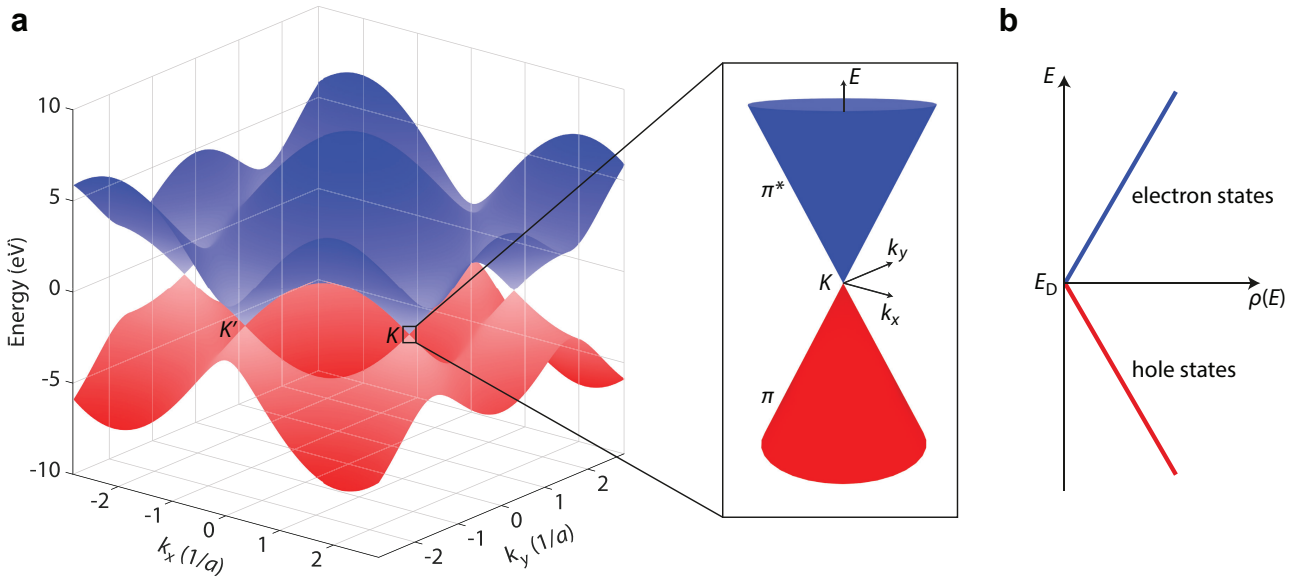

Figure 1.2: (a) Bandstructure in graphene with the lower and upper band (π and π^* respectively) touching at the Dirac points corresponding to the corners of the first Brillouin zone. The energy dispersion around the Dirac points can be approximated with a linear dependence versus the k-vector value. (b) Low-energy density of state in graphene, centred around the Dirac point. Pictures inspired from [26].

the linear expansion of the full band structure. After having defined a new wave vector centred around the Dirac point ($\mathbf{q} = \mathbf{k} - \mathbf{K}_\mathrm{D}$), the first order expansion of the spectrum 1.2 is

$$E_\pm(\mathbf{q}) = \pm\frac{3ta_0}{2}|\mathbf{q}| = \pm v_\mathrm{F}\hbar|\mathbf{q}| \tag{1.3}$$

The Fermi velocity $v_\mathrm{F} = \frac{3ta_0}{2\hbar} \approx 10^6 m/s$, is introduced, which stems from the linear dispersion. This parameter is independent from the momentum associated to charge carriers. Essential consequence of the linear dispersion is that charge carriers in graphene can be treated as ultrarelativistic Dirac fermions, having constant group velocity v_F.

1.2 Sublattice pseudospin

The low-energy form of the graphene Hamiltonian can be written accordingly to the relativistic Hamiltonian developed by Dirac himself, with the use of the Pauli matrices $\sigma_\mathrm{x}, \sigma_\mathrm{y}, \sigma_\mathrm{z}$. These matrices were originally introduced by Pauli as a mathematical instrument to describe the two degrees of freedom of the spin for a fermionic particle in the three directions [126].

$$\sigma_\mathrm{x} = \begin{pmatrix} 0 & 1 \\ 1 & 0 \end{pmatrix}, \sigma_\mathrm{y} = \begin{pmatrix} 0 & -i \\ i & 0 \end{pmatrix}, \sigma_\mathrm{z} = \begin{pmatrix} 1 & 0 \\ 0 & -1 \end{pmatrix}$$

Here we report in compact form the relativistic Hamiltonians associated to the $\mathbf{K}$ and $\mathbf{K}'$ points, where the intrinsic ability of electrons in graphene to distribute within the A and B sublattices is described by means of two Pauli matrices $\sigma = (\sigma_\mathrm{x}, \sigma_\mathrm{y})$.

$$\begin{aligned} H_\mathbf{K} &= \hbar v_\mathrm{F}\sigma \cdot \mathbf{q} \\ H_{\mathbf{K}'} &= -\hbar v_\mathrm{F}\sigma^* \cdot \mathbf{q}' \end{aligned} \tag{1.4}$$

Because of the formal analogy with the usual spin, the sublattice degree of freedom is usually referred to as pseudospin.

The Hamiltonians $H_{\mathbf{K}}$ and $H_{\mathbf{K}'}$ act separately on the cell wavefunctions (Eq.1.1) centred respectively around the $\mathbf{K}$ and $\mathbf{K}'$ points

$$\begin{aligned} H_{\mathbf{K}}\psi_{\mathbf{q}} &= \hbar v_{\mathrm{F}}\sigma\cdot\mathbf{q}\begin{pmatrix} f_{\mathbf{q},\mathrm{A}} \\ f_{\mathbf{q},\mathrm{B}}\end{pmatrix} \\ H_{\mathbf{K}'}\psi_{\mathbf{q}'} &= -\hbar v_{\mathrm{F}}\sigma^{*}\cdot\mathbf{q}'\begin{pmatrix} f_{\mathbf{q}',\mathrm{A}} \\ f_{\mathbf{q}',\mathrm{B}}\end{pmatrix} \end{aligned} \tag{1.5}$$

1.2.1 Physical interpretation of the sublattice pseudospin

The best way to grasp the physical meaning behind the pseudospin formalism is through a simplified example. Let us consider the problem of an ultrarelativistic particle having momentum $\mathbf{q} = (q_{\mathrm{x}}, 0)$ and moving along the x direction. The eigenvalue equation at the $\mathbf{K}$ point can be written in the following way

$$\hbar v_{\mathrm{F}}\sigma_{\mathrm{x}}q_{\mathrm{x}}\ \psi_{\mathbf{q}} = \hbar v_{\mathrm{F}}q_{\mathrm{x}}\begin{pmatrix} 0 & 1 \\ 1 & 0\end{pmatrix}\ \psi_{\mathbf{q}} = E_{\mathbf{q}}\ \psi_{\mathbf{q}} \tag{1.6}$$

The eigenvalues of this last equation are $E_{\mathbf{q}_1} = \hbar v_{\mathrm{F}}q_{\mathrm{x}}$ and $E_{\mathbf{q}_2} = -\hbar v_{\mathrm{F}}q_{\mathrm{x}}$, with associated eigenvectors being the standard eigenvectors of the Pauli matrix σ_{x}

$$\underbrace{\psi_{\mathbf{q}_1} = \frac{1}{\sqrt{2}}\begin{pmatrix}1\\1\end{pmatrix}}_{\text{pseudospin rightwards}} \qquad \underbrace{\psi_{\mathbf{q}_2} = \frac{1}{\sqrt{2}}\begin{pmatrix}1\\-1\end{pmatrix}}_{\text{pseudospin leftwards}}$$

For each particular energy eigenvalue, we can evaluate the group velocity associated to the

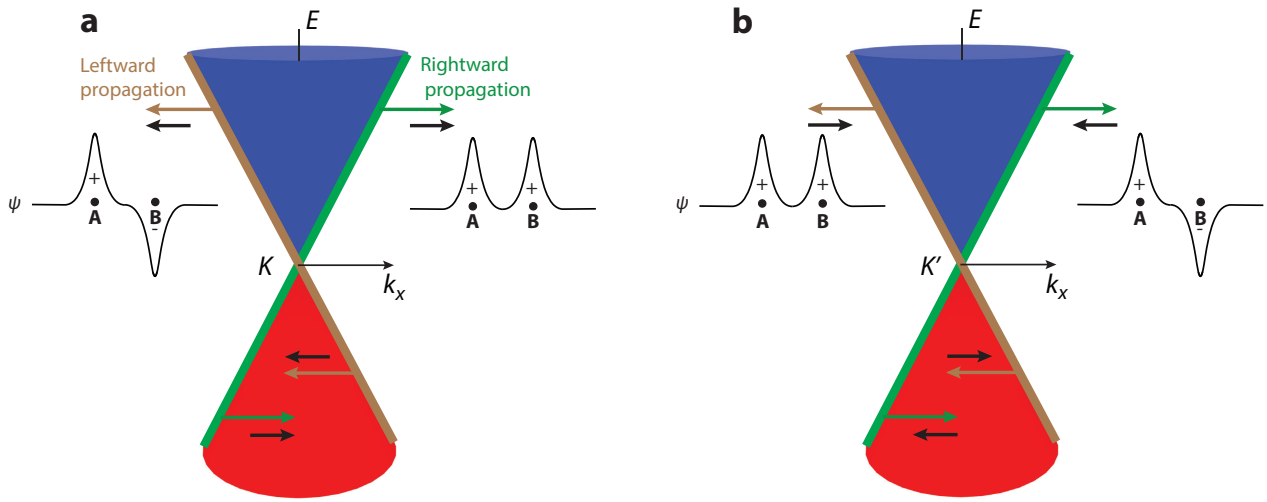

Figure 1.3: (a,b) Representation of $\mathbf{K}$ and $\mathbf{K}'$ Dirac cones with the directions of propagation for Dirac fermions. The thick black arrows indicate the pseudospin orientation describing the magnitude and sign of the wave function in the A and B lattice sites.

relativistic quasi particle

$$\underbrace{v_{\mathbf{q}_1} = \frac{1}{\hbar}\frac{\partial E_{\mathbf{q}_1}}{\partial q_\mathrm{x}} = +v_\mathrm{F}}_{\text{particle moving to the right}} \qquad \underbrace{v_{\mathbf{q}_2} = \frac{1}{\hbar}\frac{\partial E_{\mathbf{q}_2}}{\partial q_\mathrm{x}} = -v_\mathrm{F}}_{\text{particle moving to the left}}$$

It is therefore interesting to see that an electron moving to the right direction is characterized by a rightward pseudospin, with the pseudo-spinor components having the same sign in both A and B lattice sites. Moreover, its energy eigenvalue must have the same sign of the wave number q_x. Conversely, a particle characterized by a leftwards pseudospin has a direction of propagation opposite with respect to the previous case, and the energy eigenvalue and wave number have both opposite signs. The components of the pseudo-spinor show same magnitudes but different signs.

Similar calculations can be done considering the $\mathbf{K}'$ point. The only difference is now on the direction of the pseudospin that results opposite to the $\mathbf{K}$ valley case. A schematic view of the pseudospin evolution is reported in Fig.1.3, for both the $\mathbf{K}$ and $\mathbf{K}'$ valleys. The pseudospins are represented with black arrows, while the orientation of the velocity vectors are depicted with green and brown arrows.

1.2.2 Polar form of the sublattice pseudospin

The previous example of the particle moving along the x axis can be extended by considering an arbitrary wave vector $\mathbf{q}$ in the reciprocal space. In this case, the eigenvalue problem reads

$$\hbar v_\mathrm{F} \begin{pmatrix} 0 & q_\mathrm{x} - iq_\mathrm{y} \\ q_\mathrm{x} + iq_\mathrm{y} & 0 \end{pmatrix} \psi_\mathbf{q} = E_\mathbf{q}\, \psi_\mathbf{q} \tag{1.7}$$

By expressing the wave vector in polar coordinates $\mathbf{q} = |\mathbf{q}|(\cos\alpha, \sin\alpha)$ (see Fig.1.4), the previous eigenvalue problem takes the more generalized form

$$\hbar v_\mathrm{F}|\mathbf{q}| \begin{pmatrix} 0 & e^{-i\alpha} \\ e^{+i\alpha} & 0 \end{pmatrix} \psi_\mathbf{q} = E_\mathbf{q}\, \psi_\mathbf{q} \tag{1.8}$$

having eigenvalues $E_\mathbf{q} = \pm\hbar v_\mathrm{F}|\mathbf{q}|$ and eigenvectors $\psi_\mathbf{q} = \frac{1}{\sqrt{2}} \begin{pmatrix} 1 \\ \pm e^{+i\alpha} \end{pmatrix}$.

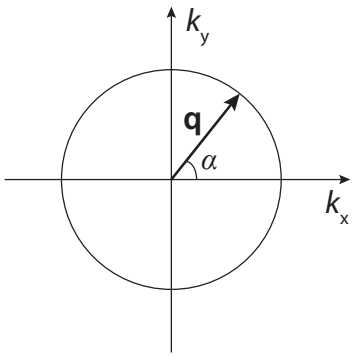

Figure 1.4: Representation of a wave vector $\mathbf{q}$ in one valley, with the polar angle α describing its angular orientation.

1.3 Klein tunneling

Let us consider now the quantum mechanical problem of a non-relativistic particle, with kinetic energy E_{kin}, striking a potential step of finite width and amplitude $U_0 > E_{\text{kin}}$. Typically, the wavefunction is entering the step region in the form of evanescent waves. However, when studying the case of a relativistic particle obeying to the three dimensional massive Dirac equation, it turns out that tunnelling can take place with certainty whatever is the height and the width of the wall. First description of this process was theoretically presented in 1929 by the physicist Oscar Klein [81]. A similar effect has been predicted in graphene, where 2D massless electrons normally incident on a potential barrier should be perfectly transmitted, in close analogy with the previous case of Klein paradox [67]. In graphene, this mechanism of "Klein tunnelling" cannot really be associated to standard tunnelling, since it does not rely on evanescent waves. However, its explanation can be found when considering an unique property of massless Dirac fermions: the sublattice pseudospin conservation [4].

1.3.1 Single valley approximation

In order to maintain the validity of the previously presented low-energy picture of electronic excitations, it is necessary to bound the dynamical states of the electrons in the close vicinity of one Dirac cone composing the Brillouin zone. Knowing that $|\mathbf{K}| \sim 1/a$, the single valley condition can be achieved by imposing the constrain $|\mathbf{q}| \ll |\mathbf{K}|$ [56].

In graphene devices, the ambipolar field effect is a phenomenon directly linking the value of the wave vector $|\mathbf{q}|$ with an external gate voltage over a graphene region. The presence of an external electric field modifies locally the electrostatic potential of graphene, generating thus a shift of the Dirac cone upwards or downwards in the energy spectrum, tuning the Fermi level to be in the upper or lower region of the cone. The spatial distribution of an electrostatic potential is therefore fundamental for the validity of the single valley approximation. From the point of view of an engineer, the main requirement for the design of a graphene device, within the single valley approximation, is to guarantee a slowly varying electrostatic potential over the lattice period $a = 0.246$ nm [4].

The possibility to guarantee a net decoupling between the Dirac cones keeps intact the vision of two independent Dirac equations describing the electronic properties of graphene. The single valley Dirac Hamiltonian can be therefore written in the form $\hat{H} = \hat{H}_{\text{kin}} + \hat{V}(x, y)$, with the slowly-varying potential matrix $\hat{V}(x, y)$ considered diagonal in the sublattice space [128].

1.3.2 Pseudospin conservation

Let us consider again the example presented in Section 1.2.1 of an electron propagating in the x direction. However, this time we consider the particular case of a particle characterized by a positive momentum eigenstate $q_{\text{x}} > 0$, normally incident on a potential step (see Fig.1.5). The Dirac Hamiltonian of the system in the $\mathbf{K}$ valley reads (the discussion for the $\mathbf{K}'$ valley goes along the same way)

$$\hat{H}_{\mathbf{K}} = \hbar v_{\text{F}} \sigma \cdot \mathbf{q} + \hat{V}(x) \tag{1.9}$$

For simplicity I impose $\hbar = 1$ and $v_{\text{F}} = 1$.

According to the Heisenberg picture, the velocity operator in the x direction, as well as its

time evolution, are both represented by

$$\hat{v}_{\mathrm{x}} = -i[x, \hat{H}_{\mathbf{K}}] = \sigma_{\mathrm{x}} \tag{1.10}$$

$$\frac{\mathrm{d}}{\mathrm{d}t}\hat{v}_{\mathrm{x}} = -i[\sigma_{\mathrm{x}}, \hat{H}_{\mathbf{K}}] = 2\sigma_{\mathrm{z}} q_{\mathrm{y}} \tag{1.11}$$

Since the system is considered invariant along the y direction, it is possible to infer that the component $q_{\mathrm{y}} = 0$ of the wave vector is conserved. Hence, representing with $|\psi(0)\rangle$ the initial state of the electron, at any time t it is possible to write the following equality

$$\langle\psi(t)| \frac{\mathrm{d}}{\mathrm{d}t}\hat{v}_{\mathrm{x}}(0) |\psi(t)\rangle = \langle\psi(0)| \frac{\mathrm{d}}{\mathrm{d}t}\hat{v}_{\mathrm{x}}(t) |\psi(0)\rangle = 0 \tag{1.12}$$

Which means that the velocity of the particle v_x (equivalently its speudospin) is always constant along x, even when the electron crosses the barrier. The normally incident electron is therefore perfectly transmitted without any backscattering process [4]. This perfect transmission is usually referred as Klein tunnelling.

1.4 Graphene p-n junctions

The lack of effective confinement associated to the linear dispersion, makes graphene unsuited for standard electronic applications such as transistors or diodes. This peculiarity forces to rethink creatively the foundations of the present electronics, looking for new inclusive strategies to put graphene in the present worldwide market or to seek novel not-existing applications as suggested in the European roadmap for graphene science and technology [51].

We proceed now with the theoretical part dedicated to the graphene p-n junction, an unusual electronic platform which allows to exploit a novel class of physical phenomena for electron optics applications.

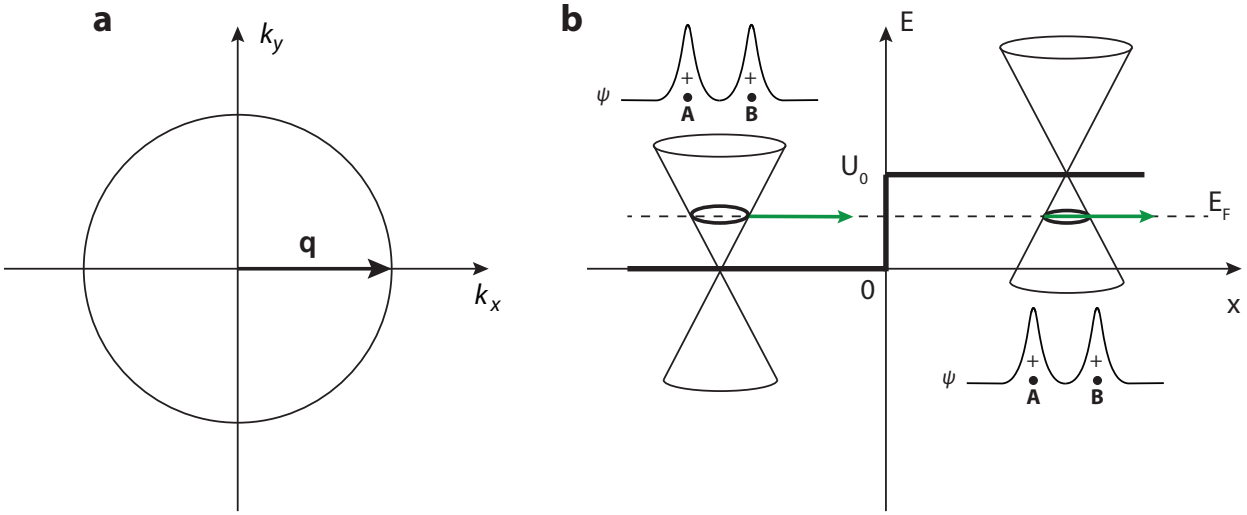

Figure 1.5: (a) Wave vector **q** for an eigenstate propagating orthogonally to the abrupt p-n interface. (b) Real space representation of a Dirac fermion striking on a potential step U_0. The Fermi energy is represented with a constant dashed line. The green arrows represents the velocity vectors of a propagating Dirac fermion. The velocity of the particle, as well as the pseudospinor components are conserved before and after the transmission across the potential step.

In ballistic graphene p-n junctions, electrons can flow through the valence band (*hole*-like Dirac fermions) or through the conduction band (*electron*-like Dirac fermions). These different behaviours can be generated in the same graphene layer via the ambipolar field effect inducing a spatial dependent electrostatic doping. The interplay of different doped regions, offers the possibility to control electrostatically the spatial arrangement of an injected current flow. At the basis of this last effect, there are electron refraction processes developing at the boundaries between different doped areas, which are effectively described by a specific Snell-Descartes law for Dirac fermions [4].

1.4.1 Snell-Descartes law for Dirac fermions

Until now, the 2D angular spreading of electrons impinging on a potential step has not been considered yet. Let us focus on the schematic of a p-n junction in Fig.1.6.a. The left and the right sides of the junction are characterized by a kinetic energy $E_{\text{kin}} = E$ and $E_{\text{kin}} = E - U_0$ respectively, where E is the energy of an incident electron from the left and U_0 the is the amplitude of the step potential. Let us consider the particular case of a bipolar (p-n) junction in which the upward shift of the Dirac cone in the right side is larger than the kinetic energy in the left region ($E < U_0$). The direction of propagation of an electron towards the interface is described by its velocity vector $\mathbf{v}_{\text{inc}}$. Both the velocity vector and the wave vector $\mathbf{q}$ can be therefore expressed in polar coordinates, as a function of the incidence angle α.

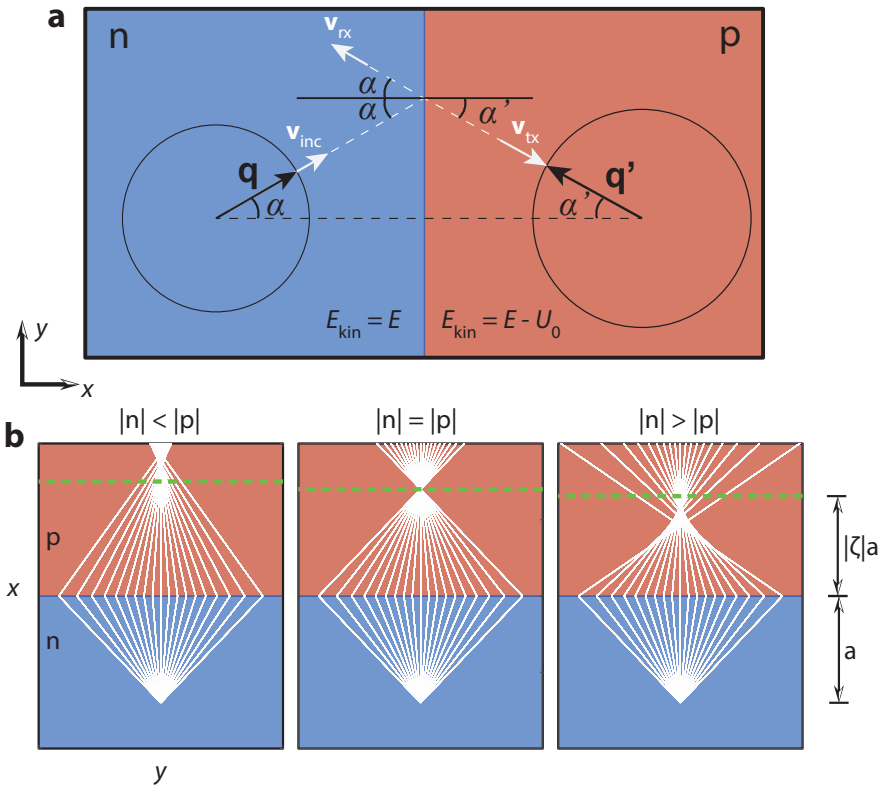

Figure 1.6: (a) Vectorial representation of the refraction and reflection of an incident wave on a p-n junction. (b) Classical refracted ray trajectories with the evolutions of a focal point in the p-doped region, according to different doping conditions on a graphene p-n junction.

$$\mathbf{v}_{\text{inc}} = v_{\text{F}}(\cos\alpha, \sin\alpha) \tag{1.13}$$

$$\mathbf{q} = q(\cos\alpha, \sin\alpha) \tag{1.14}$$

Like in any standard quantum mechanical problem of transmission and reflection over a potential energy profile, at the junction level we can expect to obtain partial transmission and reflection of the electron waves. Because of the geometrical invariance of the kinetic energy profile along the y direction, for the transmission process it is possible to impose a conservation rule on the transverse component of the wavevector describing the particle propagation. In particular, for an impinging and transmitted wave, we can write the following equality $q'_{\text{y}} = q_{\text{y}}$. Therefore, by considering the invariance of the transverse wave vector component during the transmission, and recalling the linear dispersion in graphene which sets a direct link between E_{kin} and $|\mathbf{q}|$, it is possible to write the following equation:

$$E \sin\alpha = (E - U_0) \sin\alpha' \tag{1.15}$$

We usually refer to this last equation as the *Snell-Descartes law* for Dirac fermions in graphene. Exactly like in geometrical optics, the transmission of electron waves in graphene, at abrupt potential interfaces, is fully described by a refraction law where the local kinetic energies play the essential role of refractive indices. It is important to remind here that the abruptness of an electrostatic interface must never be smaller than the atomic distance. This last constrain will preserve the validity of the single-valley approximation. I can now introduce the relative refraction index ζ, which is defined as the ratio between the energies on both sides of the junction

$$\zeta = \frac{E - U_0}{E}. \tag{1.16}$$

In the case of a p-n interface, the relative refractive index assumes negative values. This peculiarity tells us that Dirac fermions in p-n junctions can experience negative refraction processes similar to left-handed metamaterials in optics. Upon negative refraction, it is possible to transform a divergent electron beam emitted from a point source on one side of the junction,

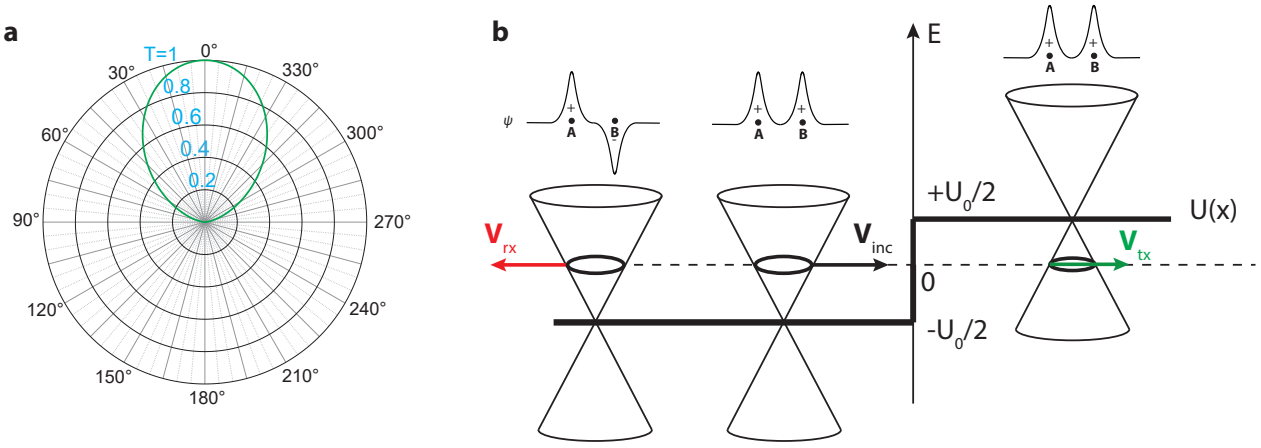

Figure 1.7: (a) Polar plot of the transmission probability in the case of a symmetric graphene p-n junction. (b) Band structure across a symmetric graphene p-n junction. The transmission process conserves the pseudospin, while the reflection at the barrier reverses the pseudospin orientation.

into a convergent stream on the other side even with a straight interface, i.e. without curvature. This phenomenon has been detected in two experimental works, one by transport [86] and one by magnetic focusing in a pn junction [30]. Schematic of the focusing process is reported in Fig.1.6.b for three different doping conditions. Perfect focusing can be achieved in the presence of a symmetric junction where $|n| = |p|$. Electron injected in the n-side at a distance a from the interface, will re-focus again in the p-side in a symmetric spot at equal distance. In the case of an asymmetric p-n junction, the focal point transforms into a cusp singularity centred at a distance $|\zeta|a$ from the junction [29].

Like in classical optics, we can use the Snell-Descartes law to define the critical angle α_c for which an impinging electron wave experiences total internal reflection at the barrier.

$$\sin(\alpha_c) = (U_0 - E)/E. \tag{1.17}$$

1.4.2 Transmission and reflection probabilities

Refraction is a wave phenomenon, resulting from the interaction of an impinging Dirac fermion on an abrupt potential step. The angular dependence of the transmission intensity can be obtained by imposing the matching of the isospin states located in the left and right sides of the p-n interface. Therefore, it is possible to carry out the calculations for the reflection R and transmission T probabilities based on the value of the impinging angle α. According to [4], these quantities are given by

$$\begin{cases} T = -\cos(\alpha)\cos(\alpha' + \pi)/\sin^2\left(\frac{\alpha+\alpha'+\pi}{2}\right) \\ R = \cos^2(\frac{\alpha-\alpha'-\pi}{2})/\sin^2(\frac{\alpha+\alpha'+\pi}{2}) \end{cases} . \tag{1.18}$$

The schematic of the transmission and reflection, with the associated angles, is available in Fig.1.6.a. In the case of a symmetric p-n junction, the transmission probability reduces to $T = \cos^2(\alpha)$. Its polar plot is reported in Fig.1.7.a, in which the absence of critical angle determines a generally big transmission for a large variety of incident angles. The possibility to transmit a broad amount of different electron trajectories is essential for the detection of clear Veselago lensing signatures [29].

1.4.3 Transport in smooth junctions

An abrupt p-n junction interface is an utopia that allows to easily handle the electron optical effects in a ballistic graphene junction. However, it is necessary now to gradually evolve this naive picture, introducing more realistic electrostatic potentials which impact on the angular transmission and reflection of incident electrons. Let us consider the piecewise potential distribution in Fig.1.8, where the potential is defined in the following way

$$U(x) = \begin{cases} -U_0/2 & x \leq -d \\ Fx & -d < x \leq d \\ +U_0/2 & x > d \end{cases} . \tag{1.19}$$

where $F = U_0/(2d)$ is the electric field of the linearly evolving potential. In the case of a smoothly varying potential, in which $\lambda_F \ll d$, the equation describing the transmission across the junction reads [4, 28]

$$T(\alpha) \approx e^{-\pi k_F d \sin^2\alpha} \tag{1.20}$$

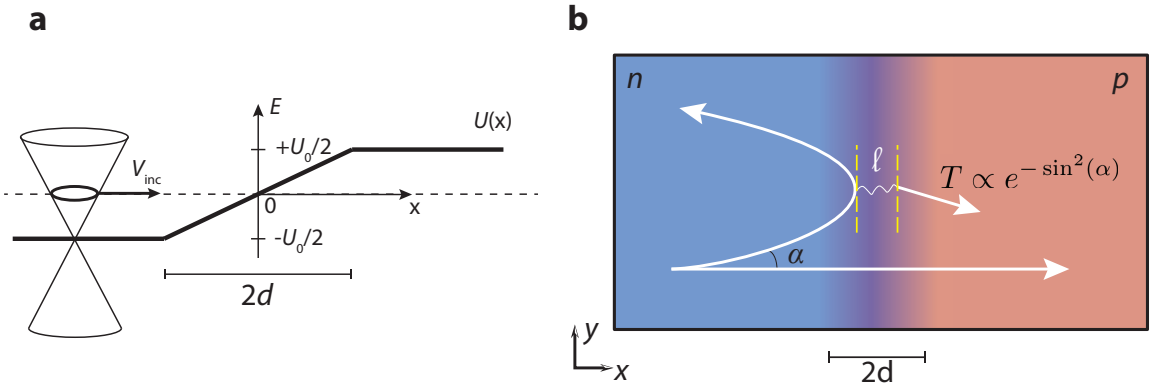

Figure 1.8: (a) Schematic representation of a smooth p-n junction electrostatic potential $U(x)$ extending along the x-axis. The junction has a potential height U_0 with a linear extension $2d$ in the middle region of the junction width. (b) 2D representation of different transmissions processes on a smooth p-n junction. Normal incident trajectories are perfectly transmitted with probability T=1. Transmission of non-orthogonal trajectories requires a tunnel process relying on evanescent waves inside the classically forbidden region of length l.

The presence of an exponential dependence on α forces a dramatic selection on the transmitted incidence angles. Indeed, an electron wave that enters the smoothly varying potential region with a non-zero q_y component, experiences a gradual deflection with the eventual impossibility to extend beyond a turning point located in the central region of the p-n junction (see Fig.1.8.b). This effect can be understood within the semi-classical theory, where a Dirac fermion can be seen as a point particle obeying to the following relativistic dispersion relation in normalized units

$$(E - U(x))^2 = v_F^2 \mathbf{p}^2 \tag{1.21}$$

The particle dynamics can be fully described considering a semi-classical relativistic Hamiltonian

$$H_{sc} = \eta(x)\ v_F|\mathbf{p}| + U(\mathbf{r}) \tag{1.22}$$
$$\tag{1.23}$$

where $\eta(x) = sign(E - U(x))$ is the spatially dependent band index. The associated equations of motion read

$$\frac{dx}{dt} = \frac{\partial H_{sc}}{\partial p_x} = \frac{\eta(x) v_F p_x}{\sqrt{p_x^2 + p_y^2}} \tag{1.24}$$
$$\frac{dy}{dt} = \frac{\partial H_{sc}}{\partial p_y} = \frac{\eta(x) v_F p_y}{\sqrt{p_x^2 + p_y^2}} \tag{1.25}$$

When the system shows a translational invariance along the y axis, the momentum p_y is constant ($dp_y/dt = dH/dy = 0$) and the time dependency can be removed by dividing together the two equations of motion. We thus obtain the equation for the semi-classical trajectories inside a smooth graphene p-n junction

$$y(x) = y_0 + \int_{x_0}^{x} \frac{p_y}{\sqrt{\left(\frac{E - U(x')}{v_F}\right)^2 - p_y^2}}\, dx' \tag{1.26}$$

It is interesting to analyse the role of the denominator in the integral of eq.1.26. When the argument of the square root assumes negative values, it becomes imaginary. This is a particular condition that manifests in the middle of a smooth junction, whenever $|E - U(x)| \leq |p_y| v_F$. When the last inequalities is verified inside the junction, the semi-classical model is no more able to describe the motion of electron waves, since classically those regions cannot be penetrated [117]. As a result, particles having $q_y = 0$ are perfectly transmitted due to the absence of backscattering (Klein tunnelling), while if $q_y \neq 0$ the transmission occur only via a tunnel process relying on evanescent waves through the classically forbidden region. In the case of the potential profile in Eq.1.19, the classically forbidden region is located at the junction center (see Fig.1.8), having an extension $l = 2d \sin \alpha$ [4].

If a perfectly abrupt p-n junction enables the focusing via negative refraction, then a smooth junction will generally blur the image generated at the focal point. The resolution lowering can be attributed to the spatial extension of the classically forbidden regions where fermions tunnel through.

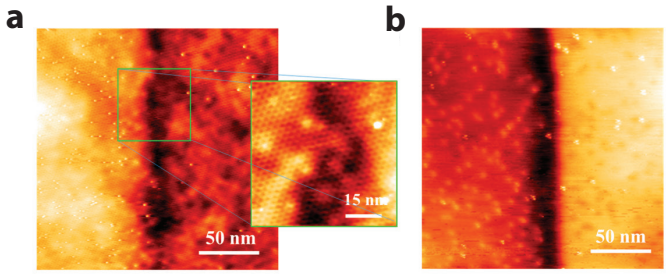

c

	PolySi Gate	Graphite Gate
RMS (nm)	2.3	0.81
Correlation length (nm)	7.7	15.5

Figure 1.9: (a) Scanning tunnelling microscopy (STM) topographic image of a graphene junction fabricated with polySi electrostatic gates (b) Topography of a junction with the interface formed with a pristine graphite flake. (c) Table of the root mean square (RMS) roughness and correlation lengths of the local density of states (LDOS) measured along the junctions interfaces. Pictures taken from [159].

1.4.4 Quality of the p-n interface

In real p-n junctions, the focusing is never ideal. When injected from a source contact, electron trajectories propagate at different angles with respect to the interface. Once reaching the potential step, each trajectory contributes to the formation of a convergent beam. But, in a realistic case not all these components will focus at the same spot. One of the most relevant imperfection that we can put under the spotlight is the junction roughness, which emerges from atomic scale imperfections. This roughness reduces the electron-optical performances of a p-n junction, randomizing the refracted trajectories [92, 159].

A recent scanning tunnelling microscopy (STM) study put in evidence the importance of the materials employed in the design of electrostatic gates in order to achieve high quality junction interfaces in graphene heterostructures [159]. The result of this study showed that heterostructures designed with naturally cleaved graphite gates reduce the problems associated to metallic gates, namely the irregular grain structures. This evidence can be observed in Fig.1.9, where STM topographic images allow to compare the roughnesses characterizing a p-n junction made with polysilicon gates (Fig.1.9.a), another one made with a pristine graphite flake placed underneath the graphene heterostructure (Fig.1.9.b).

1.5 Lensing with graphene n-p-n junctions

1.5.1 Planar Veselago lens

A p-n junction is a platform offering opportunity to refract electron waves similar to left-handed metamaterials in optical systems. The use of graphene junctions allows to design very original refracting systems like the perfect lens proposed by Veselago in 1968 [145]. An equivalent version of the Veselago lens for Dirac fermions can be obtained with the graphene double junction as shown in Fig.1.10.a.

The Veselago lens differs conceptually from the orthodox idea of lens, since it cannot focus bundle of rays coming from infinity. In order to achieve the perfect focusing, it necessarily requires the presence of a Huygens-like point source of travelling waves originating from the n-doped region. This is a strong requirement for a lens, but it generates the theoretical possibility to have image reconstruction in the other side of the lens, at distance $d - l$, with resolution below the diffraction limit [121].

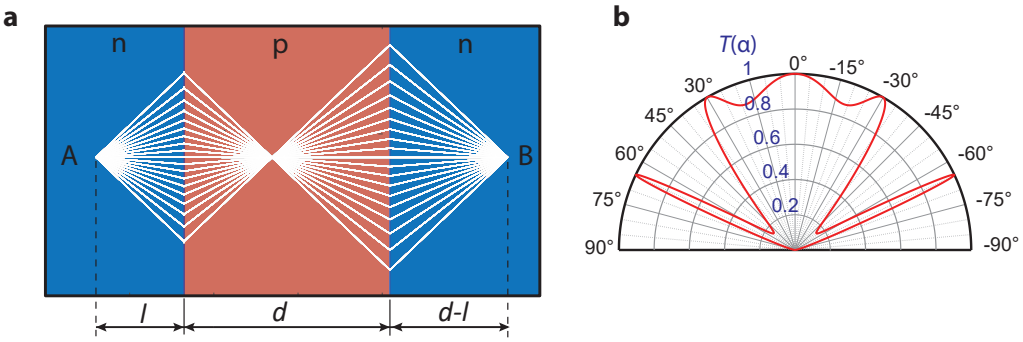

Figure 1.10: (a) Representation of a graphene Veselago lens. The ray trajectories originating at the point source A can refocus again in the n-region at point B, with perfect focusing below the diffraction limit, if $|n| = |p|$. (b) Example of transmission probability through a non-symmetric n-p-n junction with a p-region having a spatial extension $d = 110\ nm$. The kinetic energy in the n-region is $E_{\text{kin}} = 80$ meV, with Fermi wavelength of $\lambda_{\text{F}} = 50\ nm$. The potential barrier height between the n- and p-side is $U_0 = 200$ meV.

Transmission probability We present here the result of the transmission probability for a n-p-n junction, where the electrostatic potential is distributed according to the following piecewise expression

$$V(x) = \begin{cases} U_0 & 0 < x < d \\ 0 & \texttt{otherwise} \end{cases}$$

where d is the width of the potential barrier for the p-region [79]. For sake of simplicity, we assume the ideal case of infinite extended n-regions. We consider the case of a sharp barrier, with potential variations confined in small regions of length l at each interface, and with no intervalley scattering ($a \ll l \ll \lambda_{\text{F}}$).

By imposing the matching condition for the wave functions in the three regions with different doping, the transmission through the barrier takes the form [26]

$$T(\alpha) = \frac{\cos^2\theta\ \cos^2\alpha}{\left[\cos(q_x d)\cos\alpha\cos\theta\right]^2 + \sin^2(q_x d)(1 - ss'\sin\alpha\sin\theta)^2} \tag{1.27}$$

Where $\mathbf{k} = (k_x, k_y)$ and $\mathbf{q} = (q_x, k_y)$ are the wave vectors in the n- and p-region respectively.

$$q_x = \sqrt{(E - U_0)^2 / \hbar^2 v_F^2 - k_y^2}$$
$$\theta = \arctan(k_y / q_x)$$
$$s = \text{sign}(E)$$
$$s' = \text{sign}(E - U_0)$$

Figure 1.10.b shows an example of polar diagram representing the transmission probability as a function of the impinging angle α of an electron. From the picture it can be noticed that there are several angles for which the transmission is one.

1.5.2 Circular Veselago lens

Different interesting graphene platforms for electron optics can be developed by shaping the size of the doped regions. We present here the case of circular graphene lenses that can be obtained using specific gates, generating electrostatic potential variations having radial symmetry. Depending on the smoothness of the electrostatic potential, we can achieve different lensing effects that can be investigated theoretically by means of a semi-classical approach [117, 64, 152, 40].

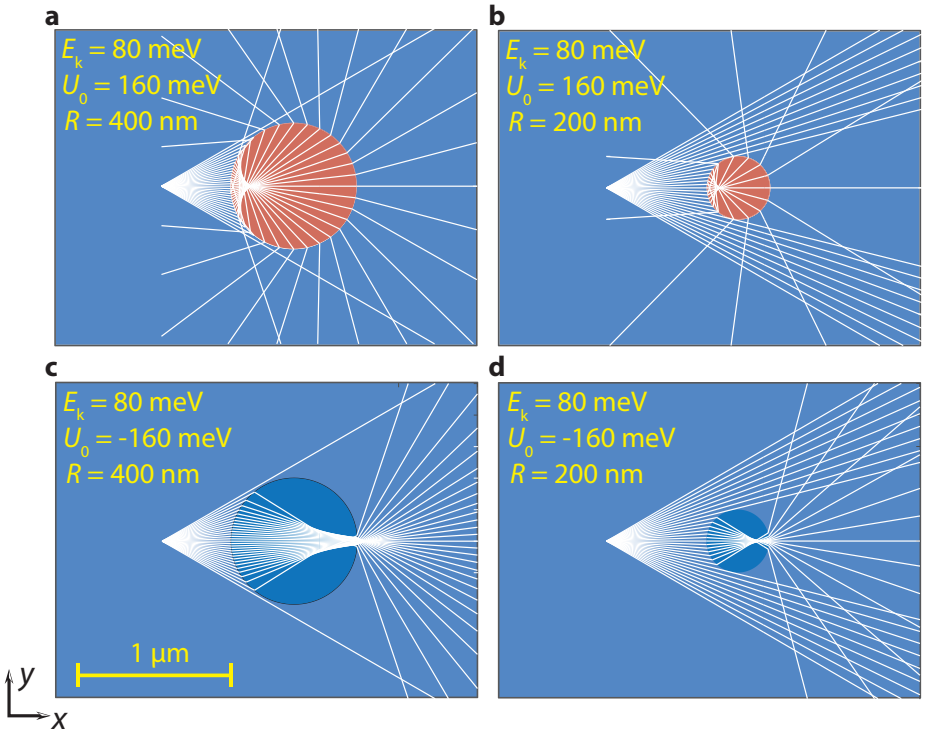

Figure 1.11: Semi-classical ray-tracing simulations of current trajectories flowing in different circular abrupt potentials. Blue and red colours represent the n- and p-doped regions respectively. E_k is the kinetic energy of Dirac fermions in the graphene sheet. U_0 is the peak value of the electrostatic potential applied on the graphene sheet for the definition of the circular perturbation. R is the radius of the circle. (a,b) In the circular Veselago lenses, the potential U_0 induces a symmetric charge inversion condition $|n| = |p|$. (c,d) Ray trajectories in unipolar circular junctions.

In the following, I will present a series of simulated semi-classical lensing effects using a home-made ray-tracing algorithm (more details on the algorithm structure are available in Chapter 3.2). It is worth to mention that the semi-classical approach for the description of a travelling wave function striking against a potential step can be considered exact whenever the condition $\lambda_F \ll a$ is satisfied [152], where a is the graphene inter-atomic distance. Alas, this last requirement is not technologically possible for realistic electron optical experiments.

Abrupt circular graphene lenses Let us consider the case of an abrupt circular graphene junction. In Fig1.11 are reported a series of semi-classical simulations of current trajectories flowing through the refractive medium for different radii and polarities of the circular region. When trajectories in the n-doped side enter the circular p-doped region, they generate inside a cusp singularity, focusing into a caustic. Since the semi-classical picture does not take into account the wave nature of Dirac fermions, we cannot recover from the calculations the quantum interference patterns that has been predicted to develop on the left side of the circle [117].

Smooth circular graphene lenses The circular step potential can be evolved into a smoothed Lorentzian profile if we consider the case of an external metallic AFM probe acting as a gate. In Fig.1.12.(a-c) are represented different semi-classical trajectories for a perturbing electrostatic potential following the phenomenological Lorentzian distribution (Fig.1.12.d) [24].

$$U(\mathbf{r}) = U_0 \frac{R_{\text{tip}}^2}{R_{\text{tip}}^2 + ||\mathbf{r} - \mathbf{r}_{\text{tip}}||^2} \tag{1.28}$$

where $\mathbf{r}_{\text{tip}}$ is the coordinate of the Lorentzian center, $R_{\text{tip}} = \sigma/2$ is the characteristic electrostatic potential decay length, and U_0 the peak value for the Lorentzian potential.

When the tip potential induces charge accumulation (Fig.1.12.a), the particle trajectories bend toward the region at higher kinetic energy, experiencing deflection with focusing behind the junction.

Figure 1.12.b illustrates the case of a strongly invasive tip potential creating a region of charge inversion. The yellow dashed line defines the charge neutrality boundaries dividing the n- and p-doped areas. Because of the potential smoothness, a Lorentzian p-n junction displays a classically forbidden region (similar to the one presented in section 1.4.3), with turning points located according to the incidence angle of the impinging particle trajectories. Contoured by a classical forbidden region, the interior of the p-type area beneath the tip acts as an electronic whispering gallery modes resonator [158, 76], a genuinely quantum behaviour that cannot be captured with semi-classical ray-tracing calculations [1]. Due to Klein tunnelling, only the trajectories orthogonal to the tip potential will flow through the scattering region.

It is necessary to stress out that there is not much difference between a strongly and weakly depleting potential. This can be inferred by visually inspecting the numerical calculations of Fig.1.12.(b-c). A depleting potential acts mostly as a beam splitter, separating even quasi parallel trajectories having low transverse momentum.

[1] The only way to visualize, within the semi-classical picture, the branches of trajectories decaying as they penetrate into the Lorentzian forbidden region, is via semi-classical *uniformization* procedures; eventually replacing the smooth potential with an abrupt potential approximation at the turning point [65]. This last numerical strategy has not been implemented in this thesis.

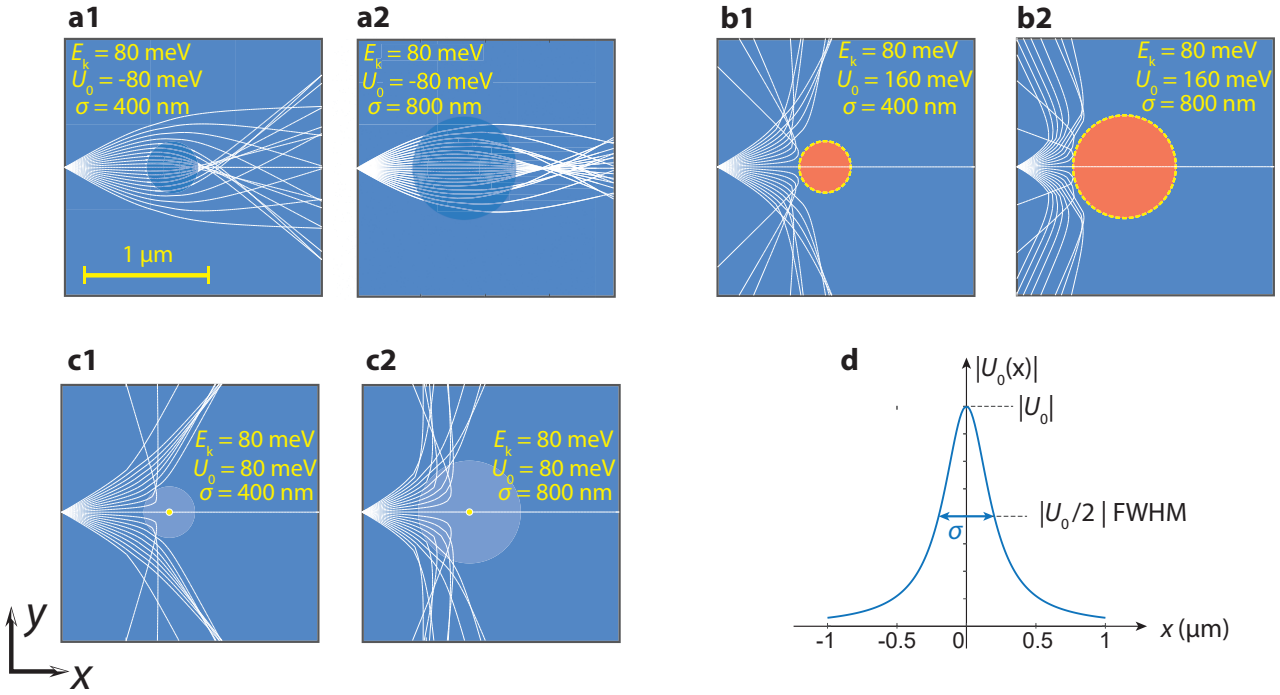

Figure 1.12: Semi-classical ray-tracing simulations of current trajectories for different electrostatic tip potentials U_0. The colored disks indicate the typical extension of the smooth Lorentzian. For each potential, we test two different values of Lorentzian FWHM extension σ. (a1,a2) Electron trajectories flowing into a region of charge accumulation. Depending on the spatial extension of the electrostatic potential, the focusing pattern on the right side displays a different distribution. (b) Trajectories in the presence of a smooth n-p junction. The electrostatic potential of the tip is able to induce a charge inversion region contoured by a dashed yellow line representing the charge neutrality condition. Not-orthogonal trajectories are influenced by the presence of turning points around the smooth interface. Only the normally incident trajectory experiences Klein tunnelling. (c) Trajectories passing through a region of weak depletion. The yellow dot in the centre represents a spot of charge neutrality. d) Example of Lorentzian potential having a spatial FWHM extension $\sigma = 400$ nm (Lorentzian decay parameter $R_{\text{tip}} = \sigma/2 = 200$ nm).

1.6 Experimental signatures of negative refraction

Until now, I have only discussed about the theoretical principles of the electron optics in graphene, without giving much details on the existing experimental studies on angle-dependent carrier transmission and Veselago lensing experiments. In this section, I present two transport experiments which provide indirect signatures of Veselago lensing in graphene heterostructures.

1.6.1 Negative refraction in graphene p-n junction

Signatures of negative refraction of Dirac fermions were observed in the transport experiment proposed by Lee et al. in 2015 [86]. The device was fabricated by encapsulation of a graphene monolayer between two flakes of hexagonal boron nitride. A local top gate in the middle of the heterostructure and a global bottom gate enabled the *in situ* control of the local chemical potentials, i.e. the local kinetic energies of Dirac fermions, in the injection/detection regions and in the central region, independently. The schematic of the device is reported in Fig.1.13.a.

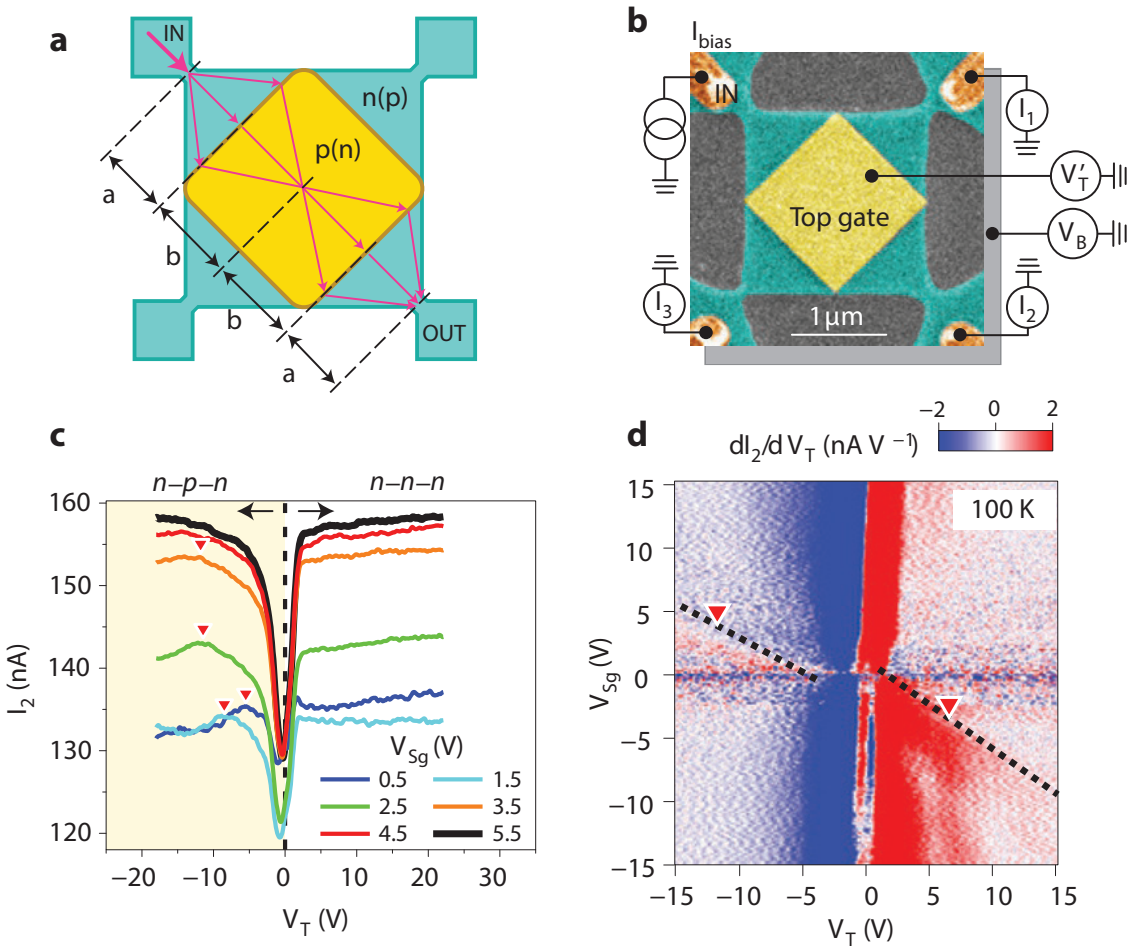

Figure 1.13: (a) Schematic of the Veselago lens with few current trajectories in the focusing condition. (b) Scanning electron micrograph of the Veselago lens device, with the schematic of the measurement set-up. (c) Drain currents I_2 as a function of the top gate voltage V_T, recorded at different values of silicon backgate voltage V_{Sg}. The temperature of the experiment was 100 K. Red triangles in the yellowish area highlight small peaks of current enhancement. (d) 2D color map of the drain current derivative dI_2/dV_T. Black dashed lines represents the theoretical location of the focusing peaks. They match with the boundaries between the positive and negative values of the derivative, which correspond to the small current peaks I_2. Pictures taken from [86].

A few electron trajectories cross the device, forming the characteristic focusing pattern of a Veselago lens. The scanning electron micrograph of the device, as well as the measurement set-up for the transport experiment are reported in Fig.1.13.b.

At the temperature of 100 K, a current of $I_{bias} = 500$ nA was injected from the upper-left contact, while the drain currents at the other leads were measured simultaneously.

Figure 1.13.c shows several drain current I_2 plotted as a function of the top gate voltage V_T, for different fixed values of silicon backgate voltage V_{Sg}. The yellowish area in the plot represents the n-p-n physical regimes of the junction. Interestingly, each plot in the n-p-n area displays a faint current peak on top of the background signal, positioned in correspondence of the red triangles. The authors noticed that the current peaks were shifting linearly with V_{Sg}, for negative values of the ratio V_T/V_{Sg}, in agreement with the theoretical Veselago focusing conditions in the device, which is expected to increase the amount of transmitted current I_2.

A confirmation of the focusing conditions is provided in Fig.1.13.d, where the numerical derivative $\mathrm{d}I_2/\mathrm{d}V_\mathrm{T}$ is shown as a function of both V_Sg and V_T. The theoretical focusing conditions are highlighted by black dashed lines, which lies exactly at the boundaries between the positive (red) and negative values (blue) of the derivative, where the I_2 peaks (the red triangles) are located.

1.6.2 Magnetic focusing with p-n junctions

An indirect observation of the electron Snell's law has been performed in 2016 [30] on a ballistic p-n junction obtained by the encapsulation of a previously exfoliated graphene flake between two flakes of hexagonal boron nitride (see Fig.1.14.a). The presence of two gates, namely the graphite gate and the silicon bottom gate, allowed an independent electrostatic control of the chemical potentials in the two sides of the device.

In presence of a weak perpendicular magnetic field, injected electrons follow cyclotron tra-

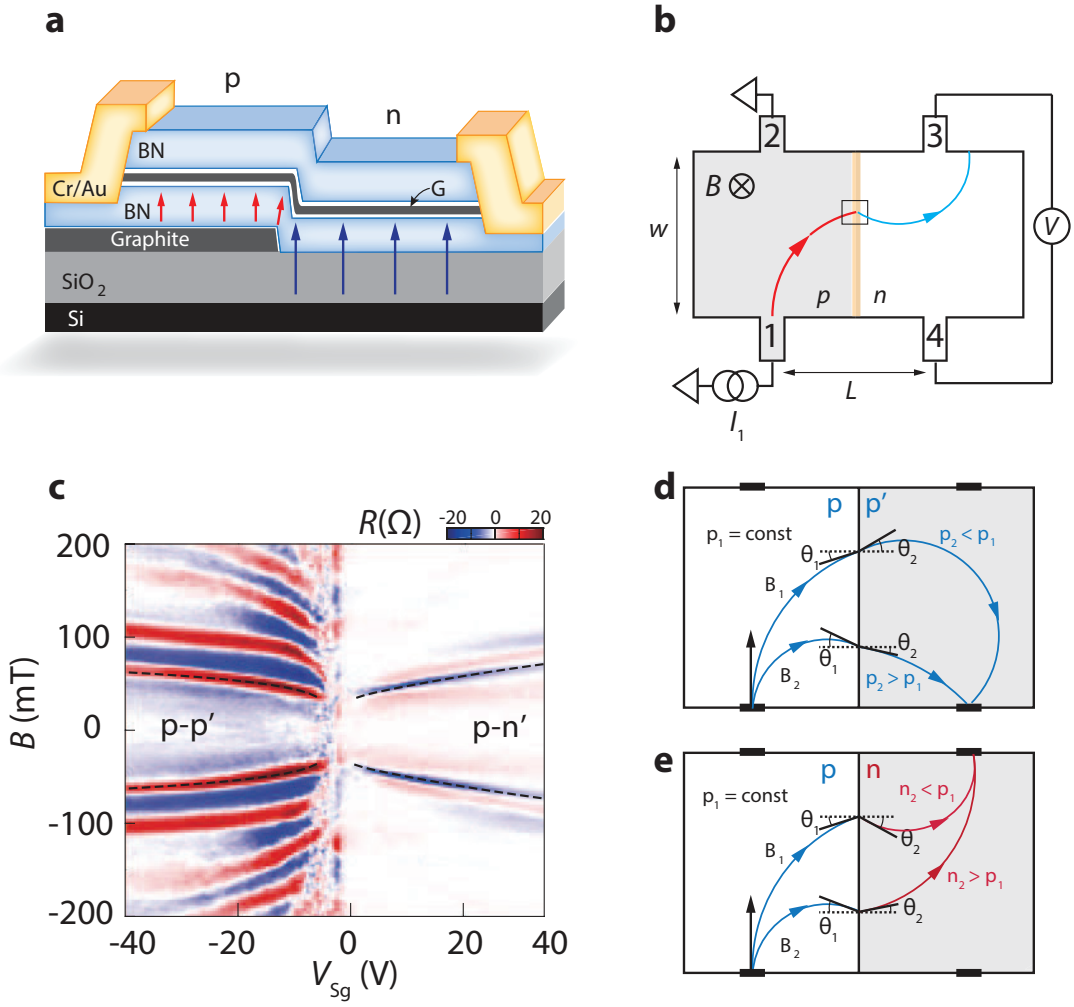

Figure 1.14: (a) Schematic of the graphene p-n junction. 1D edge contacts assure the electrical connection of the device. (b) Non-local resistance measurement schematic. (c) Magneto-transport measurements of the non-local resistance for different values of magnetic field B and silicon backgate voltages V_{Sg}. (d,e) Representation of resonance paths for two different junction polarities. Taken and adapted from [30].

jectories in the graphene plane, according to the Lorentz force. The experimental set-up is reported in Fig.1.14.b. With the presence of an electrostatically tunable interface, two transport scenarios across the junction are possible: (i) positive refractions if both sides of the junction have the same carrier polarity (n-n' or p-p' junctions); (ii) negative refractions if each side displays opposite doping conditions (n-p or p-n junctions).

The measurement is performed at a fixed graphite gate voltage $V_{\mathrm{Gg}} = -1$ V, assuring a p-type doping condition in the left region of injection. Both the magnetic field B and the silicon backgate V_{Sg} are swept, while measuring the four-wire non-local resistance $R = V_{3,4}/I_1$. The magneto-transport measurements are reported in Fig.1.14.c.

When considering the p-p' case, the experimental data put in evidence the presence of multiple focusing peaks, associated to the accumulation of carriers in the non-local voltage probe 4, for skipping orbits with an increasing number of intermediate reflections on the sample edge. Interestingly, in the p-n junction case, only the lowest resonant modes are observed (highlighted by black dashed lines), with resistance signs opposite to that of the lowest-mode peaks observed in the p-p' condition. The change in sign of the peaks, is linked to the junction polarities, which reverse the focusing into the opposite voltage probe, as illustrated in Fig.1.14.(d,e).

A detailed analysis of the focusing conditions based on ray-tracing simulations, allowed the authors to reproduce numerically the transport signatures, confirming the implication of the positive and negative refractions inside the junction.

Conclusion

In this chapter, I introduced some electronic properties of graphene arising from its peculiar chemical structure. The low-energy quasi-particles in graphene manifest the conservation of their sublattice pseudospin when transmitting through a p-n electrostatic interface. This unique property allows charge carriers to experience Klein tunnelling when impinging perpendicularly to any p-n interface. If carriers impinge with a finite angle on an ideal abrupt junction, transmission is described with an effective Snell-Descartes law for Dirac fermions.

I then explained the more realistic case of a smooth p-n junction, which displays classically-forbidden regions forcing a dramatic selection on the transmitted incident angles. Quasi-ideal electrostatic p-n junctions can be realized via the use of pristine graphite electrostatic gates, which minimize the roughness of p-n interfaces.

Within the gradient-index optics framework, the working principle of the graphene Veselago lens has been illustrated, as well as the focusing and beam splitting mechanisms of different circular electrostatic interfaces on a graphene plane.

In the last part, two experiments on ballistic graphene p-n junction heterostructures are reported, providing indirect signatures of Veselago lensing.

The objective of the thesis is to go further into the investigation of the negative refraction in graphene p-n junctions, by performing real space imaging of the electron trajectories using scanning gate microscopy.

Chapter 2

Scanning gate microscopy

Contents

Scanning probe microscopy refers to a wide branch of microscopy techniques in which an external probe enables the collection of information by scanning a local probe all over the surface of a specimen. Scanning gate microscopy (SGM) is one of these techniques, and it is applied to the imaging of electron transport in buried semiconductor quantum structure [125]. SGM is a cryogenic atomic force microscopy, exploiting an electrically polarized metallic tip directly glued on a force sensor such as a quartz tuning fork. Upon polarization, a raster scan movement of the tip over the sample surface, allows the tip to perturb electrostatically the device under analysis, inducing variations in the device conductance; the measure is acquired and recorded as a function of the tip position on the device surface.

In this thesis work I employ the SGM technique to image the transport signatures in different graphene devices, in both the ballistic and in the quantum Hall regime. In this chapter I present some technical details of the SGM microscope used during the thesis.

More details on the physical principles, which enable the electronic transport imaging, will be provided in Chapter 3.

2.1 Description of the force probe

2.1.1 Force sensing with the tuning fork

The tuning fork (TF) is a fundamental element in the set-up, allowing to measure the interaction force between the tip and the surface, and thus to detect surface topography [72]. A classical tuning fork is a mechanical oscillator with two prongs which oscillate in a mirrored fashion. The essential geometry of the structure allows the center of mass of the device to stay at rest also in working condition. If the main body of the tuning fork is made of quartz, it is possible to obtain a device able to vibrate under an imposed electric stimulus via piezoelectric effect and to detect electrically the mechanical vibrations. Quartz is a material that allows to have a weak frequency dependence on temperature, guaranteeing a highly stable frequency reference.

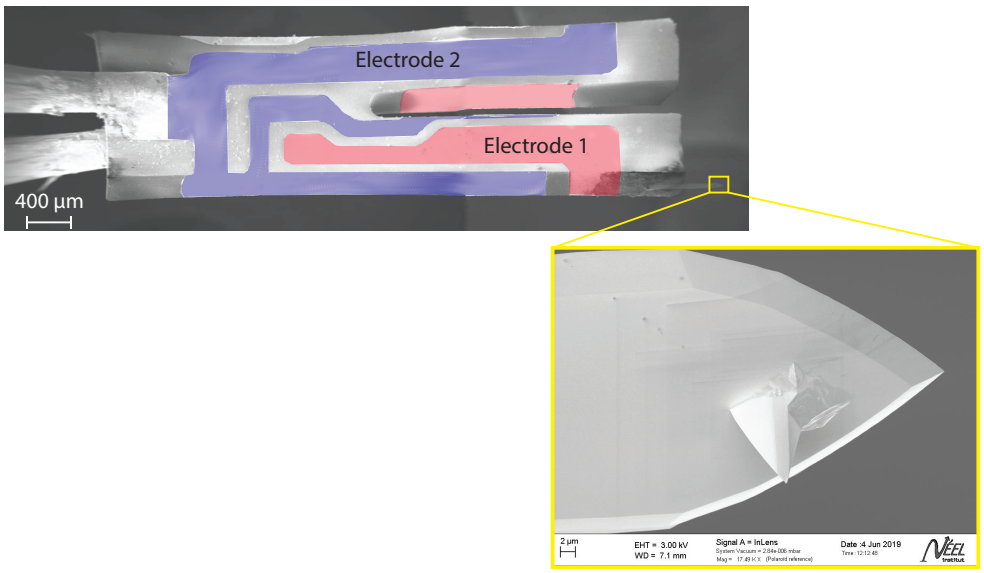

Figure 2.1: SEM micrograph of a quartz tuning fork employed in the SGM laboratory. Glued at the extreme of the lower prong there is a metallic AFM cantilever. The yellow frame represents a zoom on the cantilever tip.

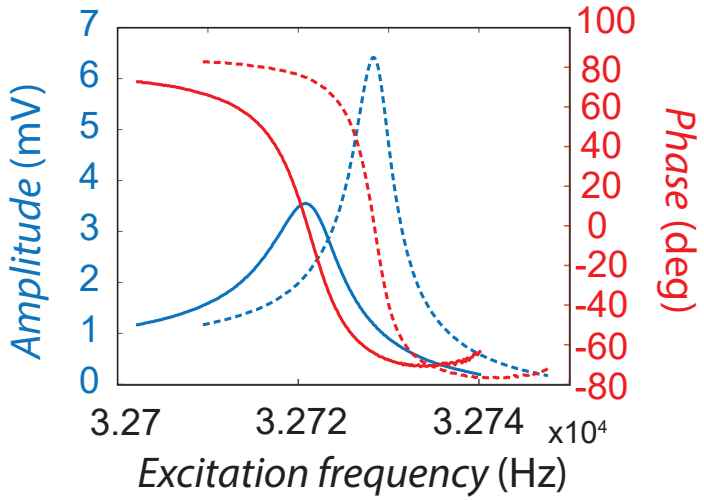

Figure 2.2: Bode diagrams of a tuning fork at room temperature. A driving signal amplitude of $V = 1$ mV rms is applied on the tuning fork. Diagram in solid lines are measured at the atmospheric pressure (Q = 4220), while diagrams at dashed lines are measured at lower pressure $P = 2.3 \times 10^{-2}$ mbar (Q = 8019).

In cryogenic scanning-force microscopy equipments, it is quite common to find piezoelectric tuning fork sensors, since they are cheap and easily available. However, the high tuning fork stiffness imposes a significant limitation in small forces detection. The quality factor of this resonator is very high, even at ambient condition ($Q \approx 10^5$) and is able to work even in liquids [72, 55].

A SEM micrograph of a quartz tuning fork for SGM experiment is reported in Fig.2.1. The electrodes connected to the prongs have different colours, and are used for the direct measurement of piezoelectric current.

The influence of presssure and temperature on the Q-factor When the tuning fork is working in a cryogenic environment, its performance is strongly dependent on the temperature and pressure. In oscillating NEMS and MEMS, the main reasons for Q-factor variations are associated to several mechanisms of intrinsic and extrinsic losses in resonators [50]. Sources of extrinsic losses can be: the gas damping and losses at supports. Indeed, the effect of the gas surrounding the tuning fork can dramatically influence the damping process. A reduction of the gas pressure increases the characteristic mean free path associated to the gas molecules ($\lambda_{\text{free}} = k_B T/\sigma P$). When the mean free path is larger than the device dimensions, the extrinsic losses reduces and the energy dissipation is mostly attributed to individual molecule collisions on the resonator. Quality factor dependence on the gas pressure is reported in Fig.2.2, where the frequency response of a tuning fork is measured at ambient pressure and at lower pressure. The quality factor in a quartz tuning fork resonator can be generally written as $Q^{-1} = Q_{\text{gas}}^{-1} + Q_{\text{i}}^{-1}$, where Q_{gas} is the extrinsic quality factor related to the pressure, and Q_{i} describes the intrinsic mechanical losses. This last contribution is a material-dependent quantity, and accounts for the acoustical attenuations of bulk acoustic waves travelling in the quartz. The effect of the temperature is therefore encoded in the intrinsic Q-factor. By lowering the temperature, the acoustic losses effect smears out, enabling a general increase of the quality factor. Sometimes, the presence of ionic impurities in quartz (like Na^+ ions) can promote interactions

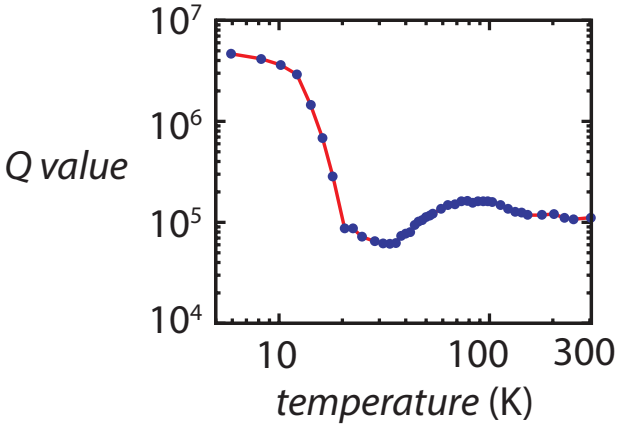

Figure 2.3: Example of temperature dependence of a quartz tuning fork Q-factor. The measurements have been carried at a constant pressure $P = 10$ mbar. Taken from [135].

between acoustic waves and thermal phonons, introducing Q factor fluctuations in a temperature range of 20 K and 50 K [135]. However, at lower temperatures this effect can be neglected. An example of temperature dependence is represented in Fig.2.3.

2.1.2 Control electronics for high-Q tuning fork

The tuning fork sensor can be represented by a harmonic oscillator with resonance frequency ω_0, characterized by a spring constant k. The coupling between the sensor and the substrate via the tip can be viewed as an additional spring constant $k_{t,s}$, equal to the gradient of the tip-sample force interaction along the vertical axis $k_{t,s} = -\partial F_{t,s}/\partial z$. The additional spring constant can take positive or negative values, corresponding respectively to repulsive and attractive tip-sample interactions.

In the hypothesis of small vibration amplitudes, the resonance frequency of the oscillator taking into account the tip-surface interaction can be written as

$$\omega_0^{'} = \omega_0 \sqrt{1 + k_{t,s}/k}. \tag{2.1}$$

A measure of the force gradient can be performed looking at the shift of the resonance frequency [49]. In conventional systems, the force sensor is driven at fixed excitation frequency, and a change in the force gradient generates a resonant frequency shift, which results in a variation of the vibration amplitude of the oscillator. However, this method is affected by a serious limitation: the employment of high quality factor force sensor restricts the detection bandwidth. The response of a tuning fork sensor may be expressed by the time constant $\tau = 2Q/\omega_0$. Since our force sensor is intended to work in cryogenic condition, with very high Q factor, the tuning fork time constant may be much too high for quick force detection, limiting the bandwidth to scanning rate below 1 Hz [72].

A powerful method to detect resonance frequency shifts, relies on a phase-locked loop (PLL) system. In this configuration the sensor is used inside an active feedback circuit, where force gradients are determined by phase-frequency measurements, and the oscillator amplitude is controlled and regulated by a second dedicated feedback loop. The introduction of a closed loop modifies the transfer function of the system, compensating the original time constant and increasing the system bandwidth.

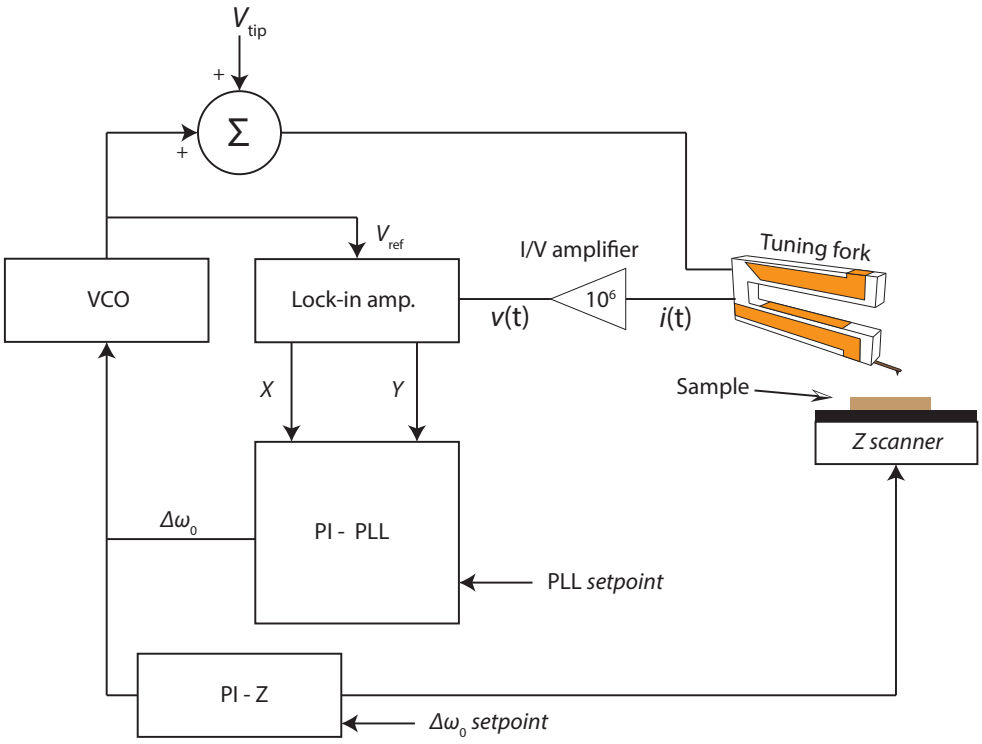

Figure 2.4: Schematic of a general SFM electronic set-up with a phase-locked loop.

PLL and z-control feedback Figure 2.4 shows the schematic of a PLL set-up for the detection of a tuning fork admittance. A voltage controlled oscillator (VCO) provides the driving voltage for the tuning fork. Once resonating, the total current $i(t)$ generated by the piezoelectric sensor is converted into a voltage signal $v(t)$ by means of an I/V converter; with a conversion constant $G = 10^6$ V/A. The voltage signal is then measured by a lock-in amplifier triggered from the external VCO signal. The real and the imaginary parts demodulated by the lock-in amplifier, respectively X and Y, correspond to the converted tuning fork current signal. The Y component is a linear indicator of the frequency deviation from the resonance condition. Therefore, it is employed by the proportional-integral controller (PI-PLL) to evaluate the variation of Y with respect to a customizable set point. The PLL output is subsequently fed to the input of the VCO, which updates its output signal frequency to the new tuning fork resonance frequency, keeping the signal Y at the desired value. The PLL output is also used as the input signal for a proportional-integral z-controller (PI-Z) for the vertical Z scanner, maintaining at the desired setpoint the tip-sample interaction.

In Fig.2.4, the presence of an analog adder enables the possibility to include a DC voltage bias V_{tip} for the electrical polarization of the metallic tip, in order to couple electrostatically this metallic tip with a sample. Electrostatic force microscopy, for instances, is a technique relying on this electrostatic coupling, widely used for the imaging of local charges and potentials. The DC voltage bias on the tip is also crucial for the SGM technique.

2.1.3 Preparation of tuning fork sensor with metallic tip

In SGM experiment, the presence of a metallic tip is necessary in order to capacitively couple the tip with the 2DEG. Since it is not common to find commercially tuning fork already equipped with a conductive metallic tip, we prepare the probe ourselves, by gluing a commercial EFM cantilever directly on one extremity of the tuning fork prong. A commercial quartz tuning

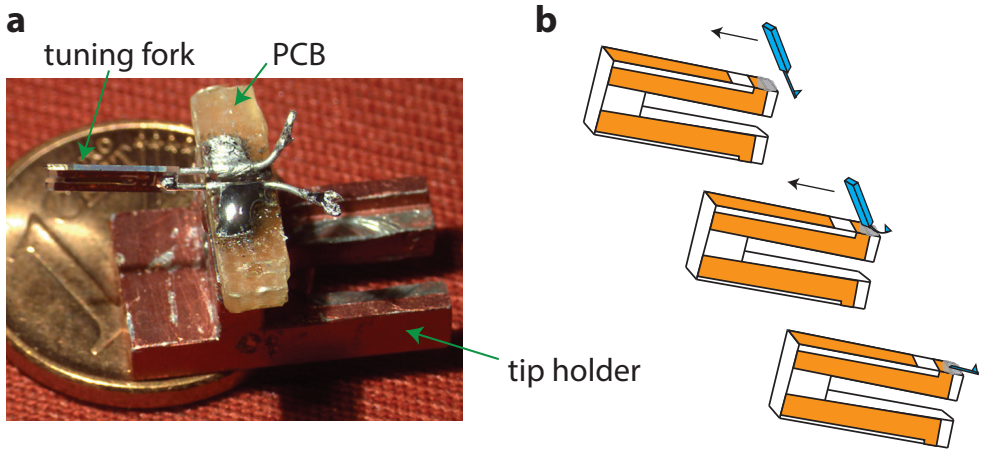

Figure 2.5: (a) Picture of a tuning fork positioned on the tip holder. (b) Representation of an EFM tip transfer process. The tip is approached in correspondence to the upper prong covered with silver epoxy (the grey layer). By moving the relative positions of the cantilever and of the tuning fork, it is possible to mechanically break and fix the cantilever on the tuning fork prong.

fork is first prepared by removing the external surrounding metallic case using a pair of pliers. Then the tuning fork electrodes are welded on a small piece of PCB, this assembly is glued afterwards on a tip holder (see Fig.2.5.a).

The next step consists on the manual deposition of a tiny amount of silver epoxy to the end of one TF prong. During this operation, it is necessary to cover also a small area of a metal electrode, which will guarantee the electrical connection between the tip and an external voltage source. An EFM cantilever chip is fixed by means of scotch tape directly on a 3-dimensional moving stage micromanipulator. The tip holder with the tuning fork is fixed as well on another micromanipulator, assuring thus a complete fine spatial control of the two objects. By gradually approaching the cantilever close to the end of TF, the mechanical contact between the two objects will end to break the cantilever, leaving about half of the latter on the silver epoxy glue. This last process is depicted in Fig.2.5.b.

2.1.4 Electrostatic force microscopy

The SGM set-up in the lab allows to perform electrostatic force microscopy (EFM). The principle of this technique is based on the dynamic non-contact atomic force microscopy, where the electrostatic force between the electrically polarized tip and a sample is probed. The electrostatic interaction can be classified as a long range force which can be detected with the tip a few hundreds of nanometers away from the sample. Since it relies on a dynamic force detection, the tuning fork is excited at its resonance frequency. The presence of low interaction forces are responsible for variations in the oscillation amplitude and phase. Variations of these last parameters provide informations about the sample's electrical characteristics.

With the PLL set-up in the lab, it is possible to detect the electrostatic force gradient via a resonance frequency shift. In the case of weak tip-sample interactions, the tuning fork frequency detuning is proportional to the vertical force gradient, and can be expressed according to the relation [72].

$$\Delta\omega \approx -\frac{\omega_0}{2k}\frac{\partial F}{\partial z} \tag{2.2}$$

where k is the fundamental tuning fork spring constant (of the order of 10 000 N/m) and ω_0 is the bare resonant frequency (32 768 Hz).

The application of a voltage between the tip and the sample generates an attractive electrostatic force that can be directly detected through a frequency shift of the tuning fork. When an electrically polarized tip is positioned above a conductive surface, a capacitively coupling between the two structures is formed. The value of this capacitance $C_{\mathrm{t,s}}$ is depending from the geometries of the surface and tip, and on the dielectric constant of the medium in-between. The electrostatic force exerted between the tip and the surface can be expressed as a function of the electrostatic energy gradient

$$F_{\mathrm{t,s}} = -\frac{\partial E}{\partial z} = \frac{1}{2}\frac{\partial C_{\mathrm{t,s}}(z)}{\partial z} V_{\mathrm{t,s}}^2 \tag{2.3}$$

When the tip moves on a surface composed of different materials, the tip-surface electrostatic interaction take into account a contact potential $\Delta\phi_{\mathrm{w}}$, obtained from the difference between the work functions associated to the tip and to the underlying surface. The detuning relation is thus described by

$$\Delta\omega = -\frac{\omega_0}{2k}\frac{\partial^2 C_{\mathrm{t,s}}}{\partial z^2}(V_{\mathrm{t,s}} + \Delta\phi_{\mathrm{w}})^2 \tag{2.4}$$

2.2 The cryogenic microscope

SGM is a microscopy technique sharing the same set-up as a cryogenic AFM. The entire microscope column is appositely designed to fit inside a standard Oxford Instrument 4He cryostat with a variable temperature insert (VTI).

Small thermal conductivity is needed in order to reduce heat transfer between the bottom of the rack, usually at 1.5 K, and the top region at room temperature.

The entire apparatus was designed for the investigation of 2D electron gasses in laterally defined nanostructures. Metals employed in the microscope body have to be non-magnetic, in order to be compatible with mesoscopic physics experiments requiring high magnetic fields.

2.2.1 The microscope head

The head of our cryogenic AFM is reported in Fig.2.6. On the top of the picture is placed the tuning fork equipped with the metallic tip. The sample holder is placed beneath the tuning fork, and it is made from a PCB plate on which the sample is fixed. The distance between the tip and the sample surface is typically fixed at 300 μm at room temperature. This spatial separation allows to minimize the risks of tip crash onto the sample during the thermal contractions of the metallic struture in the course of the system cool down.

In order to monitor the cooling down of the microscope two different thermometers are employed. A first platinum thermometer allows to monitor with good confidence high temperatures ranging from 30 K to 300 K. A carbon based thermistor is employed to detect temperature below 20 K.

2.2.2 The positioning system

Stick-slip actuators relying on individually controlled piezoelectric stacks allow for a rough sample positioning with respect to the tip. The microscope motors are organized by three different stages moving independently along the three directions and vertically assembled as

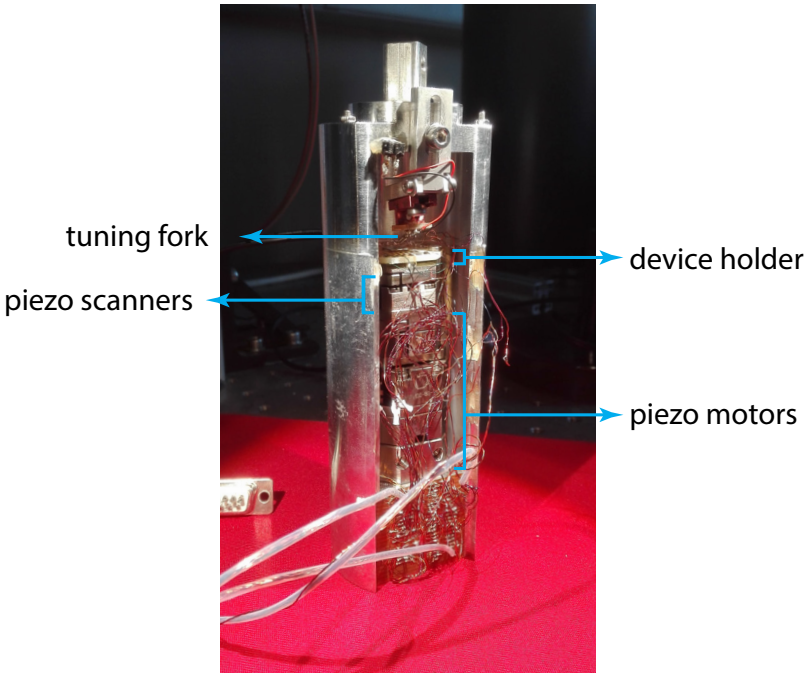

Figure 2.6: Picture of the cryogenic AFM head.

showed in Fig.2.6. Motors can be controlled manually or with a Labview program piloting an Attocube voltage generator. The resolution of the motors, at the minimum driving voltage, is about 100 nm per step, with a full travel range of 7 mm in the x- and y-directions, and 5 mm along the z-axis.

The scanner is the element allowing the finest sample displacement resolution in the three dimensions. It is composed of three PZT (lead zirconate titanate) actuators, forming x-, y- and z- stages. The surface scanning range on the horizontal plane is equal to 30 μm at both room and low temperature. The maximum vertical displacement stage is around 16 μm.

The use of a reliable positioning system is fundamental. When the sample is inserted in a cryogenic environment, there is no way to control optically its spatial displacement with respect to the fixed tuning fork. Therefore, it is desired to have a low-temperature-compatible position indexing system, enabling a reproducible sample positioning.

2.3 Operation of the microscope

In order to perform SGM experiments, first of all it is necessary to position correctly the tip in a defined region on the device surface. The main difficulty during the tip positioning is due to the absence of visual access, making impossible optical localization like in standard room temperature AFM.

2.3.1 Coarse tip positioning at room temperature

A positioning of the tip in the proximity of the sample is performed at room temperature, outside the cryostat with the x,y,z motors. The position of the sample is monitored with the help of a stereo microscope connected to a USB camera (see Fig.2.7.a). The sample is positioned about 300 μm below the tip, using the tip mirror image as an optical position reference as shown in Fig.2.7.b.

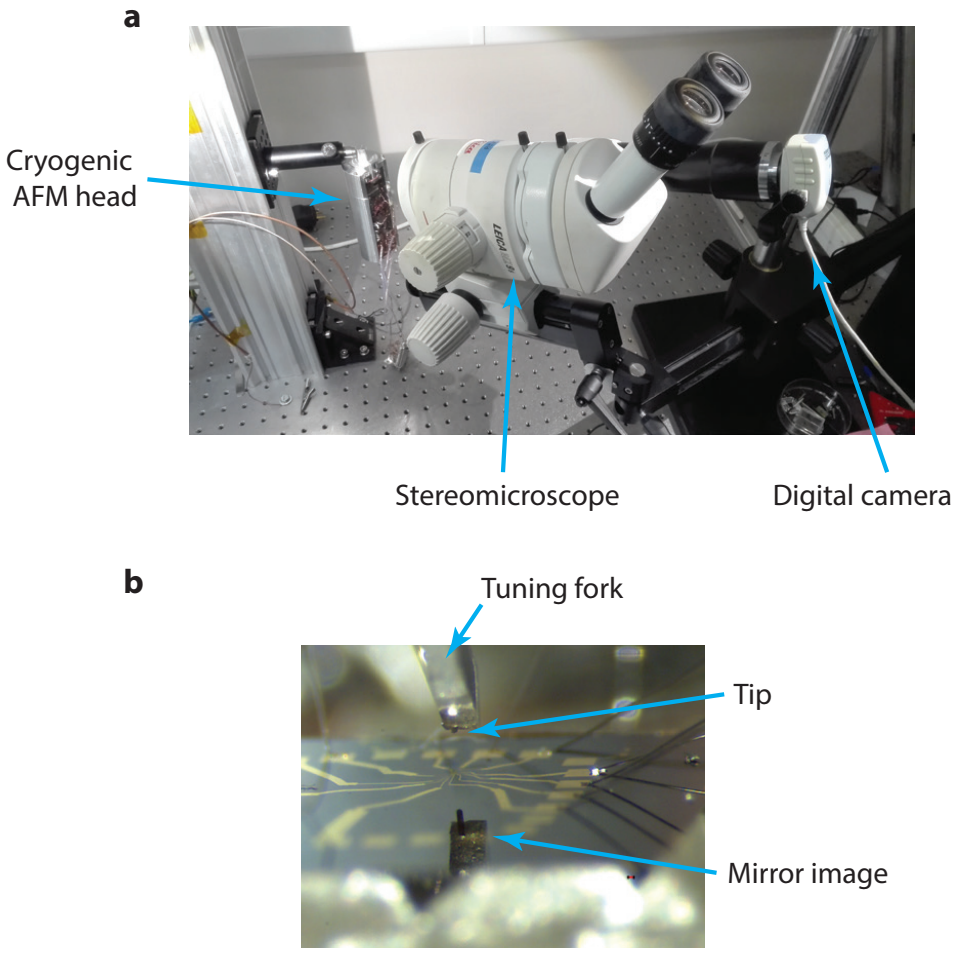

Figure 2.7: (a) Picture of the lab equipment during the manual tip positioning. The stereomicroscope enables to identify the correct position of the device under the probe. (b) Stereomicroscope picture of a tip placed over the a graphene device. We can estimate the distance of the tip from the substrate looking at the spatial position of the tip mirror image.

2.3.2 AFM tip positioning at low temperature

Once the tip positioning has been completed, the microscope is fixed at the bottom of the insert and dived inside the VTI of the cryostat. Subsequently, an automatic approach of the sample toward the tip is performed. Several sequences of z-scanner extensions and z-motor steps are done iteratively until the tip engages the surface. The engaging process stops when the frequency shift value reaches the chosen set-point (typically 0.2 Hz).

Raster scanning the maximum accessible area of 30×30 μm^2, in frequency shift feedback, we look for lithographic metallic lines connecting the device. By collecting a series of AFM maps, we compare the images with the lithography scheme, estimating thus the position of the probe with respect to the device. At this point, the piezoelectric motors are displaced in order to approach the device toward the tip.

When the topography image of a flat surface is showing a slope, the tilt angle of the scanning plane has to be adjusted. This is an important operation for subsequent EFM and SGM measurements, since the potential induced by the tip in lift-mode is strongly dependent on the tip-sample distance.

2.3.3 EFM tip positioning

When the device is nearby the tip, the alignment process cannot rely anymore on the AFM dynamic contact mode. The friction of the tip on the substrate can generate damages on the thin lithographic lines. Another drawback of the dynamic contact mode is the triboelectric effect during the contact of the tip. The deposition of unwanted charges on the insulating surface may disturb the ballistic transport in the 2DEG or graphene, and possibly generate telegraph noise affecting the device measurements.

EFM is a microscopy technique that allows to analyse the surface topography in a non invasive way. By scanning the electrically polarized tip in non-contact mode at fixed height, we record the frequency shift of the tuning fork. Which is associated to the total potential difference between the surface and the tip. With EFM it is therefore possible to image the position of metallic lines with sufficient resolution.

We present in Fig.2.8 an example of EFM mapping on a graphene device measured. The yellow window in the optical micrograph of Fig.2.8.a indicates the EFM scan region. The actual EFM map is in Fig.2.8.b and is recorded at 200 nm height above an electrode, with a tip voltage $V_{\text{tip}} = -10$ V. From the picture it is possible to identify the contacts of the device as dark regions of large attractive interaction.

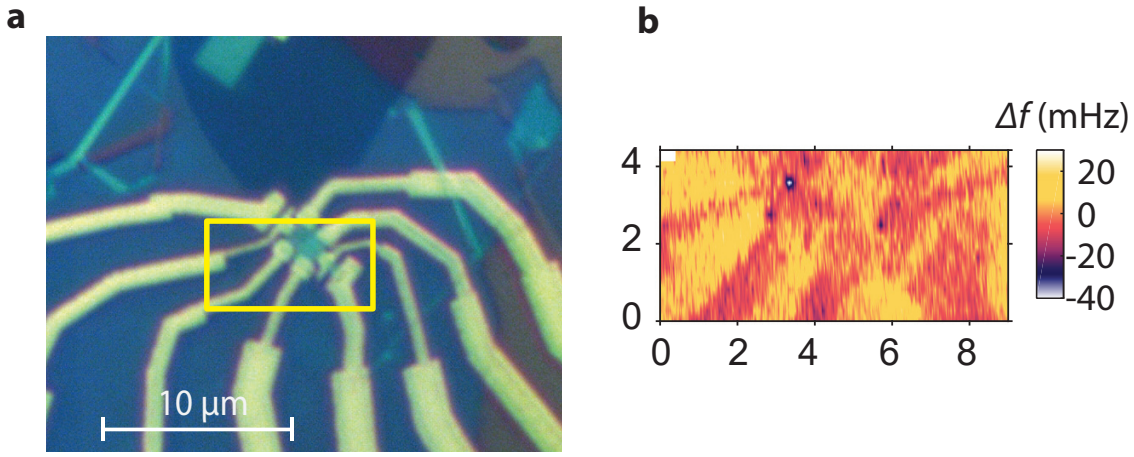

Figure 2.8: (a) Optical micrograph of the device A. The yellow frame represents the EFM scan window. (b) EFM map recorded at 200 nm of height from one electrode with tip voltage $V_{\text{tip}} = -10$ V. The map highlights the position of the device contacts.

Chapter 3

Semi-classical ray-tracing for SGM

Contents

The simulation of charge transport in nanoelectronic devices is an essential requirement in the SGM community. It allows to reverse engineer the transport signatures associated to the electrostatic perturbation of the scanning tip, making possible to grasp the transport processes encoded in the SGM maps. Nowadays there are several simulation tools available for this purpose. For instance, the open source Python package *Kwant*, which has been extensively used in our research group. It proved to be a powerful tool for numerical quantum transport experiments within the tight-binding approximation [58]. It has been employed in few SGM experiments on ballistic graphene heterostructures, giving good agreement between experiment and theory [24, 23]. In the *Kwant* approach, a graphene system is modelled as a scattering region with a series of semi-infinite metallic leads representing the contact of a quantum transport experiment. These leads behave essentially as wave guides leading plane waves in and out of the graphene region. The stationary solution of the wave function inside the scattering region is performed by matching the wave functions of the leads with the one in the scattering region, using the tight-binding Schrödinger equation [58].

Despite the versatility of the *Kwant* package, the computational cost of the algorithm increases remarkably when it is required to calculate the wave function inside a realistic mesoscopic device, with edges extending over microns. It has been noticed that the computational times required for the calculation of SGM maps can extend for months, and are essentially not practical for our experimental intentions. Moreover, besides the computational costs, it is worth to mention that quantum simulations of graphene electron optical devices can introduce other major issues, such as difficulty to discern and interpret classical features of refraction and reflection processes out of a stationary wave function pattern. The richness of details generated from the interferences and propagation of genuine quantum waves, in a medium with several electrostatic interfaces, cannot be easily handled. Therefore, I decided to change the analytical paradigm, embracing a semi-classical numerical approach based on relativistic geodesics describing the space trajectories of point-like Dirac fermions. Semi-classical approximations based on ray propagation already proved to be excellent alternatives to probe the mesoscopic realm, capturing "the answer" without superfluous details [154, 66].

The quantum and classical worlds are intimately bounded with correspondences, linking ray paths with wave phenomena. A very famous example of the wave-ray correspondence principle is related to the discovery of Maxwell's equations, experimentally validated by Hertz, which completed the corpuscular theory of light supported for a very long time by Descartes, Fermat and Newton. Nevertheless, similar links can be found also in quantum mechanics, as well as in acoustics, seismology and plasma physics, etc. [154]. Moreover, it is noteworthy that space trajectories for the description of particle dynamics are at the core of the non-orthodox pilot-wave theory (the so-called Bohmian mechanics). This has a status comparable to that of classical mechanics: particles are intended as corpuscular objects with well representable trajectories, which are guided by a much less representable wave function obeying to quantum laws and not to Newton's laws [75]. However, without diving further into theoretical aspects, I will present a list of practical fragments of the scientific literature in which the semi-classical approach has been successfully employed in SGM experiments on mesoscopic systems. The general broad agreement between the simulated classical flux and the quantum mechanical signals in the literature is reassuring for my experimental purposes, and eventually will allow to confirm the electron-optical behaviour of the graphene p-n junctions.

3.1 Experimental and numerical SGM studies of electron flows

3.1.1 Branching flow

In the year 2000, the Westervelt's research group at Harvard University demonstrated the possibility to image, with SGM, the electronic flow from a quantum point contact (QPC) in a gallium arsenide (GaAs) two-dimensional electron gas (2DEG). The pioneering thesis works of Mark Topinka [139] and Brian LeRoy [88], revealed the presence of branches of electrons propagating from the QPC (see Fig.3.1.a). These SGM experiments showed for the first time the morphology of a ballistic electron flow, decorated with outstanding interference fringes extending for several microns, far beyond the estimated thermal length $l_{\mathrm{th}} \approx 1.4\ \mu$m [140, 141, 143, 87, 91, 89, 149, 90, 142]. The experiments were conducted at the cryogenic temperature $T = 1.7$ K, on a GaAs 2DEG having mean free path $l = 11\ \mu$m and Fermi wavelength $\lambda_{\mathrm{F}} = 37$ nm. The observation of branches was an unexpected outcome, opposite to the naive idea of a perfectly ballistic flow continuing out as a smoothly widening fan [141].

In order to understand the origin of both branches and interference fringes, the experimental investigations were supported by the thesis activity of Scot Shaw [127], within the theoretical research group of Eric Heller. In order to recreate the characteristic transport signatures unravelled by the SGM technique, they simulated the propagation of a classical and quantum flux in a 2DEG influenced by a Gaussian background random potential, fluctuating with a standard deviation of 8% of the Fermi energy E_{F}. The correlation length of the disorder potential is related to the thickness of the spacer layer (22 nm) and is thus comparable with the Fermi wavelength. Figure 3.1.b shows the potential employed in both classical and quantum-mechanical simulations. The classical and quantum flux are reported in Fig.3.1.(c-d) respectively. Both simulations manifest the formation of the same branching structures. The broad agreement

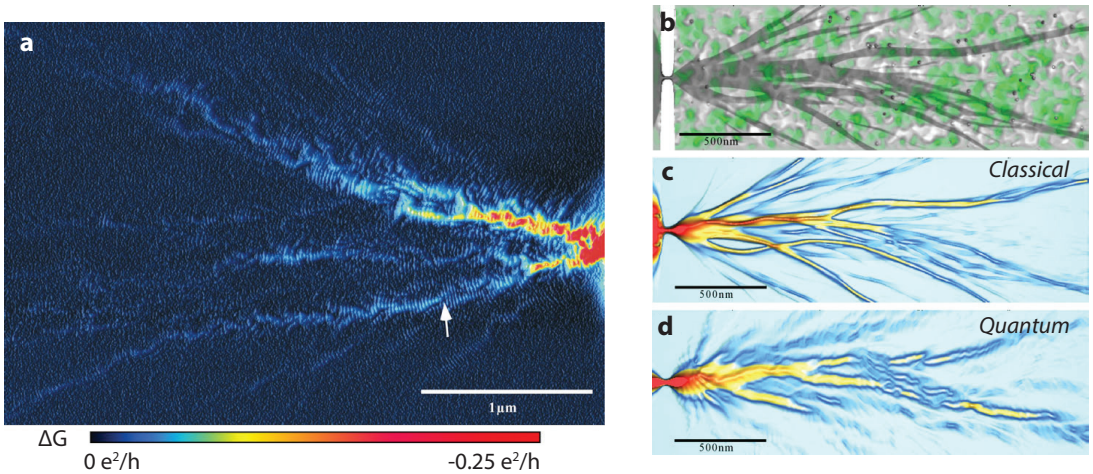

Figure 3.1: (a) SGM image of the current flow in a 2D electron gas from a QPC. The electronic flow generates branches due to cumulative effect of charge carrier deflections associated to the fluctuating random potential of the 2DEG. (b) Surface representation of the random potential for the electron flow calculation. (c) Classical ray-tracing simulation of branched electron flux propagating in the random potential. The simulation is performed considering an appropriate initial ensemble of classical trajectories. (d) Quantum mechanical result of the transmitted wave function through the QPC. Pictures taken from [141].

between the classical flux and the quantum signal leaded to the conclusion that the formation of branches in a ballistic electron flow is, a classical effect [141, 87].

The branching effect in GaAs QPC has then been observed by many groups [115, 133, 83, 22] and is therefore a very general effect (see Fig.3.2 for other examples of branching).

Stability of a branched flow How stable are the branches of a ballistic flow? Can a semi-classical approach mimic the energy-dependent behaviour of a branched flow? In order to find solutions to these questions, the research group of Klaus Ensslin in the ETH lab at Zurich published a paper in 2018 [20], where they characterized the branches developing from a quantum point contact (QPC) tuned on the second conductance plateau for several 2DEG electron densities ranging from $n = 0.99 \times 10^{11}$ cm^{-2} to $n = 2.03 \times 10^{11}$ cm^{-2}. The SGM images reported in Fig.3.3, are recorded with different depleting tip voltages guaranteeing a fixed diameter of the depletion disk below the tip. From the images we can notice a branched pattern that is weakly modified from the reduction of the electron density, with the most stable features located in the vicinity of the QPC.

In order to test the stability of classical branches emerging from the collective propagation of point-like electrons, they performed a series of calculations of transmitted classical trajectories which are reported in Fig.3.4.(a-e), and exhibit a growing complexity with the reduction of the electron charge density.

Instead of looking to single charge trajectories, which are dynamical objects showing strong spatial fluctuations as a function of the charge density, the stability of an electron flow needs

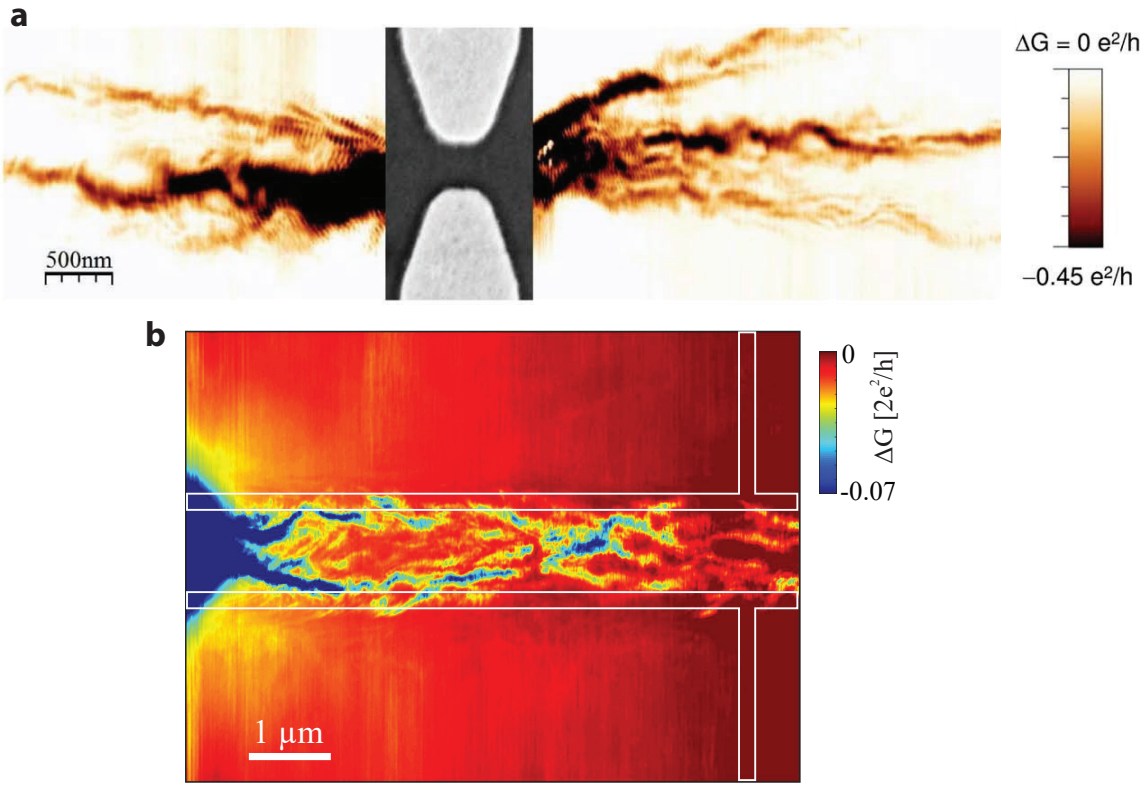

Figure 3.2: (a) Branched flow through a quantum point contact. Branches in the color plot are decorated with interference fringes which are signature of electron phase coherence. Taken from [115]. (b) SGM map of conductance in a narrow confined geometry of GaAs, showing a branched flow. Taken from [133].

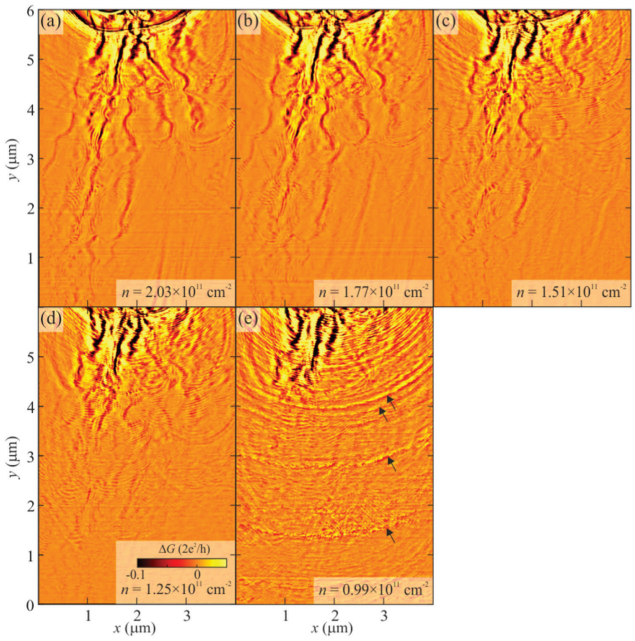

Figure 3.3: SGM images showing the stability of a branched flow pattern for different charge density conditions on the 2DEG. Pictures taken from [20].

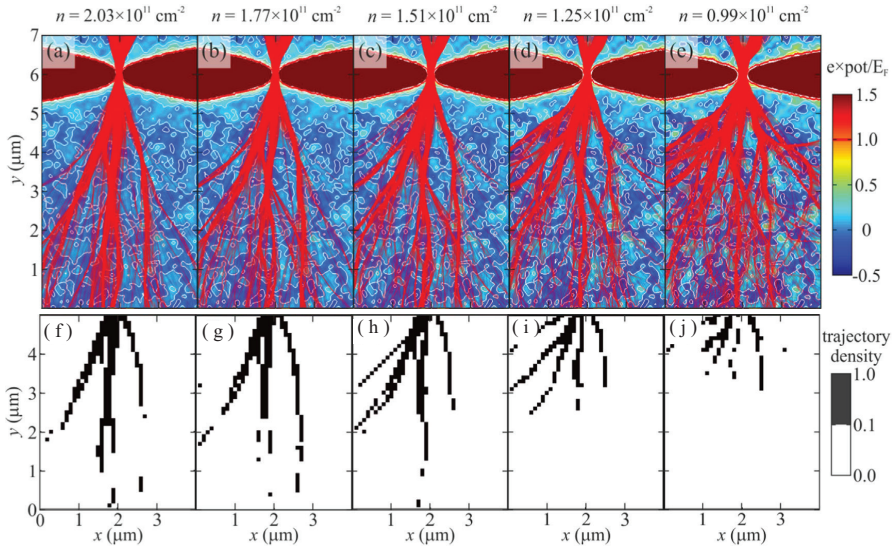

Figure 3.4: (a-e) Ray-tracing simulations of electron trajectories flowing from a QPC at different density conditions. (f-j) Density of trajectory computed from the ray-tracing simulations. Pictures taken from [20].

to be searched within bundles of trajectories forming dense ensembles. Therefore, more than comparing trajectory maps, it is better to study the associated trajectory density maps of Fig.3.4.(f-j). The maps reveal a series of normalized density branches with a signal strength represented between the arbitrary values 0.1 and 1. The patterns highlighted from the trajectory densities show a quite stable behaviour under variations of charge density. Moreover, as a confirmation of the experimental SGM observations, the most stable regions in the semi-classical simulations are the one in the close vicinity of the constriction (see also Refs. [94, 53]).

3.1.2 Magnetic steering in GaAs heterostructure

In the year 2000, SGM was employed by the David Ritchie's group at Cambridge University (UK), to analyse the spatial distribution of charge carriers trajectories through one-dimensional constrictions in a GaAs/AlGaAs heterojunction. They conducted few non-equilibrium transport experiments to image trajectories of electrons and conduction-band holes[1] injected from an external drain-source DC bias having a magnitude $|V_{ds}| \gg k_B T$. [37, 38, 39]. In one of the

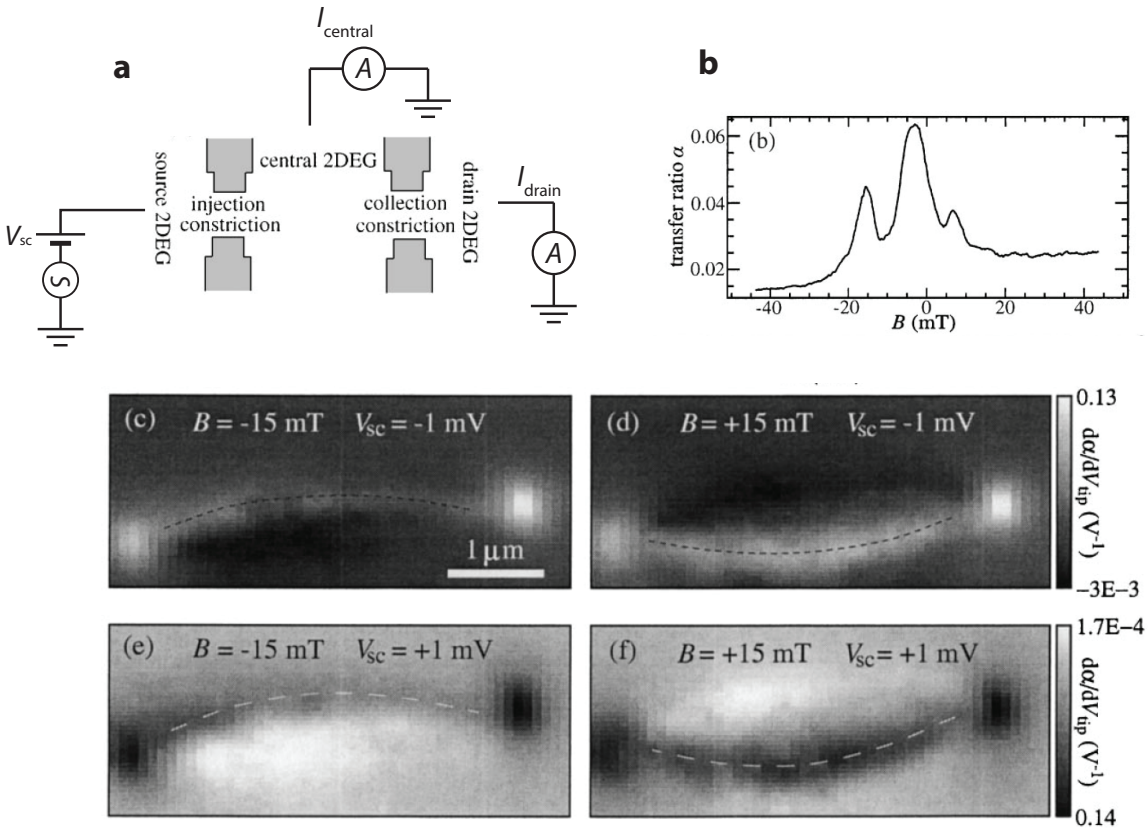

Figure 3.5: (a) Schematic of the split gate electrodes with the measurements set-up. (b) Fraction of current collected from the drain contact as a function of the magnetic steering of hot-electrons with a perpendicular B-field, at $T = 4.2$ K. (c-f) SGM images made with a tip at 60 nm off the surface with an AC voltage of 0.5 Vrms. Pictures taken from [38].

[1] At sufficiently low temperature, if the local DC source voltage is higher than the average 2DEG potential ($V_{SC} \gg V_{2DEG}$), and $|V_{SC}| \gg K_B T$ ($V_D = 0$ V), the mechanism of *hot-electron injection* promotes energetic hot-electrons above the electron chemical potential μ. Conversely, if $V_{SC} \ll V_{2DEG}$, the process of hot-electron injection stops, and eventually energetic conduction-band holes are promoted in the conduction band, below the electron chemical potential.

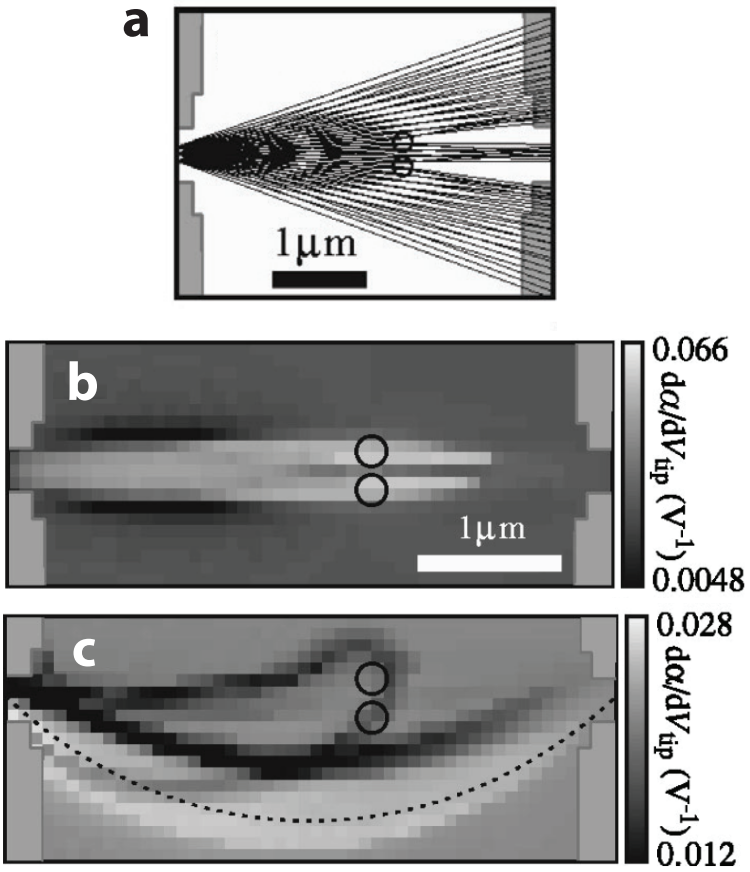

Figure 3.6: (a) Numerical simulation of trajectories originated by the injection constriction and repelled from two depleting impurities at B = 0 T. (b) Semi-classical SGM map generated by counting the amount of collected trajectories for each tip position in space on a grid, at B = 0 T. (c) Semi-classical SGM map in the presence of a perpendicular magnetic field $B = 30$ mT. Pictures taken from [39].

experiment [38], they fabricated two successive split gates having both a width of 700 nm, and separated by 4 μm. The 2DEG mobility was 2.5×10^6 cm^{2}V^{-1}s^{-1}, with a mean free path of 20 μm. The measurement set-up is reported in Fig.3.5.a, where the source region is connected to a DC signal $V_{sc} = -1$ mV, with an additional AC signal 0.5 mV$_{rms}$. The transmission across the two successive split gates was performed by measuring the fraction of current transmitted to the drain $\alpha = I_{drain}/I_{center}$.

In the absence of the tip, the magnetic field B is steering the current beam over the constriction at the drain. The fraction of drain current α is measured and reported in Fig.3.5.b, where the central peak represents the maximum electron transmission to the drain.
For the SGM imaging, the AC voltage at the source contact is removed, leaving only the DC voltage source. The SGM tip is raster scanned over the device surface with an AC rms signal of $V_{tip} = 0.5$ V, in a way that the tip always repels electrons [2]. The AC fraction of drain current α is measured in phase with the tip voltage, allowing to record SGM contrast maps of the derivative $d\alpha/dV_{tip}$. Fig.3.5.(c-f) shows the SGM maps, recorded at both -15 and $+15$ mT, with a DC source bias of -1 mV (to inject hot-electrons) and $+1$ mV (to inject conduction-band

[2]The repelling action derives from the not applied work-function compensating potential of the tip of 0.8 V.

holes). The images unravel clear signatures of carrier trajectories connecting the constrictions. Under the weak magnetic field, the SGM signal follows clear localized cyclotron orbits that can be understood in a semi-classical way. Indeed, both electrons and conduction-band holes can be magnetically steered in the same way since they have opposite effective mass and charge [38]. The reported SGM pictures allow for an estimation of the cyclotron radii for with results consistent with the semi-classical expression

$$r_{\mathrm{c}} = \frac{\sqrt{2Em^*}}{eB} \tag{3.1}$$

where E is the quasi-particle energy and m^* the electron effective mass.

In an effort to better understand the exact shape of the experimental signal showing transverse oscillations, the authors proposed a semi-classical ray-tracing approach for the numerical calculation of SGM maps [39]. Electrons are injected from a constriction inside a billiard, with energy E_{F} and with a normal angular distribution of standard deviation 17°. The ray field is represented in figure Fig.3.6.a, at $B = 0$ T, with the presence of two point charges depleting the 2DEG and therefore splitting the beam into three branches. The SGM tip is modelled as a depleting point charge perturbing the electrostatic potential according to a sphere-plane capacitance model. The semi-classical SGM signal is generated by counting the amount of ray trajectories collected at the drain, accordingly to the tip position. Therefore, a single pixel in an SGM image is obtained by simulating the ray field in the presence of a tip positioned at the exact spatial coordinates represented by the pixel. The numerical value associated to the pixel is the amount of rays collected at the drain contact. Two examples of SGM simulations are reported in Fig.3.6.(b,c), respectively under the magnetic fields $B = 0$ mT and $B = 30$ mT.

3.1.3 Magnetic focusing in GaAs heterostructure

In 2007, the Harvard group published an electron optical experiment on the transverse magnetic focusing of electron waves between two quantum point contacts (QPCs) made from a GaAs/AlGaAs heterostructure [2]. One QPC is used as a ballistic electron injector, while the other works as a collector for electron guided by a perpendicular magnetic field. In the case of ballistic transport, the signatures of focusing at the collector are represented by peaks in the collector voltage that are expected to occur only for certain values of magnetic field. From a purely geometrical point of view, the magnetic field needs to ensure a cyclotron orbit able to fit perfectly n times within the spacing determined from the point contacts distance L. The selection rule for the magnetic focusing condition relies on the equation

$$B_{\mathrm{n}} = n\frac{2\hbar k_{\mathrm{F}}}{eL} \tag{3.2}$$

where n is the electron density, k_{F} is modulus of the Fermi wave vector, and e the electron charge.

The SGM maps of the cyclotron orbits associated to the three first magnetic focusing conditions are reported in Fig.3.7.(a-c). Images are recorded with a negative tip voltage depleting the 2DEG beneath. In order to interpret the SGM signal, the authors presented a series of semi-classical transport simulations in which a pencil of classical trajectories is launched from one QPC and propagate in time through the system, under the influence of a magnetic field bending the ray trajectories [3, 2]. In Fig.3.7.(d,e) are reported two ray-tracing simulations of the electron flow at the first focusing peak ($n = 1$).

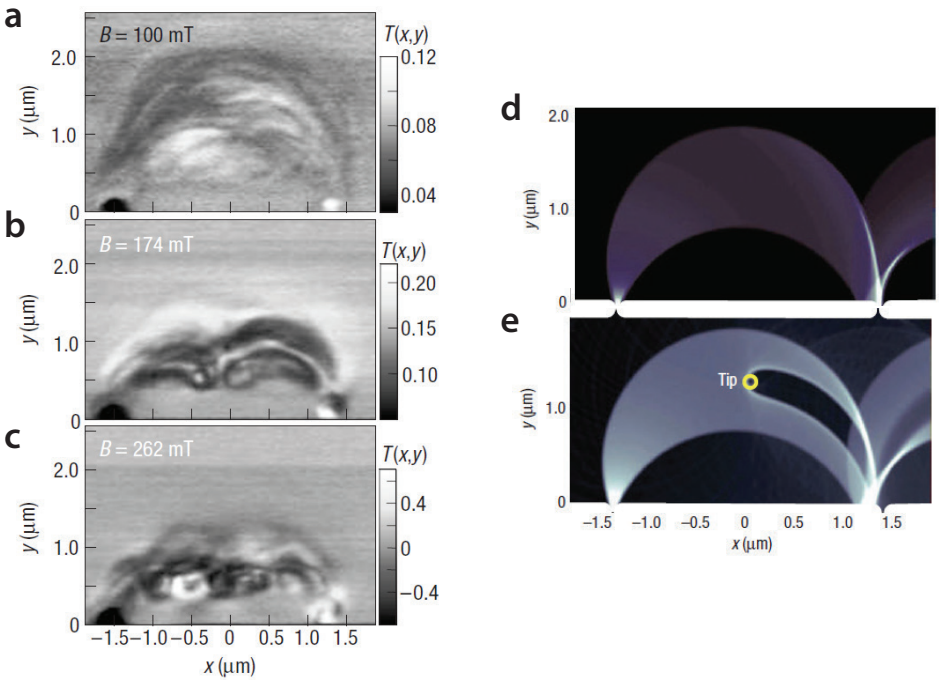

Figure 3.7: Experimental SGM maps of magnetic focusing in a 2DEG in the first three focusing conditions. (d,e) Semi-classical ray-tracing simulations of magnetic focusing flux: (d) in a flat potential, (e) with the presence of a depleting SGM tip. Pictures taken from [2].

3.1.4 Standing waves in a ballistic cavity

SGM in open 2DEG systems offers the opportunity to image the propagation of electrical current with remarkable spatial resolutions. However, the situation is different when electrons are injected in closed geometries, such as ballistic mirror cavities. We present here an experimental work published in 2018, from the Klaus Ensslin's group, where SGM is employed for the analysis of the weakly and strongly perturbative regimes of the tip potential on a mesoscopic GaAs/AlGaAs cavity resonator [134].

The above mentioned device is reported in Fig.3.8.a, where a QPC is visible at the bottom

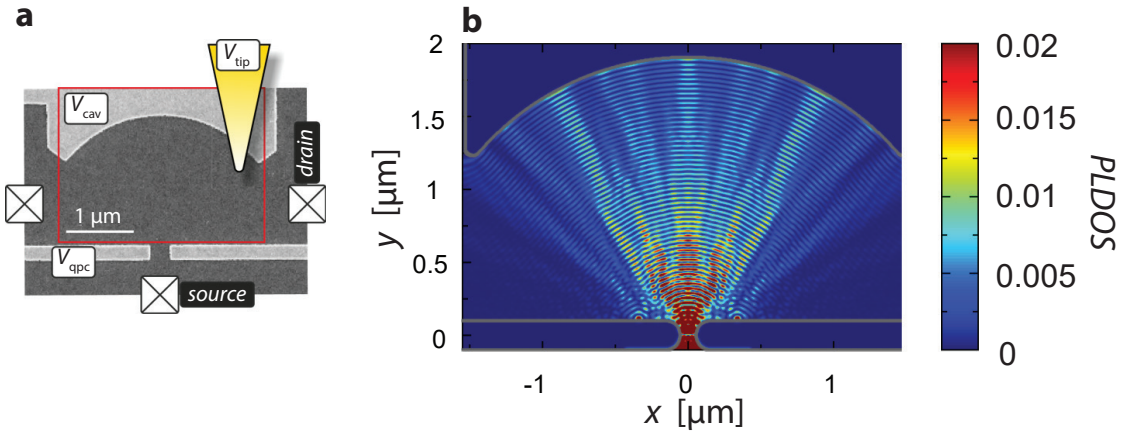

Figure 3.8: (a) SEM micrograph of the QPC and the cavity gate. The scan area is outlined with the red rectangle. (b) Calculation of the partial density of states (PLDOS) at the Fermi energy. The map shows scattering states in the cavity. Pictures taken from [134].

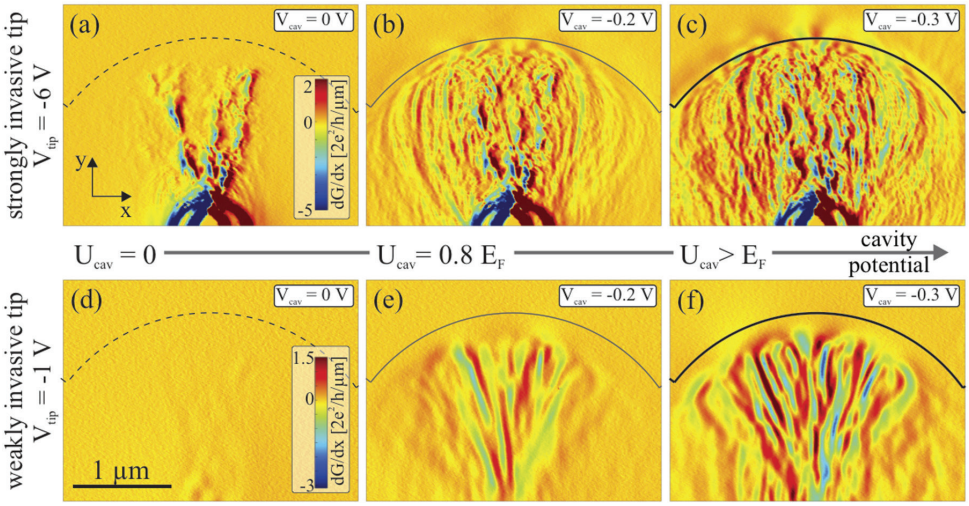

Figure 3.9: SGM maps showing the derivative dG/dx maps with two different tip voltage, considering three cavity voltage V_{cav}. Pictures taken from [134].

of the picture, controlled from the gate voltage V_{QPC}. In the upper region, a second gate defines the edge of a mirror cavity controlled by the voltage V_{cav}. The SGM tip scans within the red square at 65 nm above the surface. During the scan, the conductance is measured according to the tip position.

In an ideal mirror cavity, travelling electrons are expected to concentrate in narrow region of space, forming scattering states with eigenstates showing characteristic standing wave patterns. In Fig.3.8.b is reported the *KWANT* calculation of a partial local density of state (PLDOS) for N electronic modes injected at the Fermi energy E_{F} in the mirror cavity.

$$PLDOS \propto \sum_{\mathrm{i}=1}^{\mathrm{N}} |\Psi_{E_{\mathrm{F,\,i}}}(\mathbf{r})|^2 \tag{3.3}$$

The quantum simulation allows to visualize the smooth variation of the PLDOS in the azimuthal direction. These are extremely sensitive to disorder in the system, since charge impurities in the 2DEG can dramatically modify the scattering states in the cavities, introducing branching process that strongly distort the ideal spatial arrangement.

The SGM maps of the conductance derivative $\mathrm{d}G(x,y)/\mathrm{d}x$ are reported in Fig.3.9, and are recorded with two different depleting tip voltages: $V_{\mathrm{tip}} = -6$ V in order to create an invasive electrostatic potential perturbation ($U_{\mathrm{tip}} > E_{\mathrm{F}}$), and with a less negative voltage $V_{\mathrm{tip}} = -1$ for a weakly invasive action on the 2DEG. Another important parameter involved is V_{cav}, creating an effective electrostatic confinement of electrons whenever the condition $V_{\mathrm{cav}} < V_{\mathrm{depl.}} \approx -0.2$ V is satisfied. Fig.3.9.a shows the case of an open system (no confinement), with an evident branched flow extending close to the screening metallic gate in the top region of the map. For the scans in Fig.3.9.(b-c), the electrostatic confinement induced by the upper gate becomes more relevant, and the branch pattern is no longer the only dominant feature in the map. Evident spatial modulations add to the signal, as a confirmation of an effective gate-induced mirror action of the cavity. The rich fluctuations of the signal confirms the invasive role of the tip, backscattering the electron trajectories back toward the QPC.

The SGM signal in Fig.3.9.d is measured at lower tip voltage. The absence of a strong signal in the map confirms the less invasive action of the tip, which cannot backscatter electrons effectively. In order to recover a clear electrostatic influence of the tip, the depletion effect

from the cavity gate need to be restored. Indeed, the SGM maps under the presence of a mirror cavity in Fig.3.9.(e-f) display interesting fluctuations mainly in the azimuthal direction, confirming the gentle lensing effect of the tip on the hard-wall reflections in the cavity.

3.1.5 Magnetic focusing in graphene

In 2016, an experiment of magnetic focusing was performed by the Westervelt's group in Harvard, on a high-mobility graphene, encapsulated between two flakes of hexagonal boron nitride to form a hBN-graphene-hBN van der Waals heterostructure [14]. The measurement set-

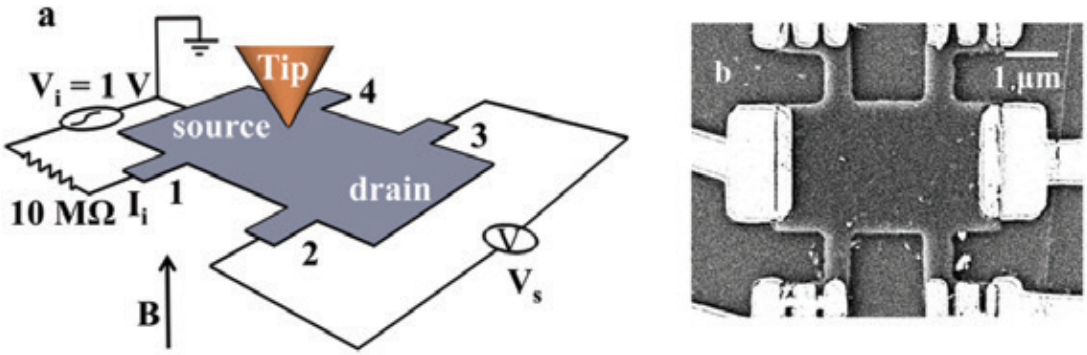

Figure 3.10: (a) Schematic of the measurement set-up used by the Harvard group for the magnetic focusing experiment in graphene. An AC current of 100 pA at 5 kHz is injected on the contact 1, while a non-local voltage V_s is measured between the contacts 2 and 3. (b) SEM micrograph of the graphene Hall bar. Pictures taken from [14].

up is reported in Fig.3.10.a. The Hall bar is current polarized from the contact 1 to the grounded source contact, while the transmission of electrons between contacts 1 and 2 is performed via the non-local measure of the output transresistance $R_m = V_s/I$. The application of a perpendicular magnetic field bends the flow of electrons, that follow cyclotron orbits having radius r_c. The tunable carrier density n in graphene affects the cyclotron radius according to the relation

$$r_c = \frac{\hbar\sqrt{\pi n}}{eB} \tag{3.4}$$

A first measure that indirectly confirms the magnetic focusing is given by the evolution of the transresistance versus the magnetic field in Fig.3.11.a. Since no current can flow through the floating contact 2, focusing of electrons will drive locally the contact potential to a downward shift. The difference between the chemical potentials at terminal 2 and 3 is therefore a practical way to access the signatures of focusing, that manifests with the transresistance (red) peaks well visible in the map. A secondary magnetic focusing condition is highlighted by the black line developing in the same plot.

In Fig.3.11.b are reported several SGM pictures of transresistance variations for various electron density and magnetic field values in the range of the first focusing peak, with cyclotron orbit diameter close to the distance between the contacts 1 and 2. The SGM pictures clearly shows half-circles joining the injector and the collector, unravelling the silhouette of cyclotron orbits in real space.

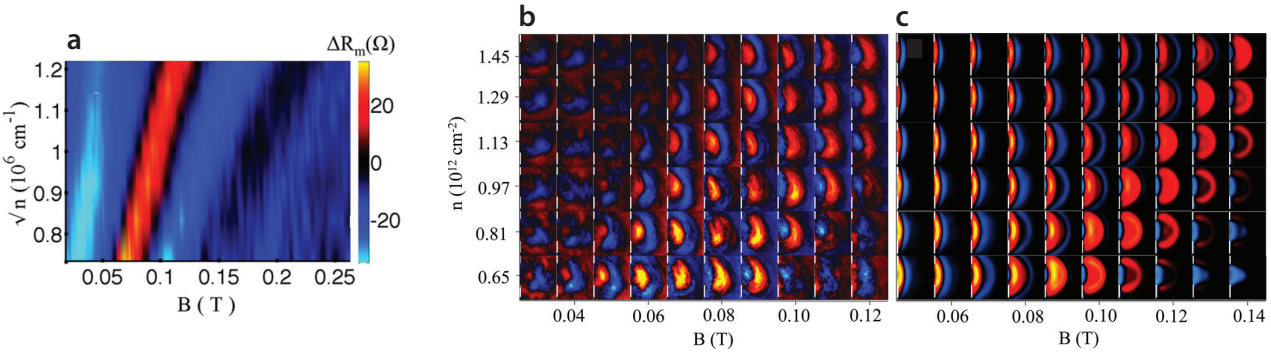

Figure 3.11: (a) Evolution of the transresistance ΔR_{m} as a function of the magnetic field and the electron density $\sqrt{n}$, at $T = 4.2$ K. (b) SGM maps of the transresistance highlighting the presence of cyclotron orbits in the device. (c) Semi-classical ray-tracing SGM simulations of Dirac fermion point particles in an ideal graphene device. Pictures taken from [14].

These experimental results can be understood in a semi-classical context using a classical model of point particle dynamics under the presence of a perpendicular magnetic field and the electrostatic perturbation of a scanning tip. The external forces acting on the particles are: (i) the Lorentz force due to the magnetic field; (ii) the deflection force of the tip is represented by the spatial gradient of the tip potential energy, which reduces the local density in the graphene layer. For each tip position, the electron trajectories are calculated, and the transmission of electrons between contacts 1 and 2 is computed counting the fraction of emitted trajectories reaching the receiving contact. A series of semi-classical SGM maps are reported in Fig.3.11.c. The ray-tracing calculations allows to better understand how the scattering centre formed by the tip acts on the transmission signal between the contacts (see also [13, 17, 16]).

3.2 Semi-classical SGM simulations in ballistic graphene

I present here an algorithm for the semi-classical calculations of SGM maps. It has been developed during the thesis in order to support the interpretations of SGM experiments in ballistic graphene devices. The numerical strategy relies on a standard ray-tracing approach, which allows the propagation of Dirac fermions point particles streaming from an ideal source region. Each trajectory is calculated by solving iteratively the Snell-Descartes law for Dirac fermions in a gradient-index electron optics medium. The Snell-Descartes law can describe the complete semi-classical dynamics of Dirac fermion particles, even in the presence of complex space-dependent electrostatic potentials.

3.2.1 Modelling the straight graphene junction

Here the ray-tracing algorithm operates in an infinite graphene plane, with an electrostatic potential evolving only in the x direction, describing the doping profile of a graphene junction centred at the spatial coordinate x_j.

An ideal abrupt graphene junction can be described as two separate regions having different kinetic energies

$$E_\mathrm{k}(x) = \begin{cases} E_\mathrm{k1} & x \leq x_\mathrm{j} \\ E_\mathrm{k2} & x > x_\mathrm{j} \end{cases} \tag{3.5}$$

However, in order to model a more realistic system, we replace the sharp potential by a smooth

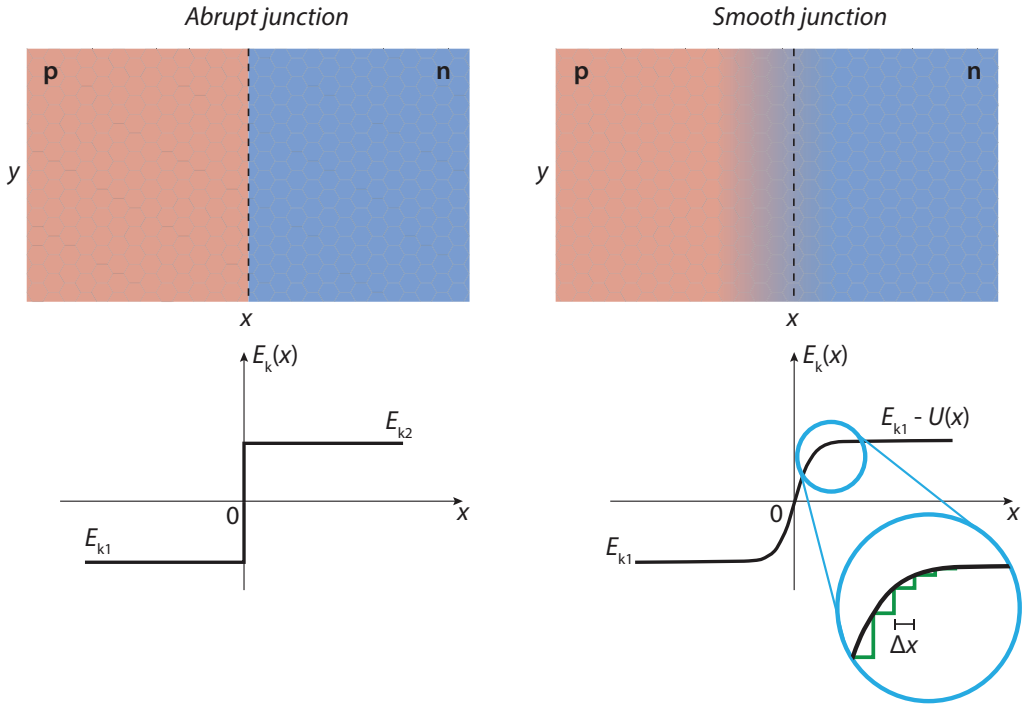

Figure 3.12: Representation of abrupt and smooth graphene p-n junctions. The colour shading of the smooth junction shows the electrostatic potential within the graphene ribbon. The respective kinetic energy profiles are plotted below each junction. The zoom highlights the mesh spacing for the potential discretization.

transition between the two regions with the following function

$$E_{\mathrm{k}}(x) = E_{\mathrm{k1}} - \frac{U_0}{2}\left(1 + \tanh\frac{x - x_{\mathrm{j}}}{\delta}\right) \tag{3.6}$$

where δ and U_0 are the parameters governing the smooth transition. The potential profiles for both the abrupt and smooth junctions are reported in Fig.3.12, where the junction position is placed at $x_{\mathrm{j}} = 0$.

A numerical implementation of the smooth junction case requires the use of a mesh, imposing a space discretization in the kinetic energy profile. Since the kinetic energy in a smooth junction is invariant along the y axis, the mesh is performed along the x-axis only, with a fixed spatial separation Δx between elements composing the profile. An example of mesh discretization can be observed in the zoom in Fig.3.12.

Such straight interfaces (abrupt or smooth), which are invariant along the y axis, are relatively easy to handle for the calculation of a refracted ray. But when the circular tip-induced potential is added to simulate an SGM experiment, the situation becomes much more complicated because the potential is not invariant anymore along the y axis and present refractive interfaces in all directions of space. A specific formalism, described in the next section, is required to deal with these arbitrary potential shapes.

3.2.2 Parametric equation for ray propagation

We consider here an ensemble of refractive interfaces representing the combination of the electrostatic potentials (pn junction, SGM tip, etc...). This ensemble of intersecting interfaces constitutes a mesh in which the ray needs to be propagated.

The propagation of a particle is described by a trajectory made of a collection of connected segments. Each segment of the trajectory resides in an uniform region of the mesh with a constant kinetic energy. To handle the complex geometries of refractive interfaces, the analytical representation of any oriented segment composing a particle trajectory follows the parametric equation

$$\mathbf{P} = \mathbf{D} + u\mathbf{E} \quad : \; u > 0, \tag{3.7}$$

for the absolute position $\mathbf{P}$ of a point located along the segment. $\mathbf{D}$ is the vantage point, representing the origin of the segment. $\mathbf{E}$ is the direction vector (not necessarily unitary), representing the space orientation of the segment according to the vantage point. u is the scalar parameter describing any point position along the segment.

This generic vectorial representation allows to easily represent a propagation process in a space having arbitrary dimensions. In the case of 2D graphene, the vectorial equation can be represented with the scalar equations

$$\begin{cases} P_{\mathrm{x}} = D_{\mathrm{x}} + uE_{\mathrm{x}} \\ P_{\mathrm{y}} = D_{\mathrm{y}} + uE_{\mathrm{y}} \end{cases} . \tag{3.8}$$

Therefore, for an initial vector $\mathbf{P}_{\mathrm{i}}$, represented by a vantage point $\mathbf{D}_{\mathrm{i}}$ and direction vector $\mathbf{E}_{\mathrm{i}}$, a ray-tracing algorithm needs to find all the possible intersections of the ray with all the lines composing the mesh of the potential. In particular, it searches for all the positive values of u such that $\mathbf{P}_{\mathrm{i}}(u, \mathbf{D}_{\mathrm{i}}, \mathbf{E}_{\mathrm{i}})$ is an intersection point with the mesh.

Once all the possible intersections $\{u_1,\ u_2,\ ...,\ u_N\}$ have been identified, the algorithm selects only the closest solution $u_{int} = min\{u_1,\ u_2,\ ...,\ u_N\}$, that represents both the ending point of the vector

$$\mathbf{P}_{i,end} = \mathbf{P}_i(u_{int}, \mathbf{D}_i, \mathbf{E}_i) \tag{3.9}$$

and the vantage point of the next segment vector $\mathbf{P}_{i+1}$

$$\mathbf{D}_{i+1} = \mathbf{P}_{i,end} \tag{3.10}$$

The calculation of the next direction vector $\mathbf{E}_{i+1}$ is performed via the Snell-Descartes law for Dirac fermions, considering the new kinetic energy in the new mesh region.

3.2.3 Numerical Snell-Descartes law

The propagation problem of a particle between two mesh elements of thickness Δx is depicted in Fig.3.13. According to the Snell-Descartes law, the relation between the incident and refracted angles for a particle in $\mathbf{P}_{i,end}$ is given by

$$E_k(x_i)\ \sin\theta_1 = E_k(x_{i+1})\ \sin\theta_2 \tag{3.11}$$

According to wave mechanics, for any refraction process at a given impinging angle, there is always an amount of the particle probability that is reflected at the interface. However, in our semi-classical approximation, this wave behaviour is neglected, considering reflections only when the impinging angle overcome a specific threshold of total internal reflection. It is possible to identify the *critical angle* θ_c, at which the particle is completely reflected and no refraction occurs:

$$\theta_c = \arcsin\left(\frac{E_k(x_{i+1})}{E_k(x_i)}\right) \tag{3.12}$$

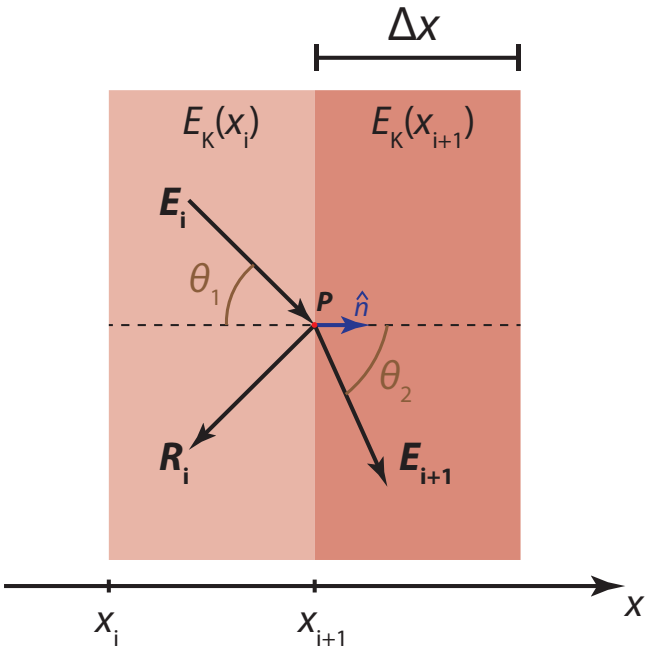

Figure 3.13: Representation of a positive refraction/reflection process at the interface between two evenly spaced vertical mesh elements. The vector $\mathbf{E}_i$ impinging in $\mathbf{P}$ can be either transmitted becoming $\mathbf{E}_{i+1}$ or reflected becoming $\mathbf{R}_i$

In order to be properly implemented in a generic ray-tracer for arbitrary orientations of the refractive interface, the Snell's law cannot be used in its usual form [48]. To rewrite the Snell's law in a more suited form, it is necessary to introduce the unit vectors pointing in the same directions as the vectors $\mathbf{E}_i$ and $\mathbf{E}_{i+1}$

$$\hat{\mathbf{e}}_i = \frac{\mathbf{E}_i}{|\mathbf{E}_i|}$$

$$\hat{\mathbf{e}}_{i+1} = \frac{\mathbf{E}_{i+1}}{|\mathbf{E}_{i+1}|}$$

Considering the unit vector $\hat{\mathbf{n}}$ (in Fig.3.13) normal to the interface between the mesh regions (oriented by convention from region i to region $i+1$ in this presentation), we can write the following system of equations

$$\begin{cases} E_k(x_i)\,\sin\theta_1 = E_k(x_{i+1})\,\sin\theta_2 \\ \hat{\mathbf{e}}_i \cdot \hat{\mathbf{n}} = \cos\theta_1 \\ \hat{\mathbf{e}}_{i+1} \cdot \hat{\mathbf{n}} = \cos\theta_2 \end{cases} . \tag{3.13}$$

From the last system of equations, we can derive a vectorial equation that represents our numerical implementation of the Snell-Descartes law

$$E_k^2(x_i)\left(1-(\hat{\mathbf{e}}_i\cdot\hat{\mathbf{n}})^2\right) = E_k^2(x_{i+1})\left(1-(\hat{\mathbf{e}}_{i+1}\cdot\hat{\mathbf{n}})^2\right) \tag{3.14}$$

The unknown of the last equation is the direction of the refracted vector $\hat{\mathbf{e}}_{i+1}$. Unfortunately, it is possible to demonstrate that in 2D there are four solutions available for $\hat{\mathbf{e}}_{i+1}$, lying on the same refraction plane (one in each of the four quadrants defined by the interface and its normal). Only one solution has a physical meaning, while the rest of them can be considered as "ghost" solutions. In order to find the physical solution to our problem, we express now the refracted vector $\mathbf{E}_{i+1}$ as a linear combination of the impinging unit vector $\hat{\mathbf{e}}_i$ and the normal vector at the interface $\hat{\mathbf{n}}$

$$\mathbf{E}_{i+1} = \hat{\mathbf{e}}_i + \mu\hat{\mathbf{n}} \quad : \ \mu \in \mathbb{R} \tag{3.15}$$

In this way, the vector $\mathbf{E}_{i+1}$ is forced to cross the normal to the interface, eliminating two of the four "ghost" solutions. The search for a physical solution reduces now on a quest for the correct value of the scalar parameter μ. The refracted unit vector, expressed as a function of μ is

$$\hat{\mathbf{e}}_{i+1} = \frac{\hat{\mathbf{e}}_i + \mu\hat{\mathbf{n}}}{|\hat{\mathbf{e}}_i + \mu\hat{\mathbf{n}}|} \tag{3.16}$$

After the substitution of Eq.3.16 into Eq.3.14, we can write

$$E_k^2(x_i)\left(1-(\hat{\mathbf{e}}_i\cdot\hat{\mathbf{n}})^2\right) = E_k^2(x_{i+1})\left(1-\left(\frac{\hat{\mathbf{e}}_i+\mu\hat{\mathbf{n}}}{|\hat{\mathbf{e}}_i+\mu\hat{\mathbf{n}}|}\cdot\hat{\mathbf{n}}\right)^2\right) \tag{3.17}$$

Substituting $\alpha = \hat{\mathbf{e}}_i \cdot \hat{\mathbf{n}}$, and working out the equations (all the algebraic passages are explained in [48]) we end up with the second order equation

$$\mu^2 + 2\alpha\mu + \left[1-\left(\frac{E_k(x_{i+1})}{E_k(x_i)}\right)^2\right] = 0 \tag{3.18}$$

This equation has two roots $\mu_\pm$, but only one is the correct solution for our physical refraction process, while the other is again a "ghost" solution with no physical meaning (it would correspond to a ray in the incident region).

Since the ray-tracing algorithm can operate with mesh elements having different curvatures (I will show an example of curved mesh later), the sign of α can be either positive or negative. Therefore, the correct physical solutions of Eq.3.18 can be found via numerical approach: testing both values $\mu_{\pm}$ in Eq.3.15, and verifying which solution maximizes the scalar product $\mathbf{E}_{\mathrm{i}} \cdot \mathbf{E}_{\mathrm{i+1}}$. Once the value of μ is found, the algorithm propagates the refracted vector $\mathbf{E}_{\mathrm{i+1}}$ in its mesh area, looking for the next intersection in the mesh of refractive indexes.

Negative refraction: This algorithm provides the physical implementation of positive refraction, but does not consider negative refractions which develops at graphene p-n junctions. An efficient way to integrate the negative refraction in the algorithm is to reflect the positive refracted ray $\mathbf{E}_{\mathrm{i+1}}$ with respect to the arbitrarily oriented normal vector axis $\hat{\mathbf{n}}$, whenever the kinetic energies of the two mesh regions are of opposite signs $E_{\mathrm{k}}(x_{\mathrm{i+1}})/E_{\mathrm{k}}(x_{\mathrm{i}}) < 0$. The expression for the negative refracted vector is given by

$$\mathbf{E}_{\mathrm{i+1}} = 2\alpha\hat{\mathbf{n}} - \hat{\mathbf{e}}_{\mathrm{i}} + \mu\hat{\mathbf{n}}. \tag{3.19}$$

Reflection processes: The algorithm can handle also the computation of reflections, whenever the incident angle θ_1 is greater than the critical angle θ_{c}:

$$\theta_1 = \arccos\left(\hat{\mathbf{e}}_{\mathrm{i}} \cdot \hat{\mathbf{n}}\right) \;\geq\; \theta_{\mathrm{c}} = \arcsin\left(\frac{E_{\mathrm{k}}(x_{\mathrm{i+1}})}{E_{\mathrm{k}}(x_{\mathrm{i}})}\right) \tag{3.20}$$

In case of reflection, the new reflected vector $\mathbf{R}_{\mathrm{i}}$ can be obtained from the following equation.

$$\mathbf{R}_{\mathrm{i}} = \mathbf{E}_{\mathrm{i}} - 2\left(\mathbf{E}_{\mathrm{i}} \cdot \hat{\mathbf{n}}\right)\hat{\mathbf{n}} \tag{3.21}$$

3.2.4 Modelling the tip potential

In Section 3.2.1 we have seen that the propagation of Dirac fermion through a straight graphene junction can be influenced by the evolution of the kinetic energy function $E_{\mathrm{k}}(x)$ along the x axis only. However, it is now necessary to introduce the electrostatic of a SGM tip. This portion of the algorithm has to be sufficiently flexible to work for any arbitrary tip position on the infinitely extended graphene plane. The tip-induced potential in the graphene

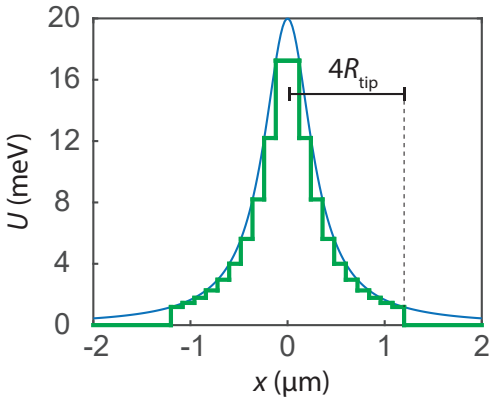

Figure 3.14: Profile of the tip potential along the radial axis (blue line). Discretized approximation of the potential profile for the ray-tracing algorithm (green line). In this example the spatial extension is limited to the arbitrary cut-off value of $4R_{\mathrm{tip}}$.

plane is modelled as a Lorentzian distribution in the form

$$U(\mathbf{r}) = U_0 \frac{R_{\text{tip}}^2}{R_{\text{tip}}^2 + ||\mathbf{r} - \mathbf{r}_c||^2} \tag{3.22}$$

where U_0 is the peak height of the potential, R_{tip} is the characteristic electrostatic potential decay of the Lorentzian, and $||\mathbf{r} - \mathbf{r}_c||$ is the distance from the tip centre.

In order to introduce numerically this potential profile in the program, we must limit the 2D extension of the tip potential within an arbitrary cut-off radius of a few times R_{tip}[3] . For a cut-off of $4R_{\text{tip}}$, we can partition the circumference of radius $4R_{\text{tip}}$ into a series of N concentric sub-circles having radius $r_i = i4R_{\text{tip}}/N$, where $i = \{1, 2, ..., N\}$. Each annulus between the i-th and (i+1)-th circumference represents a region of space of constant tip potential value U_i

$$U_i = U_0 \frac{R_{\text{tip}}^2}{R_{\text{tip}}^2 + r_i^2}. \tag{3.23}$$

An example of Lorentzian discretization, with $N = 10$, is represented in Fig.3.14. The Lorentzian has a peak potential $U_0 = 20$ meV and a decay parameter $R_{\text{tip}} = 0.3$ μm. The effect of the cut-off at $4R_{\text{tip}}$ visibly limits the spatial extension of the Lorentzian.

Fig.3.15 gives a pictorial representation of the mesh structure when a discretized Lorentzian potential is superimposed over the graphene plane. The concentric circles, describing the tip extension, intersect with the mesh on the junction. Together, they define closed areas at constant kinetic energy, with edges that refract the propagating rays. An example of trajectory is represented from the collection of violet arrows undergoing Klein tunnelling through the mesh elements. Another example of ray intersection is provided in the zoom within the yellow

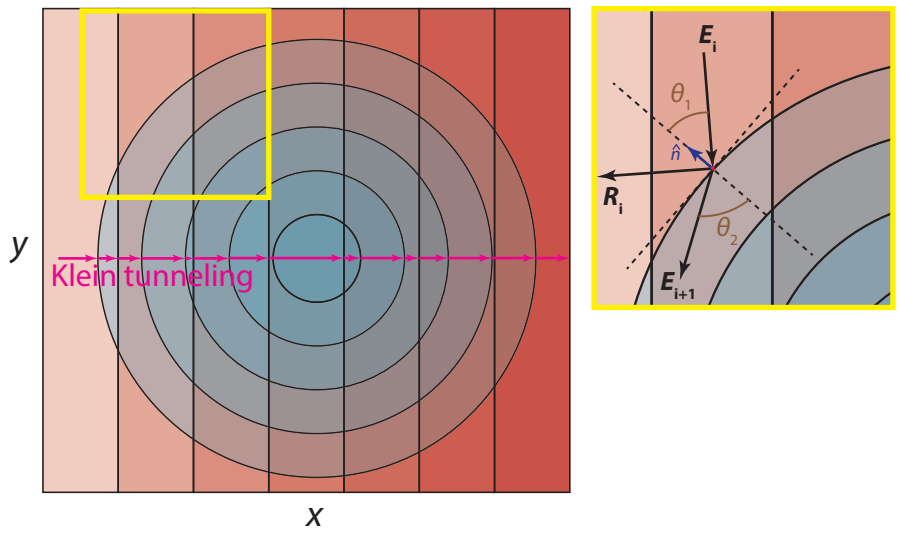

Figure 3.15: Mesh elements in the presence of a SGM tip. The vertical mesh on the graphene junction intersects with the circumferences composing the tip potential mesh. Violet arrows describe a Klein tunnelling trajectory passing through the mesh elements without deflection. In the yellow box is reported a zoom with an example of reflection/refraction process for an impinging ray on the outermost circle.

[3]The cut-off length can be chosen arbitrarily. For the simulations in the experimental chapter, the cut-off length is fixed at $8R_{\text{tip}}$.

box. The algorithm recognizes intersections with the circles composing the tip potential, and therefore it computes the normal vector $\hat{\mathbf{n}}$ at the intersection point $\mathbf{P}$

$$\hat{\mathbf{n}} = \frac{\mathbf{P} - \mathbf{r}_c}{|\mathbf{P} - \mathbf{r}_c|}. \tag{3.24}$$

This definition gives a normal vector oriented outwards the circles whatever the direction of the incident ray (inwards or outwards). The algorithm presented in Section 3.2.3 is however insensitive to the orientation of $\hat{\mathbf{n}}$, and treats the reflection/refraction with the numerical approach previously described.

3.2.5 Source and contacts

The calculations of semi-classical SGM maps requires to have: (i) a source of Dirac fermions injected into a graphene p-n junction; (ii) a tip raster scanning over the graphene layer, locally influencing the kinetic energy of the particles; (iii) an ensemble of absorbing contacts, which stop the particle trajectories and count, for any given tip position, the number of rays (amount of charge carriers) striking on them. These three ingredients are schematized together in Fig.3.16.a. The source region (see Fig.3.16.b) is an ideal source of rays, characterized by a fixed width W, which emits an uniformly distributed amount of N_{rays} propagating at the Fermi energy with an emission angle of the collimated beam $\alpha_{\max}$, in such a way that all the rays originate from a unique point located behind the source (see Section 3.3.1 for details on beam collimation).

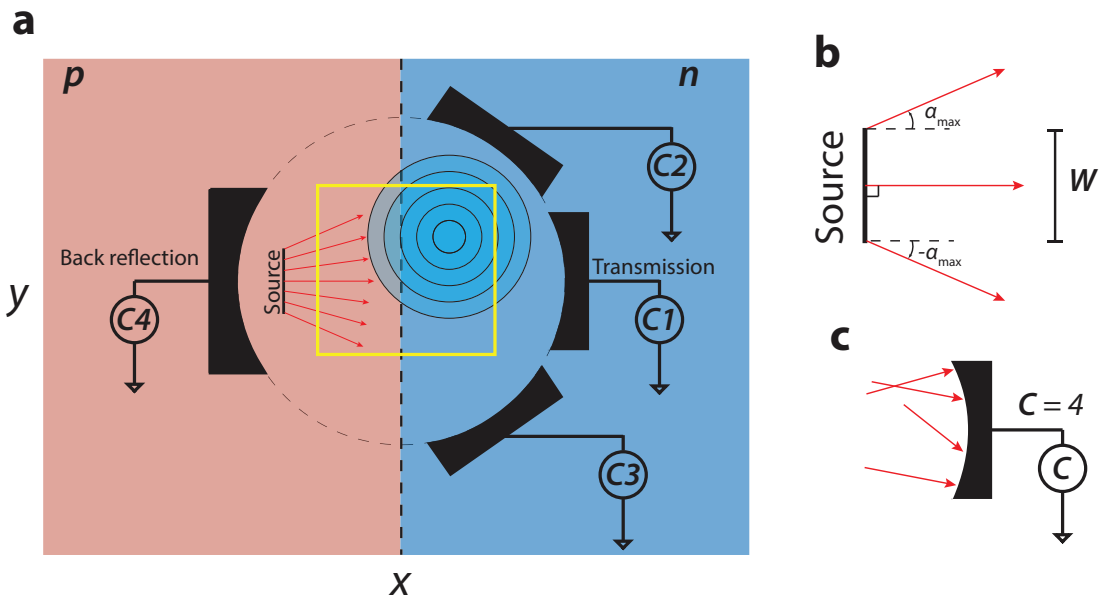

Figure 3.16: (a) Illustration of the numerical experiment for the calculation of semi-classical SGM maps. Rays are generated from a source region and propagate in the infinitely extended graphene p-n junction. The junction is highlighted by the vertical dashed line. The concentric circles represent the electrostatic spatial influence of the tip. The probe is raster scanned within the yellow scan window frame. A series of black contacts collect the carriers trajectories and count the amount C of impinging trajectories. (b) The collimated source region is characterized by a vertical extension W and generates an amount of N_{rays} with uniform angular distribution having maximum angle $\alpha_{\max}$. (c) Example of counting process with 4 rays reaching an absorbing contact.

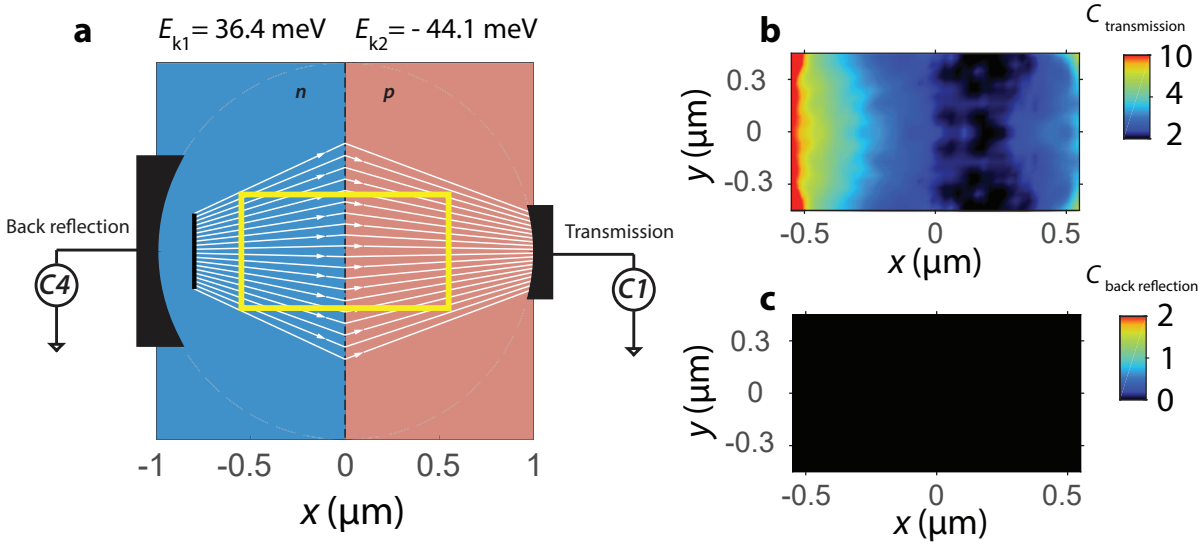

Figure 3.17: (a) Ray-tracing simulation of a trajectory field in an ideal abrupt graphene p-n junction. Kinetic energies for the two segment regions are reported in the upper part of the scheme. Two contacts for the detection of back reflection and transmission are distributed behind and in front of the source. (b,c) Semi-classical SGM maps of transmission and back reflection. The absence of signal in the back reflection map confirms the good transmission of the junction despite the presence of a scanning tip.

The absorbing contacts count the amount C of impinging rays, as depicted in Fig.3.16.c, in order to estimate the fraction C/N_{rays} of particles transmitted toward the contact. Contacts are distributed around a circle of radius 1 μm, detecting rays in different locations within the graphene junction. Right in front of the source region we have the collinear *transmission* contact which records the fraction of trajectories directly transmitted across the junction. Below and above the *transmission* contact we can identify two non-collinear contacts for the detection of weakly deflected trajectories. Right behind the source there is a contact for the detection of *back reflections*: with this term, I will refer to any process that causes particle trajectories to change direction and return to the source. This signal can be of interest in order to study the total reflections associated with smooth p-n junction.

The space coordinates of the tip centre $\mathbf{r}_c$ are arbitrarily restricted within the yellow scan window frame represented in Fig.3.16.a. The frame is pixelized into a series of $N \times M$ points corresponding to the spatial positions of the tip centre, as well as the positions of the pixels composing the SGM maps. For each tip position, there is a specific current trajectory distribution. The generation of SGM maps relies on the collection of the amount of rays absorbed from a contact for a given tip location.

3.2.6 SGM maps for an abrupt p-n junction

I present here the results of the semi-classical SGM calculations in the case of an abrupt p-n junction. In Fig.3.17.a Dirac fermions are originating in the n-doped region of the junction and propagating toward the p-doped region. The electron source is emitting $N_{\text{rays}} = 20$ uniformly distributed rays with maximum emission angle $\alpha_{\max} = 25°$. The ray-tracing simulation of the particle trajectories are shown with the white lines in Fig.3.17.a, in the absence of the tip. The kinetic energies for both sides of the junction are reported in the upper part of the schematic and correspond to a perfect focusing on the transmission contact.

The SGM tip is then modelled with an arbitrary Lorentzian potential creating electron accumulation with a peak potential $U_0 = -20$ meV and decay parameter, $R_{\text{tip}} = 370$ nm. According to the numerical procedures explained in 3.2.4, the Lorentzian profile is partitioned within a cut-off radius of $8R_{\text{tip}}$ using an ensemble of $N = 300$ circles. The scan window of the tip is represented by the yellow frame in Fig.3.17.a.

The SGM maps of the transmission and back reflection are reported in Fig.3.17.(b-c). The transmission map in Fig.3.17.b shows the evolving amount of rays impinging on the transmission contact according to the tip position. A region of high transmission is located on the very left part of the map, whereas the right part (the p-doped region) is more characterized by low transmission. Surprisingly, the back reflection map of Fig.3.17.c is not showing any signal evolutions, meaning that within the scan frame, the tip is not able to activate back reflection processes in the p-n junction.

In order to show the influence of the tip on the particle trajectories, we analyse the trajectory fields in Fig.3.18, for three different tip positions in the scan window. The positions are represented by the yellow markers in the SGM map. Fig.3.18.b represent the case when the tip is localized in the n-doped region of the junction. If we compare Fig.3.18.b with the unperturbed trajectories (Fig.3.17.a), we notice that the tip creates regions of high current density (well packed white lines) right in front of the junction region. A different scenario is observed in Fig.3.18.(c-d), where the Lorentzian potentials acts almost as a beam splitter in the p-doped region, significantly lowering the current density in front of the transmission contact.

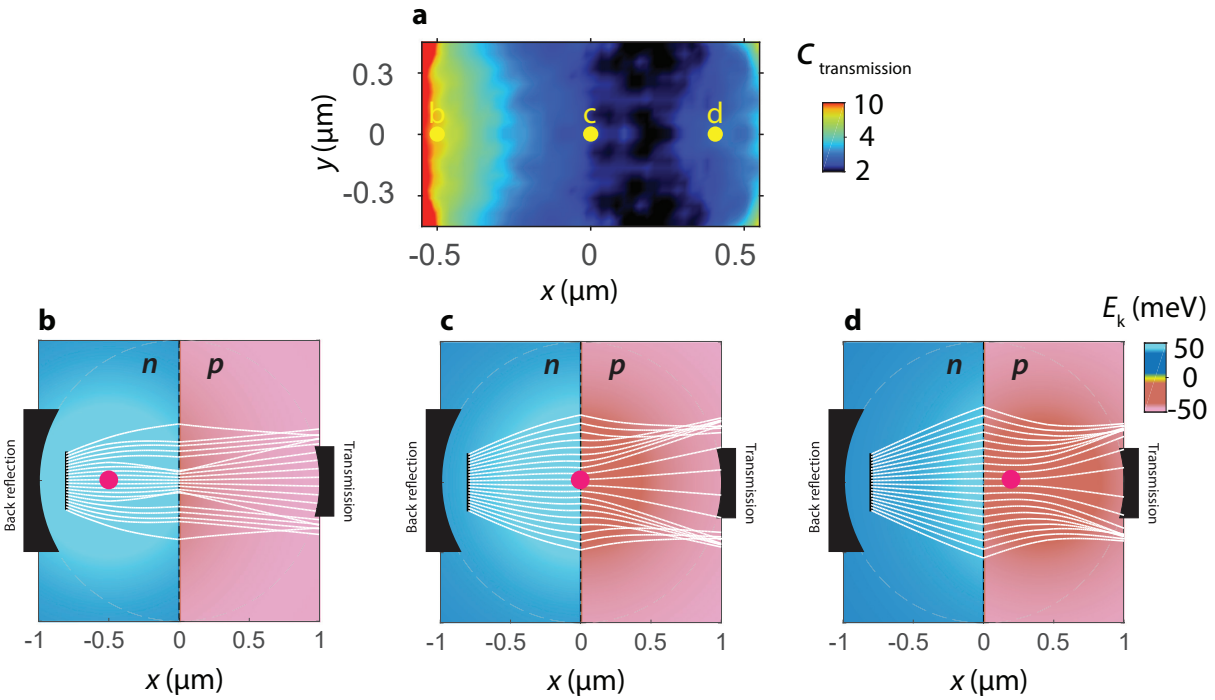

Figure 3.18: (a) Semi-classical SGM maps of transmission. Yellow markers show three different tip positions on the map where the trajectory fields were computed. (b-d) Ray-tracing trajectory fields computed for a SGM tip centred at the coordinates $x_c = -0.5,\ 0,\ 0.4$ μm respectively (see violet markers).

3.2.7 SGM maps for a smooth p-n junction

As already explained in Chapter 1.4.3, the presence of a smooth transition between the n- and p-doped regions in a graphene junction determines the formation of *classically forbidden* region manifesting turning points for classical trajectories. The physical effect of this forbidden region can be visualized in the ray-tracing simulation of Dirac fermion trajectories in Fig.3.19.a. Trajectories which are not perfectly orthogonal to the potential step are gradually back reflected, changing the direction of propagation with respect to the initial conditions at the injection. In the simulation, the graphene junction is characterized by the following kinetic energy profile

$$E_{\mathrm{k}}(x) = 36.4 - \frac{U}{2}\left(1 + \tanh\frac{x}{\delta}\right) \tag{3.25}$$

where $U = 80.5$ meV and $\delta = 0.3$ μm. The energy profile is plotted above the unperturbed trajectory field in Fig.3.19.a.

By scanning the SGM tip within the yellow frame, we compute the numerical SGM maps for both the back reflection and transmission contacts. The weak signal in the transmission SGM map of Fig.3.19.b confirms the reduced amount of particle trajectories crossing the barrier, but the presence of the tip enables a few trajectories to pass to the p-doped region thanks to the ray bending induced by the tip potential. The SGM map of back reflection in Fig.3.19.c, presents a very strong signal containing interesting informations concerning the transport processes in a smooth graphene p-n junction.

An insight in the actual transport, in the presence of a scanning gate is provided in Fig.3.20, where current paths are computed for three different tip positions represented by the yellow markers in Fig.3.20.a. When the scanning gate is positioned on the left region of the junction,

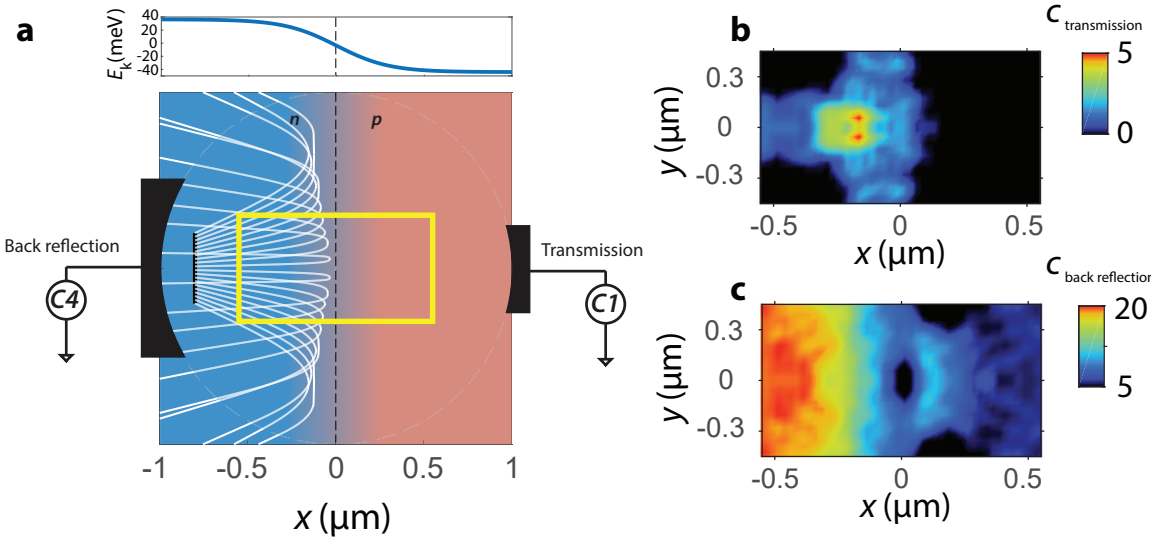

Figure 3.19: (a) (*upper part*) Kinetic energy plot profile characterizing the smooth p-n junction. (*lower part*) Ray-tracing trajectory field for an amount of $N_{\mathrm{rays}} = 20$ rays generated from the source region. Trajectories not orthogonal to the potential interface are subjected to turning points causing back reflections inside the n-doped region. Only horizontal rays (not represented) would pass to the right via Klein tunnelling. The yellow frame represents the scanning window where the numerical SGM mapping is performed. (b,c) Semi-classical SGM maps of transmission and back reflection for a smooth graphene p-n junction. While the transmission map displays a weak signal, the back reflection map is characterized from stronger signal variations, highlighting interesting transport properties under the presence of the scanning tip.

the lensing effect of the tip enhances the *back reflection process*, increasing the current density in front of the back reflection contact (Fig.3.20.b). A different scenario appears when the tip is positioned in the middle of the junction in Fig.3.20.a. In such condition, the back reflection process at the contact region is strongly reduced and many particle trajectories seem to find their way through the potential step of the junction, as already mentioned for the transmission map. According to the trajectory field in Fig.3.20.d, when the tip moves forward, further into the p-doped region, the back reflections are re-established. Another common feature appearing in Fig.3.20.c and Fig.3.20.d, is the behavior of the trajectories emitted at high angles, which are *trapped* at the junction and follow vertically the junction interface without being reflected nor transmitted. All these unusual trajectory behaviours can be explained from a gradient-index optical viewpoint, invoking the roles played by the mesh elements of the junction and the tip potential.

3.2.8 Tunnelling through classically forbidden regions

The *back reflections* in Fig.3.20.b are the results of theoretically predicted turning points, classically separating the n-doped and p-doped regions. They represent points of maximum penetration at which the local kinetic energy is sufficient to cause total internal reflection of the ray. The theoretical details have been introduced in Chapter 1.4.3. Turning points in Fig.3.20.b are typically located far from the tip centre, where the local evolution of the potential is mostly governed by the vertical mesh elements of the junction and only weakly influenced by the circular tail of the tip potential.

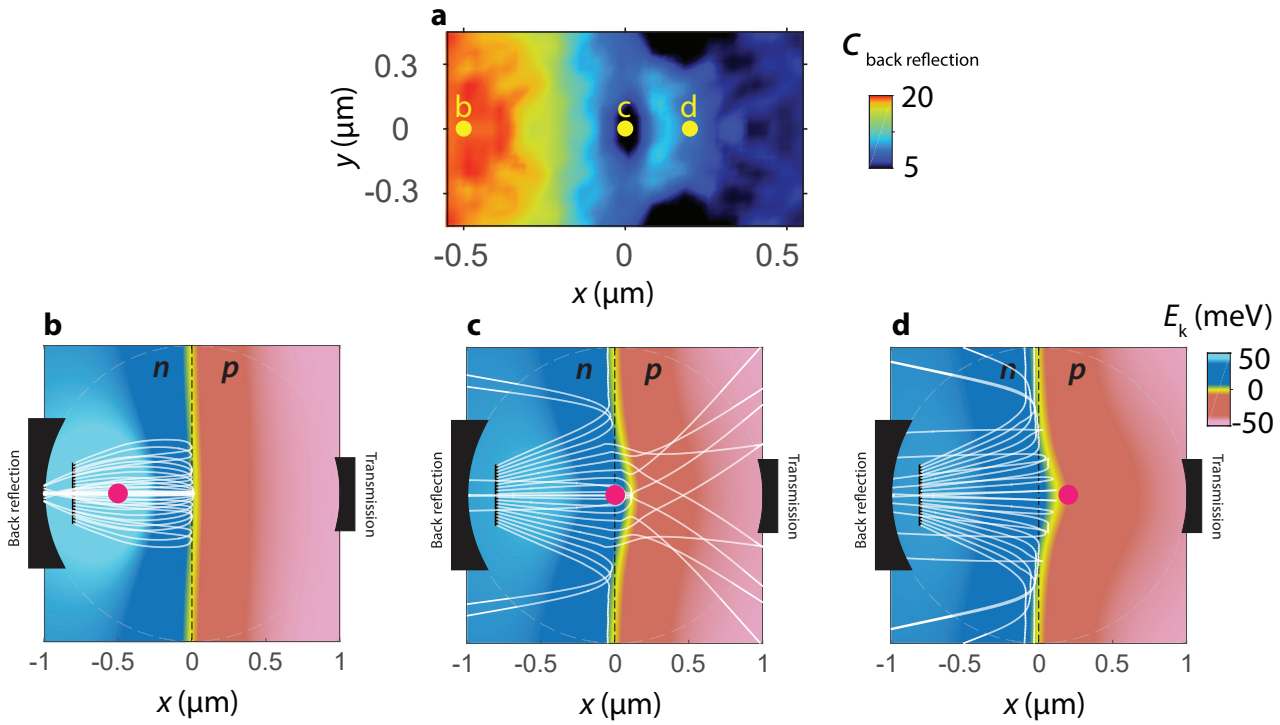

Figure 3.20: (a) Semi-classical SGM maps of back reflection. Yellow markers show three different tip positions on the map where the trajectory fields were computed. (b,c) Ray-tracing trajectory fields computed for a SGM tip centred at the coordinated $x_c = -0.5,\ 0,\ 0.2\mu$m, respectively, and $y_c = 0$ (see violet makers).

The interpretation of the *tunnelling* trajectories composing the pattern in Fig.3.20.c is however much more complex, since this time the barrier physics is altered to a greater extent by the invasive circular tip potential, which lies exactly at the middle of the junction. The orientation of the trajectories approaching the junction is dominated first by the kinetic energy variations imposed by the vertical mesh of the junction and afterwards by the concentric circles composing the tip potential mesh. According to the direction taken by the propagating particle, it is possible that a particular ray strikes a mesh element of the tip with a significantly high incident angle. This condition is reported in Fig.3.21.a, for a single trajectory from the ray field in Fig.3.20.c. The red marker indicates the intersection point with a circle composing the tip potential mesh. A detail of the intersection is reported in the zoom of Fig.3.21.b, where the vertical lines represents the mesh elements of the junction, while the diagonal line is a portion of the mesh composing the tip potential. The incoming ray in region I impinges with a grazing incidence angle on one edge of region II, which is characterized with a lower kinetic energy. As a result, the ray is forward reflected, and it will propagate under the invasive influence of the tip toward the classically separated p-doped region.

It should be noted that such transmission is not predicted by continuous gradient-index optical equations for ray dynamics, since theoretically rays are always back reflected from turning points located close to the p-n interface. The observed transmissions are therefore associated to a forward reflections due to the not sufficiently refined mesh of the complex gradient index medium, which causes the travelling particle to reach a region of space beyond the classical turning point.

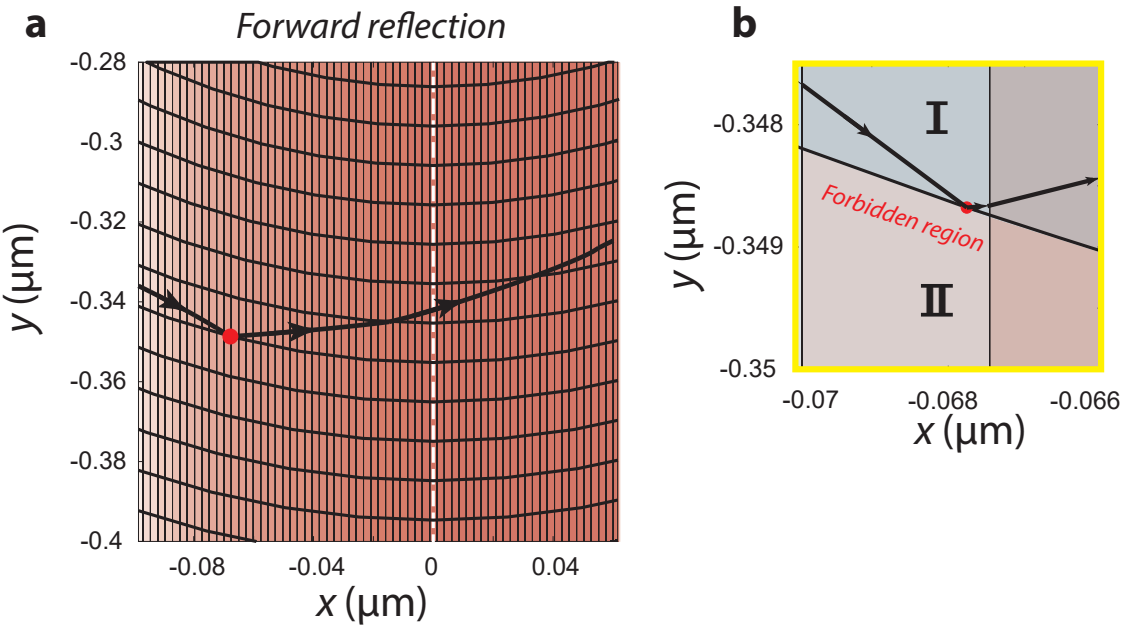

Figure 3.21: (a) A single electron trajectory (bold black arrow) taken from the trajectory field of Fig.3.20.c. The particle is propagating in the partitioned mesh areas inside the graphene junction, with the SGM placed at the middle of the junction. The vertical lines are representing the mesh composing the graphene junction, while the equidistant arcs represents the tip potential mesh elements. The red marker is highlighting the tip-induced forward reflection process, causing a forward reflection of the rays with consequent tunnelling through the junction. (b) Zoom of the forward reflection after the trajectory interaction with the tip.

These simulation artefacts can be seen as the optical analogue of frustrated total internal reflections, which causes Dirac fermions to tunnel through the junction. The tunnelling processes are chaotic outcomes, strictly depending on the initial space coordinates and momentum of the injected particle, as well as on the complex structure of the mesh. The mesh dependency can be visualized in Fig.3.22.(a-c), where the Lorentzian potential is discretized with three different amounts $N = \{300,\ 301,\ 302\}$ of evenly spaced circles. The pattern formed by the transmitted rays changes quite remarkably according to the N parameter, suggesting the presence of a chaotic dynamics in the classical limit. Nevertheless, the tunnelling processes can be removed from the simulation with a sufficiently high value of mesh elements composing the Lorentzian potential. In Fig.3.22.(d-e) are reported two ray fields simulations for $N = \{800,\ 801\}$, for which only the classical pattern of total internal reflection is observed, even if we can still appreciate a small dependence of the ray patterns from the N parameter.

The second anomalous behaviour that characterizes the trajectory dynamics in the simulations is the *trapping* along the p-n interface. It occurs when the propagating Dirac fermion overcomes a first turning point, and starts to experience a series of total reflections and transmissions which localize the particle in the vicinity of the junction. These kind of particle trajectories are continuously subjected to an unstable equilibrium condition, reflected back and forth in an almost vertical propagation as depicted in Fig.3.23.b.

To summarize, if *reflections* due to the turning points are standard manifestation of classical Dirac fermions dynamics in smooth graphene p-n junctions, then *tunnelling* and *trapping* are unpredictable outcomes developing in the close vicinity of the junction, under the presence of a

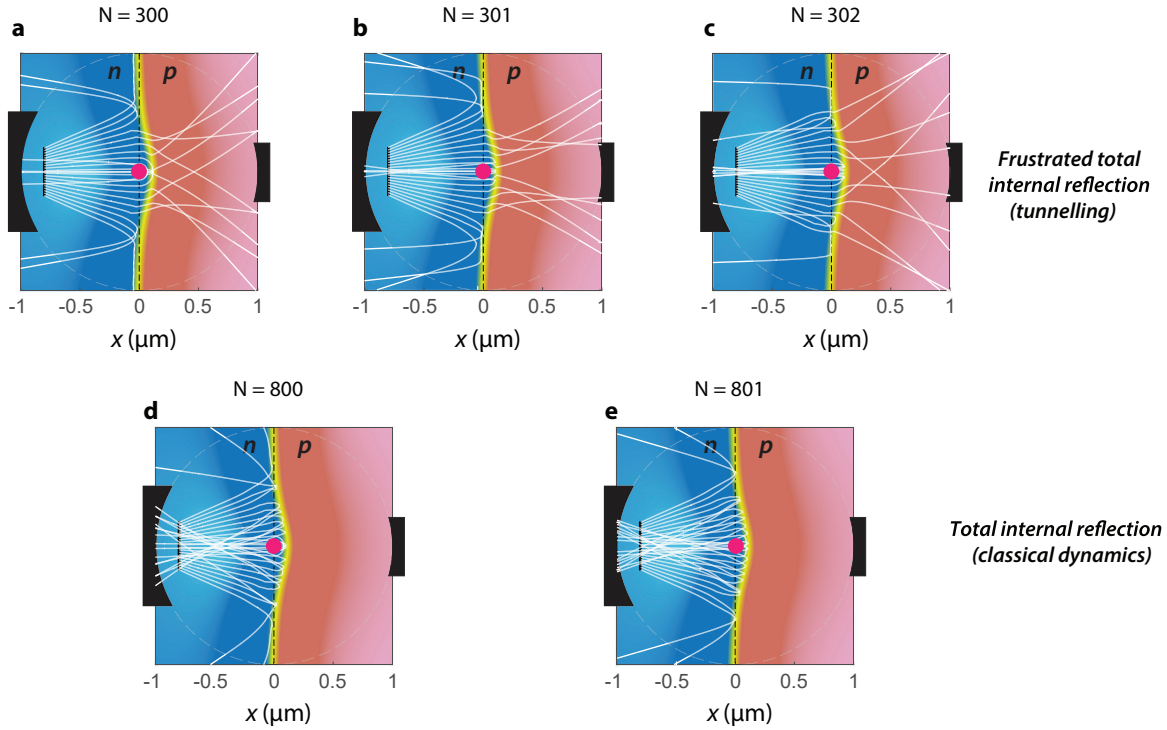

Figure 3.22: (a-c) Ray-tracing trajectory fields as a function of three close values N of circles composing the mesh of the tip potential. The rays crossing the junction are artefacts which mimic frustrated total internal reflections at the barrier that are not expected for a classical model. These trajectories are particularly sensitive to small variations of the N parameter, confirming the presence of classical chaotic dynamics developing at the junction. (d-e) The pattern of total reflection is restored when the number of the tip mesh elements N increases.

SGM tip generating a complex potential mesh. Such artefacts are however not completely useless, and can be used as indicators of richer dynamics that needs to be investigated with proper quantum mechanical approaches, either with fully quantum trajectory methods following a de Broglie-Bohm approach, or via more evolved semi-classical approximations. Concerning the latter, in certain regimes, it is possible to describe quantum tunnelling via standard semi-classical approximations relying on perturbations to known classical solutions [6]. In such semi-classical methods, the single propagating particle can be described via expected values of quantum observables, which are classical canonical variables associated to a classical Hamiltonian, with a quantum contribution coming from higher order moment statistics (i.e. the variance of travelling wave packets) subjected to the uncertainty principle [6]. Similarly to the results obtained in Refs. [6, 46], the unusual trajectory dynamics discussed in this section are indeed ruled from uncertainty, which is artificially introduced from not sufficiently refined mesh elements. Moreover, the trajectory behaviours presented in [6, 46] are surprisingly very similar to the one presented here. Unfortunately, the absence of a rigorous statistical analysis on our ray-tracing results, does not allow any further speculation on the numerical validity of the tunnelling trajectories. However, in Chapter 5.6 I will compare these results with experimental data, providing interesting hints of on the relevance of the present ray-tracing approach for both the transmission and back reflection SGM mapping.

3.3 Design of graphene p-n junction devices

In Section 3.1, we presented a series of SGM experiments providing visual informations concerning the possibility to sculpture in space the current flow inside mesoscopic devices. By playing with electrostatic and magnetic fields, it is possible to refocus electron waves, to make electron analogue of wave-guide and lenses. All these applications belong to the domain of electron optics in the solid state, and are all based on the possibility to play with ballistic electrons and to address them using a simplified concept of electron trajectories. As an attempt to push forward this technological branch with ballistic graphene systems, we proceed now on the presentation of the design elements characterizing our graphene p-n junction.

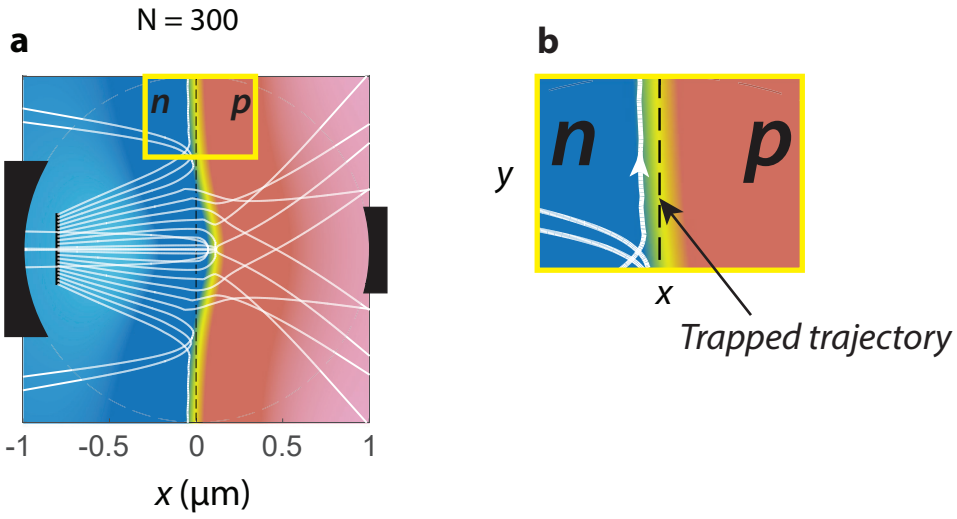

Figure 3.23: (a) Ray-tracing trajectory field on a graphene smooth p-n junction with a SGM tip at the centre, exhibiting the three possible trajectory behaviours: *reflection*, *tunnelling* and *trapping*. (b) Detail of a trapped trajectory following the edge of the junction.

3.3.1 A pinhole collimator for Dirac fermions

One of the main challenges for the SGM observation of the negative refraction and Veselago lensing in graphene p-n junctions is to be able to inject a sufficiently collimated beam of electrons. The collimation can reduce the detrimental electron scattering at the edges of the device, and allow to localize more in space the current beam. A narrower beam improves the device sensitivity to electrostatic tip perturbations, obtaining higher signal to noise ratio during SGM measurements. Collimation is essentially the narrowing of the angular injection distribution of an electron flow. It can be performed in ballistic semiconductor 2DEG via a potential energy barrier in a quantum point contact (QPC) imposing a constrain on the transverse electron momentum values (*barrier collimation*), and with the smooth opening of the QPC saddle point potentials toward a large Fermi gas (*horn collimation*) [10].

In graphene, however the collimation effect must be achieved with other strategies beyond the QPC geometry, since Dirac fermions are transparent to electrostatic potentials and therefore cannot be confined. One example of Dirac fermion collimator can be obtained by combining the negative refraction effect with the Klein collimation at a parabolic p-n junction [95, 11]. However, we present here another collimator that has been fabricated during the thesis: the *pinhole* collimator, introduced first in Ref.[7]. The pinhole is etched in an h-BN/graphene/h-BN heterostructure with two chambers connected to two independent 1D edge contacts like in Fig.3.24.a. The bottom chamber is connected to a current source, providing the injection of charge carriers into the graphene layer. The collimation effect is directly linked to the upper ohmic contact, which is connected to ground. The upper contact absorbs and filters away a fraction of stray carriers having high transverse momentum q_y, and letting the low q_y carriers free to propagate.

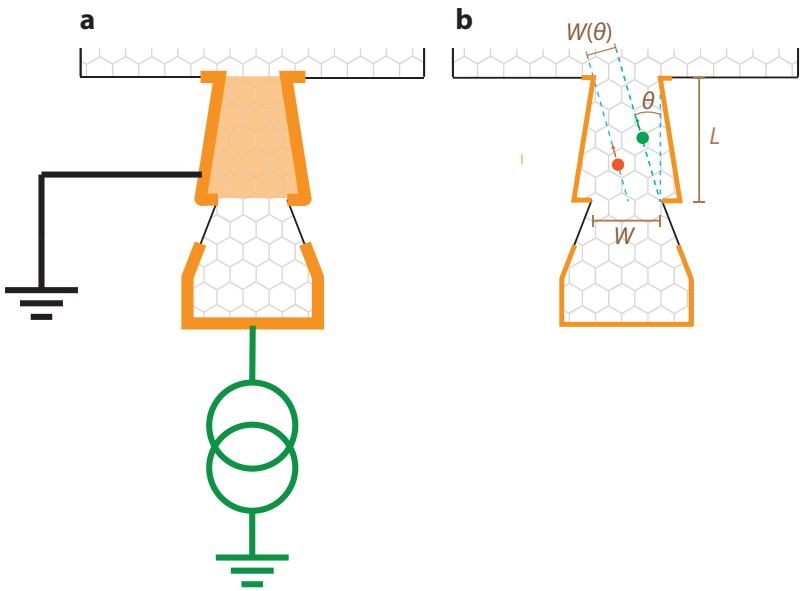

Figure 3.24: (a) Pinhole collimator for Dirac fermions. Two ohmic contacts are connecting laterally the graphene heterostructure. The bottom contact is connected to a current source for carrier injection, while the upper contact (the filtering chamber) removes stray carrier trajectories not participating to the collimated flow. (b) Geometrical representation of particles (green and red) propagating with the same propagation angle θ. While the green particle will be emitted by the collimator, the red particle will hit the edge of the reflectionless ohmic contact and will be absorbed.

Before giving more details on the working mechanism of the collimator, it is worth to mention that a collimation process is a concept coming from classical mechanics. Nevertheless, its adaptation in graphene can be supported within semi-classical arguments: (i) considering the propagation of non-interacting Dirac fermions and (ii) considering specific etched constriction geometries, in which we can guarantee the adiabatic invariance of the product $S = |q_y|W$, where W is a generic width of the graphene system in which carriers propagate [10].

Classical Sharvin conducance The working principle of the pinhole collimator can be discussed via the calculation of its classical "Sharvin" conductance. The presented calculations are inspired from the supplementary materials in Ref.[7]. A generic current flux density in a 2D ballistic graphene channel can be written according to the drift equation

$$J = env_{\mathrm{D}} \tag{3.26}$$

where n is the charge carrier density and v_D the classical drift velocity of Dirac fermions which corresponds to the quantum mechanical group velocity [70], which in graphene is a constant, called Fermi velocity, associated to the graphene linear dispersion according to the relation

$$v_{\mathrm{D}} = v_{\mathrm{F}} = \frac{1}{\hbar}\frac{\mathrm{d}E}{\mathrm{d}|\mathbf{q}|} \tag{3.27}$$

By introducing this equation in Eq.3.26, we can express the current flux density with the exact differential equation

$$\mathrm{d}J = \frac{e}{\hbar}\frac{\mathrm{d}E}{\mathrm{d}|\mathbf{q}|}\,\mathrm{d}n \tag{3.28}$$

The geometry of the pinhole collimator can be thought as a narrow channel connecting two reservoirs having Fermi energy mismatch ΔE_{F}. Therefore, by integrating in energy the last equation, we can write the current density as a function of the energy mismatch

$$J = \frac{e}{\hbar}\frac{\mathrm{d}n}{\mathrm{d}|\mathbf{q}|}\,\Delta E_{\mathrm{F}} \tag{3.29}$$

We can study the angular dependence of the current flux in the collimator by differentiating both sides of Eq.3.29 with respect to the angle of propagation θ of a charge carrier (see Fig.3.24.b)

$$\frac{\mathrm{d}J}{\mathrm{d}\theta} = \frac{e}{\hbar}\frac{\mathrm{d}^2n}{\mathrm{d}\theta\mathrm{d}|\mathbf{q}|}\,\Delta E_{\mathrm{F}} \tag{3.30}$$

The term $\frac{\mathrm{d}^2n}{\mathrm{d}\theta\mathrm{d}|\mathbf{q}|}$ in Eq.3.30 can be developed by looking at the 2D Fermi sphere in Fig.3.25, where the Dirac fermion momentum is expressed as a function of the angle of propagation θ. For a given Fermi energy, the electron density of the infinitesimal area element (red square in Fig.3.25) is

$$\mathrm{d}n = g_{\mathrm{k}}\frac{|\mathbf{q}_{\mathrm{F}}|\mathrm{d}\theta\mathrm{d}|\mathbf{q}|}{2\pi^2} \;\Rightarrow\; \frac{\mathrm{d}^2n}{\mathrm{d}\theta\mathrm{d}|\mathbf{q}|} = \frac{|\mathbf{q}_{\mathrm{F}}|}{\pi^2} \tag{3.31}$$

where $g_{\mathrm{k}} = 4$ accounts for the spin and isospin degeneracy.

Therefore, by expressing the Fermi energy mismatch as a function of an external voltage bias $V_{DS} = \Delta E_F/e$, we can write the equation of the angular flux density as

$$\frac{dJ}{d\theta} = \frac{2e^2}{h}\frac{|\mathbf{q}_F|}{\pi}V_{DS} = \frac{2e^2}{h}\sqrt{\frac{n}{\pi}}V_{DS} \tag{3.32}$$

This equation has the same structure and can be compared with the current flux obtained for a generic ballistic 2D channel between two Fermi gases [122].

We assume now an uniform angular injection of electrons from the source ohmic contact of Fig.3.24. From geometrical arguments it is evident that an injected particle propagating with a certain angle θ, can either escape the constriction (like the green particle in Fig.3.24.b) or being absorbed in the upper ohmic contact connected to ground (like the red particle in Fig.3.24.b). Therefore, for any propagation angle θ, there is an effective constriction width $W(\theta)$ for the propagating particle:

$$W(\theta) = [\, W - L|\tan(\theta)|\,]\cos(\theta) \quad : \; |\theta| < \text{atan}(W/L) \tag{3.33}$$

If the condition $|\theta| < atan(W/L)$ is not fulfilled, the particle is absorbed and removed by the grounded contact.

I now write the angular classical conductance of the pinhole collimator using Eq.3.32 and 3.33 together [7]

$$G(\theta) = \frac{2e^2}{h}\sqrt{\frac{n}{\pi}}\,[\, W\cos(\theta) - L|\sin(\theta)|\,] \quad : \; |\theta| < \text{atan}(W/L) \tag{3.34}$$

A plot of the angular conductance $G(\theta)$ for a specific pinhole collimator, having parameters $W = 400$ nm and $L = 700$ nm is reported in Fig.3.26. The function drops to zero when carriers have emission angle $\theta = \pm\text{atan}(W/L)$, i.e. when the particles hit the grounded edges composing the filtering chamber of the pinhole. For a sufficiently small ratio W/L, the pinhole collimator therefore realizes an efficient collimation of the electron beam.

SGM studies of pinhole collimators During the times of this thesis, the research group of Robert Westervel at Harvard published two articles related to the SGM imaging of collimated flows of both electrons and holes in a graphene heterostructure [15, 12]. They reviewed the semi-classical collimation arguments proposed in [7] and characterized via SGM technique a similar version of the previously described pinhole collimator. An example of the experimental

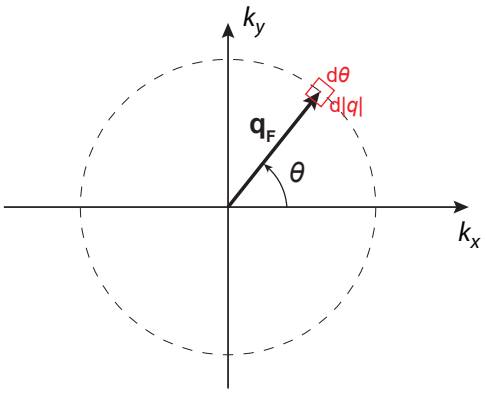

Figure 3.25: 2D Fermi sphere.

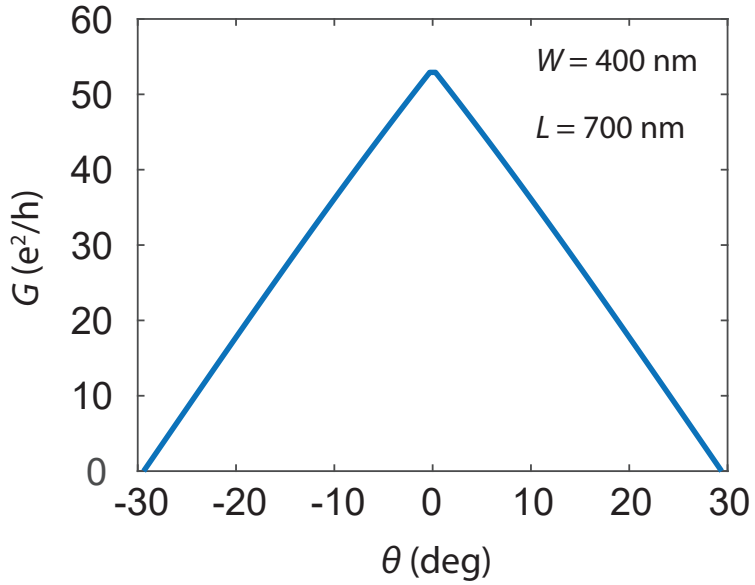

Figure 3.26: Angular classical conductance of a pinhole collimator.

SGM imaging of the electron/hole flow is shown in the upper part of Fig.3.27. In the lower part of the image there are two ray-tracing SGM simulations, which were performed in order to analyse the SGM experimental results.

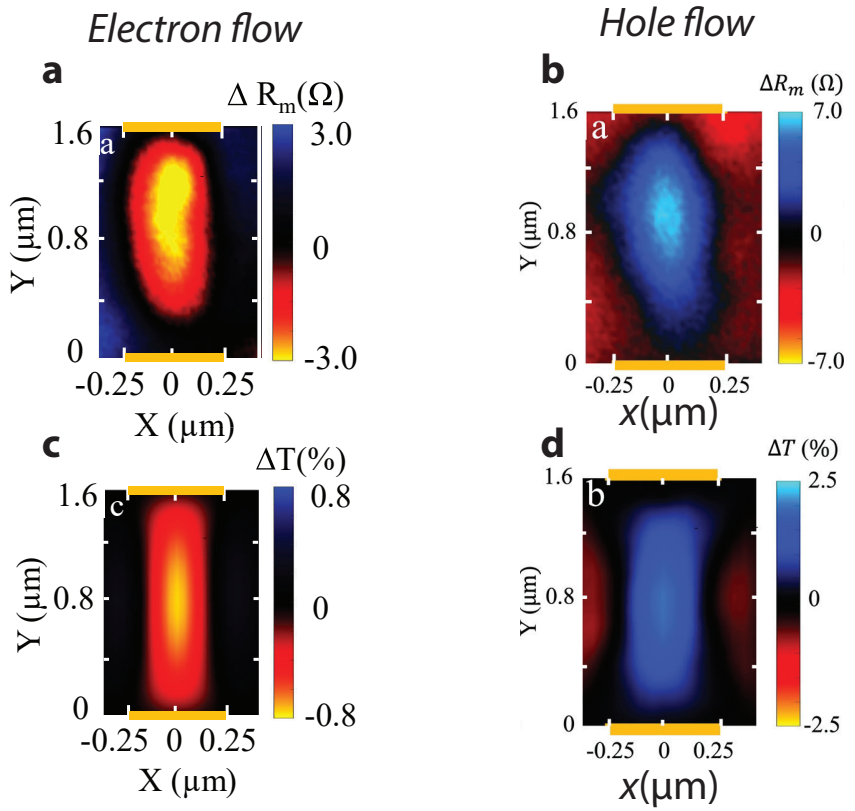

Figure 3.27: (a,b) Experimental SGM maps of electrons and holes flow in a graphene heterostructure. (c,d) Ray-tracing simulations employed for the interpretation of the experimental maps. Taken from [15, 12].

3.3.2 Reflectionless boundaries around the active region

One of the main reason for the integration of pinhole collimators in our device structure is to reduce as far as possible electron scattering at the edges of the device, addressing the current only toward the p-n junction region. In ballistic devices, scattering at boundaries would lead to complicated reorganization of carriers in the graphene layer, making therefore the SGM signal unreadable. However, a possible strategy for the minimization of scattering at boundaries relies on the application of large metallic edge contacts creating ohmic connections around the active region of the junction. The large metallic contacts are typically connected to ground, acting mostly as reservoirs for particle absorption. We will assume in the following that the large absorbing contacts are reflectionless, that is, electrons do not experience any reflection process and are immediately thermalized at the temperature and chemical potential of the contact.

The final layout of the graphene p-n junction is reported in Fig.3.28.a. It is equipped with two collinear pinhole collimators at each extremity of the junction, represented from the edge contacts 1,2 and 5,6. The central region, where the junction is located, is the active region of the device, where the reflection and refraction processes develop. A series of four large edge contacts (3, 4, 7, 8) have been distributed around the active region to remove the reflections. In Fig.3.28.b is reported an optical micrograph of a fabricated device following the presented scheme.

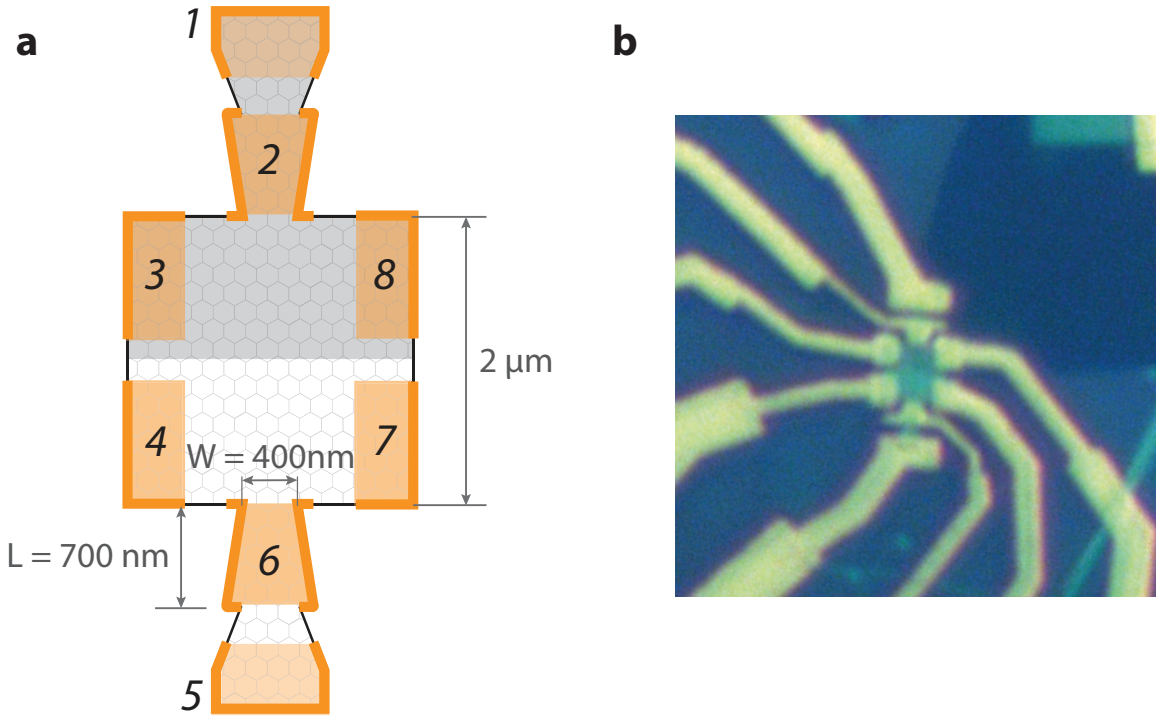

Figure 3.28: Schematic (a) and optical micrograph (b) of a graphene p-n junction for electron optics. Contacts 1, 2 and 5, 6 are pinhole collimators for Dirac fermions, while contacts 3, 4, 8, 7 are absorbing edge contacts to reduce scattering events at the edges of the heterostructure.

Conclusion

In the first part of this chapter, I summarized a list of past publications where semi-classical simulations have been employed in different SGM experiments of electron optics. The purpose was to provide a series of examples showing the strength of the semi-classical ray-tracing method to reverse-engineer the quantum mechanical SGM signals in mesoscopic billiards. The semi-classical approach seems to be less indicated in the case of closed geometries, when the LDOS of an electronic systems is concentrated in narrow cavity resonators.

Then, I presented the algorithm that I have developed for the ray-tracing simulations of SGM maps in multi-terminal graphene p-n junctions, discussing the simulated signals in both the abrupt and smooth junction case. I discussed on the numerical artefacts obtained during the simulations of current trajectories in the smooth p-n junction, which have been interpreted as indicators of rich charge dynamics developing at the junction level.

The last part is dedicated to the design elements of the graphene p-n junctions for electron optics measured during the thesis. I described the possibility to control the collimation of an electron beam with a specific pinhole collimator for Dirac fermions, and explained the importance to have reflectionless boundaries around the active region of a graphene p-n junction for a clean SGM transport imaging.

Chapter 4

Graphene device fabrication

Contents

The goal of this chapter is to present the fabrication process of the devices used in the SGM measurements. The devices are composed of an exfoliated graphene flake, encapsulated between two hexagonal boron nitride (hBN) flakes to improve its quality. The resulting heterostructure is then positioned halfway over a thin pristine graphite flake, while the rest is directly placed on the SiO_2 substrate. Graphene is then contacted by metallic electrodes patterned by e-beam lithography and deposited by metallic evaporation. During the thesis, I fabricated 22 stacks and 13 devices, among which 6 could be measured. I managed the entire process, including exfoliation, van der Waals stacking, electron-beam lithography, etching, and metal deposition.

4.1 Principles of graphene encapsulation

The first studies of graphene devices (from 2004 to 2010) were performed on samples obtained by connecting graphene flakes directly deposited on silicon substrates [111, 157]. Unfortunately the mobility of these devices were strongly influenced by the roughness of the SiO_2 substrate [74], and by the charge inhomogeneities trapped inside the silicon substrates [69, 54]. A major improvement of the mobility was obtained with suspended graphene structures and subsequently via the employment of hBN as a substrate material [44], providing a physical separation between graphene and the silicon oxide. hBN shows a crystalline honeycomb lattice very similar to that of graphene, with a lattice constant that differs by about 1.7%. Because of the lattice similarity, graphene on hBN has a reduced amount of corrugation and mechanical strain with respect to graphene devices directly deposited on SiO_2 substrates. hBN is a good electrical insulator with a large band gap ($E_g \simeq 5.7$ eV), a moderate dielectric constant ϵ_r^{BN} ranging from 3 to 4 (similar to $\epsilon_r^{SiO_2} = 3.9$) and an extremely small surface reactivity.

The transfer process of graphene on the top of hBN can significantly improve the mobility of graphene devices [44]. However, in 2013 the transferring technique developed further, allowing to position a heterostructure of hBN/graphene over an exfoliated graphite flake [68]. Rapidly, a third technological development was introduced by Wang and co-workers, who managed to encapsulate a graphene flake between two flakes of hBN, forming a hBN/graphene/hBN heterostructure, a so-called stack [147]. The encapsulation process is reported in Fig.4.1. First a hBN flake is picked up with a sticky polymer of Polypropylene Carbonate (PPC). The hBN flake on the polymeric stamp is then approached toward the graphene flake and brought in contact. Thanks to the attractive van der Waals interactions between the two flakes, the graphene flakes adheres to hBN. The same operation is then iterated again to pick-up a second hBN flake, obtaining the fully encapsulation of graphene between two hBN crystals.

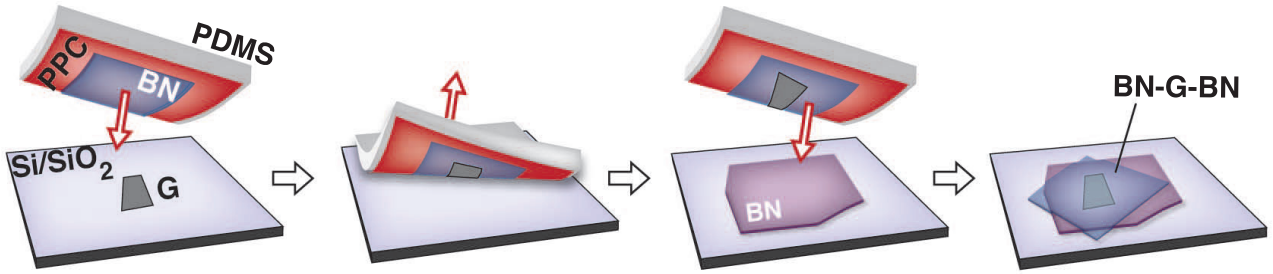

Figure 4.1: Illustration of the van der Waals pick-up method for the fabrication of a hBN/graphene/hBN heterostructure. Taken from [147].

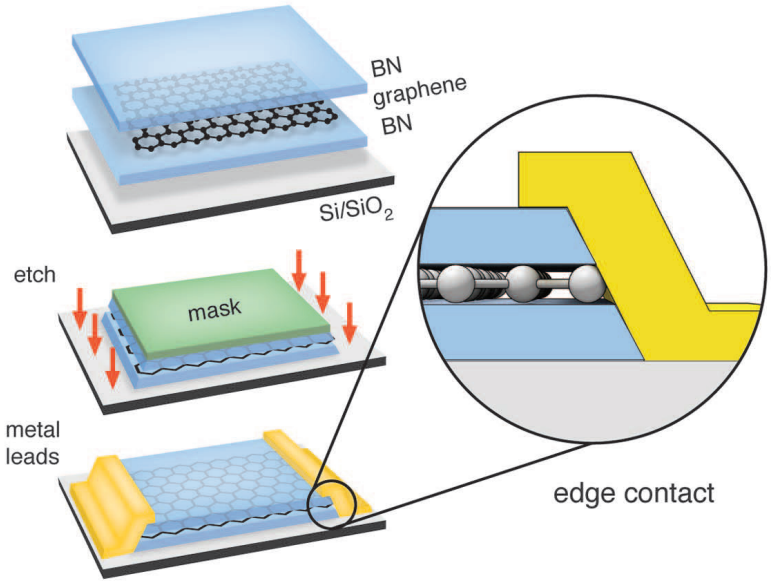

Figure 4.2: Schematic of the fabrication process for the definition of the ohmic contacts in encapsulated graphene devices. The heterostructure undergoes a reactive ion etching process. During the etching, a mask protects portion of the stack, exposing only the edges of graphene. Metal is deposited on the edges of the heterostructure, creating one dimensional edge contacts. Taken from [147].

This encapsulation allows to protect graphene from any external contamination, even during lithographic processes, since the surfaces around graphene are never put in contact with resist material. This protection allows to obtain devices with ultra-high electron mobility over 10^6 $cm^2V^{-1}s^{-1}$, and mean free path exceeding the size of micron-size devices.

Once graphene is encapsulated, it is necessary to contact it with metallic electrodes for transport measurement. Wang *et al.* developed a nanofabrication process for contacting the encapsulated graphene flakes (see Fig.4.2), which is based on a selective reactive ion etching of the heterostructure allowing to expose the edges of graphene. After the etching, the leads are obtained via the deposition of suitable metals contacting the exposed edges of the heterostructure [147]. This method is now a standard process for the fabrication of high-mobility samples, where transport can be ballistic over tens of microns [105, 153, 136].

4.2 Graphene p-n junction heterostructure

I report here the technological steps required for the fabrication of a heterostructure for a graphene p-n junction.

4.2.1 Crystal exfoliation

The first step for the fabrication of a p-n junction consists in the realization of a crystal stack for the encapsulation of graphene. In order to obtain crystal flakes, macroscopic crystals of graphite and hBN are exfoliated mechanically using scotch tape. Specifically, few fragments of graphite and hBN are positioned on an adhesive tape, which is then folded and unfolded several times, obtaining an homogeneous distribution of thin crystals on the tape surface, as illustrated in Fig.4.3.a.

After the mechanical cleavage, the tape is then positioned over a clean Si/SiO_2 substrate, gently rubbed for few minutes, and then peeled off slowly such that few flakes from the cleaved crystals remain deposited on the substrate. This method allows to obtain crystals of various thickness, from monolayer to few microns thick crystals.

Optical identification of crystal flakes: Once exfoliated, the flakes need to be carefully checked to identify which ones are suitable for the fabrication of high-mobility heterostructures. Flakes need to be atomically flat, free from terraces and cracks. They must be clean and free from glue residues coming from the scotch tape. The most efficient way to locate graphene, graphite and hBN flakes on the silicon substrate, is through optical microscopy. In particular, graphite and hBN flakes can be easily recognized, since they appear optically with a characteristic violet and blue colours on the substrate, as illustrated from the optical images in Fig.4.3.(b,c). The thickness of the SiO_2 composing the substrate is crucial to distinguish the graphene flakes; an oxide thickness of 285 nm allows for the optical observation of very thin flakes down to the single layer. An example of graphene optical image is highlighted in dashed lines in Fig.4.3.b.

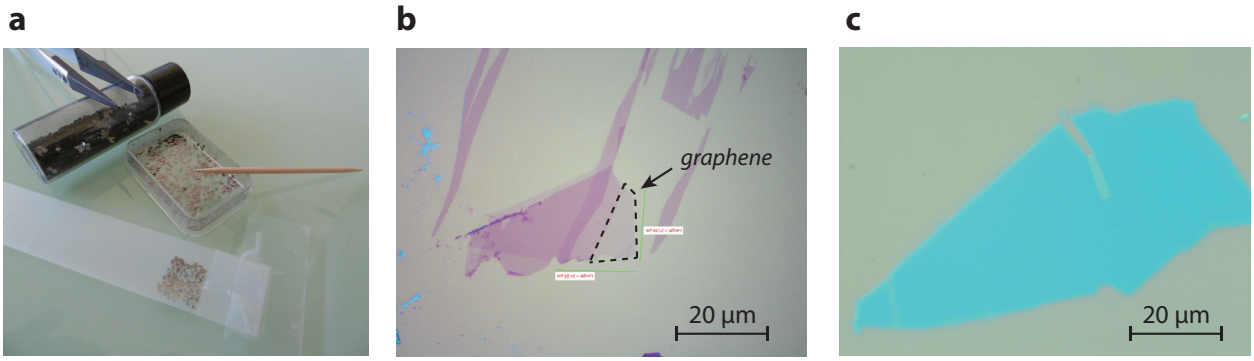

Figure 4.3: (a) Exfoliation of pristine graphite crystals on a scotch tape. The tape is folded on itself several times to cleave the crystals into thinner layers. (b) Optical image of different violet graphite flakes. A graphene flake is delineated by a black dashed line. The contrast of the flakes increases with the amount of layers composing the crystals. (c) Optical micrograph of a quite homogeneous hBN flake having a thickness of 15nm.

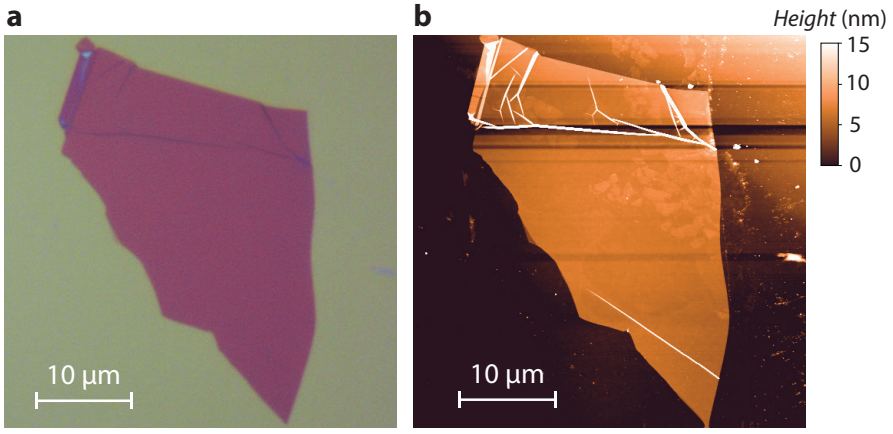

Figure 4.4: (a) Optical micrograph of a grahite flake (b) AFM topographic characterization of the same graphite flake. The average thickness of the flake is 6 nm.

Atomic force microscopy characterization: Optical imaging provides a good base for identifying suitable flakes for a stack, but it does not allow to identify with reliability small features beyond the diffraction limit imposed by the light. For a better characterization, the atomic force microscopy (AFM) provides a topography image of the flake surface, revealing any dirt or residues from the exfoliation. The AFM topography is also employed to measure precisely the flakes thickness. An example of AFM topography is reported in Fig.4.4.b.

4.2.2 van der Waals pick-up technique

For the case of a p-n junction, once the four flakes of graphene, graphite and hBN have been selected, the next step is to stack them using the van der Waals pick-up technique.

The stamp preparation: For the stacking of the flakes, a transfer microscope is required, allowing to pick-up the flakes from the substrates of exfoliation by using a stamp of PPC. The stamp is prepared on a glass slide, where a thin film of PPC is deposited on a solidified droplet of PDMS[1]. A piece of scotch tape is finally added on the top of the PPC film, fixing the polymeric film over the dome-shaped PDMS (see Fig.4.5.a).

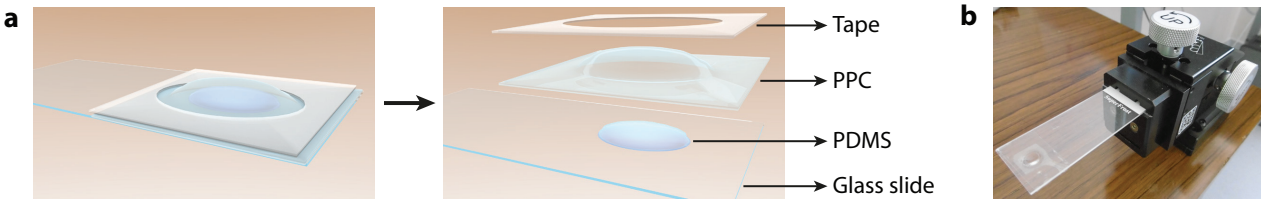

Figure 4.5: (a) Representation of the stamp for the pick-up process. A droplet of cured PDMS is deposited on a glass slide, and a PPC film is placed on top. A holed scotch tape is positioned on the glass slide in order to block the PPC on the PDMS. Adapted from [33]. (b) The stamp is then inserted in the micromanipulator, ready for the stacking process.

[1]PDMS = Polydimethylsiloxane

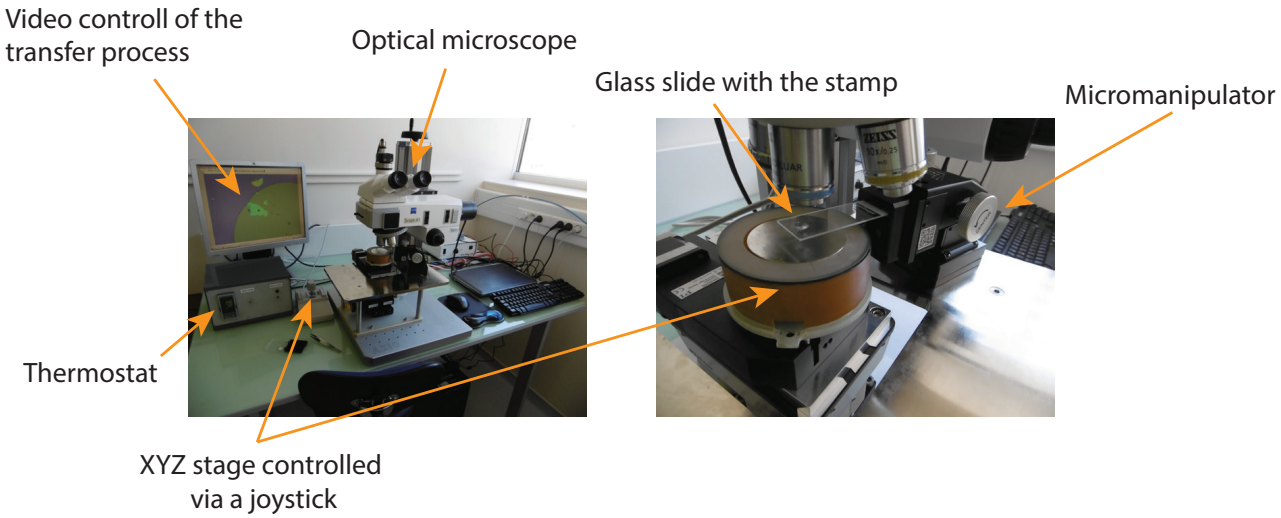

Figure 4.6: Transfer microscope set-up for the fabrication of graphene heterostructures. The sample substrate is fixed on the XYZ stage with a vacuum holder. The stage is controlled by a joystick which can move in the three directions.

The transfer set-up: The prepared stamp is then positioned above the substrate hosting the crystal flake, and brought into contact closely to the position of the flake. In order to perform this fine positioning, the set-up in Fig.4.6 is used. The set-up is based on an optical microscope connected to a camera for the observation of the stacking process. The substrate is positioned under the microscope, by using a moving piezoelectric platform controlled by a joystick. The platform can move in the three spatial directions, and it is isolated from unwanted mechanical vibrations.

During the alignment, the substrate is blocked on the piezoelectric platform with a vacuum holder. By moving the focal point of the microscope it is possible to know precisely the relative distance between the glass slide and the substrate, perfectly controlling the position of the PPC film with respect to the flake location.

The pick-up process: In order to take out a flake from its substrate with the PPC, the stamp touching the substrate surface is heated up by the electric heating system of the moving platform. With a thermostat it is possible to control the temperature of the substrate, changing then the viscosity of the polymer in contact with it. The polymer can stick and release flakes at low (around 38°C) and high temperatures (around 50°C) respectively.

When the PPC is in contact with the substrate, a clear circle representing the touching area of the PPC is observed through the optical microscope (Fig.4.7.a). Around the edges of the circle, a series of Newton rings develop, and their colour evolution allows for a better knowledge of the expansion of the PPC over the substrate.

In order to trap the desired flake on the polymer, it is necessary to increase slowly the temperature, making the PPC front to gradually expand until the flake is circumscribed inside the circle, as illustrated in Fig.4.7.(b,c). At this point, a lowering of the temperature assure the sticking of the flake to the polymer, and by moving down the z-axis of the platform, a detaching of the flake from the substrate occurs. To pick-up a second flake, the same process is reiterated with a careful relative positioning of the two flakes, both in position and angle. The adhesion of the two flakes is promoted by van der Waals interactions, inducing the flake trapped on the PPC to stick on the second flat crystal. Using this method, it is thus possible to pile up many

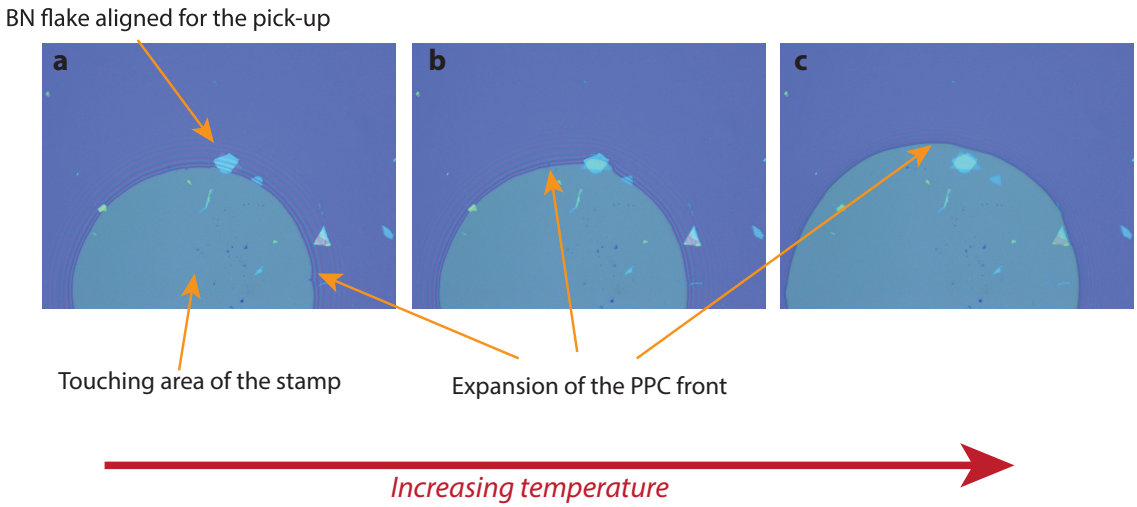

Figure 4.7: Optical images showing the expansion of the PPC front with the temperature during the van der Waals pick-up process.

flakes on top of each other.

During the last step, in order to deposit the completed stack on a substrate, it is necessary to carefully contact the stack on the chosen substrate and to increase slowly the temperature until 120°C, making the PPC to liquefy completely. The stamp is then removed and on the substrate is left the stack with some unwanted residues of PPC, that are eliminated rinsing the substrate with acetone.

Figure 4.8 shows the optical micrograph of a final stack for the fabrication of a p-n junction. The positions of the top and bottom hBN flakes are contoured by dashed lines. The graphene flake is half above the graphite backgate and half above the silicon backgate.

4.2.3 Thermal annealing

During the stacking, several air or water bubbles can be trapped between crystals, potentially affecting the final mobility of graphene. In order to avoid this drawback, it is necessary to eliminate the bubbles with a thermal annealing process performed at 300°C inside a oven in vacuum conditions below 10^{-6} mbar.

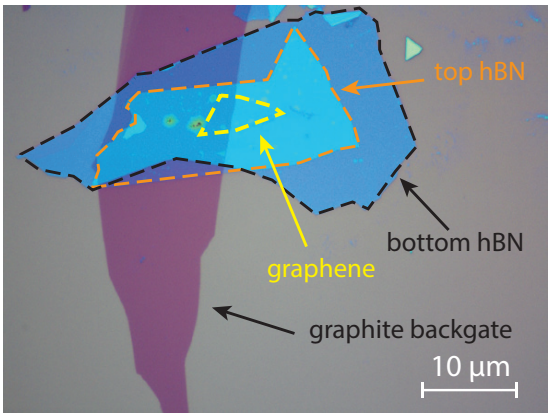

Figure 4.8: Optical micrograph of a heterostructure employed for the creation of a graphene p-n junction.

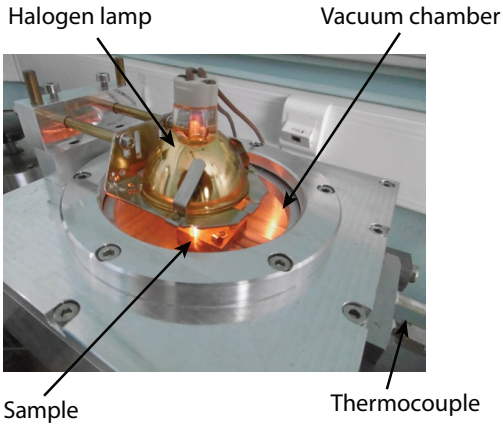

Figure 4.9: Picture of the oven for the vacuum annealing.

A picture of the oven is provided in Fig.4.9. In the figure, a thermocouple is inserted inside the vacuum chamber, where a block of copper holds in place the sample. A halogen lamp located above the vacuum chamber is directly shining the light on the sample, inducing heating. The temperature increase provides more flexibility and mobility to the flakes, which facilitates the escape probability of the trapped air and water molecules. Unfortunately, the results of the thermal annealing on the bubbles are not predictable. Sometimes the annealing is not effective or damages the crystals of the heterostructure. Figure 4.10 shows the evolution of the bubbles inside a heterostructure before and after an annealing of three hours at 300 °C. The bubbles that were initially scattered inside the area surrounded by the dashed line, reduce and coalesce in well defined points, improving the cleanliness of the stack.

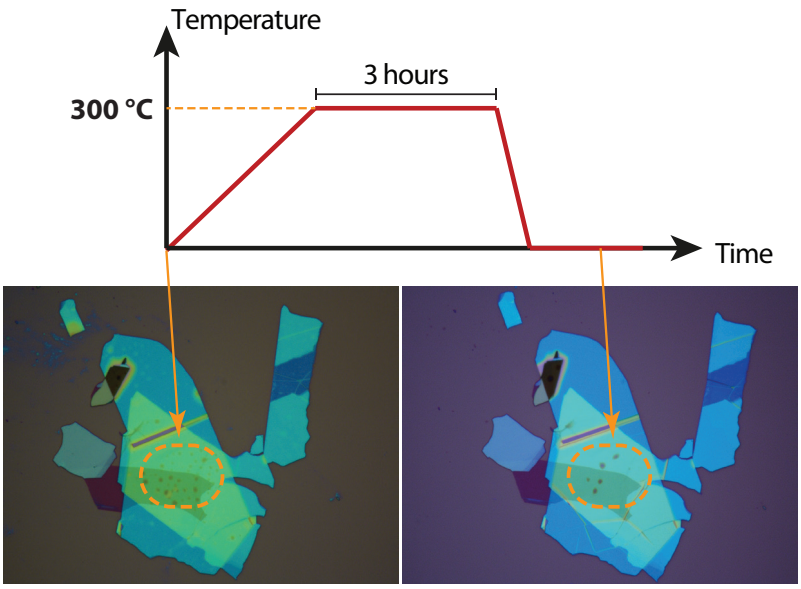

Figure 4.10: Schematic of the temperature evolution during a vacuum thermal annealing. Below the plot, two images show the evolution of the bubbles inside the heterostructure, before and after the thermal cycle.

4.3 Lithography process

At this point, the stack can be processed and transformed into a p-n junction. The nanofabrication process is based on several electron beam (e-beam) lithography steps, performed using a commercial e-beam writer with interferometric platform, which can write lithographic features with a resolution below a few tens of nanometer.

4.3.1 Markerfield and pads

The necessity to write the lithographic pattern at a very precise position with respect to the stack, requires the pre-patterning of several markers all around the device. The ensemble of these markers is called markerfield and it is composed of lithographically patterned gold squares of 8×8 μm^2 evenly spaced along the wafer with a distance of 50 μm. The markerfield is employed to incorporate precisely optical pictures inside the lithographic design pattern and for the alignment of the e-beam during the lithography exposure. During the lithography for the markerfield, the contact pads are simultaneously defined, which will be used for the wire bonding of the sample. After the development of the exposed positive PMMA resist, the lithographic pattern is metallized with e-beam evaporation technique, depositing first 5 nm of titanium (the adhesion layer) and subsequently 45 nm of gold.

4.3.2 Contacts and device shape

A second lithography step is required for the creation of the electrical contacts. After the development of the exposed PMMA resist, the heterostructure is directly etched within the developed PMMA lines via a reactive ion etching process with a a gas of CHF_3 and O_2. The etching time is adapted in order to fully etch the top hBN flake, exposing thus the graphene

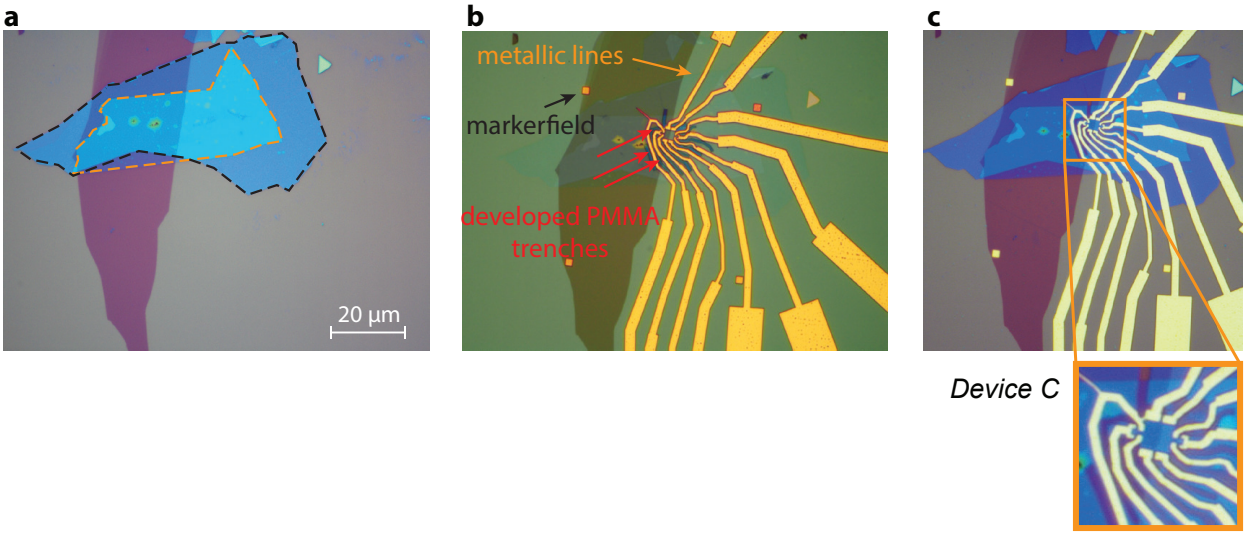

Figure 4.11: (a) Heterostructure at the beginning of the lithographic process (b) Optical micrograph of heterostructure connected to a series of metallic lines and covered with PMMA. The four squares around the heterostructure represent the markerfield. Close to the graphene location, there are a series of developed PMMA trenches for the final shaping of the graphene p-n junction. (c) Optical micrograph with a zoom of the p-n junction (device *C*) measured in Chapter 5.1.

edges. After the etching, a bilayer of chromium (5 nm) and gold[2] is deposited in the PMMA lines using e-beam evaporation, creating thus one-dimensional electrical contacts with the graphene flake [147].

Once the graphene flake has been contacted with metal lines, the natural shape of the graphene flake needs to be adjusted according to the shape of a graphene p-n junction for electron optics. Therefore, a third lithography step is required, to open PMMA trenches between the metallic contact lines, in order to etch and shape the original edges of the flake. Pictures of the device *C* during the lithography steps are reported in Fig.4.11.

It is worth to mention that the fabrication process of devices *A* and *B* presented in Chapter 5.1 was slightly different than the process of device C presented above. For these two samples, I used the HSQ hard mask proposed in Ref. [147]. Unfortunately the yield of working devices processed with HSQ is very low, since it statistically increases the risk of contamination of the exposed graphene edges. A much higher yield of working devices has been obtained with the technique presented in this chapter.

[2]The gold thickness is usually one and a half times the thickness of the heterostructure

Chapter 5

SGM on ballistic graphene pn junctions

Contents

The objective of the thesis project is to employ the SGM technique for the spatial imaging of the transport processes inside a gate-tunable p-n junction. In this chapter, I present the imaging of the ballistic electron flows, and inspect the negative refraction processes and the back reflections developing in the two regions of the p-n junction. The experimental data are interpreted with a series of ray-tracing simulations in the semi-classical limit, which allow to reverse-engineer the transport signatures encoded in the SGM signals.

5.1 Devices geometry

I introduce here three graphene p-n junctions obtained by depositing encapsulated hBN-graphene-hBN[1] heterostructure on the edge of a thin graphite flake. The devices integrate essential features to control the flow of electrons, such as pinhole collimators for a directional electron injection, and grounded lateral edge contacts for the reduction of scattering at boundaries of the junction active region. Their working principle is explained in Chapter 3.3.

Figure.5.1 shows the schematic of the three devices together with their relative optical micrographs. In the device A, the graphene billiard is a square of area 2×2 μm^2, while devices B and C are slightly bigger, with areas 3×3 μm^2. The thicknesses of the crystal flakes employed in the three heterostructures are reported in the Table 5.1. Device A and B display a pair of pinhole collimators having width $W = 400$ nm and separation length $L = 700$ nm,

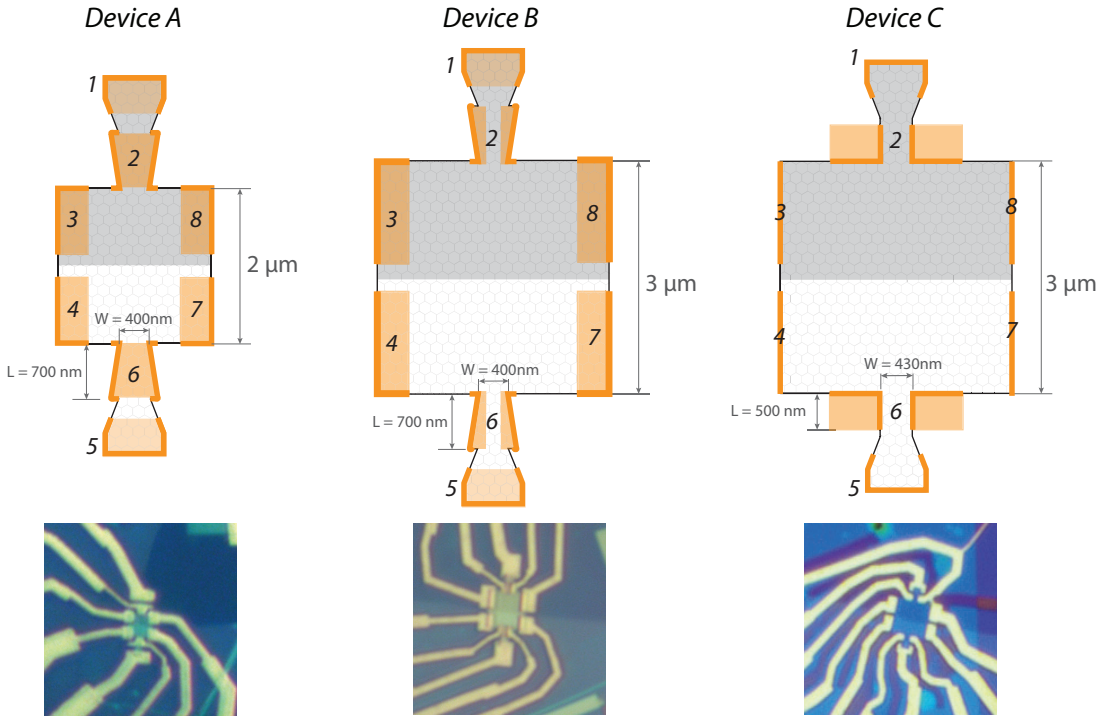

Figure 5.1: Schematics of the graphene p-n junctions measured during the thesis with their optical micrographs. The device A is characterized by a squared junction billiard of $2 \times 2\mu$m^2, whereas devices B and C have a surface of $3 \times 3\mu$m^2. Shaded grey regions highlight the position of the graphite backgate. The orange lines define the ohmic contacts distributed around the devices. Orange areas allows to visualize the spatial extension of the metal deposition over the heterostrutures.

[1] hBN = hexagonal boron nitride

enabling a maximum angular emission of 30 °. The filtering chamber of the pinhole collimators in the device A, namely contacts 2 and 6, are covered by chrome-gold metal on the top surface of the heterostructure. In the device B, the ohmic contacts of the filtering chambers do not overlap completely with the surface of the heterostructure, minimizing the metallic screening influences in the close vicinity of the injection regions. Thanks to a novel fabrication process, the device C displays ohmic contacts without metal covering the heterostructure. In this last device, the pinhole collimator dimensions are slightly different from the previous junctions, having parameters $W = 430$ nm and $L = 500$ nm.

Table 5.1: Table of the flakes thickness in the p-n junction devices.

Device	Top hBN	Bottom hBN	Graphite
A	10 nm	29 nm	10 nm
B	8 nm	12 nm	11 nm
C	10 nm	16 nm	5 nm

5.2 Polarity regimes of the junction

The electrostatic control of the carrier density in the graphene junctions is performed via the application of a voltage on the silicon V_{Sg} and graphite V_{Gg} bottom gates. According to the charge carrier type induced in the two separated regions (n_{Sg} and n_{Gg}) of the junction, it is possible to identify four different polarity regimes which are illustrated in Fig.5.2.a. In particular, we can identify a couple of unipolar (n-n', p-p') and bipolar (p-n, n-p) regimes, which characterize an artificial gate-tunable junction [59, 67, 123].

The identification of the physical regimes can be performed via the characterization of the four-wire longitudinal resistance measured from either side of the junction interface. Fig.5.2.b shows the measurements performed at the temperature $T = 1.5$ K in the device B. The schematic of the measurement method is reported in the inset of Fig.5.2.b, where the longitudinal resistance $R_{\mathrm{L}} = (V^+ - V^-)/I$ is measured as a function of the voltages V_{Sg} and V_{Gg}.

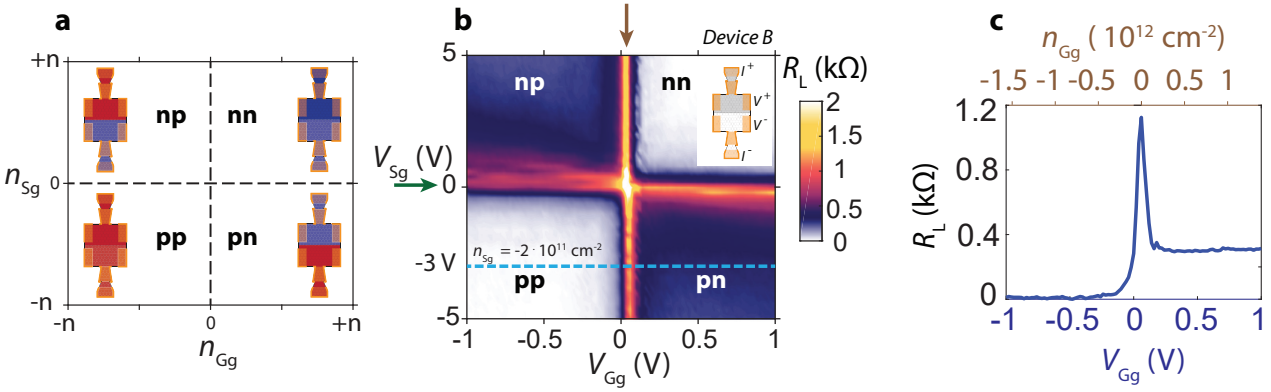

Figure 5.2: (a) Classification of the bipolar and unipolar regimes in an artificial gate-tunable graphene junction. According to the sign of the electron density in the two sections, it is possible to identify 4 different operating regions. (b) Dependence on V_{Sg} and V_{Gg} of the 4-wire longitudinal resistance R_{L}. (c) R_{L} line cut at $V_{\mathrm{Sg}} = -3$ V, performed along the blue dashed line in (b).

In the colormap it is possible to identify 4 regions with low resistance, associated to the n-p, n-n', p-p', p-n regimes. The high resistance lines, delimiting the operating areas, are indexed with green and brown arrows, and represent the charge neutrality conditions in the two regions of the device. The resistance map draws evident perpendicular lines which intersect into a central region of highest resistance. The orthogonality of the lines confirms the weak mutual electrostatic coupling between the field effects of the bottom gates. The electrostatic field generated by the global silicon backgate is therefore completely screened by the metallic character of the graphite flake.

A line cut on the 2D resistance map is shown in Fig.5.2.c. It displays a very sharp resistance peak at the charge neutrality, located at a slightly positive voltage $V_{\mathrm{Gg}}^{\mathrm{CNP}} = 0.06$ V. The fact that a charge neutrality condition is reached in the proximity of zero gate voltage, suggests that the sample is clean and therefore not very affected by charge impurities. From the linecut in Fig.5.2.c, it is possible to notice an asymmetry of the curve around the charge neutrality point. The origin of such asymmetry is attributed to the effect of the junction potential on the transport properties in the device. The junction resistance displays higher values if both sides of the junction have opposite carrier type ($n_{\mathrm{Sg}} n_{\mathrm{Gg}} < 0$) [96]. This effect takes into account the action of the step potential in the bipolar regime: if charge carriers strike on a p-n junction with sufficiently large incidence angles, they are systematically back reflected.

Fig.5.3 shows a comparison between the longitudinal resistance maps in the three graphene junctions. The device *A* shows a series of marked fluctuations in the p-n region, which have been interpreted as interference in the silicon backgate region, in the close vicinity to (or even inside) the filtering chamber of the local pinhole collimator.

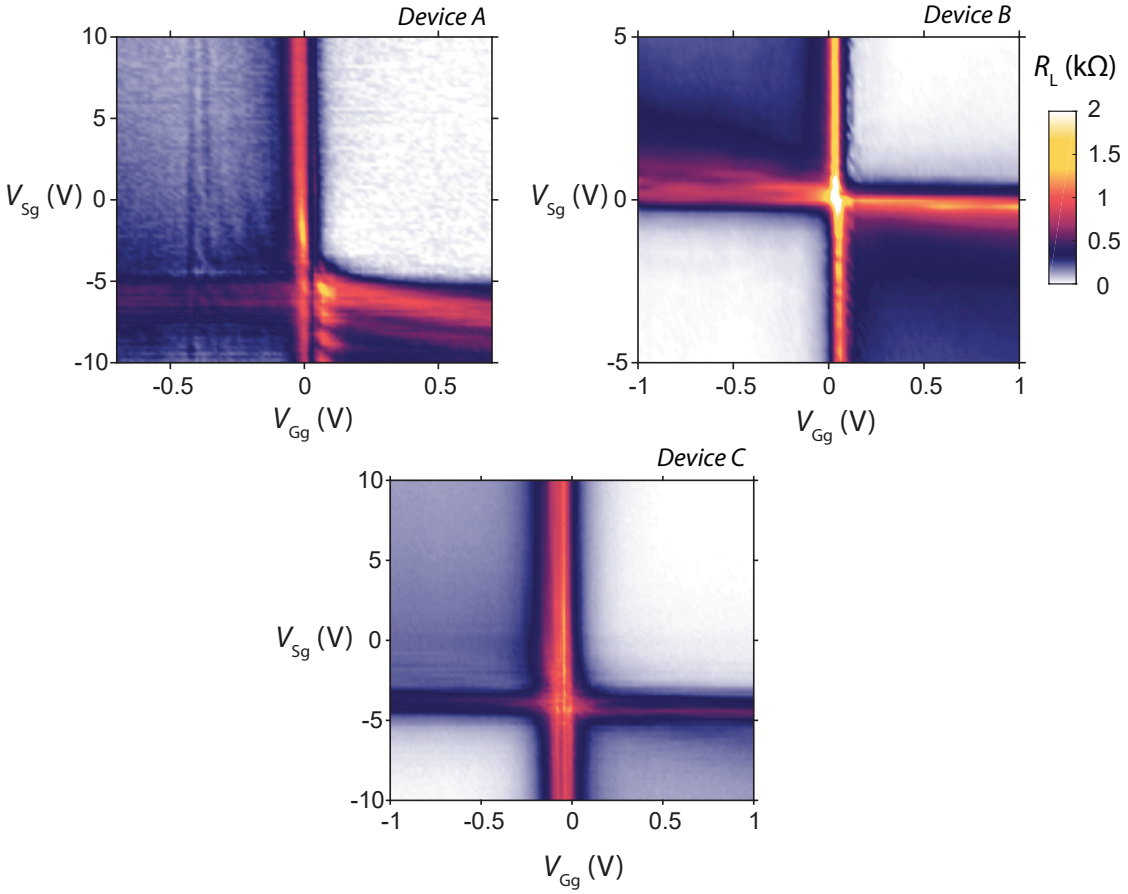

Figure 5.3: Four-wire longitudinal resistance maps for the devices A, B and C.

Table 5.2: Table of the capacitances and charge neutrality conditions of the junctions.

Device	**Graphite cap.** C_{Gg}	**Silicon cap.** C_{Sg}	$V_{\mathrm{Gg}}^{\mathrm{CNP}}$	$V_{\mathrm{Sg}}^{\mathrm{CNP}}$
A	119 nF/cm^2	11 nF/cm^2	0.03 V	-5 V
B	288 nF/cm^2	11.6 nF/cm^2	0.06 V	0.2 V
C	216 nF/cm^2	11.5 nF/cm^2	-0.04 V	-4 V

The calculation of charge carrier densities in the two bulk regions of the junction have been estimated, using an infinite parallel plate capacitance model, with the estimated capacitances reported in Table 5.2. This approach requires the knowledge of the crystal flakes thickness, which can be obtained from the AFM topographical characterization of the heterostructure (Table 5.1), and the dielectric constants of the SiO_2 layer ($\epsilon_r^{SiO_2} = 3.9$) and of the hBN flakes ($\epsilon_r^{BN} = 3.9$).

5.3 Imaging ballistic electron flow in graphene

Before proceeding with the SGM imaging of the transport processes inside a p-n junction, it is useful to inspect first the SGM transport signatures of a collimated beam in unipolar regimes, when carriers are not influenced by classically forbidden regions at the p-n interfaces. For this purpose, I present here a series of SGM maps obtained from the device C, in the unipolar regime n-n', providing spatial insights on the evolution of a collimated electron beam, as a function of the doping variations in one region.

The measurement set-up is reported in Fig.5.4.a. The device is current polarized, injecting 300 nA from the source contact of the silicon backgate region. The silicon backgate voltage is kept fixed at $V_{\mathrm{Sg}} = 17.2$ V, providing a local electron density $n_{\mathrm{Sg}} = 15.2 \times 10^{11}$ cm^{-2}. In order to collimate the injected beam of electrons, the ohmic contacts in the filtering chamber of the pinhole collimator are grounded. The lateral edge contacts around the junction billiard are connected to ground in order to prevent scattering on the wall of the billiard. The measurement of the current transmission is performed via the readout of the drain current I_1. All the measurements here are performed in a VTI cryostat at the temperature $T = 1.5$ K. In order to image the electron flow, the SGM probe is scanned at 200 nm height from the device surface, within the yellow square of area 2.2×2.2 μm^2 visible in the schematic of Fig.5.4.a. The tip is electrically polarized with a voltage $V_{\mathrm{tip}} = -10$ V, creating a repulsive potential bump in the graphene layer which deflects ballistic trajectories, repelling away free electrons. SGM maps were recorded at different voltage values V_{Gg} of the graphite bottom gate.

The SGM maps reported in Fig.5.4.(b-h) show the evolutions of a collimated electron flow for different n-type doping conditions in the graphite gate. For each map, the voltage values and relative carrier densities are specified in Fig.5.4.i. In order to compare the SGM current signals with the same colorbar, the experimental data have been rescaled with min-max normalization, transforming the absolute current minima into a 0 and the maxima into 1. The real values of current minima and maxima for each map are reported in Fig.5.4.j. The physical position of the junction is pointed in the SGM maps with a white dashed line.

Figure5.4.(b-f) illustrates a series of SGM maps of the drain current I_1. The maps are characterised by a well localized vertical current drop in the middle of the scan region. The vertical transmission drop can be interpreted considering the electrostatic influence of a depleting SGM tip, in the proximity of a ballistic stream of conducting electrons. Specifically, in high-quality samples, when the tip is far from the transport region, electrons are usually able to stream

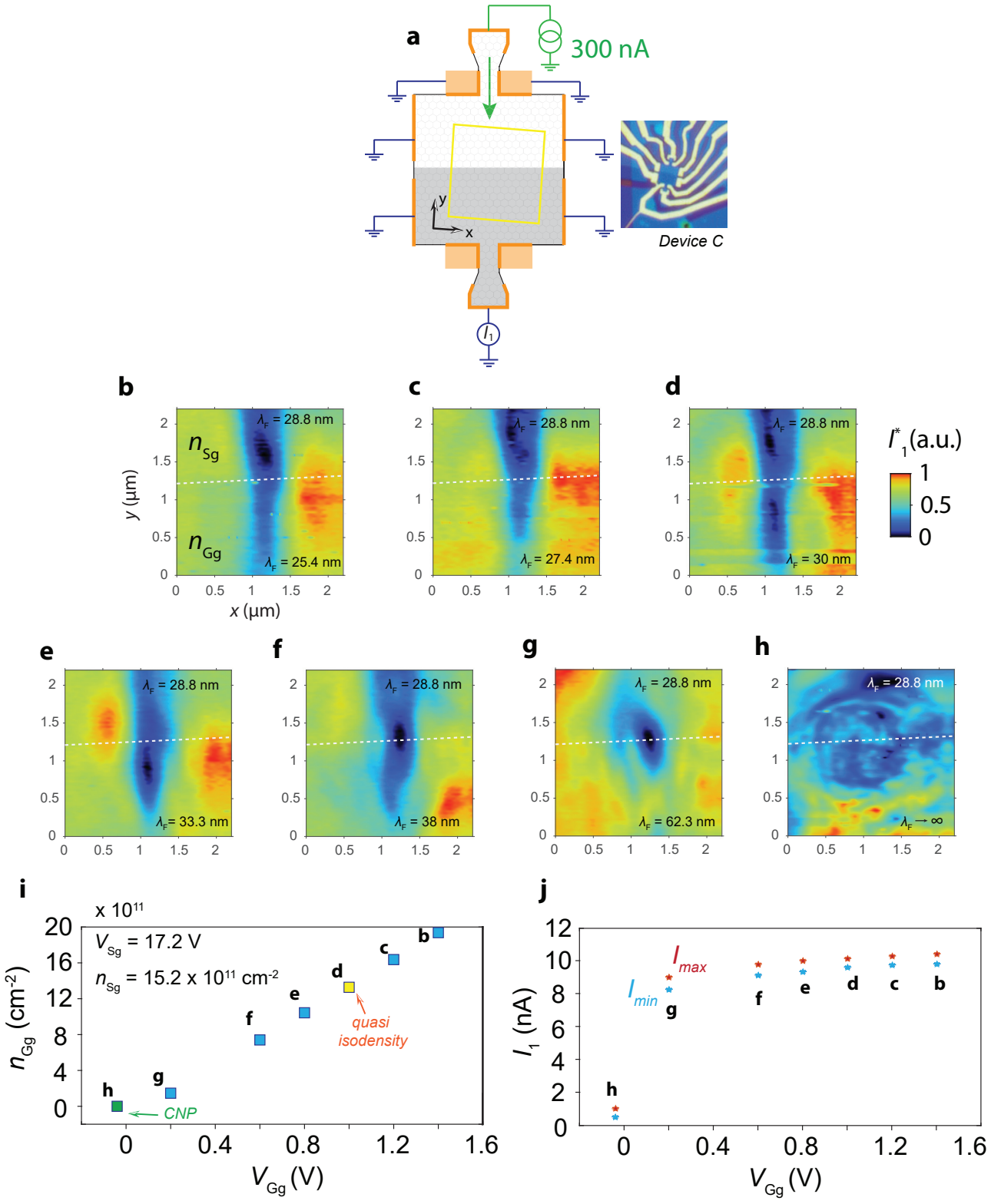

Figure 5.4: (a) SGM measurement set-up for the imaging of ballistic electron flow in unipolar regime in the device C. The yellow frame represents the SGM scan window. (b-h) Space evolution of the transmitted current for decreasing electron density n_{Gg} in the graphite gate region, for fixed tip voltage $V_{\mathrm{tip}} = -10$ V. The characteristic pattern of uniform electron flow survives at large range of n_{Gg}. (i) Charge carrier densities for each SGM map. (j) Real values of the transmitted current maxima and minima for the SGM data rescaled with min-max normalization.

ballistically from the emitter (pinhole collimator) toward the collector contact. However, when the tip is positioned in the middle of the transport region, its diverging lensing effect scatters the electronic flow, inducing a dramatic drop in the transmission signal. A similar lensing effect was already observed in ballistic graphene devices in [14, 15].

The smoothness and homogeneity of the signals composing the current maps, reveal the absence of hard scattering processes affecting the transport. However, the presence of weak spatial distortions along the maps may unravel a series of background potential fluctuations in the graphene plane, which can be attributed to charge inhomogeneities in the heterostructure.

In order to develop further the data interpretation, and to show how the electrostatic perturbation of the scanning tip influence the final appearance of the SGM maps, I present in Fig.5.5 a ray-tracing numerical simulation of a semi-cassical SGM map of current transmission on an uniformly n-doped graphene system[2]. For the calculation, I considered a bundle of collimated electron trajectories with an initial diameter of 400 nm, propagating along the y-axis for $2\,\mu$m, with a maximum angle emission of $\alpha_{\max} = 11\,^{\circ}$. The kinetic energy in the graphene billiard is arbitrarily chosen to be $E_{\mathrm{k}} = 120$ meV corresponding to the density $n = 9 \times 10^{11}$ cm^{-2}. The SGM tip is generating a depleting Lorentzian potential with peak potential $U_0 = 60$ meV, with characteristic electrostatic decay radius $R_{\mathrm{tip}} = 75$ nm. The tip is scanned within the yellow window, while the transmission contact counts the amount of impinging trajectories on it (for more details on the numerical approach, see Chapter 3).

The semi-classical SGM map in Fig.5.5.b seems to capture some essential features of the SGM maps in Fig.5.4.(b-f). Specifically, the middle region of the simulated map shows an evident signal drop along the propagation direction. Moreover, the cone-shaped SGM signatures observed in the experimental maps, with a reduced SGM signal when moving the tip away from the injector, seems to be well represented in the numerical simulation.

According to Fig.5.4.(g-h), the homogeneous electron flow starts to disappear in Fig.5.4.g, when the Fermi wavelength imposed by the graphite bottom gate becomes greater than $\lambda_{\mathrm{F}} = 60$ nm. A possible explanation for this pattern variation is the total internal reflection taking place at the junction level. A reduction of the electron density in the graphene segment governed by the graphite gate, determines a reduction of the semi-classical critical angle. Therefore, an incoming electron from the silicon backgate region, having impinging angle greater than the critical one, will be totally reflected. This total reflection can spoil the transmission across the junction, reducing the amount of current transmitted through the n-n' junction.

The pattern displayed in Fig.5.4.h is particularly interesting. The graphite region is now at the charge neutrality condition, and the SGM map shows a fluctuating map of transmitted current I_1. In this situation, the current is confined is the top region and escape the device via the lateral contacts. This complex flow of reflected electrons gives a complex pattern in the top part of the SGM map. In the bottom part however, the repulsive tip potential induce charge inversion, with a local accumulation of holes which allows a small current to propagate in this otherwise insulating region. At charge neutrality, the carrier density is zero on average, but can present charge puddles which complicate the analysis. In the ideal case, a junction can fulfil geometrical optics conditions only when $\lambda_{\mathrm{F}} \ll L$, where L is the spatial extension of one segment of the junction, i.e. the graphite gate segment $L \approx 1.5\,\mu$m [150]. Under this condition, the electronic transport in the junction is expected to be governed by interesting effects of electron diffraction. The SGM map of Fig.5.4.h could be therefore interpreted as a structured electronic diffraction pattern arising when the graphite gate reaches the charge neutrality condition.

[2]The parameters of this simulation do not fit with the experimental data.

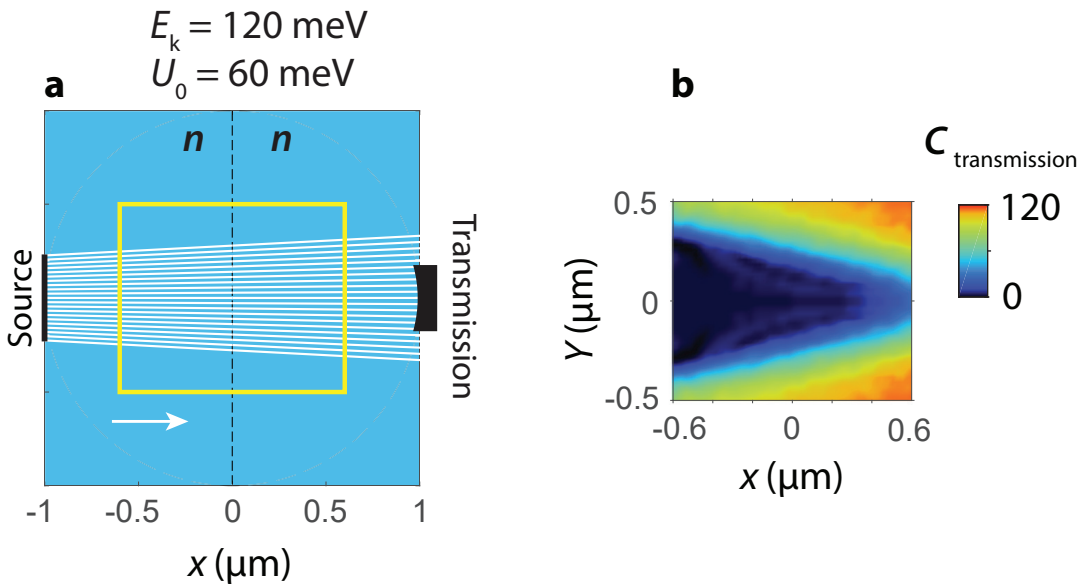

Figure 5.5: (a) Beam of collimated Dirac fermions propagating from left to right, equivalent to the direction from top to bottom in the experimental maps in Fig.5.4. The emission diameter is 400 nm, with beam divergence of $\theta = 11\,°$. (b) Ray-tracing calculation of the SGM map for the transmitted current. We considered a tip scanning at 200 nm from the device surface, with the tip voltage $V_{\text{tip}} = -10$ V. In these conditions, the tip-induced potential peak is $U_0 = 60$ meV, obtained considering a capacitance of 3.3 nF/cm^2 for electrodes separated by 200 nm. The electrostatic decay parameter for the simulation is $R_{\text{tip}} = 75$ nm.

5.3.1 Tip polarity influence on the transmission

In the following, I discuss the evolution of the drain current I_1 with the voltage polarity imposed on the scanning tip. The experimental data are measured with the set-up of Fig.5.6.a. In order to study the tip voltage influence on the transmitted current I_1, I take as a reference the SGM transmission map in Fig.5.6.b, which has been measured at $V_{\text{tip}} = -10$ V. Similarly to the previous SGM maps in Fig.5.4, the reference map of Fig.5.6.b shows a ballistic electron flow across the device C. The bulk electron density in the silicon region is fixed at $n_{\text{Sg}} = 8.1 \times 10^{11}$ cm^{-2} (corresponding to a voltage $V_{\text{Sg}} = 7.2$ V), while the density in the graphite backgate region is $n_{\text{Gg}} = 12.7 \times 10^{11}$ cm^{-2} (corresponding to a voltage $V_{\text{Gg}} = 0.9$ V).

The influence of the tip polarity on the transmission signal can be measured by performing a single-line spectroscopy along the green dashed line in the SGM reference map, testing many different tip voltages. The spectroscopy measurement is reported in Fig.5.6.c. For negative tip voltages, the transmitted current displays a signal reduction in accordance with the reference SGM map signal. The tip is depleting the bulk electron density, inducing a signal drop in the region where the electric current is flowing. Interestingly, at positive tip voltages, the transmitted signal shows a contrast inversion: the precedent regions of current minima turn into maxima. This effect of SGM contrast inversion is a semi-classical phenomena, that can be understood invoking the ballistic lensing effect of the SGM tip.

In Fig.5.6.d is reported a simulated semi-classical SGM spectroscopy on a ballistic electron flow, which has been performed with similar numerical parameters employed for the simulation in Fig.5.5.[3]. As with the signal evolution in the SGM experiment, the numerical simulation also

[3]The simulated spectroscopy does not take into account any workfunction compensation of the SGM probe, that would account for a small vertical shift of the plot.

displays a maximum of transmission for positive tip voltages. This situation reflects the smooth circular n-n'-n lens (with n'>n) explained in Chapter 1.5.2, which deflects a diverging beam, forming locus of electron focusing in front of the collector. The simulation shows a reduced transmission for negative tip voltages, when the tip is positioned on the central axis of transport. The lensing effect reduces locally the carrier density, almost splitting the electron beam, reducing thus the overall transmission of Dirac fermions toward the collector. Nevertheless, an increase of transmission can be noticed when the negatively polarized tip is tangent to the electron beam, since the most divergent trajectories which were not collected in absence of the tip are now deflected into the collector.

The numerical calculations show a good qualitative agreement with the experimental data, even if the experimental spectroscopy displays an asymmetry along the x-axis. The origin of the asymmetry can be attributed to : (i) the intrinsic charge inhomogeneities on the graphene flake; (ii) the non-ideality of the ohmic contacts employed for the SGM imaging. If the ohmic contact are not perfectly in line with the transport direction, it can be shown that the final SGM signal suffers from axial distortions which impacts on the symmetry of the spectroscopy.

Another experimental example of the tip polarity influence on the SGM imaging of a transmission current flow, is illustrated in Fig.5.7, where a ballistic electron flow in the device *A* is recorded for both positive and negative tip voltage. The maps are recorded close to the isoden-

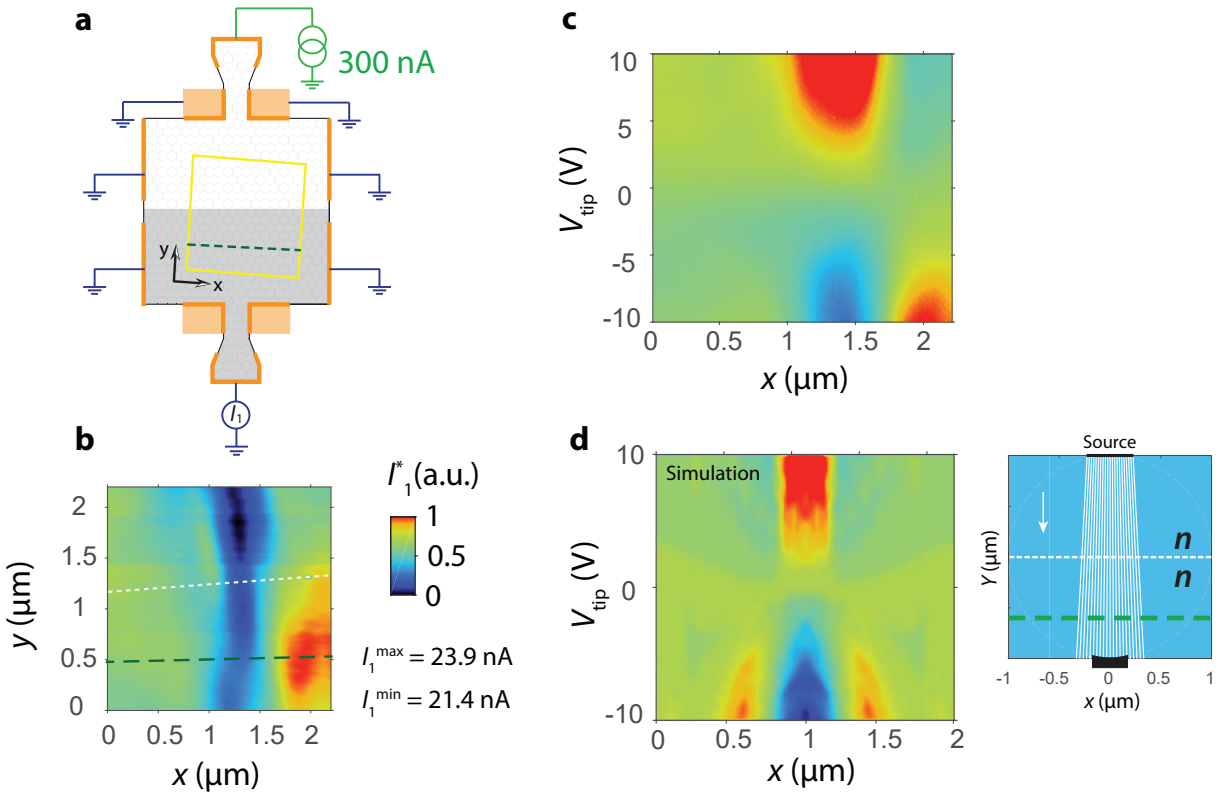

Figure 5.6: (a) SGM measurement set-up for the device C. Green dashed line represents the single-line scan for the SGM V_{tip} spectroscopy. (b) SGM reference map of ballistic current transmission from top to bottom, recorded at $V_{\text{tip}} = -10$ V, for different electron densities in the two regions (see text). (c) SGM V_{tip} spectroscopy. (d) Numerical simulation of a SGM V_{tip} spectroscopy. (right side) Ray-tracing trajectory field for the SGM spectroscopy simulation. The green dashed line represent the tip scan line where the simulation has been performed.

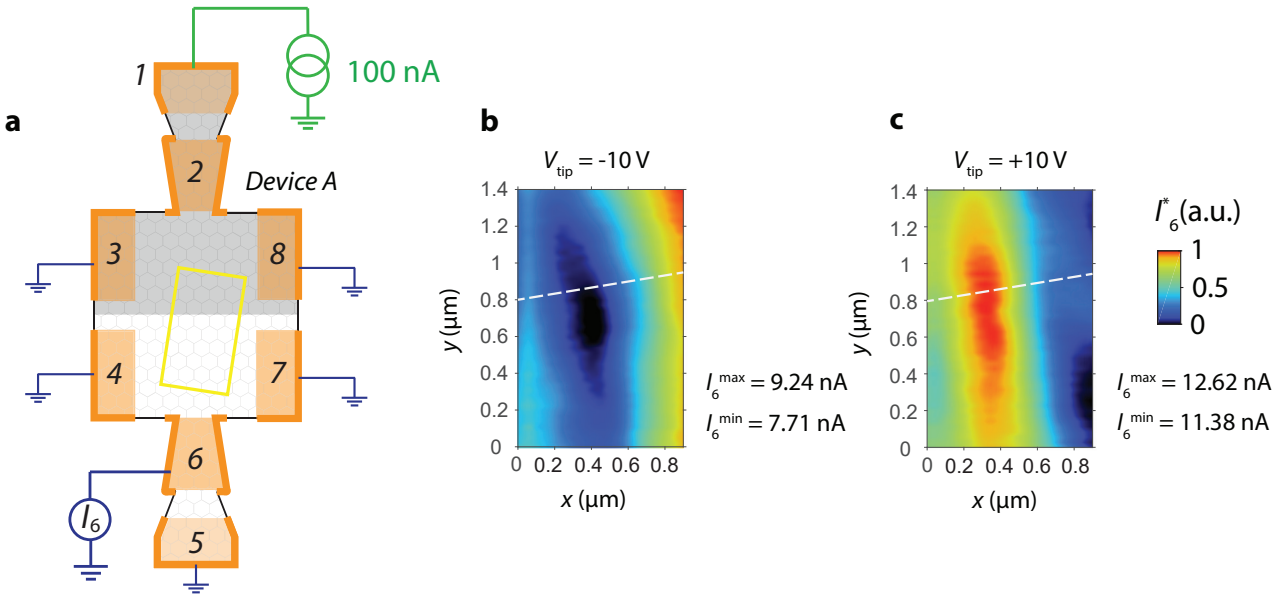

Figure 5.7: (a) Experimental SGM measurement set-up for the device A where the current is injected in the graphite gate region on the top. (b-c) SGM transmission maps at $V_{\text{tip}} = -10$ V and $V_{\text{tip}} = +10$ V of a homogeneous electron flow in quasi isodensity condition.

sity condition, with $n_{\text{Sg}} = 3.44 \times 10^{11}$ cm^{-2} and $n_{\text{Gg}} = 3.49 \times 10^{11}$ cm^{-2} of electron carriers. The tip is placed at 150 nm from the device surface. A comparison between the maps puts in evidence the contrast inversion associated to the lensing effect of the SGM probe.

5.3.2 Probing positive refraction

The SGM method applied in the unipolar regime allows for a relatively easy interpretation of the electron trajectories mapping. An uniform collimated flow appears as a narrow channel propagating along the transport direction. However, different doping conditions in the two regions of the graphene junction can introduce positive refraction processes at the junction interface. In the SGM maps of current transmission I_1 in Fig.5.4.(b-f), the electron waves seem to propagate straight on the device, probing the weak inhomogeneities of the system, but without showing net positive refraction features at the n-n' interface, since the trajectories are essentially normal to the interface. In the following I present a SGM experiment intended to extract information on the positive refractions on a graphene n-n' junction. I show a series of SGM maps in the n-n' unipolar regime on the device A, considering different doping conditions between the electron densities in the two regions of the junction.

The measurement set-up is reported in Fig.5.8.a. A current $I = 100$ nA is injected in the upper region of the device, flowing first inside the junction region governed from the electrostatics of the graphite bottom gate. First the SGM mapping is performed in quasi-isodensity condition, setting the electron densities at: $n_{\text{Sg}} = 3.44 \times 10^{11}$ cm^{-2} and $n_{\text{Gg}} = 3.49 \times 10^{11}$ cm^{-2}. Afterwards, the current is forced to propagate from lower to higher electron density regions, by decreasing the graphite bottom gate voltage, while keeping fixed the silicon bottom gate voltage. From a semi-classical perspective, this is equivalent to re-collimate a ballistic diverging beam closer to the normal direction at the interface. In order to obtain more prominent spatial signatures of positive refraction at the junction level, I maximized the angular beam divergence at the injection, by putting on a floating position the ohmic contacts in the pinhole filtering

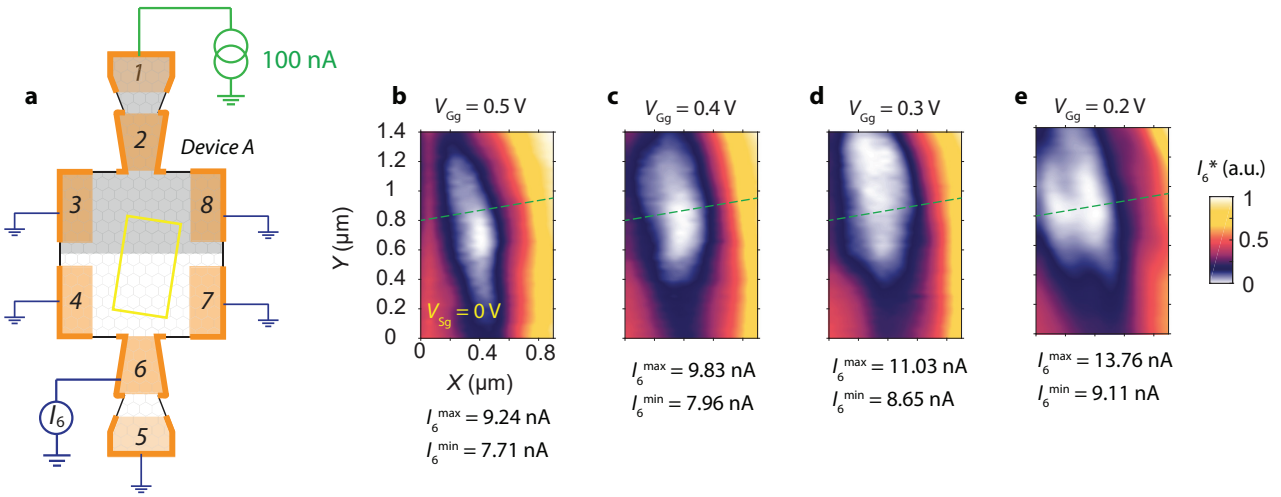

Figure 5.8: (a) SGM measurement set-up for the device A. (b-e) Experimental SGM maps of current transmission in the n-n' unipolar regime with V_{tip} = -10 V. The electron density in the silicon bottom gate region is fixed at $n_{\text{Sg}} = 3.44 \times 10^{11}$ cm^{-2}. The electron dopings in the graphite bottom gate region are: (b) $n_{\text{Gg}} = 3.49 \times 10^{11}$ cm^{-2}, (c) $n_{\text{Gg}} = 2.75 \times 10^{11}$ cm^{-2}, (d) $n_{\text{Gg}} = 2 \times 10^{11}$ cm^{-2}, (e) $n_{\text{Gg}} = 1.26 \times 10^{11}$ cm^{-2}.

chamber at the injector. SGM maps of the drain current I_6 are recorded using a tip voltage of $V_{\text{tip}} = -10$ V, scanning at 200 nm from the device surface. The physical position of the junction is pointed in the SGM maps in Fig.5.8.(b-e) with a green dashed line.

In quasi-isodensity condition (Fig.5.8.b), the SGM map unravels a narrow beam of current drop, propagating in the middle of the device. This result is very similar to the SGM map in isodensity for the device C in Fig.5.4.c. Here, since the injected beam is not collimated, there should be many trajectories which end up in the lateral ohmic contacts. These trajectories are however not visible in the SGM map of Fig.5.8.b which represents only the transmitted current I_6, explaining the similarity with Fig.5.4.c recorded with a collimated injection.

According to Fig.5.8.(b-e), by gradually depleting the charge density over the graphite bottom gate region, the spatial extension of the SGM signal, in the upper regions of the maps, expands remarkably along the x-axis. The broadening of the current drop is directly reflecting the collimation effect at the n-n' interface which redirects the wide-angle injected trajectories onto the collector of the current I_6 measured in the SGM map. The increasing width of the injected beam, that appears in the successive SGM maps with lowering density, is therefore a signature of the positive refraction at the n-n' interface. The increasing mean current from 8.5 to 11.4 nA is also an indication of this collimation.

Another specificity in each SGM map is the presence of a weak beam distortion below the junction, on the silicon backgate region. To qualitatively explain these distortions unravelled from the SGM maps, I present here two semi-classical SGM simulations under the presence of a refractive n-n' abrupt junction with and without a local potential inhomogeneity. Let us consider a uniform pencil of ballistic ray trajectories experiencing positive refraction at the junction as depicted in Fig.5.9.a. The dark blue area represents the graphite backgate region, with a local kinetic energy $E_{\text{k}} = 34.3$ meV. The light blue area is associated to the silicon backgate region having a kinetic energy $E_{\text{k}} = 57.5$ meV. The electron kinetic energies are scaled to closely fit the experimental parameters of the SGM map in Fig.5.8.e. The tip depletes the graphene layer with a Lorentzian electrostatic potential having maximum tip potential $U_0 = 25$ meV and radius decay parameter $R_{\text{tip}} = 200$ nm. The simulated SGM map in

Fig.5.9.b is obtained by scanning the tip within the yellow window shown on the left. The positive refraction at the interface appears in the SGM map as a cone-shaped signal which is wide at the top (injection) and sharp at the bottom (detection). This particular shape can be compared with the isodensity simulation in Fig.5.5.b showing also a cone-shaped signal, but of uniform slope. The widening of the signal in the upper part in Fig.5.9.b is similar to that of the experimental SGM maps in Fig.5.8, giving strength to our interpretation.

In Fig.5.9.c, ray trajectories have been calculated considering the presence of an impurity creating electron accumulation in the silicon backgate region, represented in the billiard with a green disk. The impurity influence is modelled as a Lorentzian potential, having peak value $U = -25$ meV. In Fig.5.9.c, the dimension of the green disk allows to visualize the radius decay parameter of the Lorentzian potential of 150 nm. The semi-classical SGM map is reported on Fig.5.9.d. A comparison between the two simulated maps allows to asses several differences. While the first map displays a perfect axial symmetry around $x = 0$, the second map shows an evident warping associated to the presence of the impurity. Since the detection contact is located at the bottom, the warping of the SGM signal extends in the whole map.

It is important to remark that even if a local charge accumulation in graphene generates well known lensing effects on electron trajectories [104], the possibility to extract information on the disorder distribution with SGM maps seems limited.

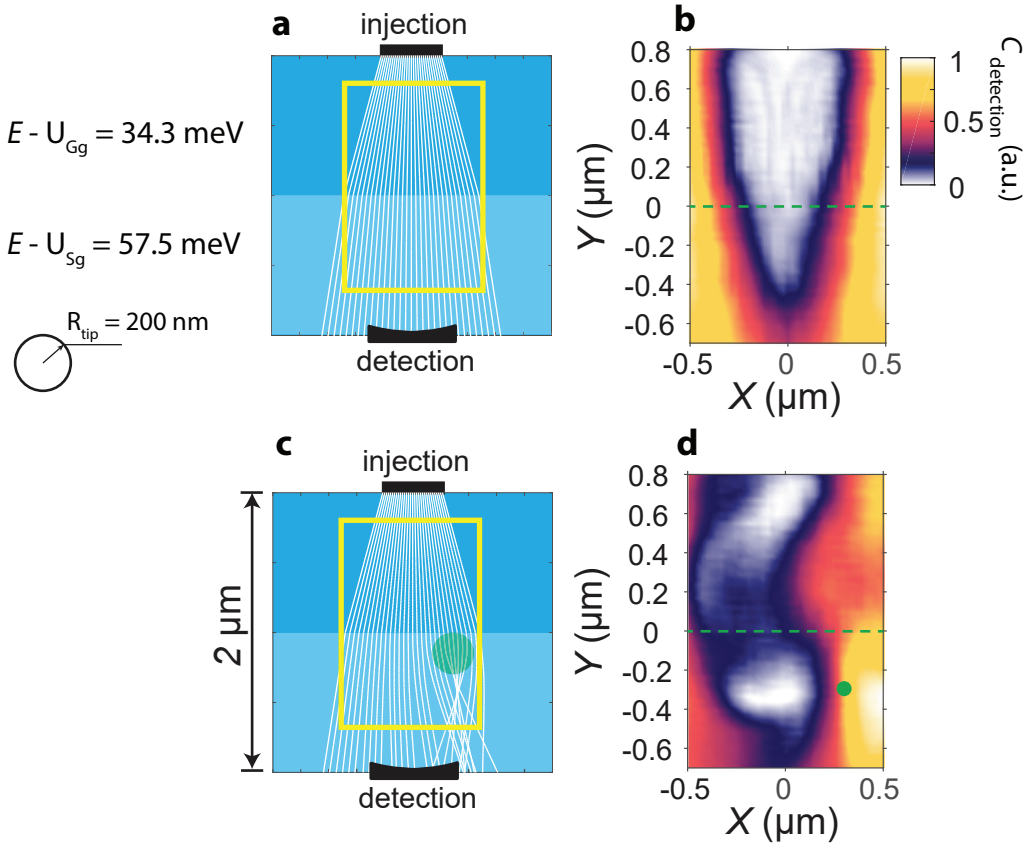

Figure 5.9: Semi-classical ray trajectories and corresponding simulated SGM maps in the absence (a-b) and presence (c-d) of a charge impurity within the silicon region. The charge position is labelled with a green disk. The impurity creates a Lorentzian-distributed charge accumulation region, having maximum potential $U = -25$ meV and decay length parameter $R = 150$ nm.

Unfortunately, the SGM maps do not put in evidence positive refraction processes at the single trajectory level, which would be required to check the Snell-Descartes law for individual angles. In the SGM literature, it has been shown that sharp local features, associated to single trajectory signatures, occurred mainly when: (i) the LDOS of an electronic systems was strongly concentrated in space within narrow geometries [134]; (ii) in open ballistic systems with charge impurities deflecting and confining effectively electronic modes [141]. These two requirements are not respected in the presented device in unipolar regime, mainly because of the extended device sizes letting a large spatial spreading of the LDOS, and because of the difficulty to effectively confine current lines of Dirac fermions with the charge impurities. All these specificities accounts for the difficulty in the SGM map interpretation on graphene junctions. Nevertheless, the qualitative agreement between the experiments and the simulated maps is a good proof of consistency of the semi-classical understanding of the transmission through a unipolar junction. I will show below that bipolar graphene junctions generates completely different SGM maps, with the possibility to characterize negative relative refraction indexes.

5.4 Imaging transport in p-n junctions

Despite some theoretical SGM groundworks applied on clean encapsulated graphene devices [109, 110, 108], only few SGM experiments have been recently accomplished in the ballistic regime [24, 12, 15, 14]. Furthermore, SGM observation of current distribution across an electrostatic p-n junction has never been conducted, leaving untackled the challenge of a direct imaging of Veselago lensing and reflection processes on a graphene interface. We present here a series of SGM experiments on graphene p-n junctions, mapping the transmitted and reflected currents as a function of the tip position. The interpretation of the SGM maps is performed with the help of the ray-tracing simulations.

5.4.1 Current transmission through a p-n junction

The scheme of the experiment is presented in Fig.5.10.a. The device A is current biased, injecting 100 nA from contact 5 at the bottom. The filtering chamber (contact 6) is connected to the ground via a current amplifier. The current transmission is measured via the drain contact 1. The silicon backgate voltage $V_{\mathrm{Sg}} = 0$ V and the graphite backgate voltage $V_{\mathrm{Gg}} = -0.25$ V are chosen in order to have an electron and hole charge densities $n_{\mathrm{Sg}} = 3.44 \times 10^{11}$ cm^{-2} and $p_{\mathrm{Gg}} = 2.08 \times 10^{11}$ cm^{-2} respectively. Within this charge configuration, the p-n junction relative refraction index is $\zeta = -\sqrt{p/n} = -0.78$. The SGM maps are recorded by scanning the electrically polarized tip within the yellow window, positioned at 150 nm height from the device surface. The temperature for the experiment is fixed at $T = 1.5$ K.

The experimental SGM maps of I_1 are reported in Fig.5.10.(b-c), recorded with SGM tip voltages of -10 V and +10 V. In order to compare the SGM signals with the same colorbar, the experimental data have been rescaled with min-max normalization, transforming the absolute current minima into a 0 and the maxima into a 1. The absolute values of current minima and maxima are reported on the right side of each SGM map. The physical position of the junction is pointed in the SGM maps with a white dashed line. For the SGM map at $V_{\mathrm{tip}} = 10$ V (Fig.5.10.b), the transmitted current displays a region of maxima localized inside the n-doped region of the junction. Conversely, a dramatic current drop is observed when the tip moves inside the p-doped region. The high-contrast map reverses behaviour when the scanning tip reverses its polarity, as reported in the SGM map of Fig.5.10.c.

In the following, I provide an explanation of the observed features, with the help of a series of ray-tracing trajectories for an ideal electronic beam impinging on a p-n interface (Fig.5.10.d). The electron beam is injected from the bottom region of the billiard, and experiences negative refraction when transmitted across the abrupt p-n potential step. The kinetic energies are selected in order to closely match the experimental conditions. The SGM tip generates a local Lorentzian-like variation of the kinetic energy, with a radius decay parameter $R_{\mathrm{tip}} = 300$ nm. We consider two tip potentials $U_0 = \pm 35$ meV, which do not generate charge inversion conditions inside the junction billiard.

The semi-classical SGM maps are reported in Fig.5.10.(e,f) and capture some essential features of the experimental SGM images, allowing to partially decrypt the physical processes involved in the experimental SGM maps. The lensing effect of the SGM tip on Dirac fermions manifests with drops of the transmitted signal when the tip reduces locally the charge density in either region of the junction. Conversely, when the tip induces charge accumulation, the transmitted signal is less reduced and eventually increased with respect to the average current in the SGM map. The best matching between the experimental and the simulated data can be noticed inside the p-doped regions. The upper region of the experimental SGM map in

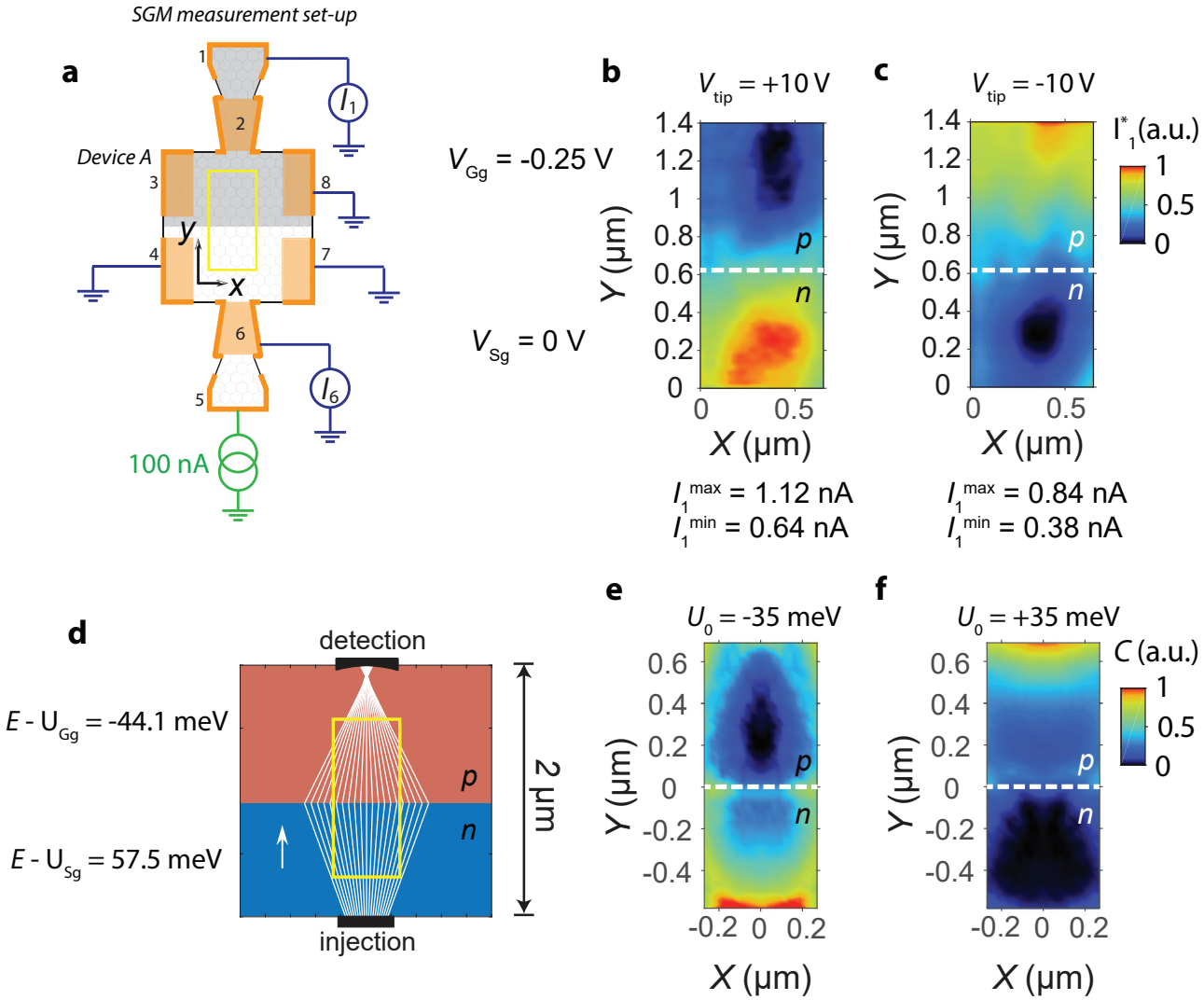

Figure 5.10: (a) Scheme of the experiment for the device A. The SGM probe scans inside the yellow window at 150 nm from the device surface. (b,c) SGM maps of current transmission I_1 for positive ($V_{\text{tip}} = 10$ V) and negative ($V_{\text{tip}} = -10$ V) tip voltages. (d) Ideal ray-tracing trajectory field travelling through an abrupt p-n junction. (e,f) Semi-classical simulations of SGM maps using two opposite tip potentials.

Fig.5.10.c, reveals the presence of a local maximum of transmission. This maximum can be observed also in the simulation of Fig.5.10.f, and as I will show later (in Section 5.5), it can be attributed to the proximity of the SGM probe on a focal point produced by the Veselago lensing effect of the junction.

5.4.2 Tip polarity influence on the SGM maps

For a full characterization of the tip influence on the current transmission signal I_1, I present here a SGM tip spectroscopy performed along the green dashed line crossing vertically the whole SGM map of Fig.5.11.a. While scanning continuously the vertical line, the tip voltage is swept between the values $V_{\text{tip}} = +10$ V and $V_{\text{tip}} = -10$ V. Exactly like in the precedent experiment, the back gate voltages are the same, with the tip positioned at a distance of 150 nm from the sample surface.

The spectroscopy is reported in Fig.5.11.b, and maps the transmitted current I_1 as a function of the tip voltage V_{tip} and of the position along the scan line. The vertical white dashed line separates the n- and p-doped regions of the junction. Strong signal variations are visible on the left side of the map, evidencing the great influence of the tip in the proximity of the injection region. Depending on the sign of V_{tip}, the transmitted current increases or reduces in accordance to the lensing effects of the tip on the current trajectories along the device. Along the red dashed line at $V_{\text{tip}} = 0.5$ V, the current I_1 does not display any signal variations. Therefore, the spectroscopy allow us to identify $V_{\text{tip}} = 0.5$ V as the tip voltage value required to compensate the effect of the intrinsic contact potential between the SGM tip and the device heterostructure, i.e. the difference between the materials workfunctions $e\Delta\phi_w$. Therefore, at $V_{\text{tip}} = 0.5$ V it is possible to identify the value of the unperturbed transmitted current inside the p-n junction: $I_1 = 0.84$ nA.

The p-doped region in the spectroscopy of Fig.5.11.b displays a weak current drop at higher positive tip voltages, while no significant signal variations are observed at negative tip voltages. The reduced tip influence in the p-doped region can be attributed to a scanning line not perfectly axial along the main transport direction in the junction, with a slight left shift w.r.t the

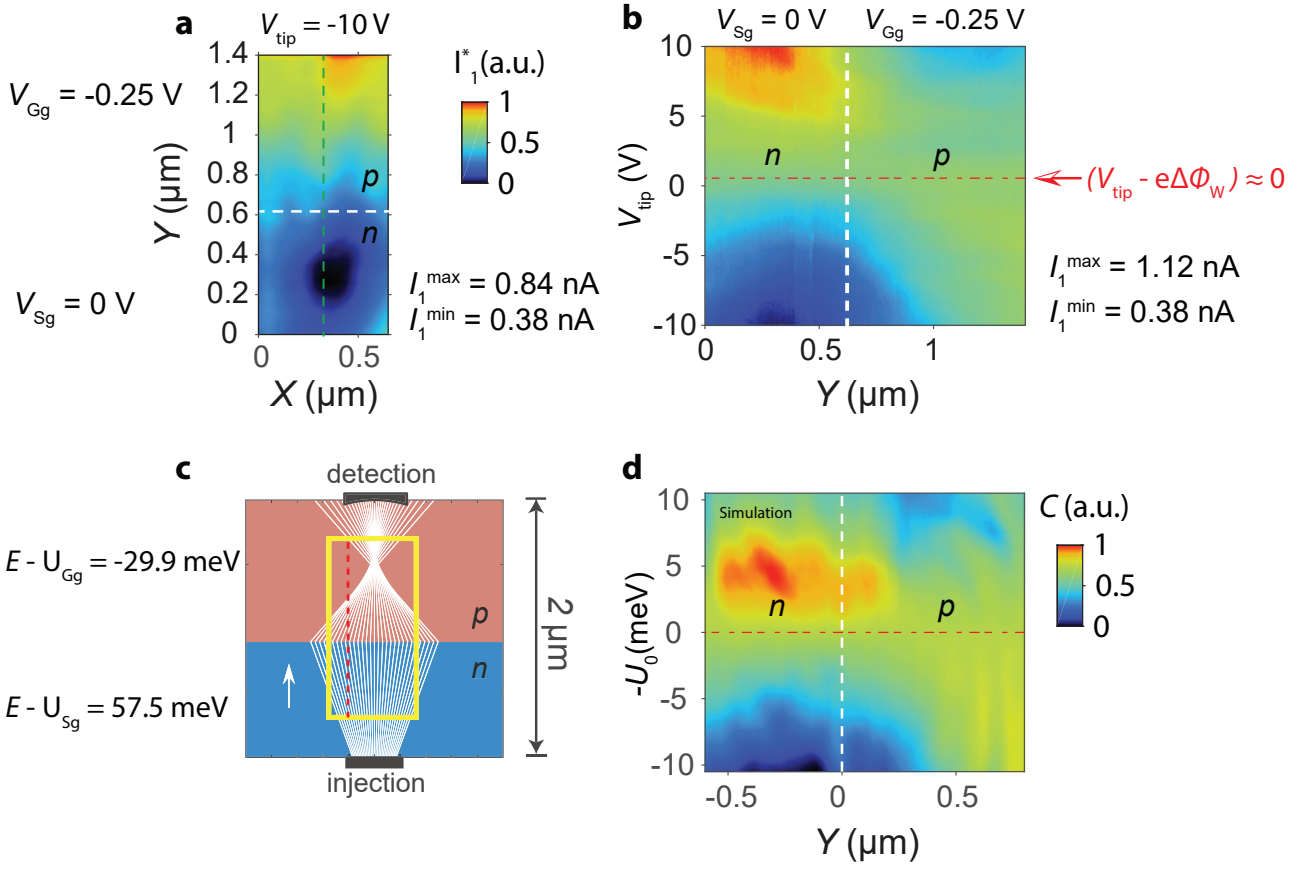

Figure 5.11: (a) Reference SGM map in the device A. The spectroscopy is performed along the green dashed line. (b) V_{tip} spectroscopy on a graphene p-n junction showing the effect of the tip-induced potential on the current transmission. The voltage value corresponding to the workfunction compensation for our commercial Pt/Cr metallic tip is pointed with a red arrow and is equal to $V_{\text{tip}} = 0.5$ V. (c) Ray-tracing trajectories propagating in an ideal p-n junction. The red dashed line represents the tip position for the semi-classical spectroscopy calculation. (d) Simulated semi-classical V_{tip} spectroscopy.

transport axis as noticeable in the reference SGM map of Fig.5.11.a. In order to discuss this last point, I present here an analysis of the spectroscopy features, with the help of a semi-classical simulation. Let us consider the ray-tracing trajectory field in Fig.5.11.c[4]. The single line spectroscopy is calculated along the red dashed line inside the yellow scan window. The red dashed line is positioned laterally to the current trajectories. Similarity to the precedent SGM simulations, the probe generates a Lorentzian potential change in the graphene layer. The interval of peak potential values employed in the numerical spectroscopy spans from $U_0 = -10.5$ meV to $U_0 = 10.5$ meV, with a decay radius $R_{\text{tip}} = 300$ nm. The simulated spectroscopy is reported in Fig.5.11.d. A comparison between the experimental and simulated maps reveals several similarities, such as a large contrast on the n-side and a weaker and asymmetric contrast on the p-side. The global resemblance between the experimental and numerical spectroscopies, allows us to validate our semi-classical understanding of the transport signatures of the transmission processes under the electrostatic presence of a scanning gate.

[4]The kinetic energy in the graphite region does not fit with the experimental data, therefore the simulation allows only for a qualitative understanding of the physical processes involved in the p-n junction.

5.5 Imaging Veselago focusing

Unveiling optic-like phenomena in two-dimensional electron gas has emerged in the years as an entire thrilling research domain. At its core lies the idea to probe and study the wave-like behaviour of charge carriers in solid state systems. If in the past electron optics was mainly performed in high-mobility semiconductors, with the advent of ballistic graphene devices, we have now the possibility to access to a new class of devices relying on original ultrarelativistic physics. The purpose of this experimental section is to use the SGM technique in order to directly image micron scale Veselago lensing processes inside graphene p-n junctions.

Upon negative refraction, a diverging current beam is predicted to re-focus on the other side of the junction, forming a locus at high electron density. The caustic position obeys to the Snell-Descartes law for Dirac fermions and can be therefore controlled according to the charge densities characterising the junction regions. The experimental results proposed here represent the first observation of spatially resolved Veselago lensing in graphene p-n junctions. The experimental data and their relative interpretations are corroborated with semi-classical SGM simulations providing a support to reverse engineer the observed transport signatures.

5.5.1 Imaging the caustic of an electron beam

Fig.5.12.a shows the schematics of the SGM imaging experiment. The device A is current polarized, injecting 100 nA from the region over the silicon backgate. The filtering chamber (contact 6) is grounded via a current amplifier, allowing to reduce the electron beam collimation angle at the injection, while measuring the absorbed current. The presence of a well collimated beam reduces total internal reflection processes at the junction, increasing thus the fraction of transmitted current. The transmission current is collected by the drain contact 1. The silicon backgate voltage is fixed at $V_{\mathrm{Sg}} = 0$ V, providing an electron density $n_{\mathrm{Sg}} = 3.44 \times 10^{11}$ cm^{-2}, while the graphite backgate voltage is $V_{\mathrm{Gg}} = 0$ V, setting a hole density $p_{\mathrm{Gg}} = 0.22 \times 10^{11}$ cm^{-2}. In this carrier configuration, the relative refractive index is $\zeta = -0.25$. The SGM probe scans within the yellow window at 150 nm height from the device surface, with a tip voltage $V_{\mathrm{tip}} = -10$ V.

The SGM map of the current transmission is reported in Fig.5.12.b. The n-doped and p-doped regions are visually separated with a white dashed line. While the n-doped region is characterized by a strong current drop almost extended in the whole area, the p-doped section instead present a well developed locus of current maxima. The bottom apex of the locus is pointed in the map with a green arrow. The maxima distribution in the p-region expands vertically in the map, showing some similarities with theoretical LDOS thigh-binding simulations and numerical conductive AFM maps of Veselago lensing of a perfect graphene p-n junction [84].

In order to confirm that the observed SGM current maxima distribution corresponds to a caustic of electrons generated by Veselago lensing, I performed numerical simulations with the semi-classical SGM approach. In Fig.5.12.c is reported the ray-tracing propagation of several current lines across an ideal p-n junction. The kinetic energies of the junction are chosen in order to closely match the experimental conditions, with the same relative refractive index. Some trajectories impinging on the potential step with angles greater than the critical one, are totally reflected by the junction (red trajectories). The tip influence is modelled with a Lorentzian potential having peak potential $U_0 = 35$ meV, and decay radius $R_{\mathrm{tip}} = 300$ nm. The semi-classical SGM transmission map is calculated within the yellow window in Fig.5.12.c.

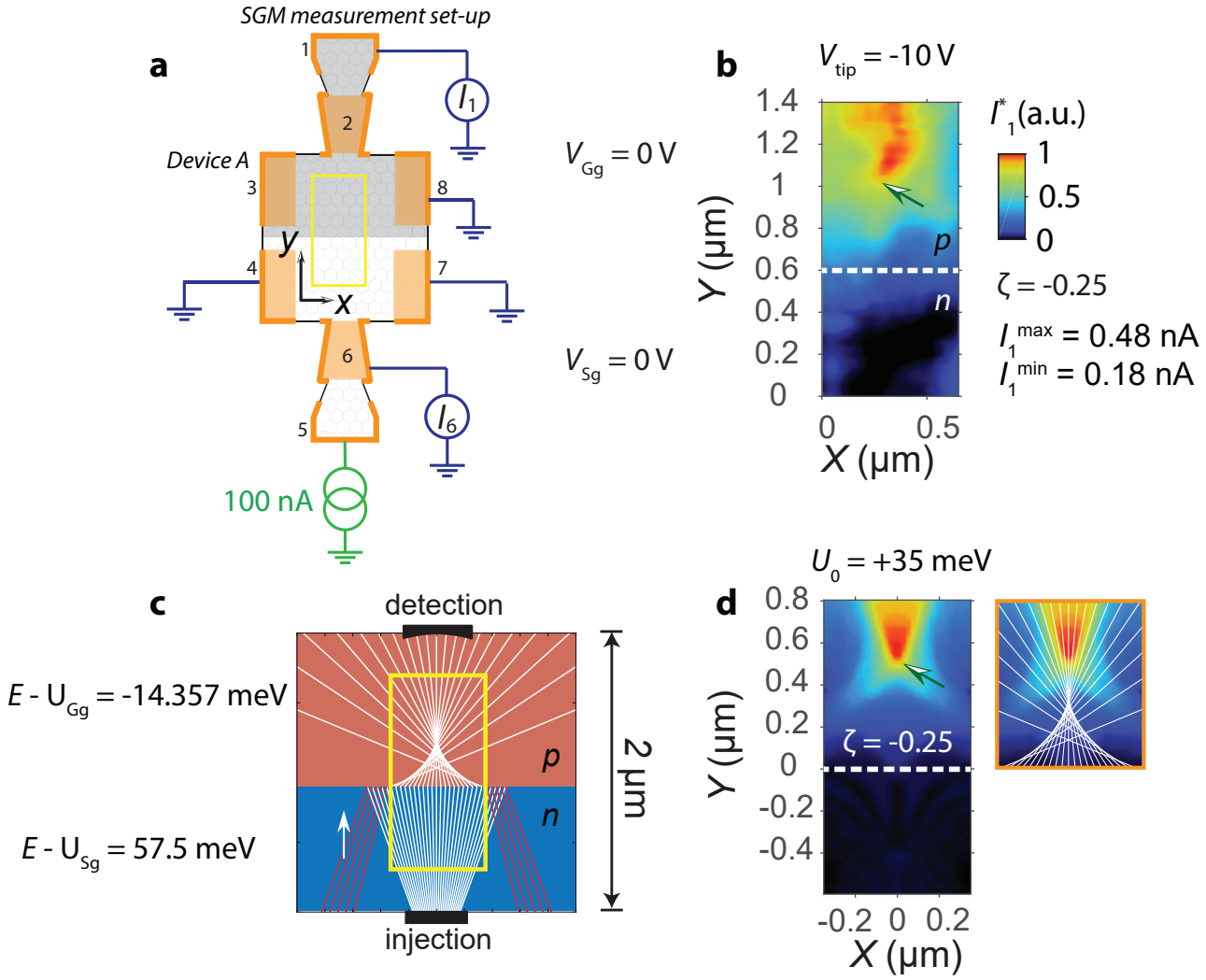

Figure 5.12: (a) Scheme of the experiment in the device A. The yellow rectangle represent the SGM scan window inside the device. (b) Current transmission SGM map through the junction at $\zeta = 0.25$, with current maxima forming a caustic pattern in the p-doped region. (c) Simulation of few electron trajectories propagating in an ideal p-n junction. Kinetic energies match the experimental conditions. An ideal caustic pattern of Veselago focusing is generated inside the yellow scan window. (d) Simulated SGM map highlighting the SGM ability to image Veselago focal points. On the right, comparison between the simulated SGM image and the trajectories in absence of the tip.

The semi-classical SGM map is reported in Fig.5.12.d. Similarly to the experimental map, the simulated signal in the n-doped region is characterized by a dramatic drop that extend over the whole area. Interestingly, the p-doped region manifests the presence of a localized maxima which has been pointed out with a green arrow. This last feature looks very similar to the one observed experimentally, even if the background signal is not completely matching with the experimental map. In the right side of Fig.5.12.d, I compare the spatial distribution of the refracted trajectories with the simulated SGM signal in the p-type area. The maxima are distributed slightly above the real location of the focal point, at the extremity of the caustic pattern. The qualitative agreement between the experiment and the semi-classical model allows us to extract the electron-optical signature of Veselago lensing from the SGM data.

5.5.2 Spatial evolution of a focal point

Fine spatial control of a Veselago focal point is a fundamental requirement for a proper electron optical platform. A density variation in one junction segment must tune the focal point position according to the theoretical principles introduced in chapter 1.4.1.

In graphene p-n junctions, the vertical position y_f of a focal point inside the p-doped region, follows the Snell-Descartes law and can be expressed by the following parametric equation

$$y_f = |\zeta(V_{Sg}, V_{Gg})|\, y_0 + y_J \tag{5.1}$$

where $\zeta(V_{Sg}, V_{Gg})$ is the relative refractive index depending by the backgate voltages, y_0 is the distance to the interface of an ideal focal point generated during the injection in the n-doped region, and y_J is the physical position of the interface.

Concerning the y_0 parameter, since the current is injected from a pinhole collimator, from geometrical arguments I estimated the image position of the initial focal point (green markers in Fig.5.15) which is generating the equivalent collimated electron beam. Its vertical distance to the interface is a technological parameter depending on the device lithographic layout, and is equal to $y_0 = 1.35$ μm in the device A, as illustrated in Fig.5.15.a3.

In Fig.5.13.(a-f) I report a series of SGM maps of current transmission, according to variations in the graphite backgate voltage V_{Gg}. The electron density in the silicon backgate region is fixed at $n_{Sg} = 3.44 \times 10^{11}$ cm^{-2}. The values of the relative refractive indexes ζ are reported in the maps, and allow us to interpret the space evolution of the SGM signal in the p-doped region. In the first four maps of Fig.5.13.(a-d), the Veselago focal point is predicted to be outside the SGM scan window. The absolute current maxima are located at the very top of the SGM maps, and are predicted to evolve into a focal caustic pattern inside the scan window as the voltage V_{Gg} reduces in magnitude (absolute values). In the last two SGM maps of Fig.5.13.(e,f), the theoretical focal point positions y_f are inside the scan window and are indicated with violet dashed lines. A series of current maxima seems to extend more inside the scan area, generating the SGM signature of the caustic pattern obtained in Fig.5.12.d.

I therefore investigated the experimental SGM maps with the help of semi-classical ray-tracing SGM simulations. The simulations are reported in Fig.5.14 for different relative refractive indexes. The kinetic energies are chosen in order to be close to the experimental transport conditions of Fig.5.13.(a-f). Like in experimental data, when the relative refractive index ζ is high, the simulated SGM maps display transmission maxima at the very top of the scan region. By reducing the value of the parameter ζ, the SGM maxima start to enter more inside the scan window, gradually drawing the characteristic SGM signature of a caustic pattern, as observed in the experiments.

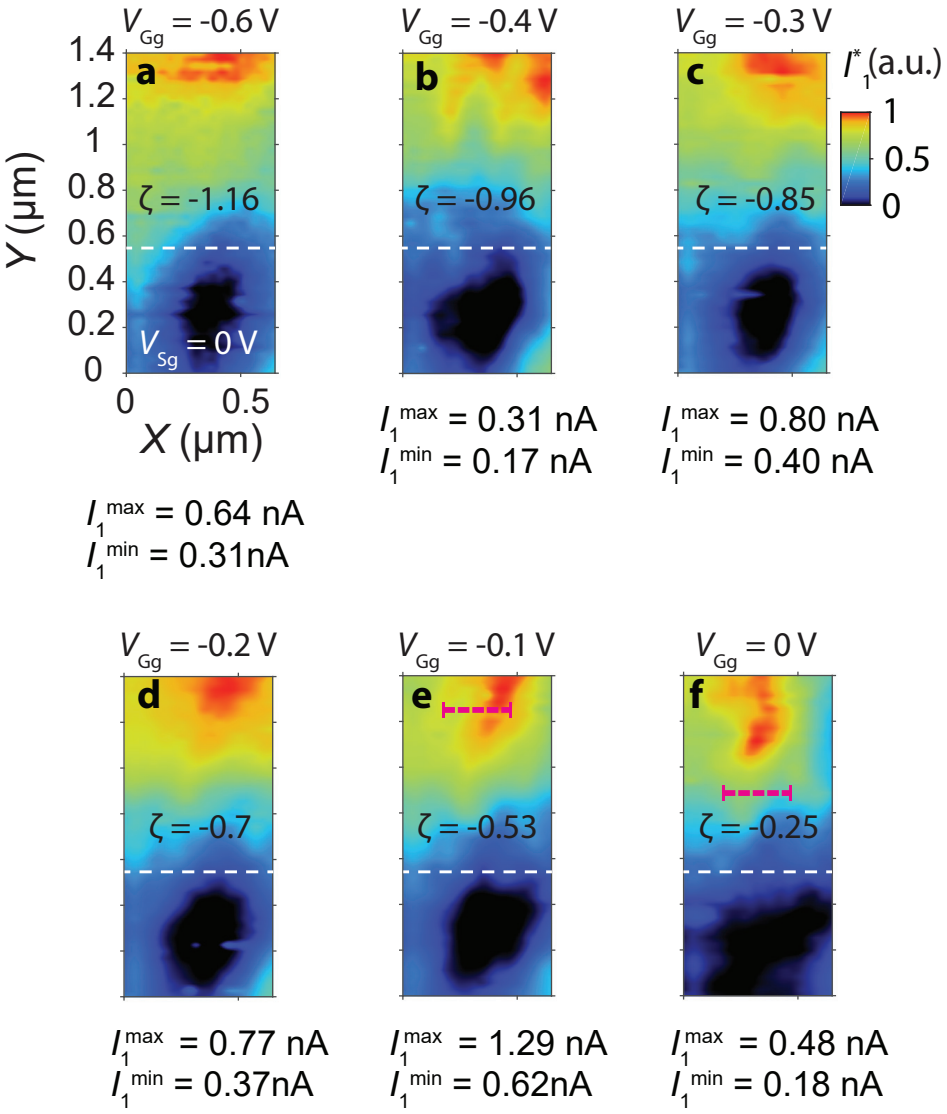

Figure 5.13: (a-f) Six SGM images of electron flow in graphene p-n junctions. The SGM tip voltage is set at $V_{\text{tip}} = -10$ V. The maps are recorded with several graphite backgate voltages. (a-d) In the first four images the Veselago focal point is predicted to be outside the scan window. (e,f) A reduction of the voltage V_{Gg} shifts the Veselago focal point inside the scan window. The last two maps display current maxima localized inside the scan area, in the proximity of the predicted location of caustics. The theoretical vertical position of the focal point is labelled with violet horizontal lines.

In order to complete the characterization of the Veselago lensing signatures on the SGM maps, it is also possible to test the dependence of the vertical position of the focal point y_{f}, as a function of the silicon backgate voltage V_{Sg}. To make this test, the graphite backgate voltage is fixed at $V_{\text{Gg}} = -0.25$ V, having thus a constant p-type doping in the graphite section. For any reduction of the silicon backgate voltage V_{Sg}, there will be an upward shift of the focal point, as illustrated in Fig.5.15.(a1-a3). In the figures, the yellow markers are representing the location of the focal point y_{f} inside the p-doped region of the junction. The theoretical behaviour of the focal point along the vertical y-axis, is reported versus V_{Sg} in Fig.5.15.b, using a thick yellow line. The line has been plotted with the parametric equation given in Eq.5.1,

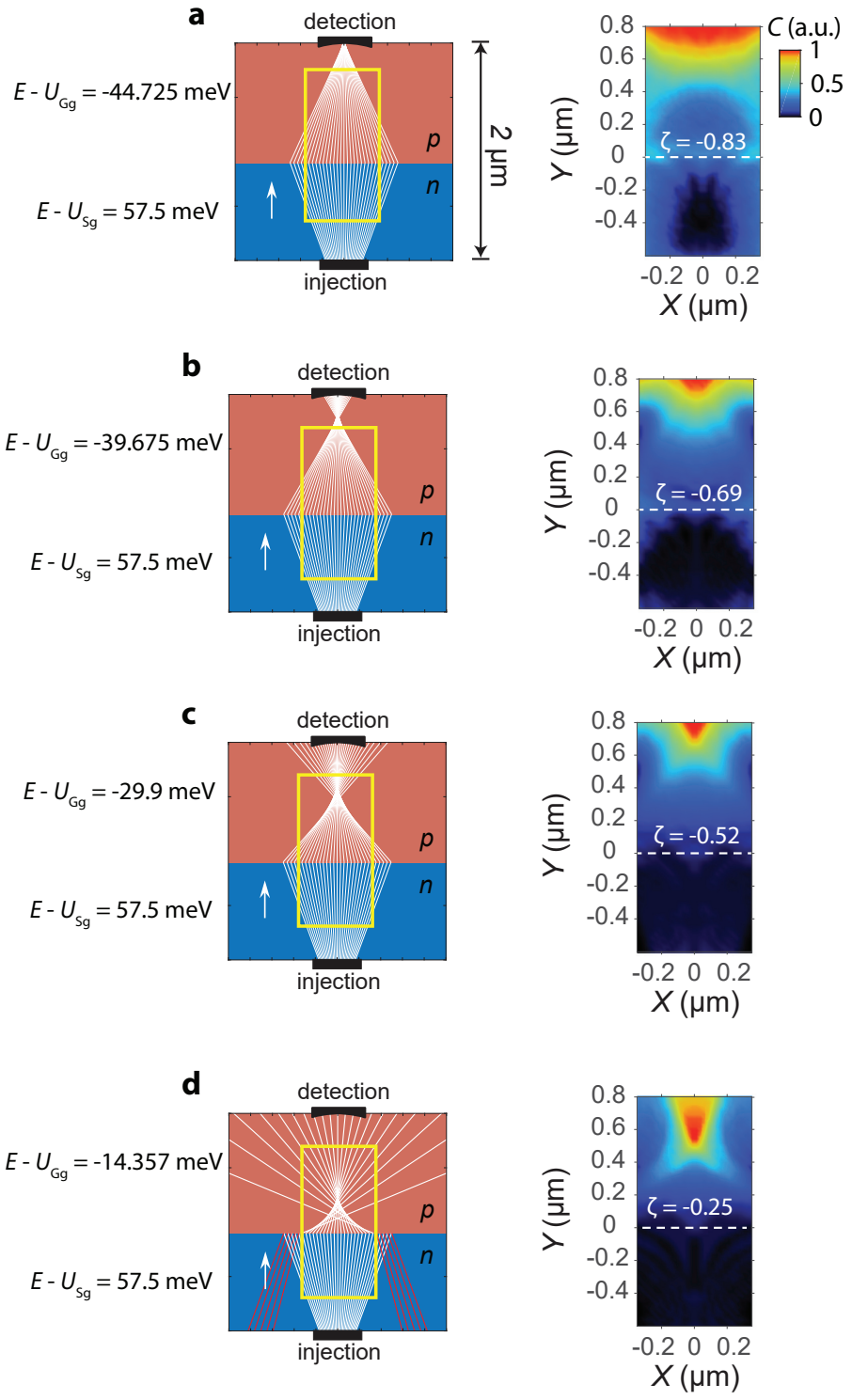

Figure 5.14: (a-d) Semi-classical trajectories and corresponding simulated SGM maps showing the ideal evolution of a SGM map according to variations of the kinetic energy in the p-doped region. The tip parameters are the same as in Fig.5.12.d.

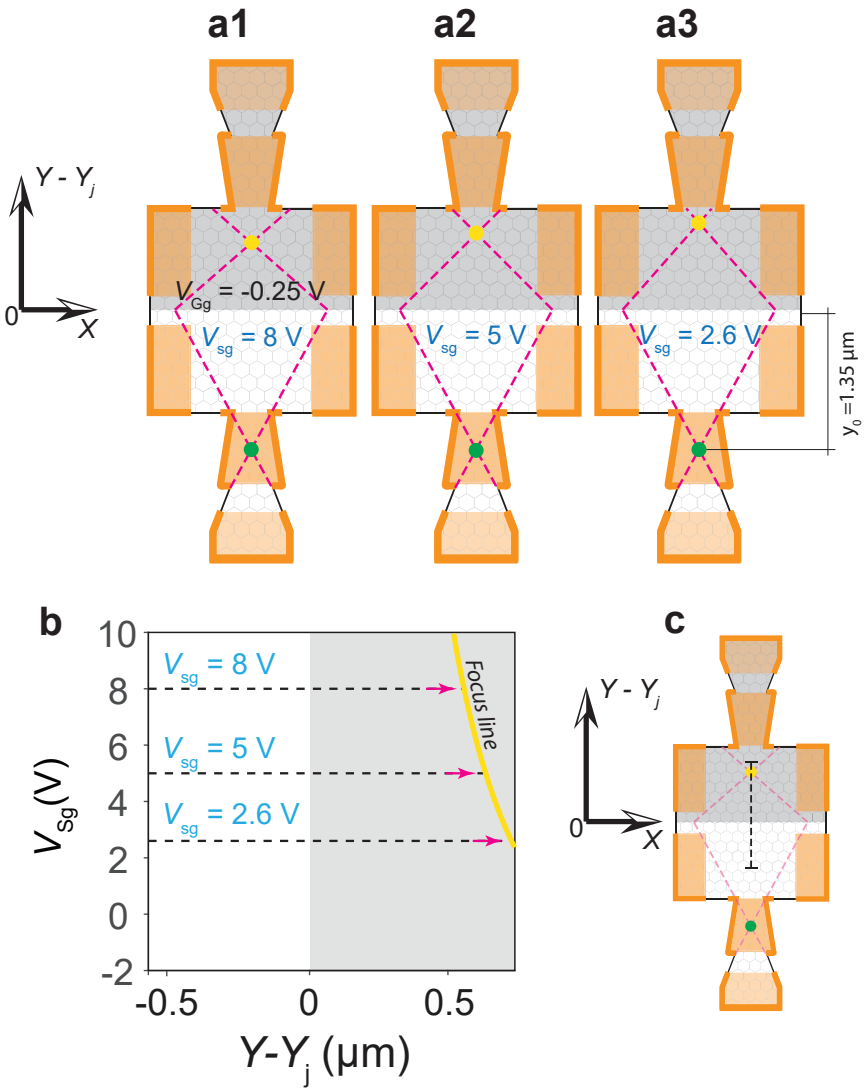

Figure 5.15: (a1-a3) Schematics of the p-n junction with three values of silicon backgate voltage V_{Sg}. The collimated current injection is characterized by the image position of a fixed focal point (green marker), spaced from the junction by $y_0 = 1.35$ μm. The yellow markers represent the physical position of the Veselago focal point in the p-doped region, according to the Snell-Descartes law. (b) Theoretical diagram of the vertical evolution of a Veselago focal point. The thick yellow line in the plot represents the positions of different Veselago focal points according to different values of V_{Sg}. (c) The position of the $y - y_j$ axis is reported on the device schematic by a black dashed line.

using the experimental parameters. The vertical extension of the interval $y - y_j$ is reported with a black dashed line over the device schematic in Fig.5.15.c.

This theoretical trend can be inspected experimentally via SGM by performing a silicon backgate voltage spectroscopy along a single vertical line-scan. The spectroscopy was performed at 150 nm from the device surface, along the green dashed line in the reference map of Fig.5.16.c. The tip voltage is fixed at $V_{\text{tip}} = -10$ V. For each tip position along the vertical line, the silicon backgate voltage is swept between the values $V_{\text{Sg}} = -2$ V and $V_{\text{Sg}} = 10$ V, locally changing the electron density. During the measurements, the graphite backgate voltage is fixed at $V_{\text{Sg}} = -0.25$ V, defining a constant p-type doping in the graphite section.

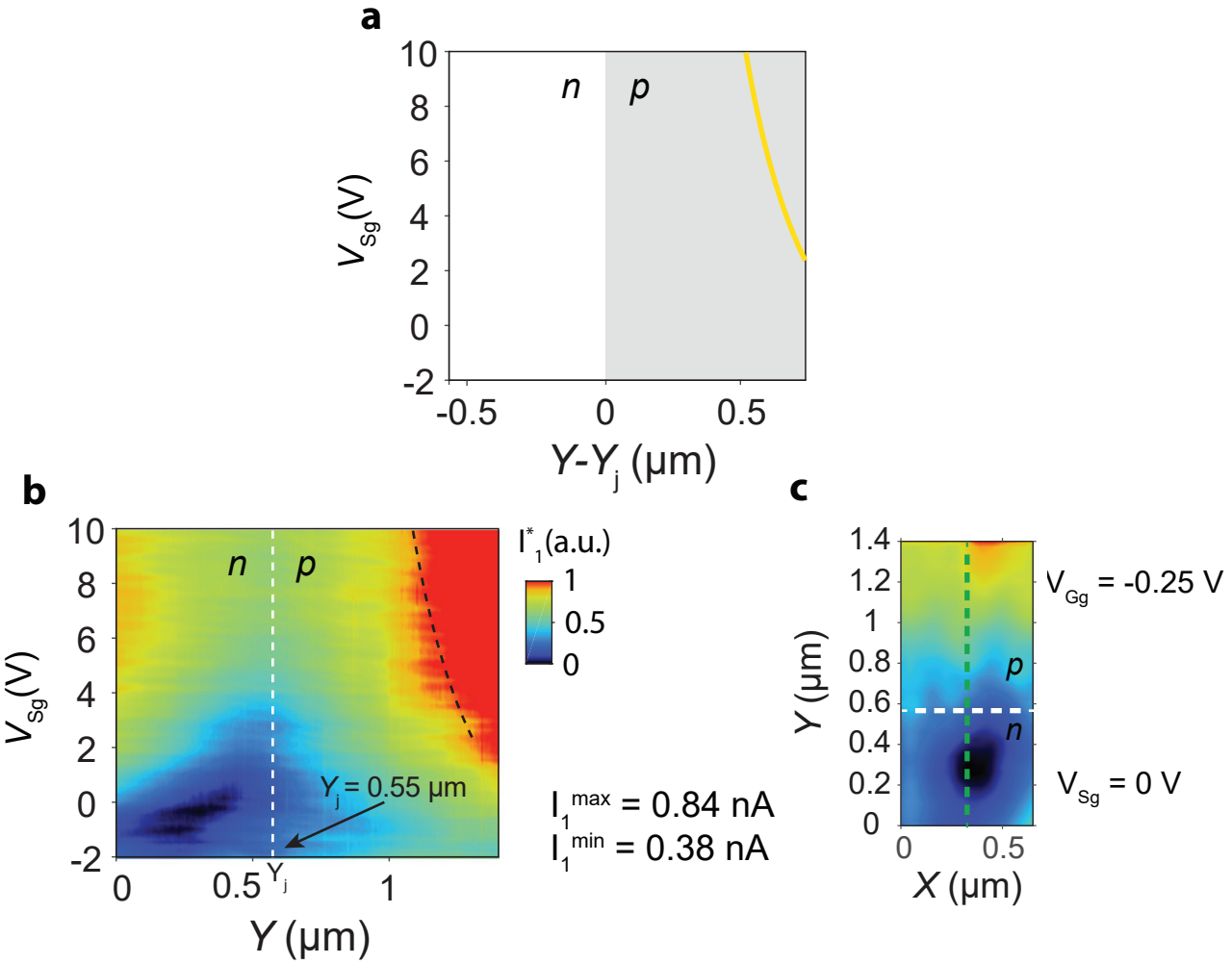

Figure 5.16: (a) Theoretical schematic of the Veselago focal point vertical evolution. The thick yellow line in the plot represents the various focal point positions according to different values of V_{Sg}. (b) Single-line SGM spectroscopy performed with $V_{\mathrm{tip}} = -10$ V. The black dashed line in the spectroscopy is the theoretical yellow line in (a), it contours a series of current maxima in the right side which represent the evolution of a Veselago focal point. (c) Reference SGM map of the spectroscopy which has been performed along the green dashed line. The white dashed lines in (b) and (c) represent the positions of the junction $y_{\mathrm{j}} = 0.55$ μm.

The experimental spectroscopy of the transmitted current I_1 is reported in Fig.5.16.b, and can be compared with the theoretical plot in Fig.5.16.a. In Fig.5.16.b, a vertical white dashed line points out the physical position of the junction at $y_{\mathrm{J}} = 0.55$ μm. This precise value was obtained via a precedent EFM mapping of the device position. In order to emphasise the Veselago lensing mechanism encoded in the spectroscopy, I superposed on the map a black dashed curve representing the theoretical evolution of the focal point y_{f} presented in Fig.5.16.a. It is of interest to notice that the curve well contours the region of current maxima in red, following the SGM signal associated to the Veselago focusing process in the device.

5.6 Back reflections at the junction

If on one hand, ballistic graphene p-n junction is a suitable platform to achieve fine spatial control over a Veselago focal point, on the other hand realistic junctions present non-idealities perturbing the charge dynamics. One of the major issue is the electrostatic smoothness of graphene p-n interfaces. It can introduce semi-classical turning points at the junction level as explained in Chapter 1.4.3, with significant probabilities of reflection at the junction.

5.6.1 Back reflection pattern versus density

I present here the SGM characterization of the back reflections[5] processes developing in the device *A*. I use the same measurement set-up employed for the current transmission measurements (see Fig.5.17), in which the back reflections can be detected via the measurement of the current I_6, which incorporate the current contribution of the filtering chamber composing the pinhole collimator, and a signal contribution from carriers reflected at the junction. For seek of simplicity, in the interpretations of the next SGM images, I consider the first contribution as a constant term with respect to the tip position.

The graphite backgate voltage is fixed at $V_{\mathrm{Gg}} = -0.25$ V, inducing a hole density in the graphite region $p = 2.08 \times 10^{11}$ cm^{-2}, which corresponds to a local Fermi wavelength $\lambda_{\mathrm{F}} = 78$ nm. The SGM maps of the current I_6 in Fig.5.18, were recorded for different silicon backgate voltage V_{Sg}, using a tip voltage $V_{\mathrm{tip}} = 10$ V, with the probe lifted at a distance of 150 nm from the device surface. Similarly to the current transmission maps, the back reflection maps are rescaled using the min-max normalization procedure [6]. All the physical current values, as well as the bottom gate voltages and the estimated Fermi wavelengths are printed next to the SGM maps.

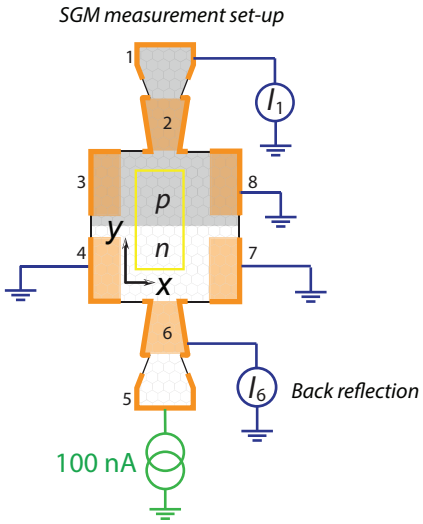

Figure 5.17: Measurement set-up for device *A*. The back reflections can be detected via the readout of the current I_6. The SGM tip is raster scanned whithin the yellow window inside the device.

[5] With the term *back reflection*, I refer to any process that causes trajectories to change direction of propagation at the p-n interface and return back to the source region.

[6] The minimum current value of a map corresponds to a zero in the colour bar, while the maximum is converted into a 1.

In Fig.5.18.(a-c), measured closer to the charge neutrality in the n-doped region, the maps show a series of marked fluctuations which represent branches of electrons expanding from the pinhole collimator. The branches become smoother when the V_{Sg} voltage goes to higher voltage values, disappearing almost completely in Fig.5.18.(e-f). Modifications in the current flow, from a branched flow in the lowest electron density condition, to a uniform straight flow in the highest n-doping regimes, can be understood considering the effects of the potential inhomogeneities. In graphene, the potential fluctuations are stronger at lower charge densities, due to the weaker screening [124]. In addition, for small carrier density, and by consequence for large wave length, potential fluctuations induce larger ray deflections and thus wider branched flow. Close to charge neutrality, the electron flow is thus strongly influenced by the bare disorder, forming a series of evident branching patterns. At higher electron densities, available carriers screen self-consistently the fluctuating bare potential [1], reducing the amount of scatterers which are responsible for the branch formation.

5.6.2 Tip-enhanced tunnelling

An interesting feature that can be observed in the SGM maps of Fig.5.18.(a,b), is the sudden drop of the back reflection current I_6 right in front of the junction region, in the middle of the white dashed line. This effect can be interpreted considering the electrostatic lensing effect of the tip on the current trajectories. As presented in Chapter 1.5.2, the SGM tip potential is able to bend and focus current trajectories when inducing local regions of charge accumulation. If the charged tip is positioned axially to the transport region, in the middle of the p-n junction, its electrostatic potential generates a deflection of the p-n interface, with the tail of the tip potential gradually guiding the ballistic flow almost orthogonally to the electrostat-

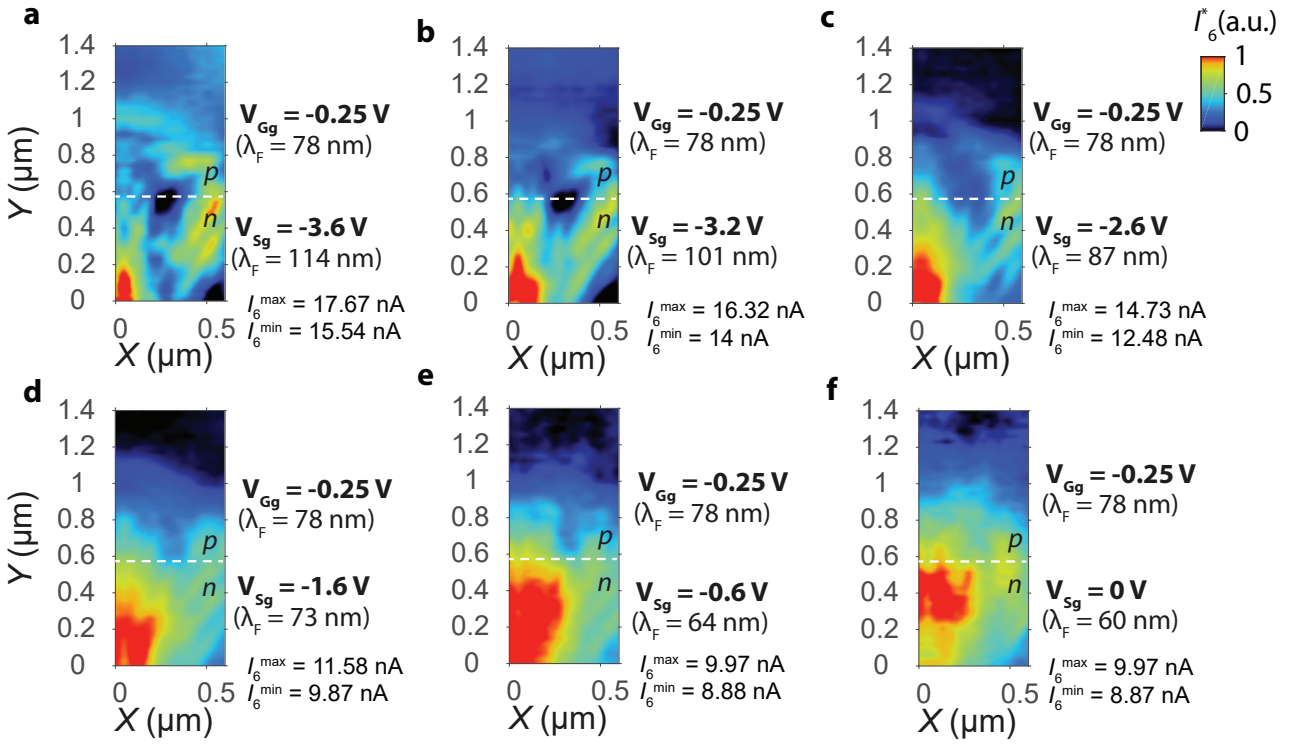

Figure 5.18: (a-f) SGM maps of the current I_6 in the device A, with tip voltage $V_{tip} = 10$ V, illustrating the back reflection developing at the p-n interface. The position of the p-n interface is labelled with a white dashed line.

ically deformed junction. This complex effect, which is discussed deeply in Chapter 3.2.7, is illustrated here with a series of semi-classical ray-tracing simulations in Fig.5.19. A pencil of ray trajectories are injected in a p-n region, having kinetic energies that fit the experimental conditions of the map in Fig.5.18.b. The smoothness of the electrostatic interface in the simulation has been chosen arbitrarily, and extends for almost 300 nm in the graphene plane (the junction potential is described from the equation Eq.3.25). The tip electrostatic is modelled as a Lorentzian potential creating electron accumulation, having peak potential $U_0 = -20$ meV and decay paramter $R_{\text{tip}} = 370$ nm.

According to the different positions of the SGM probe (labelled with a violet marker), the ray fields evolve remarkably. In Fig.5.19.(a,c), the smoothness of the potential profiles reflect back the semi-classical current trajectories, producing a sufficiently high signal in the back reflection contact. On the contrary, when the tip is at the centre of the junction (Fig.5.19.b), the semi-classical algorithm fails and many trajectories find their way through the semi-classical forbidden region. As stated in Chapter 3.2.7, the tunnelling processes in Fig.5.19.b can be attributed to the insufficient mesh elements in the simulations. However, I will show now that this numerical artefact captures surprisingly well the peculiarity of the measured SGM signal. In Fig.5.20 I report a comparison between the experimental SGM map shown in Fig.5.18.b and the simulated back reflection map described in Chapter 3.2.7. It is possible to notice three interesting agreements between the two maps: (i) the n-doped region of both maps manifests current maxima, even if the maxima in Fig.5.20.b are strongly influenced by branching processes which are not considered in the simulation; (ii) both maps around the middle region of the junction show a signal drop, which somehow confirm the validity of the ray-tracing tunnelling trajectories shown in Fig.5.19.b; (iii) the p-doped regions are characterized by a residual non-zero signal, representing the non-perturbed back reflections generated by the junction.

As it is possible to observe in Fig.5.18, the drop of the reflected current I_6 in the middle junction, is quite evident when the n-doped region has low electron density (high values of λ_F). Conversely, this particular signature disappears at higher electron densities. An explanation of this trend could be that the subtle effect of tip-induced tunnelling can only develop at low carrier density, since the shape of the classically forbidden region is strongly deformed from the tip potential. Moreover, at higher electron density, the n-doped region can screen the electrostatic influence of the tip, reducing this unexpected tunnelling effect induced by the tip potential.

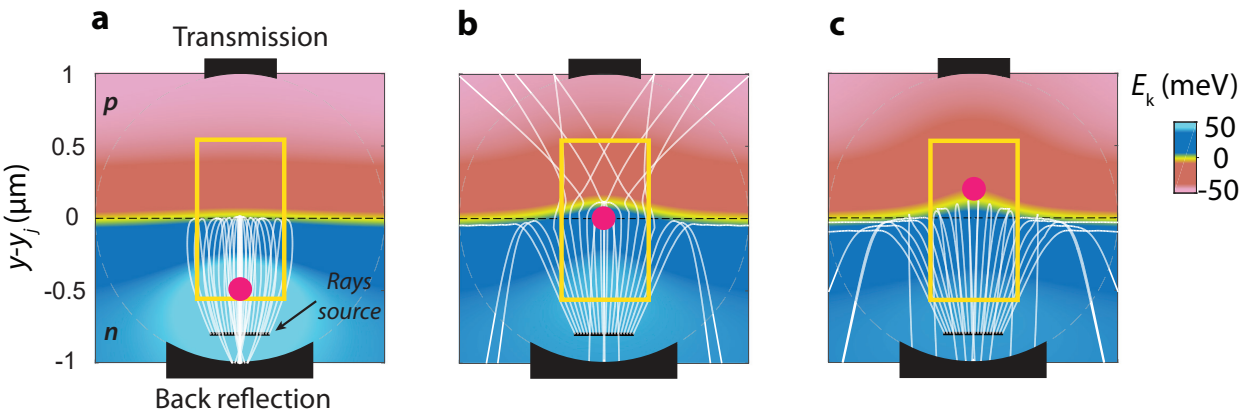

Figure 5.19: (a-c) Ray-tracing calculation of electron trajectories across a smooth p-n junction, under the presence of a SGM tip inducing electron accumulation. The tip position in each map is labelled with a violet marker.

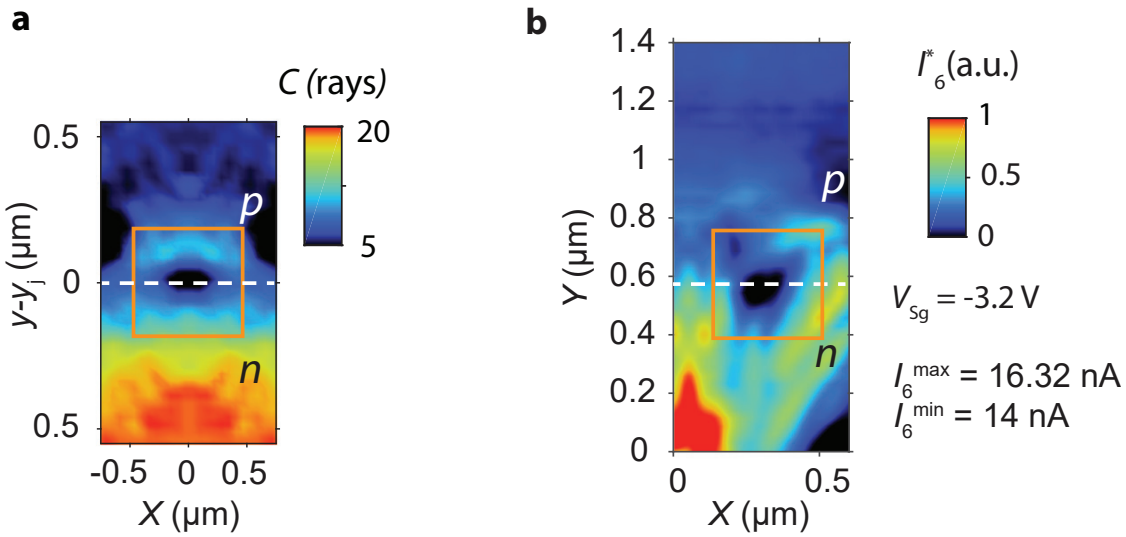

Figure 5.20: (a) Ray-tracing SGM simulation of the back reflection signal. For more details on the map calculation, see Chapter 3.2.7. (b) Experimental SGM map of the current I_6, representing the back reflection processes under the presence imaged by the SGM tip. The orange frames highlight the region with the tip-enhanced tunnellings observed in both the numerical (left) and the experimental (right) SGM maps.

5.7 Branching in graphene p-n junctions

Branched flow is an ubiquitous phenomenon in the whole universe. It occurs in many physical systems whenever there is propagation of waves impinging on refracting medium. Branching can be observed at various length-scales: electron waves propagating on the micron scale in semiconductors, acoustic waves in the atmosphere, tsunami waves on the oceans, and even on the galactic scale with the propagation of microwaves generated from pulsars [65].

In the year 2001, a groundbreaking SGM experiment performed on a quantum point contact obtained from a high mobility GaAs 2DEG, showed the branching phenomena in a ballistic system with mean free path of about 10μm [141]. Since then, the dynamical properties of branched electron flow in 2DEGs has been investigated in more details theoretically and experimentally [106, 78, 77]. However, up to now ultra-relativistic branching of Dirac fermions in encapsulated graphene has never been observed with SGM.

Weak disorder in graphene manifests in the form of charge inhomogeneities [99, 156, 101] that are able to modify the current trajectories, exhibiting lensing mechanisms with the formation of branches and cusp singularities [104]. The lensing action of impurities allows to make a direct connection between statistical spatial distribution of the random potential and the distribution of caustics in a graphene layer. The dynamical properties of these caustics have been recently described in [104], showing the relevance of the ray-tracing approach in the statistical analysis.

5.7.1 Branching in transmission maps

In order to analyse the branching effects on a p-n junction, we current bias the device B, injecting 90 nA from the bottom region of the device, in the graphite gate region (See Fig.5.21.a). The silicon backgate voltage is $V_{\mathrm{Sg}} = -1.466$ V, setting a hole density of $p_{\mathrm{Sg}} =$

1.21×10^{11} cm^{-2}. The graphite backgate voltage is $V_{Gg} = 0.2$ V, inducing an electron density of $n_{Gg} = 2.52 \times 10^{11}$ cm^{-2}. The relative refraction index of the p-n junction is $\zeta = 0.69$. The SGM probe is positioned at 200 nm from the device surface. The measurement of the current transmission I_1 allows for the generation of the SGM maps reported in Fig.5.21.(b,c), with a tip voltage of $V_{tip} = 10$ V and $V_{tip} = -10$ V respectively. For each map, the position of the p-n interface is indicated by white dashed lines.

At first glance, it is possible to recognize the characteristic high contrast current patterns already observed in the transmission processes through a graphene p-n junction. Looking at the maxima distribution in the bottom part of Fig.5.21.b, it is possible to notice the presence of a bifurcation in the SGM signal, forming an evident pair of branches that are indexed with purple arrows. A series of smaller branches, pointed with blue arrows, distribute around the main bifurcation. These localized maxima expand in space as a widening fan toward the junction interface. The derivative of the signal inside the orange box allows to better appreciate the structured pattern. The observation of branching in the SGM map can be attributed to potential fluctuations in the graphene billiard, with cumulative effects on the

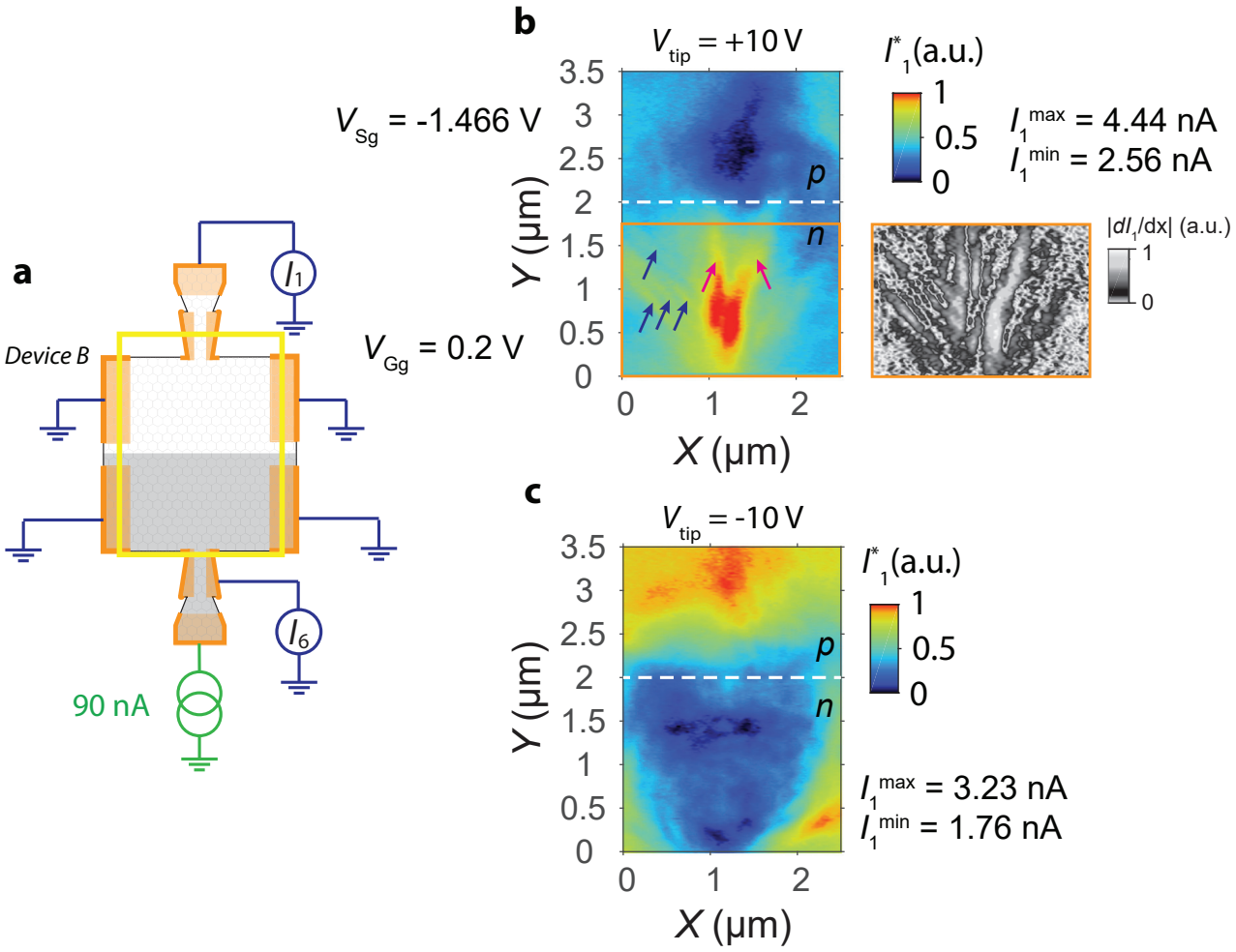

Figure 5.21: (a) Scheme of the experiment on device *B*. The SGM scan window is fully extended on the whole device surface. (b) SGM map of current transmission at positive tip voltage ($V_{tip} = 10$ V). Branches appear in the n-doped region of the junction, within the orange box, and are indexed with coloured arrows. On the right is reported the derivative of the signal inside the orange box. (c) SGM map at negative tip voltage ($V_{tip} = -10$ V).

current trajectories which generate long-lived bifurcation patterns. The branching is observed for positive tip voltage, a situation in which the trajectories are refocused by the lensing effect of the tip-induced potential. The SGM map at negative tip voltage (Fig.5.21.c) shows a current signal which distributes in space simply as a widening fan from the injection point, surprisingly this time without the presence of an evident branching pattern. The polarity of the scanning tip therefore plays a crucial role in highlighting the branches positions. Interestingly, the small current fluctuations in the n-doped region of Fig.5.21.c, look very similar to the fluctuations characterizing the SGM maps in Fig.5.4.(g,h), and probably can be associated to non-trivial tip-induced classically forbidden regions inside the n-doped segment of the junction.

I present in the following an explanation of the branching generation under the presence of a single isolated charge impurity. In order to create an effective branching, I employed an impurity characterized by an invasive potential with a localized electrostatic action. Although the proposed model looks simple, it represents the fundamental mechanism that can be encountered in more complex smooth disordered systems, and allows for a sufficient understanding of

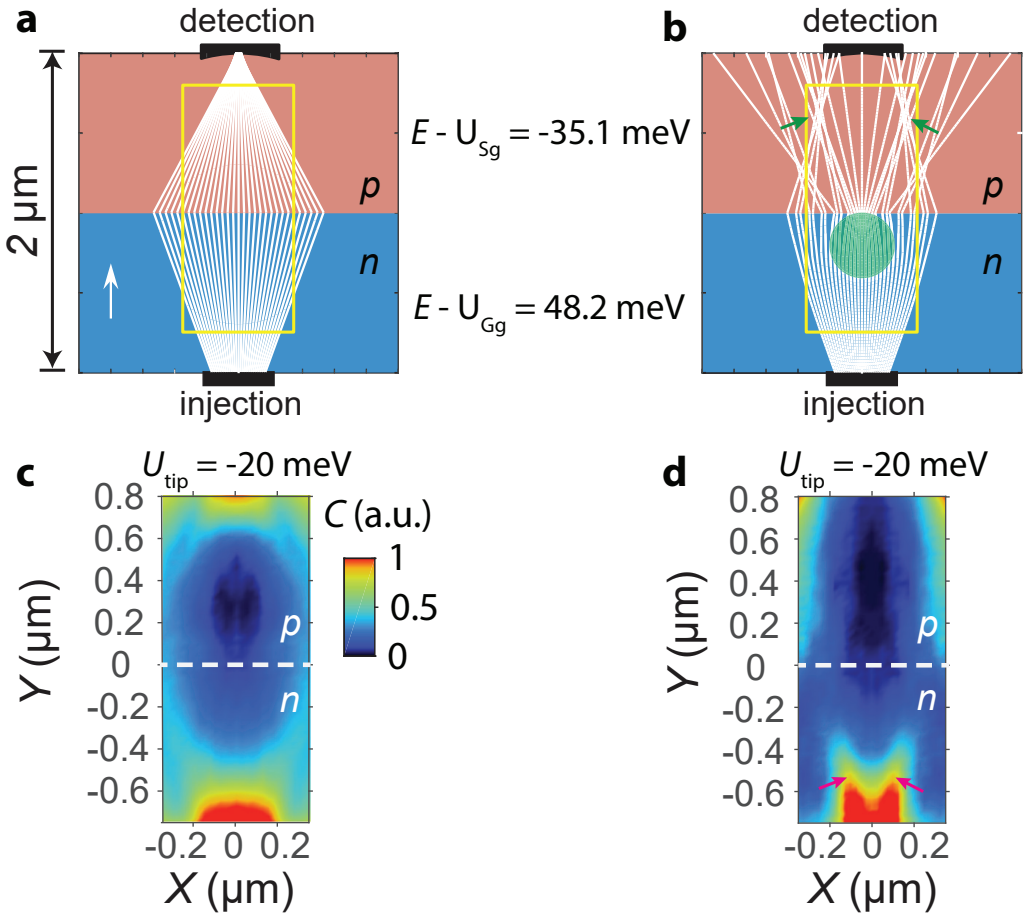

Figure 5.22: (a,b) Semi-classical current trajectories propagating in a clean graphene junction (a) and in the presence of a Lorentzian-like charge accumulation (b). The position of the impurity is indicated with a green disk, with diameter corresponding to the FWHM of the Lorentzian potential distribution. Green arrows indicate the positions of caustic events originated from the impurity. (c,d) Simulated SGM maps (for a positive tip voltage) in the absence (c) and presence (d) of the charge inhomogeneity. Violet arrows in (d) are pointing the bifurcation in the SGM transmission map.

the phenomenon [53]. Nevertheless, it is important to precise that branching is a consequence of complex disorder, and is governed by two statistical parameters: the potential strength and the correlation length [119, 66].

Figure 5.22.(a,b) show respectively the calculated ray field distribution in a pristine graphene p-n junction and in the presence of an invasive charge accumulation region (green disk) within the n-doped region of the junction. The kinetic energies of the graphene billiard closely match the experimental conditions of the maps of Fig.5.21. The charge impurity is modelled as a Lorentzian potential having decay potential $R = 200$ nm and a peak potential $U = -23$ meV. A comparison between the two ray fields allows to better understand the influence of the impurity in the branching process. If the pristine system displays a perfect Veselago lensing in the p-doped region, the current pattern bifurcates in the p-doped region under the presence of a charged impurity.

The semi-classical SGM transmission maps are reported in Fig.5.22.(c,d). Calculations are performed considering a n-doping Lorentzian tip potential with decay parameter $R_{\text{tip}} = 300$ nm and peak potential $U_0 = -20$ meV. While the SGM map in the pristine graphene system (Fig.5.22.c) does not display any branching pattern in the n-doped region, the map under the impurity influence (Fig.5.22.d) develops a pair of branches pointed out with two violet arrows. These numerical results account for a qualitative understanding of the branching phenomena in the SGM signal.

5.7.2 Branching in back reflection maps

The branching process in the SGM signal was previously discussed for the current transmission signal. Here, in order to evidence the branching nature of the fluctuations in the SGM maps of back reflections, I provide in Fig.5.23 a comparison between the SGM transmission map of the device B, previously presented in Fig.5.21.b, and the associated SGM map of back reflection which has been recorded simultaneously.

Both signals exhibit marked spatial fluctuations. The arrows pointing out the branches in Fig.5.23.b are positioned without modification over the back reflection map in Fig.5.23.c. Arrows highlighting the spatial correlations between the two maps, where a high current in the transmission map corresponds to a low current in the back reflection map, suggesting a common origin of the recorded fluctuations. The anti-correlation between the two maps may be interpreted in the following way : the attractive tip potential reinforce the transmission when located straight on a branch, but deviate the trajectories when located on the side of a branch, inducing a strong back reflection.

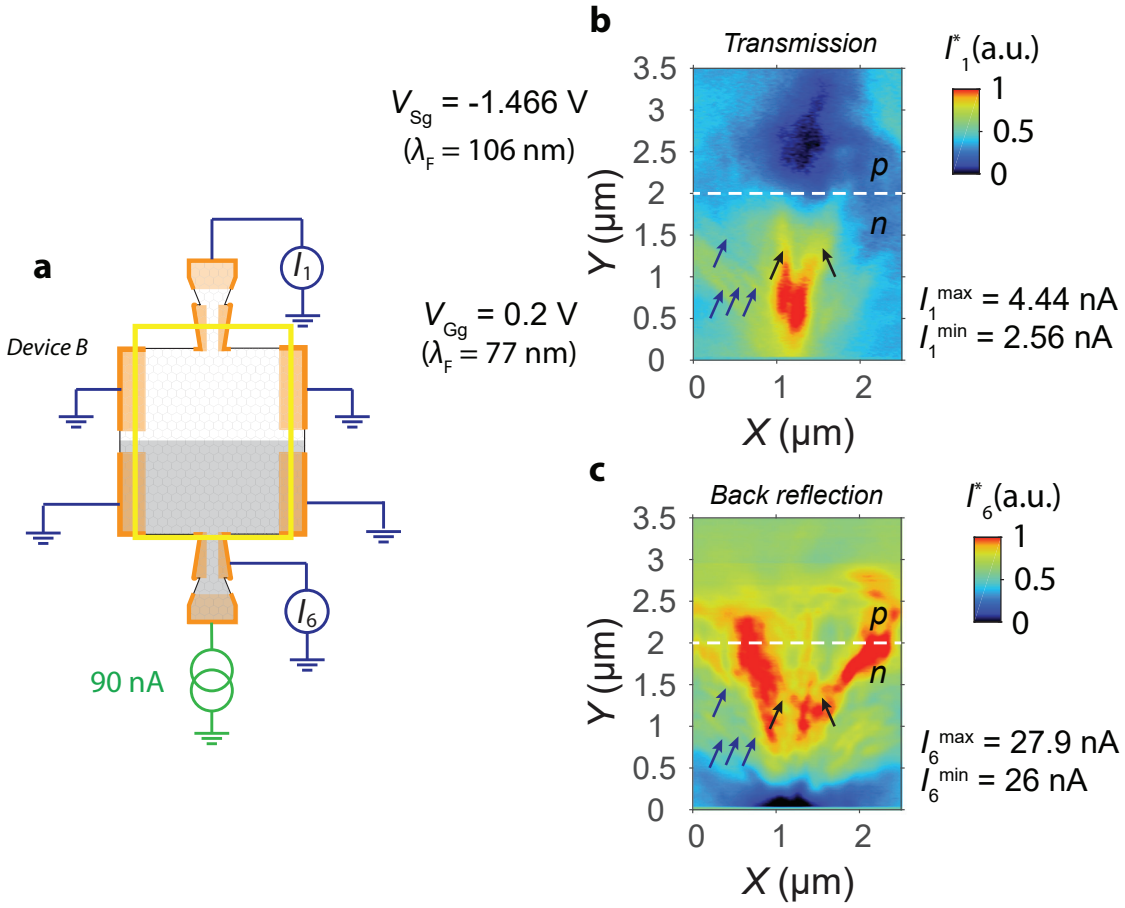

Figure 5.23: (a) Schematic of the SGM experiment on the device *B*. (b) SGM map of current transmission I_1 at positive tip voltage $V_{\text{tip}} = 10$ V, showing evident branching inside the n-doped region of the junction. (c) SGM map of the current I_6 illustrating the back reflections in the junction. The branched features in the map are of the same origin as the branches in (b).

Conclusion

In this chapter, I reported SGM experiments performed on three graphene p-n junction devices. The scanning gate maps revealed the ballistic propagation of the electron flow and signatures of positive refraction in the unipolar configuration. The map features were interpreted with the help of ray-tracing simulations, which allowed to discuss the role of charge inhomogeneities in the final appearance of the maps.

In the bipolar regime of the junction, I obtained high-contrast SGM images of the current transmission across the p-n junction. A series of ray-tracing simulations confirmed the validity of the semi-classical approach to understand the transport signatures in presence of a scanning gate. The SGM maps indicate the formation of an electron caustic produced by the Veselago lensing effect and provide information about the spatial evolution of the focal point after the junction interface.

The pattern of back reflection currents developing at the p-n interface was also studied by SGM. With the help of the ray-tracing approach, I described the spatial evolution of the reflected current, revealing the presence of an unexpected tunnelling process at the junction, activated by the electrostatic action of the tip. Finally, the branching phenomena inside the devices have been analysed in both the transmission and back reflection maps.

Chapter 6

Imaging quantum Hall backscattering in graphene

Contents

Graphene under high magnetic field goes into the quantum Hall regime, with ideally non-dissipative transport happening on the edges of the graphene layer. In mesoscopic samples however, backscattering between the counter-propagative edge channels is possible even at integer filling factor. This failure of the topological protection of the quantum Hall quantization results from the presence of localized states in the bulk of the device which are significantly coupled to the edge modes. This theoretical explanation however lacks of experimental investigations of the microscopic mechanism involved in these couplings. In this chapter, I report a detailed scanning gate investigation of the quantum Hall backscattering in high-mobility graphene devices equipped with local graphite backgates.

6.1 Quantum Hall effect in graphene

In this section I provide a series of theoretical explanation on the origin of the integer quantum Hall effect based mainly on the Refs. [42, 73, 56].

6.1.1 Graphene Landau levels

The application of a perpendicular magnetic field on a graphene layer splits its density of states into a series of discrete Landau levels. In the case of a conventional semiconducting 2DEG, the Landau levels spectrum follows the harmonic oscillator relation $E_{\mathrm{N}} = \hbar\omega_{\mathrm{c}}\left(N + \frac{1}{2}\right)$, where $N \in \mathbb{N}$ is the Landau level index, and $\omega_{\mathrm{c}} = eB/m^*$ is the cyclotron frequency, which depends on the magnetic field B and the electron effective mass m^*. In graphene, the Landau levels energy spectrum is relativistic and can be written

$$E_N = \mathrm{sign}(N)\, v_F \sqrt{2\hbar e|N|B} \tag{6.1}$$

where the sign of N characterize hole-like ($N < 0$) or electron-like ($N > 0$) behaviours of charge

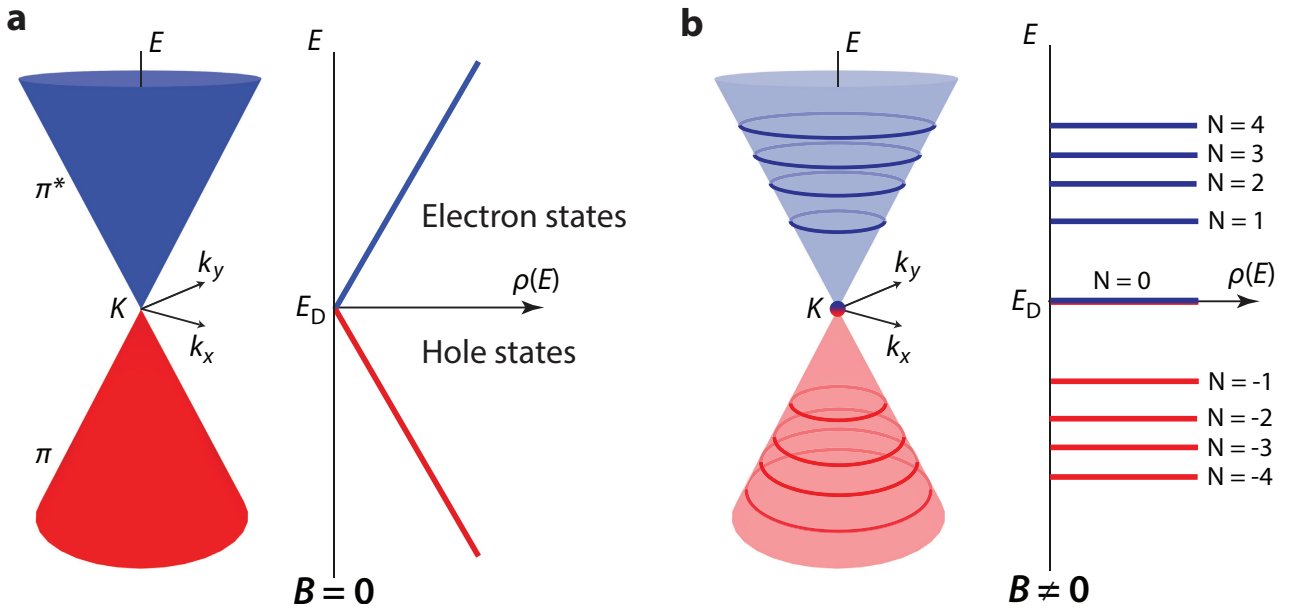

Figure 6.1: (a) Graphene Dirac cone and the relative density of states ρ at zero magnetic field. (b) Energy band-structure and density of states of graphene under a constant magnetic field B, highlighting the discrete distribution of Landau levels. Adapted from [33]

carriers. According to Eq.6.1, the Landau levels spectrum follows a square root dependency on the index N and magnetic field B. A comparison between the graphene energy dispersions in the absence and presence of an external magnetic field is provided in Fig.6.1. From Fig.6.1.b it is evident that the spacing between Landau levels reduces for higher N values. This peculiarity differs from standard semiconductor 2DEG having parabolic dispersion, where Landau levels are equidistant in energy. In graphene, the cyclotron gap represents the distance between two consecutive Landau levels, and can be written as

$$\Delta E_{\mathrm{N}} = v_{\mathrm{F}}\sqrt{2\hbar eB}\left(\sqrt{N+1}-\sqrt{N}\right) \tag{6.2}$$

Similarly to the zero-field case, graphene energy spectrum under magnetic field needs to account for the valley pseudospin, which introduces a two-fold valley degeneracy term $g_{\mathrm{v}} = 2$ to each Landau level. Each Landau level is highly degenerate, and in the non-interacting picture, the complete degeneracy n_{LL} writes

$$n_{\mathrm{LL}} = g_{\mathrm{s}}\, g_{\mathrm{v}}\, BS/\phi_0 = 4\phi/\phi_0 \tag{6.3}$$

where $g_s = 2$ is the usual spin degeneracy of electrons, $\phi = BS$ is the magnetic flux threading the graphene layer on a surface S, and $\phi_0 = h/e$ is the magnetic flux quantum. It is therefore possible to infer that, for each flux quantum, there are four states available in each Landau level. Each state occupies a surface $\delta A = 2\pi l_{\mathrm{B}}^2$ on the graphene layer, where the magnetic length $l_{\mathrm{B}} = \sqrt{\hbar/eB} \approx 26$ nm at 1 T.

The ratio between the number of charge carriers in the graphene plane and the amount of flux quanta threading the system is called filling factor ν and writes.

$$\nu = \frac{nS}{n_{\mathrm{LL}}} = \frac{n\phi_0}{4B} \tag{6.4}$$

where n is the charge carrier density in the graphene layer. The filling factor ν is a continuous parameter, which is a function of n and B. For integer values $\nu(N) = 2(2N+1)$, the Fermi energy E_{F} lies between two Landau levels and therefore, at low temperatures, all Landau levels below E_{F} are fully occupied.

6.1.2 Edge channels

The Landau levels spectrum is usually obtained considering an infinite graphene plane. In this ideal picture, charge carriers follow (quantized) semi-classical cyclotron orbits, forming closed circular loops in space, without contributing to the electrical transport process.

A different scenario appears when considering the physical edges of a sample, since it is expected that the wave function of electrons ψ vanishes. The description of this physical problem was provided by Halperin, in the case of conventional semiconductor 2DEG [62], where the vanishing of the wave function at the edges causes an upward shift of all the eigenenergies associated to the Landau levels. This upward shift is equivalent to a confining potential $V(x)$ at the edges, restricting electrons inside the sample. This approach can also be applied in graphene etched heterostructures without electrostatic gating, where the boundary conditions can also be thought as effective confining potentials that cause upward energy bending for electron-like Landau levels ($N > 0$), and downward bending for hole-like Landau levels ($N < 0$). At the physical edge, the zeroth Landau level ($N = 0$), which is shared by both electron-like and hole-like quasiparticles, it splits into two spin-degenerate electron-like and hole-like Landau levels, which evolve upward or downward according to the different effective confining potentials. More

details about the edge state dispersion are given in Appendix A based on the theoretical work by Brey and Fertig in 2006 [21].

Edge dispersion gives rise to a transport regime where electrical current localizes at the edges of the device, following a series of conductive edge channels. This mechanism can be understood looking at Fig.6.2.(a,b), where the Fermi level E_F lies within a cyclotron gap, between two consecutive Landau levels. Close to the sample edges, the Fermi level crosses one or several Landau levels. At the intersection, one-dimensional conducting edge channels arise, as presented in Fig.6.2.(c,d), forming a continuous one dimensional conductive channel following the edges of the graphene sheet. Edge states propagate following the directions described by the arrows in the picture, with a group velocity v_g given by

$$v_g = \frac{1}{\hbar}\frac{\partial E_N}{\partial k} = \frac{1}{\hbar}\frac{\partial V(x)}{\partial k_y} = \frac{1}{eB}\frac{\partial V(x)}{\partial x} \tag{6.5}$$

which is non-zero at the edges of the graphene layer. This equation shows that the group velocities on opposite edges of the sample have opposite signs, and are therefore counter-propagating (or chiral). Therefore, all the edge channels on one side of the sample propagate in the same direction. Under this condition, as pointed out by Büttiker in [25], the backscattering

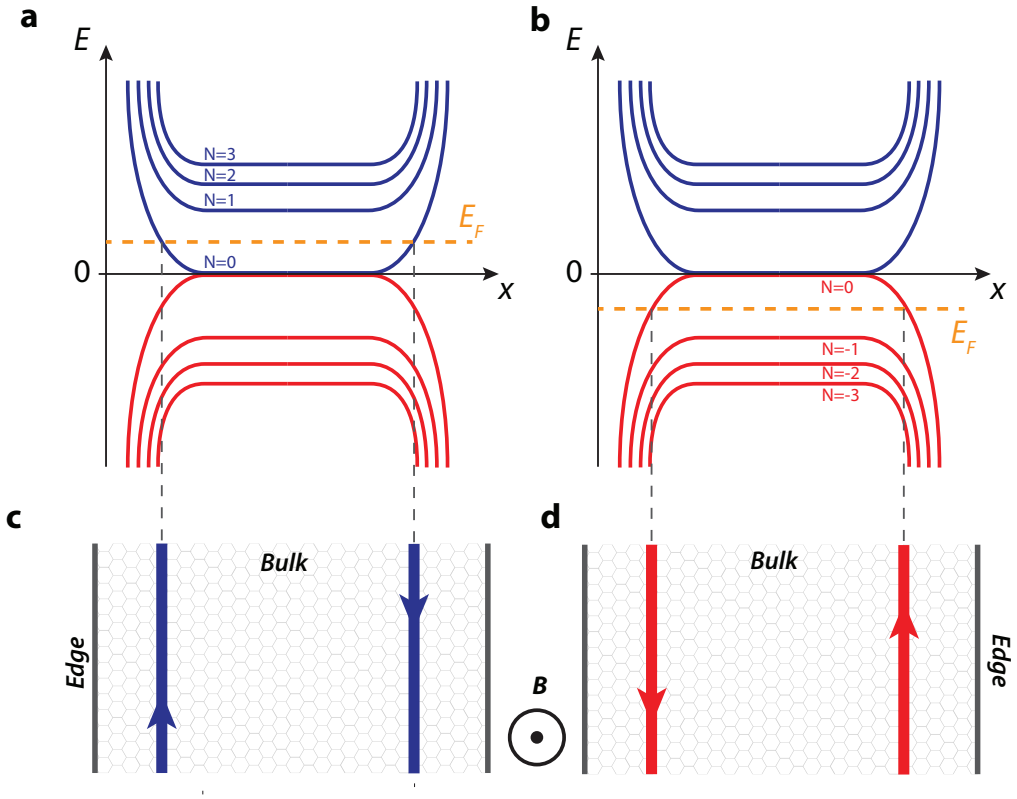

Figure 6.2: (a,b) Bending of the graphene Landau levels (LLs) approaching the edges of the graphene flake. Electron-like LLs are represented in blue while hole-like LLs are represented with red lines. When the Fermi energy E_F (orange line) lies between two adjacent LL in the bulk, it crosses a LL at the edges of the sample resulting in the formation of conductive edge channels. (b,d) Electron (in blue) and hole (in red) edge channels propagating close to the edges of graphene.

along a single edge is prevented and only forward scattering due to impurities is allowed. Backscattering is possible only if two different counterpropagating edge channels are brought sufficiently close to each other. However such situation is ideally prevented in large devices, since counter-propagating edge channels are usually separated by several microns, a distance much larger than the magnetic length parameter l_B.

Edge channel recontructions The previous picture of propagating edge channels assumes the crossings of Landau levels with the Fermi level at a single points in the x direction. However, an edge channel made of an infinitely narrow width, requires the presence of a local abrupt increase of carrier density, which is not physically realistic. Therefore, in order to restore the physical reliability of the edge channel picture, it is necessary to include the self-consistent screening effect of the edge channels over the evolving electrostatic potential, as proposed by Chklovskii, Shklovskii and Glazmann [31].

In the screening mechanism, charges composing the electron gas under perpendicular magnetic field rearrange themselves, screening an external electrostatic potential, lowering thus the total electrostatic energy of the system. The screening mechanism is observed only in regions of the 2DEG at partial filling of a Landau level, in which the density of states at the Fermi level is non-zero. On the contrary, regions of integer filling factor ν do not screen the external potential variations, since the Fermi level lies in the cyclotron gap, where the density of states vanishes. The screening ability of a 2DEG is usually introduced with the concept of compressibility of an electron gas, which is directly proportional to the rate of change of the charge density to

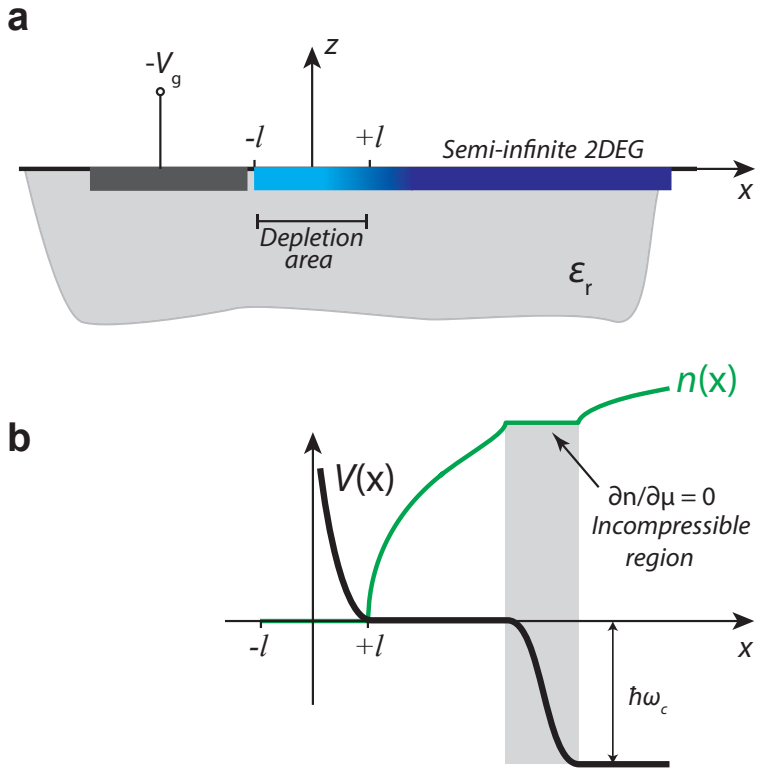

Figure 6.3: (a) Gate-induced boundary in a 2DEG. The negative voltage $-V_g$ creates a depletion area in the semi-infinite 2DEG plane. (b) Generation of an incompressible region close to the edge of the semi-infinite 2DEG, at bulk filling factor $\nu = 1.5$. The electron density $n(x)$ and the electrostatic potential profile $V(x)$ are plotted together. The gray-shaded area represent the incompressible region where $\partial n/\partial \mu = 0$. Inspired from [31].

variations of the local chemical potential: $\chi \propto \partial n/\partial \mu$. If the Fermi level is inside a cyclotron gap, the absence of available states does not allow any screening, and therefore the system is incompressible, with $\partial n/\partial \mu = 0$. Conversely, if the Fermi level lies inside a Landau level, the system turns compressible and screens the external potential.

In the screening model proposed in Ref. [31], they considered a semiconductor 2DEG subjected to a lateral confining potential ($-V_g < 0$) from a nearby gate, creating a depletion region where the electron density is zero. The external potential is considered to vary smoothly at the scale of the magnetic length l_B. The schematic of the gated 2DEG is reported in Fig.6.3.a. At thermodynamic equilibrium, the electron density $n(x)$ is calculated self-consistently within the Thomas-Fermi approximation (form more details, see the work of Lier and Gerhardts [93]).

Generally, in the absence of magnetic field, the density of states of a 2DEG is constant, and therefore the chemical potential evolves linearly together with the electron density. However, in the quantum Hall effect the density of states shows Landau levels, and the chemical potential is obliged to increase step-like whenever a Landau level is filled. This effect is shown in Fig.6.3.b, where are represented both the electron density $n(x)$ and the gate-induced self-consistent electrostatic potential $V(x)$ on the semi-infinite 2DEG. The incompressible region at full Landau level filling, is represented by the electron density plateau where the electrostatic potential is not screened. In the adjacent compressible regions, electrons can re-arrange at the Fermi level, and can therefore screen the variations of the electrostatic potential which stays pinned.

The spatial evolution of compressible and incompressible regions, follows the local filling factor in the 2DEG. In the vicinity of a device boundary, when the electrostatic confining

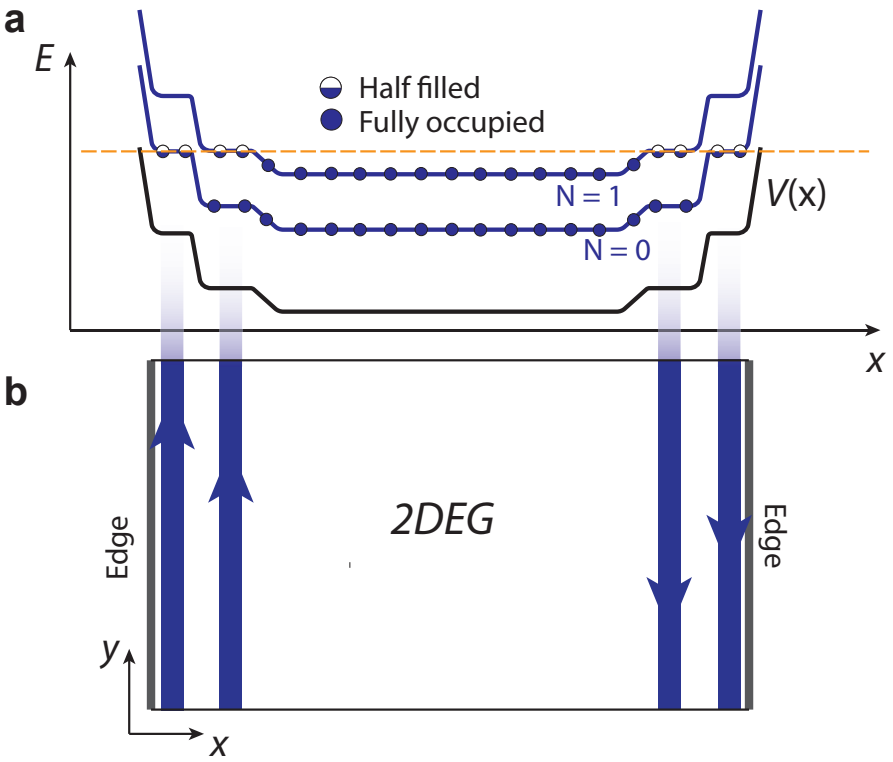

Figure 6.4: (a) Spatial evolution of the Landau levels and of the electrostatic potential $V(x)$ of a 2DEG under electrostatic confinement. Circles represent the local filling of the Landau levels. Compressible strips (edge channels) manage to screen the electrostatic potential $V(x)$. (b) Space distribution of edge channels for a given Fermi level E_F (orange dashed line). Edge channels form compressible strips separated by incompressible regions.

potential starts to grow, the Landau levels bend up until they cross the Fermi level E_F, with the formation of a compressible edge channel. In the region occupied by the edge channel, Landau levels are progressively emptied, with the local onset of strong screening. The compressible edge states acquire therefore a finite spatial lateral extension, as depicted in Fig.6.4. Compressible and incompressible regions form an alternate succession of parallel strips which distribute along the sample edges.

It is worth to mention that the model of edge-state reconstruction proposed in Ref. [31], was introduced for semiconductor 2DEGs, having smooth confining potentials. In graphene, reconstruction processes under electrostatic-induced boundaries were observed via scanning tunnelling microscopy [60] and Kelvin probe force microscopy [80]. However, the electrostatic reconstruction on the physical edges of pristine graphene flakes is an ongoing debate, and no experimental evidences have been published so far.

Charge accumulation at the edges Another physical effect that can alter the conventional picture of the quantum Hall edge states in graphene, is the formation of regions of electrostatic charge accumulation at the physical edges of a graphene system. This electrostatic effect was developed in the theoretical paper of Silvestrov and Efetov [129]. In this article, they described the screening of the potential generated by a highly-doped silicon backgate, on a graphene ribbon, separated from the silicon gate by 300 nm of SiO_2.

Via the ambipolar field effect, the application of a voltage on the backgate induces charge carriers in the graphene layer. In the electrostatic calculations, the image charges generated by the graphene charges below the Si/SiO_2 interface, create an electric which partially screens the backgate field. The relatively large distance between the image charges and the graphene strip is responsible for a local fringing field, causing charge accumulation along the boundaries of the micron-sized graphene sheet. This nonmonotonic charge arrangement is particularly important in the quantum Hall effect, since it can lead to the formation of unexpected additional edge states close to the physical edges. Therefore, instead of having compressible edge states propagating along an edge in a single direction, the edge accumulation can induce both upstream and downstream modes on the same edge, separated from each other by a narrow incompressible strip having few-hundred nanometers thickness.

The reduced physical separation between counterpropagating edge modes undermines the fundamental mechanism of quantum Hall topological protection, and it has been already invoked in a few local probe experiments involving scanning microwave impedance microscopy [41], and scanning gate microscopy [97, 107]. A detailed explanation on the edge accumulation process under the presence of edge disorder, is given in the supplementary material provided in Ref. [107].

6.1.3 The impact of disorder

Charge inhomogeneities impact on the level spectrum under magnetic field, but allow for the observation of the quantum Hall plateaus in transport measurements. This disorder modifies the shape of the Landau levels composing the density of states, broadening the final appearance of the peaks, with extended states in the centre and localized states around (see Fig.6.5.a). If the Landau levels broadening is greater than the cyclotron gap, with the extended states which overlap in the successive Landau levels, then the system turns into the Shubnikov-de Haas regime, where the longitudinal resistance oscillates but never goes to zero at integer filling factor. However, as long as the extended states do not overlap, the quantum Hall regime is preserved.

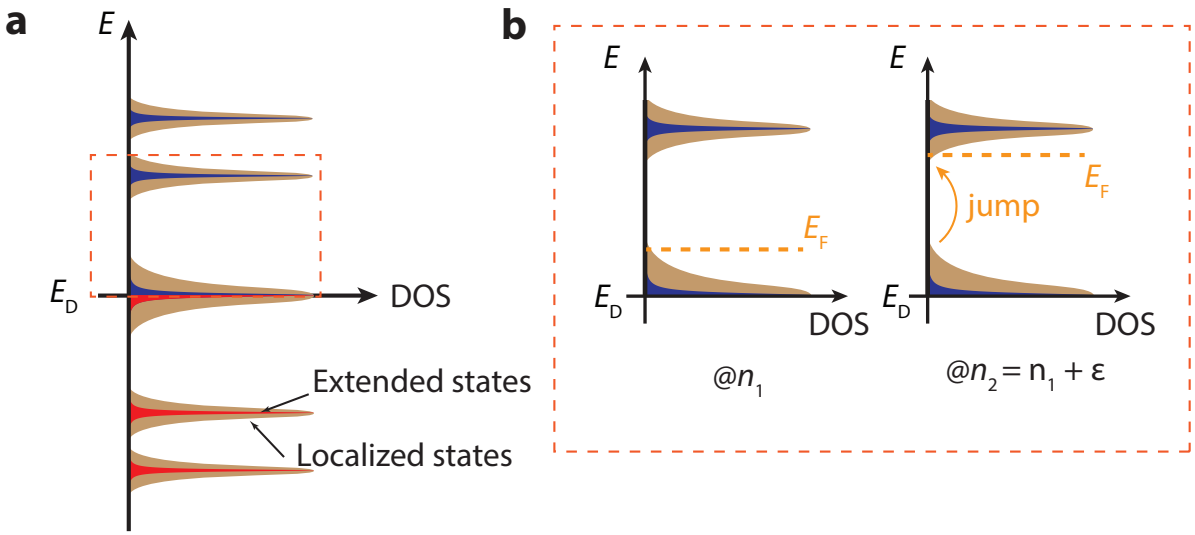

Figure 6.5: (a) Graphene density of states (DOS) under the presence of charge disorder introducing level broadening. In the quantum Hall regime, the extended states of the Landau peaks are fully separated with the DOS falling to zero inside a cyclotron gap in the case of weak disorder. (b) When the Fermi level is located exactly at the last localized state of a Landau level, due to the absence of available states in the gap, a slight increase of the electron density would require a jump of the Fermi level in the next Landau level.

Disorder manifests as a series of randomly distributed hills and valleys of potential fluctuation, which modifies the flat bands in the bulk. Whenever these fluctuations cross the Fermi level, they form a collection of localized closed orbits in the bulk. An overview of the filling of localized states is reported in Fig.6.5.b in the case of weak disorder. In the left drawing, where the Fermi level initially lies exactly at the last upper localized state of the Landau level $N = 0$. When the charge density in the graphene plane is slightly increased, the Fermi level jumps directly into the lowest localized state of the Landau level $N = 1$. The energy jump is required since no state is present inside the cyclotron gap.

In order to visualize the space distribution of the localized states during the filling of a Landau level, we can focus our attention on the illustration of Fig.6.6. In Fig.6.6.a, because of the spatial fluctuations of the bulk energy levels, the intersection between the Landau level $N = 1$ and the Fermi level, generates the filling of a few localized electronic states in the bulk. These localized electrons are trapped in isolated closed contours at isopotential, and therefore do not contribute on the conduction process. Conversely, the edge channels coming from the level $N = 0$ form extended states distributed along the whole edges of the sample, and therefore contribute to the electrical transport.

If the Landau level $N = 1$ is gradually filled, the amount of populated localized states in the bulk increases in quantity and size. In macroscopic devices, the spatial extensions of localized states are usually described via a length scale parameter called the *correlation length* ξ_p, which increases faster when the Fermi level approaches the middle of a Landau level [47]. Close to the half filling of $N = 1$, the ξ_p parameter reaches a value so high that localized states start to form large clusters of joint localized states, which merge together through isopotential lines connected by saddle points [132]. An example of bulk percolation is represented in Fig.6.6.b. In this condition, there is one main conductive state (light blue line) connecting the two sides of the sample, breaking the topological separation between the counterpropagating edge channels, and causing backscattering.

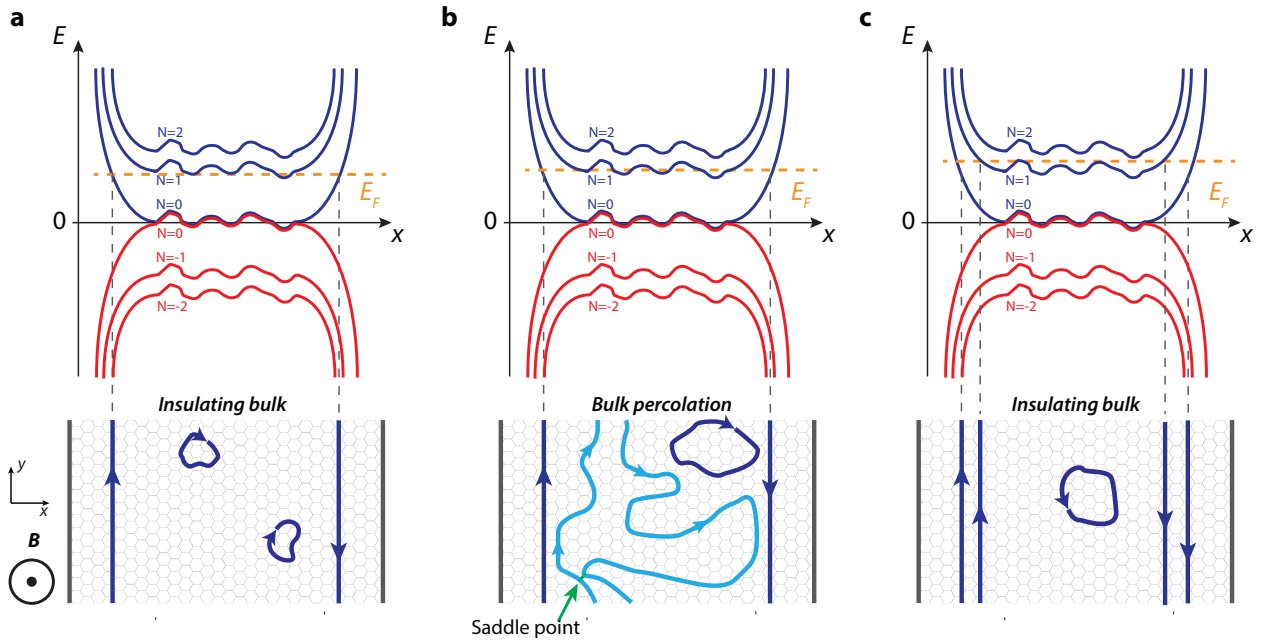

Figure 6.6: Schematic of the Landau levels in the presence of disorder and the corresponding edge channels in the sample. (a) The Fermi level allows the filling of the first localized states of the $N = 1$ Landau level. (b) The Fermi level is almost in the middle of the Landau level. One extended state percolates in the bulk, connecting both sides of the sample and giving rise to backscattering at the saddle point (green arrow). (c) The Landau level $N = 1$ is almost full, but a localized antidot remains in the bulk.

Quantum Hall percolation According to the classical theory of quantum Hall percolation, the correlation length $\xi_{\rm p}$ is a parameter that depends intrinsically on the random background potential generated by the disorder. For any slowly varying background potential, the correlation length diverges when the Fermi level $E_{\rm F}$ approaches a critical energy $E_{\rm c}$ which is close to the centre $E_{\rm N}$ of the Landau level band. This transition from insulating to percolating bulk is usually described via the power law

$$\xi_{\rm p} \propto |E_{\rm F} - E_{\rm c}|^{-\gamma_{\rm p}} \tag{6.6}$$

where $\gamma_{\rm p} = 4/3$ is a universal critical exponent for ideal macroscopic quantum Hall systems [47]. The whole classical percolation theory holds for non-interacting carriers in a slowly varying potential evolving on a length scale λ, satisfying the condition $\lambda \gg l_{\rm B}$, where $l_{\rm B}$ is the magnetic length. The inequality allows us to consider two decoupled components of charge carrier motions in the quantum Hall regime: the rapid dynamics associated to the cyclotron frequency ω_c, and the slow drift of the orbit guiding centre with velocity v_g which follows equipotential lines of the quantum Hall system [27]. The equipotential lines can host extended eigenstates at specific critical energy $E_{\rm c} = E_{\rm N} + V_0$, where V_0 is a particular value of the disorder distribution $V(x, y)$. From a microscopic point of view, when the Fermi level approaches the critical energy, the localized-state clusters grow in size and merge together via saddle point of potentials, extending across the entire system. The extended state thus formed, determines the onset of dissipative transport in the whole sample, since carriers are allowed to move from one sample edge to the opposite one.

This classical theory treats the quantum Hall transitions, from quantized to dissipative regimes, as a classical phase transition, with one single universal critical exponent for macroscopic devices. However, in 1983 Trugman pointed out that the classical theory was neglecting

tunnelling between close by clusters, having isopotential contours slightly separated on the scale of the magnetic length l_B [144]. Chalker and Coddington reviewed this classical picture, introducing quantum tunnelling mechanisms at the onset of the classical percolation [27]. In particular, they showed that before the merging of two neighbouring localized clusters, a series of quantum tunnelling processes are activated at the points of closest distance, still represented by saddle points in the disorder potential. An example of distributed percolation mechanism through quantum tunnelling in the bulk is reported in Fig.6.7.a, while the schematic of a tunnelling saddle point between to localized states is illustrated in Fig.6.7.b.

When the tunnelling process is included in a quantum Hall percolation model, the *localization length* ξ now describes the quantum coherent extension of electrons in the system. Under the presence of intrinsic disorder, the envelope of the wavefunctions associated to the localized states in the bulk are usually represented as decaying exponentials, localized to the extent of ξ [18, 8]

$$|\psi(\mathbf{r})|^2 \propto exp(-|\mathbf{r}|/\xi) \tag{6.7}$$

For any value of the ratio λ/l_B, tunnelling processes between localized states exist but they are significant only for eigenstates having energies in a small range around the percolation energy. The width of this energy window increases as the ratio λ/l_B lowers [27]. This property open the possibility to observe weak tunnelling coupling between edge states in circumstances which are relatively far from the percolation condition. In narrow Hall bar geometries, these circumstances of tunnelling are much more probable than in macroscopic devices, as will be shown in the experimental part of the chapter.

Another contribution to the finite range of filling factors allowing tunnelling at the saddle points, is the electrostatic screening effect, which reconstruct the localized states into finite-width compressible states [35].

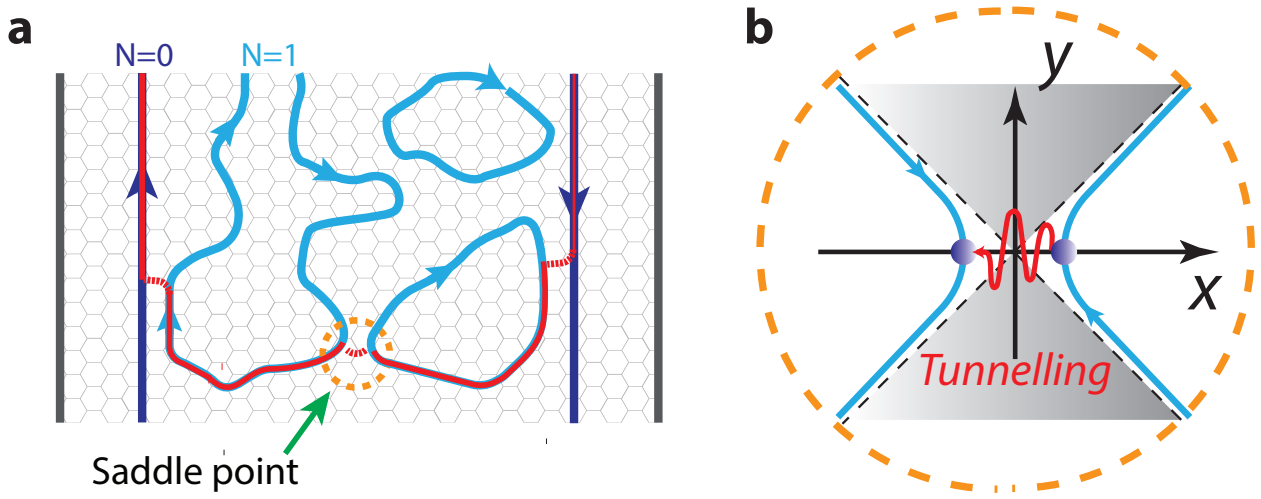

Figure 6.7: (a) Quantum tunnelling between localized bulk states, around dots for a Fermi level slightly below the energy of the N=1 Landau level. A beginning of a full percolation path through the bulk is shown in red. (b) The tunnelling between localized states manifests around saddle points of the disorder potential, where the localized states are at the closest distance.

Coulomb interactions in localized states In the standard single-particle description of the integer quantum Hall effect, the electron-electron interactions in localized bulk states are often neglected. However, they are of fundamental importance for a complete description of the percolation mechanisms, since they can strongly impact on the backscattering processes. As opposed to extended electrons, localized electrons are confined to a small region of space determined by the localization length ξ [18, 8]. This Anderson localization is usually introduced with the decaying exponential function of Eq.6.7.

The gradual population of such a small localized state generates a series of jumps in the local electrostatic potential $U(\mathbf{r})$ which has been experimentally measured using a scanning single electron transistor (SET) in an 2D electron gas of GaAs [71] and on a graphene monolayer [98]. In the latter, they monitored the change in the local electrostatic potential, when modulating the graphene charge carrier density n with a backgate voltage, thereby measuring the quantity $\partial U(\mathbf{r})/\partial n$. At thermodynamic equilibrium, any change in $U(\mathbf{r})$ is equal in magnitude and opposite in sign to changes of the local chemical potential $\mu(\mathbf{r})$ in the graphene plane [1]. Therefore, with a scanning SET, it is possible to locally map $\partial\mu(\mathbf{r})/\partial n(\mathbf{r})$, the so-called inverse compressibility, which gives informations on the properties of the many-body density of state of graphene ($DOS \propto \partial n(\mathbf{r})/\partial\mu(\mathbf{r})$) in the quantum Hall regime and at the local scale.

An example of inverse compressibility map versus carrier density n and magnetic field B is reported in Fig.6.8.a, where a series of incompressible signatures define a rich pattern of fine structures parallel to the black lines at constant integer quantum Hall filling factor ν. Each line in the local compessibility map reflects the charging with a single electron of a localized

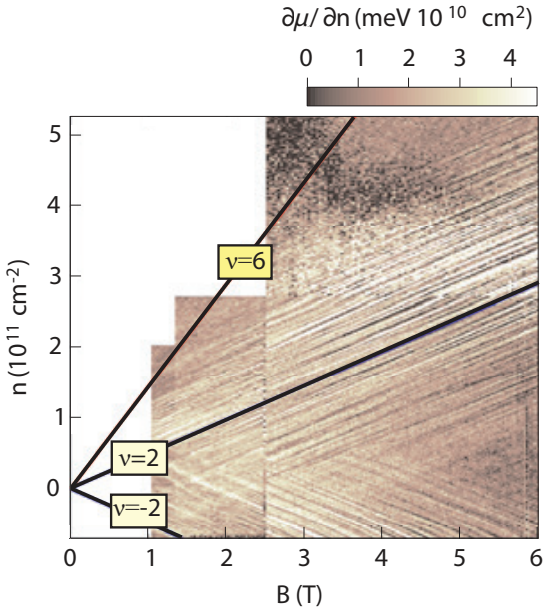

Figure 6.8: Colour map of the inverse compressibility as a function of the average carrier density and external magnetic field. Measurement is taken with a a scanning SET located above a graphene flake. Localized states appear in the map as dark lines running parallel to the thick lines of constant integer filling factor. Taken from [98].

[1] The Fermi level (alternatively the electrochemical potential), at thermodynamic equilibrium, is a constant and can be expressed as the sum of a local chemical potential $\mu(\mathbf{r})$, which accounts for both kinetic and interaction energies per particle, and a local effective single-electron potential $U(\mathbf{r})$: $E_F = \mu(\mathbf{r}) + U(\mathbf{r}) = constant$. Therefore we can infer that $\partial U(\mathbf{r})/\partial n = -\partial\mu(\mathbf{r})/\partial n$.

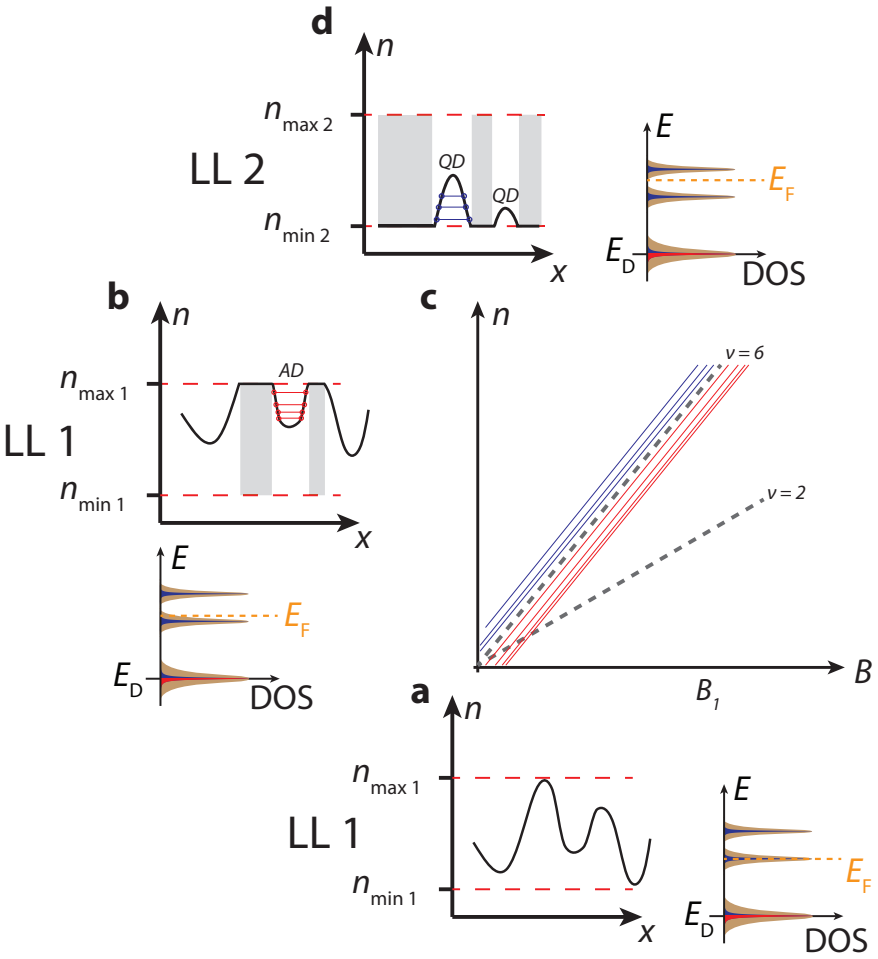

Figure 6.9: Schematic of the behaviour of localized states in the presence of Coulomb repulsion. (a) When far from the integer filling factor condition, charge carriers can easily distribute in space, screening the non-uniform electrostatic potential. The values $n_{\min}$ and $n_{\max}$ represent the minimum and maximum density within a Landau level. (b) If the Landau level is almost filled, regions in the graphene layer become incompressible and only tiny compressible areas remains. These areas form quantum antidots (ADs) with energy spectra filling (red lines inside the AD) governed by charging effects. (c) Schematic explaining the signatures observed in the inverse compressibility map. Each localized state generates a line running parallel to the line of compete filling $\nu = \ 2, \ 6 \ldots$. (d) At filling values $\nu > 6$, the bulk shows compressible areas behaving as quantum dots (QDs), displaying similar signatures of their counterpart ADs. Image inspired from [98, 71, 100].

state in the close proximity to the SET [98]. The charging lines decorating the map and their parallel character can be understood considering the interplay between the disorder electrostatic potential, and the localized charge reorganization in the bulk of graphene, which is driven by repulsive Coulomb interactions.

In order to grasp the localization mechanism driven by Coulomb interaction, I present the schematic of Fig.6.9, which allows to interpret the signatures in the previous inverse compressibility map. The filling of a Landau level (LL) requires a comprehensive amount of charge carrier Δn_{LL} given by the expression

$$\Delta n_{\mathrm{LL}} = n_{\max} - n_{\min} = 4B/\phi_0 \tag{6.8}$$

Fig.6.9.a represents the density profile for the half-filling of LL $N = 1$. As already mentioned, when the Fermi level lies in the middle of a Landau level, the bulk density can easily adjust its spatial distribution in order to completely screen the fluctuating disorder potential. Each added electron is therefore experiencing a screened flat potential, populating a continuous amount of available bulk delocalized states, which are not detected from the inverse compressibility map.

However, as the density increases, the system gradually approaches the $\nu = 6$ condition. At this stage, there are regions in which the electron density completely fills the available states of the $N = 1$ LL, and therefore the local density saturates to the upper threshold value n_{max}, and fails to screen the local disorder potential. These regions are highlighted with grey shadowed regions in Fig.6.9.b and represent the insulating incompressible states in the bulk. The incompressible regions contour a series of compressible pockets, where the Landau level is not completely filled. Because of the finite sizes of these isolated compressible regions, they display a quite large charging energy. These compressible states behave essentially as the counterpart of a regular quantum dot (QD), and they are usually referred to as antidot (AD). As reported in Fig.6.9.c, once the charge density is sufficiently high, the localized states around the next LL $N = 2$ generate a series of narrow pockets of electron accumulation behaving as QDs which are governed again by Coulomb blockade physics.

The localization picture provided here allows to link the measured SET spectra to the depopulation of ADs from the almost-filled Landau level or to the filling of QDs belonging to the next Landau level. The Coulomb blockade mechanism is responsible for the number and intensity of charging lines (schematized in Fig.6.9.d), which do not depend on the magnetic

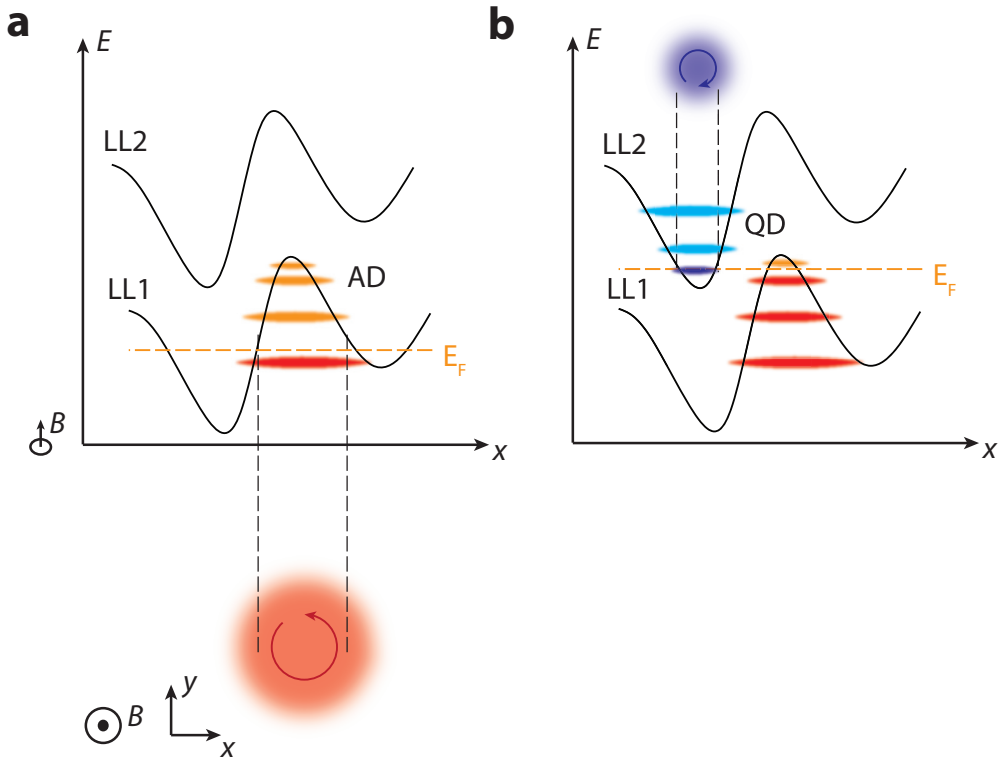

Figure 6.10: (a-b) Schematic representation of discrete single-particle states forming in a quantum antidot (quantum dot) in the landau level N=1 (N=2) in the bulk. Quantum Hall states form closed chiral orbits around the potential hills and valleys. The Fermi level position is placed at two different filling conditions of the localized states.

field. The slope of those lines is given only by the relation $\mathrm{d}n/\mathrm{d}B = \nu(N)\, e/h$, and are therefore parallel to the constant quantized slopes of the quantum Hall phases.

A graphical representation of both QD and AD in the bulk, with their relative discrete energy levels, is reported in Fig.6.10. In the line profile, the Fermi level is tuned and allows for the population of the discrete states available. According to the semi-classical picture, the electrons trapped inside QD and AD follow closed orbits and are physically separated by an incompressible cyclotron gap which limits the charge transfer between them to discrete Coulomb blockade resonances.

6.1.4 Quantum Hall transport properties

In 1980, von Klitzing and coworkers discovered the quantum Hall effect in a two dimensional electron gas under a high magnetic field [82]. In a Hall bar device (see Fig.6.11), they observed the presence of quantized plateaus of transverse resistance R_{xy}, occurring as function of the gate voltage, together with minima of zero longitudinal resistance R_{xx}. In 2005, transport signatures of the quantum Hall effect were observed for the first time in graphene by Novoselov and Geim [111]. The plateaus of transverse conductance appear at specific integer values of the quantum of conductance e^2/h.

$$G_{\mathrm{xy}} = \frac{e^2}{h}\nu(N) \tag{6.9}$$

The values taken by the filling factor on the plateaus depends by the 2D electron system involved, and in the graphene case it takes the characteristic values $\nu(N) = \pm 2(2N+1)$. The quantized transport regime is observed when the Fermi level lies in the cyclotron gap between two adjacent Landau levels (see Fig.6.12). On the contrary, if the Fermi level is in the middle of a Landau level, bulk states extend in the sample causing backscattering processes which are measured as deviations from the quantized plateau values.

It is worth to mention that disorder has a crucial role in the formation and robustness of the quantum Hall plateaus. Since the Fermi level is always pinned on the highest occupied state, in the absence of disorder a slight change in the carrier density from an external gate or a variation of the magnetic field would cause the Fermi level to jump from one Landau level directly to the next one without the appearance of quantum Hall plateaus.

The plateau formation goes along with the ideal dissipation-less transport inside a Hall bar. In this quantized regime however, dissipation is always intrinsically present. In particular, by measuring the two-terminal resistance within the current biased contacts in Fig.6.11, we can directly measure a Hall resistance $R_{\mathrm{xy}} = V_{\mathrm{xy}}/I$, confirming the dissipation of an electrical power

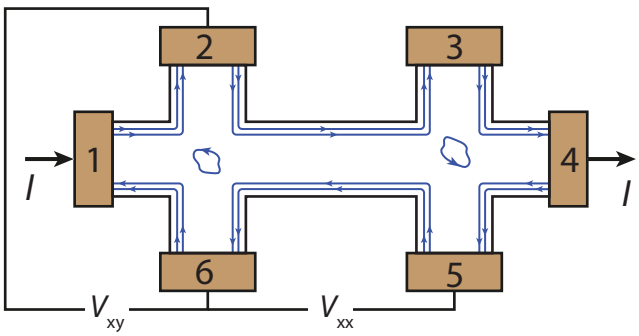

Figure 6.11: Schematic of a Hall bar device.

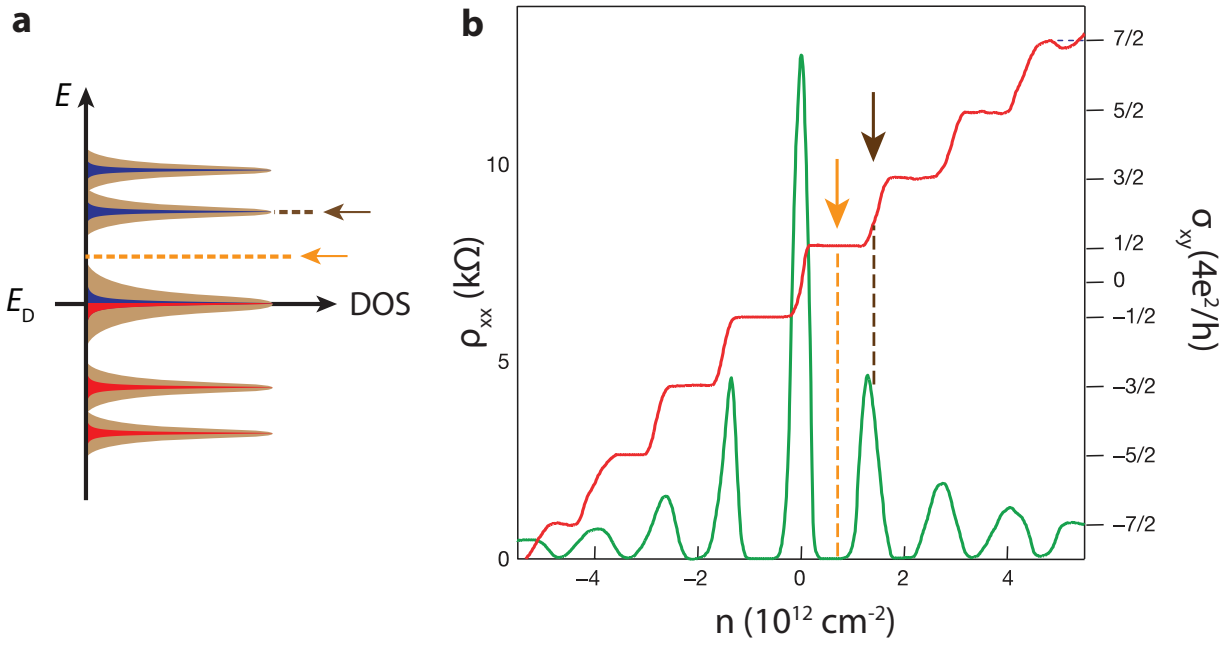

Figure 6.12: (a) Graphene density of states (DOS) under high magnetic field. (b) Hall conductivity σ_{xy} (red) and longitudinal resistivity ρ_{xx} (green) of graphene as a function of charge carrier density n at $B = 14$ T and $T = 4$K. The transverse conductivity exhibits quantized plateaus following the sequence given by Eq. 6.9, while the longitudinal resistivity simultaneously drops to zero. Taken from [111].

$|R_{xy}|I^2$. The heat is usually developed within hot spots located in the proximity of the current biased contacts, but not along the sample thanks to the presence of the celebrated topological protection. Dissipation along the sample can manifest whenever the longitudinal resistance $R_{xx} = V_{xx}/I$ becomes non-zero, i.e. at the transitions between different quantum Hall phases [148]. During the transitions, when the Fermi energy is at a density of states maximum, transport becomes dissipative with the innermost quantum Hall edge channel percolating through the whole sample. During the percolation, charge carriers experience backscattering processes, making their way from one edge of the device to the other, returning back into the contact of current injection.

6.2 Probing backscattering in mesoscopic Hall bars

Electron transport in the integer quantum Hall regime is often explained with a simple picture of non-dissipative one-dimensional chiral edge channels circulating around a two-dimensional electron system submitted to a perpendicular magnetic field. This scholastic viewpoint conflicts with the theory presented at the beginning of this chapter. There are a series of theoretical arguments which alter significantly this simple description such as, for instances, the complex electrostatic screening induced by electrons occupying highly-degenerate Landau levels. The resulting spatial carrier distribution in a real quantum Hall system is therefore much more subtle than in the naive edge-state picture. The consequence is that electron transport in such a reconstructed potential is a complex distribution of current flows, not only at the edges, but everywhere the residual disorder or external gates make the electrostatic potential not flat.

Interestingly, the celebrated topological protection in the quantum Hall regime is experimentally obtained only in the limit of large devices where backscattering through the bulk is exponentially suppressed. In a mesoscopic device however, when the percolation length is larger than the physical separation between the edges at any filling factor, this protection fails and backscattering currents are observed even at integer filling factors [130, 52, 57, 137]. Whereas early studies analysed the percolation process at plateau transitions in macroscopic Hall bars, the development of scanning probe experiments allows nowadays spatial investigations of carrier density and current flows at the microscopic scale. Scanning gate microscopy (SGM) is a suitable technique to probe electron systems buried a few tens of nm inside heterostructures. It has been used to investigate the quantum Hall effect in semiconductor 2DEGs [151, 9, 61, 116, 114, 102, 103, 118, 138] and graphene devices [34, 32, 19, 97, 107].

In this section, I will explain the backscattering mechanisms in mesoscopic samples and their spatial investigation by SGM. These mechanisms rely specifically on quantum antidots belonging to the Landau level responsible for the formation of current-carrying edge modes. It is important to point out that localized states behaving as quantum dots are not considered as a primary source of backscattering since, as presented in section 6.1.3, they typically originate from localized states belonging to higher Landau levels, and energetically decoupled from the edge modes via the cyclotron gap.

6.2.1 Backscattering in 2DEG devices

A detailed scanning gate investigation of the backscattering mechanisms in Hall bar devices was reported in the work of Paradiso *et al.* [114]. The authors successfully managed to manipulate the spatial position of the edge states in a GaAs Hall bar, via the application of a negative depleting tip voltage V_{tip}. They observed that the electrostatic perturbation of the tip can increase the coupling between counterpropagating edge states, inducing non-trivial backscattering events mediated by antidots (AD) in the bulk.

An example of backscattering map from Ref. [114] is reported in Fig.6.13.a (the Hall bar edges are contoured in black dashed line). In the picture, the backscattering process is represented by the spatial evolution of the source-drain conductance G_{T} displaying an unperturbed plateau at $G_{\text{T}} = 2e^2/h$. In the map, the conductance reduces when the tip approaches the middle region of the Hall bar, forming a series of lobes with contour lines depending on the disorder distribution in the device.

The modulus gradient $|\nabla G_{\text{T}}(x, y)|$ of the previous SGM map is reported in Fig.6.13.b, and highlights the presence of arc-shaped fine structures outside the central region of the Hall bar. These resonances disappear when approaching the middle region of the device, where the conductance G_{T} approaches the plateau value $G_{\text{T}} = e^2/h$. In the paper, the authors discussed about the origin of these resonances, showing their dependence as a function of both the magnetic field B and the tip voltage V_{tip}. They proposed a heuristic model for the interpretation of the SGM maps, where the resonances are represented by coherent Aharonov-Bohm interferences and/or Coulomb blockade resonances through bulk ADs participating in the backscattering mechanism. Coulomb diamonds in the tunnelling through quantum Hall antidots have been observed by SGM in Refs. [102, 103].

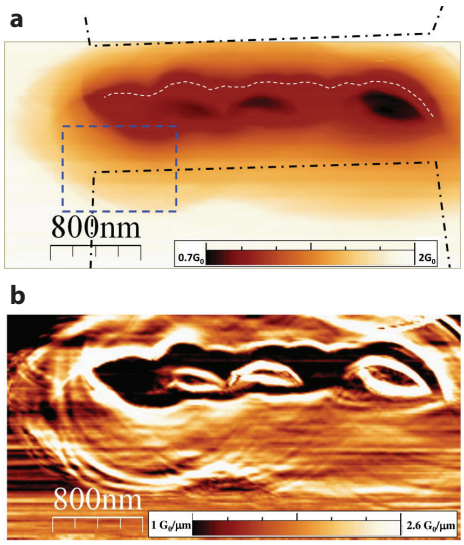

Figure 6.13: (a) SGM map of the source-drain conductance G_{T} unravelling the tip-induced backscattering in a GaAs Hall bar. (b) Modulus gradient of the conductance $|\nabla G_{\mathrm{T}}(x, y)|$, highlighting arc-shaped resonances in the SGM map. Taken from [114].

6.2.2 Imaging backscattering in graphene

Here I provide additional explanations of the above mechanism, based on the schematic of Fig.6.14.a, which refers to the geometry of a graphene sample studied experimentally in Section 6.4. In the schematic, I present the specific case of a graphene Hall bar characterized by two regions at different filling factors. The negative voltage ($V_{\mathrm{tip}} < 0$) applied on the SGM tip induces an extra upward shift of the electrostatic potential, depleting the graphene layer and thus locally changing the filling factor in the device. By moving the probe in space, it is therefore possible to manipulate edge channels with sub-nanometer resolution, and to bring them one by one in contact with the edge channels circulating on the opposite side of the sample.

In Fig.6.14.(b-d) is reported the energy of the electron LL $N = 0$ in the Hall bar, inside the yellow square of 1×1 μm^2 in Fig.6.14.a. The energy of the Landau level is influenced by the depleting Lorentzian potential of the tip, whose center position is located at the blue marker. In green are illustrated the edge states propagating around the area at integer filling $\nu_{\mathrm{Sg}} = 2$. Two fixed quantum antidots (AD1, AD2) in the bulk, have been introduced to depict the role of depleting impurities. Depending on the position of the SGM tip, the upper edge channel is more and more deflected toward the inner region at integer filling factor. In Fig.6.14.b, the tip position is still quite far from this region, but the reduced spacing of the incompressible regions between the edge states and the first antidot AD1 allows already a weak double-barrier tunnel coupling (white dashed lines). A tunnel current between the counter-propagating edge states via the antidot AD1 is usually referred to as indirect backscattering mechanism [114]. When the tip moves deeper into the integer filling factor area (Fig.6.14.c), it causes the merging of the upper edge state with AD1. The previous double tunnelling barrier configuration turns into a single tunnel barrier, generating thus a direct backscattering process between the edge states. At the same time, because of the physical proximity of AD2 with the edge modes, the activation of a second backscattering process develops across the Hall bar. Fig.6.14.d illustrates the maximum tip position before the complete pinch-off of the edge channel transmission from source to drain. Both AD1 and AD2 have merged with the upper edge state, and the physical

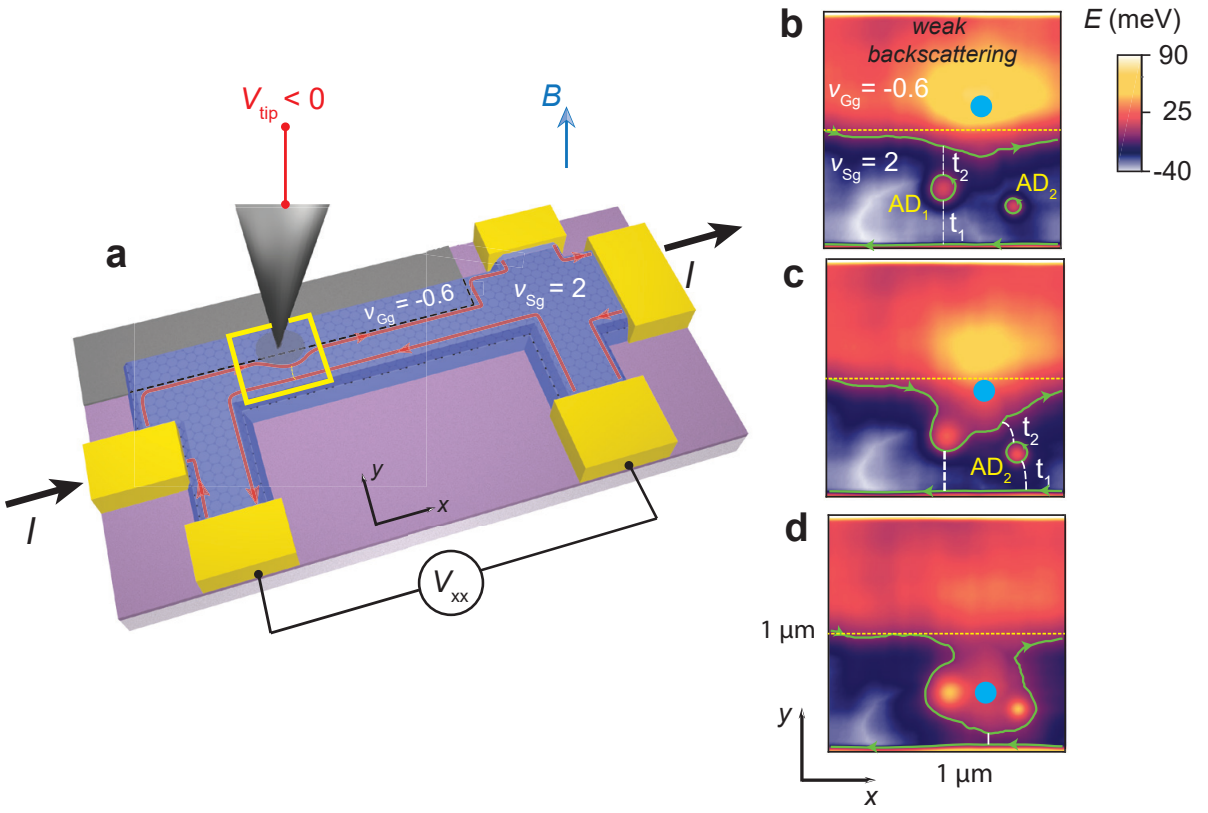

Figure 6.14: (a) Manipulation of the edge channels by the SGM tip in a device with two regions of different filling factors (see Section 6.4 for more details). The depleting tip voltage repels the upper electron channel, and approaches it toward the counterpropagating channel. (b-d) Representation of the electron Landau level (LL) N=0 within the yellow window in (a). The LL energy is depicted for three different tip positions, labelled with the blue marker and for a common depleting tip voltage described in the footnote here below[2]. Edge channel at the Fermi energy $E_F = 0$ meV (green lines) propagate around the region at filling factor $\nu_{Sg} = 2$ and interact with the antidots (AD) induced by the potential fluctuations in the bulk.

proximity between the counter-propagating modes produces an intense backscattering signal that can be detected as a strong uniform divergence of the longitudinal resistance.

Therefore, the SGM technique applied with the recording of the longitudinal resistance, enables to probe in space the backscattering events in a Hall bar, mapping in space the preferred spots of local percolation at which dissipation of the quantized transport takes place. In addition, the backscattering paths mediated by localized states are expected to give rise to interaction signatures in the measurement of the longitudinal resistance. In particular, the double tunnel barrier configuration of Fig.6.14.b can manifest Coulomb blockade effects on top of coherent Aharonov-Bohm oscillations [114, 130].

The SGM tip can cause two kinds of effects in space on the compressible states: (i) the tail of the tip potential can modulate the size of the localized states, tuning and detuning for instance the single-charge transfer through an AD in a double-tunnel-barrier configuration; (ii) the central part of the tip potential has a stronger influence on the carrier density and is thus

[2]The charge density variation induced by the tip voltage on the graphene layer is modelled as a Lorentzian distribution: $\Delta n_{\rm tip}(\mathbf{r}) = C_{\rm tip}V_0/e\ \frac{R_{\rm tip}^2}{R_{\rm tip}^2+||\mathbf{r}-\mathbf{r}_c||^2}$, where $C_{\rm tip} = 4.4$ nF/cm^2 is a lever-arm parameter, $V_0 = -10$ V is the tip voltage and $R_{\rm tip} = 150$ nm is the radius decay parameter of the Lorentzian.

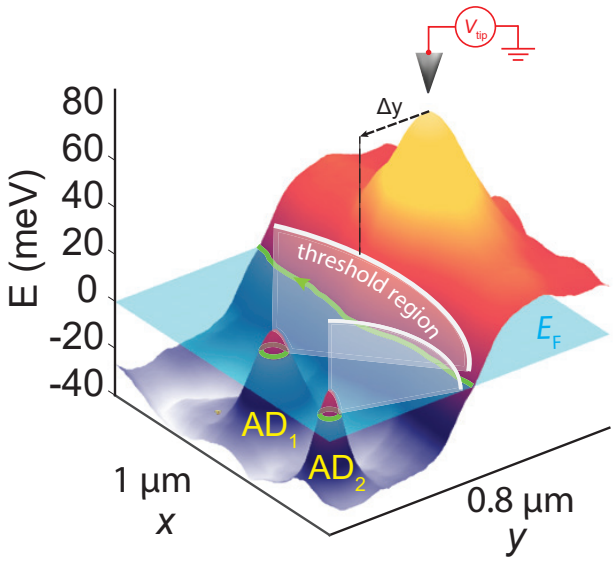

Figure 6.15: Illustration of the arc-shaped regions where the SGM can induce a percolation of an edge state into a localized state.

more involved in the edge states deflection and percolation mechanism.

While the first contribution manifests typically as resonances in R_{xx}, with a specific arc-shaped pattern, the second contribution appears as a smoothly space-dependent signal. Paradiso *et al.* [114] showed that the arc-shaped pattern of the R_{xx} signal corresponds to a spatial invariance of the tunnelling condition for a given radial distance of the tip with respect to the central location of the ADs. To illustrate this effect, I make use of the illustration in Fig.6.15, which represents a 3D view of Fig.6.14.b. In the figure, the tip is scanning along the y-axis, increasing locally the electrostatic potential. At some point, there is a threshold distance for which the tip forces the edge channel to merge with the AD1. Merging does not happen for a single tip position, but for a collection of positions composing the white arc in the illustration. A similar arc-shaped threshold condition can be found as well for the second antidot AD2.

6.2.3 Backscattering with charge accumulation at the edges

As introduced in 6.1.2, in back-gated graphene heterostructures, it is possible to obtain non-monotonic confining potentials at the edges. An example of this effect is reported in Fig.6.16.a, where the Landau levels are deformed according to the electrostatic accumulation close to one edge. Under this condition, it is therefore possible to have two different counterpropagating edge modes belonging to the same Landau level and separated by a narrow incompressible state. In the same figure there is a single localized AD which can mediate tunnelling processes between the edge modes. This indirect backscattering is represented in Fig.6.16.(b,c), where the electrostatic potential of the tip can initiate the charge transfer only if the Fermi level is aligned with the discrete energy levels in the AD. The charge tunnelling via the AD can manifest as a series of Coulomb blockade peaks in the longitudinal resistance, representing single-electron charge transfer between the counterpropagating edge modes.

The mechanism of AD-mediated backscattering at the edges is used in Ref. [107] to explain the SGM ring-shaped resonances observed along the edges of a back-gated and etched graphene heterostructure. However, the authors underline that the physical origins of the observed features are still not clear. The presence of atomic defects at the physical edges of graphene seems

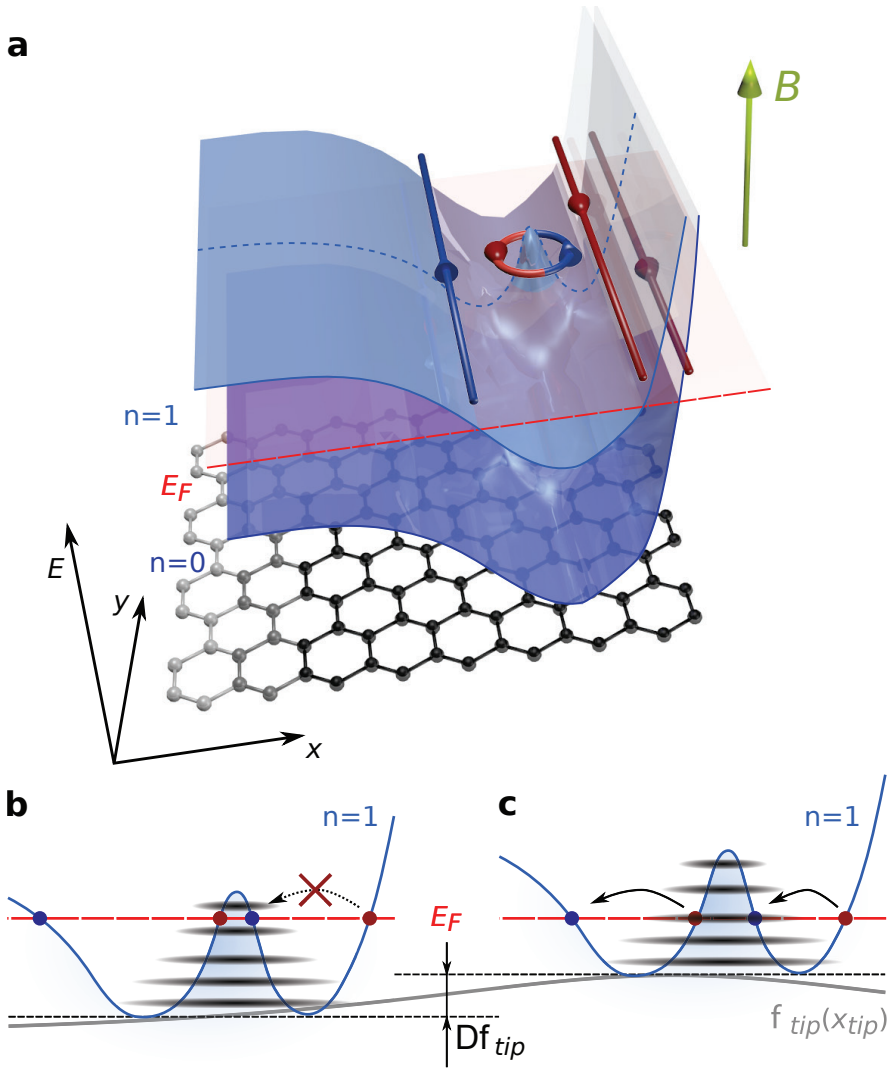

Figure 6.16: (a) 3D view of the two lowest electron Landau levels (LLs). Due to the edge electrostatics, the LLs are bent and the LL $N = 1$ crosses the Fermi level, generating two downstream edge channels (in red) and one upstream edge mode (in blue). An AD induced by a charge impurity is positioned between the counterpropagating channels. (b,c) Cross-section of the LL $N = 1$ showing the AD discrete energy levels and the edge modes with respect the Fermi level E_F, for two different electrostatic tip perturbation. When the edge modes are aligned with the AD energy levels, backscattering via resonant tunnelling occur. Taken from [107].

not to be the preferred hypothesis, since it is not evident how they could contribute electrostatically in the formation of similar electrostatic potentials. The observed ADs were located between 50 and 150 nm from the edges, which is quite far from the physical graphene edge. Other possible explanations could be: (i) the presence of strain fluctuations in the heterostructure, causing charge inhomogeneities in graphene [36]; (ii) the trapped carbon impurities in the flakes of hexagonal boron nitride employed in the graphene heterostructures [112].

6.3 SGM on a graphene n-p-n junction

In this section I present the SGM experimental results obtained on a graphene n-p-n junction in the quantum Hall effect. The first transport measurements on a graphene n-p-n junction in low mobility graphene were performed in the group of Philip Kim in 2007 [113], and later in high mobility graphene in the group of Goldhaber-Gordon in 2014 [5]. They observed the selective equilibration between edge channels at the electrostatic interfaces of the junction, when the four-fold degeneracy of the Landau levels is lifted.

In the following, I do not investigate with SGM the equilibration process at the interfaces, but I present some experimental data on the SGM imaging of the backscattering processes inside the n-p-n junction in the n-n-n isodensity condition. The reason to use a n-p-n junction is to reach a higher mobility in the central region thanks to an ultra-flat graphite bottom gate instead of the usual Si/SiO_2 substrate.

The sample is fabricated following the well established van der Waals pick-up technique, enabling the encapsulation of a graphene layer within two hexagonal boron nitride (hBN) flakes. The fabricated heterostructure is finally deposited on the top of a thin 4.5 μm-wide pristine graphite flake on a SiO_2 substrate. Suitable etching of the hBN(16 nm)/graphene/hBN(33 nm)/graphite(9 nm) structure, followed by a metal deposition process, allows to define six ohmic contacts with the graphene layer, on the edges of the heterostructure. Figure 6.17 shows the schematic of the n-p-n junction with the optical micrograph. The grey-coloured area in Fig.6.17.a represents the region of the device influenced by the graphite bottom gate, governing the local graphene filling factor ν_{Gg}. The densities in lateral regions of the junction are controlled by the silicon backgate, setting a filling factor ν_{Sg}.

The transport measurements are performed at the temperature $T = 1.5$ K, inside a VTI ^{4}He cryostat. The characteristic mean free path in the graphene flake is 1.8 μm, with mobility of 360 000 $cm^2V^{-1}s^{-1}$ at a charge carrier density of $n \sim 2.2 \times 10^{11}$ cm^{-2}.

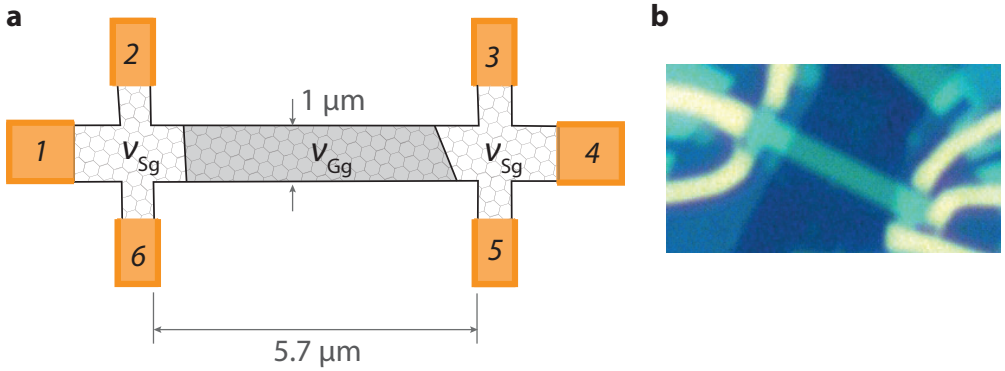

Figure 6.17: (a,b) Schematic and optical micrograph of the measured n-p-n junction defined in a graphene heterostructure. In the schematic, the ohmic contacts are labelled with numbers.

6.3.1 Equilibration in n-p-n junctions

According to the theoretical framework of ballistic chiral edge channels, as represented in Fig.6.18.a, the total number of injected edge channels is M. Due to the electrostatic influence of the central backgate, N channels are transmitted and $M - N$ are backscattered.

According to the filling factors in the junction, the following cases are possible:

- The polarities in the two regions are the same ($n - n^{'} - n$ or $p - p^{'} - p$). According to Fig.6.18.b, if the filling factors in region A and C are greater than the one in B ($\nu_{Sg} > \nu_{Gg}$), then only ν_{Gg} number of channels would be transmitted through the region B, and the other channels would be backscattered. Conversely, if $\nu_{Sg} < \nu_{Gg}$, then ν_{Sg} channels would be transmitted through all the regions and the additional channels would circulate in region B, with carrier equilibration along the sample edges (see Fig.6.18.d).
- The polarities in the two back-gated regions are opposite ($n-p-n$ or $p-n-p$). Then in region A and C, edge channels turn clockwise with the same chirality, while it is opposite in region B since the direction of propagation depends on the polarity of the region. In this situation, different edge channels equilibrate along the junctions (see Fig.6.18.e)

The SGM characterization of the backscattering will be performed in the filling factors

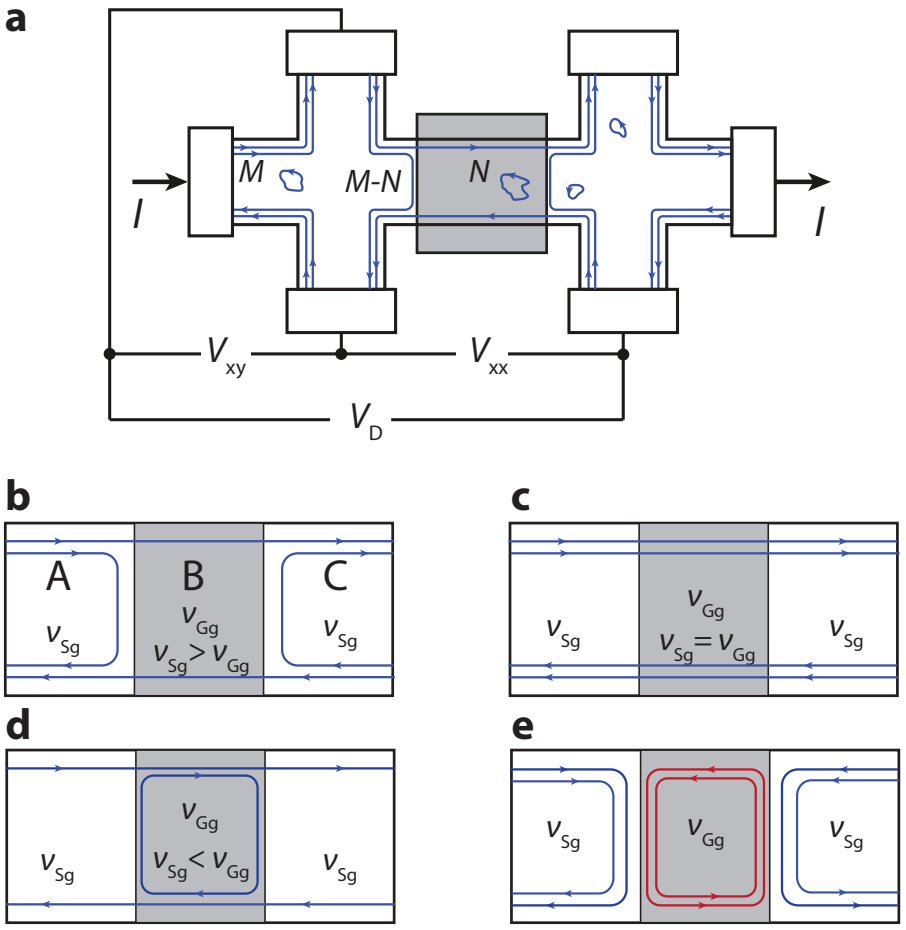

Figure 6.18: (a) Measurement set-up of a n-p-n junction in the quantum Hall regime. V_{xy} is the Hall voltage, V_{xx} the longitudinal voltage, V_D is the diagonal voltage. (b-e) A n-p-n junction displays three regions A, B, C. While A and C are described by a common filling factor ν_{Sg}, B is characterized by the filling factor ν_{Gg}. According to the values of the filling factors, different transport regimes are attained: (b,c) Edge state transmission regime: $\nu_{Sg} \cdot \nu_{Gg} > 0$ and $|\nu_{Sg}| \geq |\nu_{Gg}|$. (d) Partial equilibration regime: $\nu_{Sg} \cdot \nu_{Gg} > 0$ and $|\nu_{Sg}| < |\nu_{Gg}|$. (e) Full equilibration regime $\nu_{Sg} \cdot \nu_{Gg} < 0$.

Table 6.1: Longitudinal, diagonal and Hall resistances for different filling factors conditions of a n-p-n junction.

Filling factors	R_{xx}	R_D	R_{xy}
$\nu_{Sg} \cdot \nu_{Gg} > 0, \quad \lvert\nu_{Sg}\rvert \geq \lvert\nu_{Gg}\rvert$	$\frac{h}{e^2}\frac{\lvert\nu_{Sg}\rvert-\lvert\nu_{Gg}\rvert}{\lvert\nu_{Sg}\rvert\cdot\lvert\nu_{Gg}\rvert}$	$\frac{h}{e^2}\frac{1}{\lvert\nu_{Gg}\rvert}$	$\frac{h}{e^2}\frac{1}{\lvert\nu_{Sg}\rvert}$
$\nu_{Sg} \cdot \nu_{Gg} > 0, \quad \lvert\nu_{Sg}\rvert < \lvert\nu_{Gg}\rvert$	$\frac{h}{e^2}\frac{\lvert\nu_{Gg}\rvert-\lvert\nu_{Sg}\rvert}{\lvert\nu_{Sg}\rvert\cdot\lvert\nu_{Gg}\rvert}$	$\frac{h}{e^2}\frac{2\lvert\nu_{Gg}\rvert-\lvert\nu_{Sg}\rvert}{\lvert\nu_{Sg}\rvert\cdot\lvert\nu_{Gg}\rvert}$	$\frac{h}{e^2}\frac{1}{\lvert\nu_{Sg}\rvert}$
$\nu_{Sg} \cdot \nu_{Gg} < 0$	$\frac{h}{e^2}\frac{\lvert\nu_{Sg}\rvert+\lvert\nu_{Gg}\rvert}{\lvert\nu_{Sg}\rvert\cdot\lvert\nu_{Gg}\rvert}$	$\frac{h}{e^2}\frac{2\lvert\nu_{Gg}\rvert+\lvert\nu_{Sg}\rvert}{\lvert\nu_{Sg}\rvert\cdot\lvert\nu_{Gg}\rvert}$	$\frac{h}{e^2}\frac{1}{\lvert\nu_{Sg}\rvert}$

condition $\nu_{Sg} = \nu_{Gg}$ (see Fig.6.18.c), achieving thus a homogeneous propagation of edge channels throughout the device, without equilibration processes. The different configurations can be identified during the experiment by measuring the resistance and comparing its value with the equations given in Table 6.1 for the longitudinal, diagonal, and Hall resistances [113]. Such equilibration processes in n-p-n junctions have been observed by SGM in a graphene Hall bar [19] using the tip as the central gate of the junction.

6.3.2 Polarity regimes at zero field

At zero magnetic field, carrier densities in the junction are controlled by the two independent gate voltages: the silicon backgate voltage V_{Sg} and the graphite backgate voltage V_{Gg}. According to the relative signs of the local electron densities (n_{Sg} and n_{Gg}) it is possible to define four different physical regimes which are summarized in Fig.6.19.a.

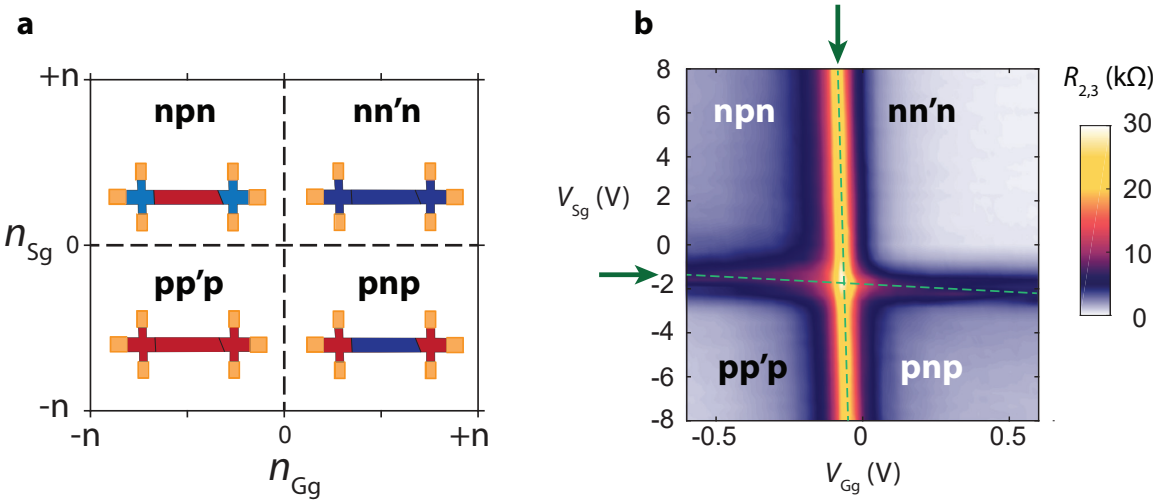

Figure 6.19: (a) Subdivision of the physical regimes in a gate-tunable graphene n-p-n junction. According to the relative signs of the electron densities in the three regions, we can identify 4 different operating conditions. (b) Four-wire measurement of the longitudinal resistance at zero magnetic field and $T = 1.5$ K, highlighting the four operating regions of the junction, separated by the charge neutrality conditions along the green dashed lines.

In order to identify the charge neutrality points in the three regions of the n-p-n junction, we characterize the dependence of the longitudinal resistance versus the gates voltages, by current-biasing the device with 30 nA between contacts 1 and 4, at zero magnetic field. The four-wires measurements of the longitudinal resistance $R_{2,3}$ is reported in Fig.6.19.b. The charge neutrality conditions for both the graphite and silicon regions are highlighted with a pair of green dashed lines along the maxima in the 2D plot. Since the graphite bottom gate is extended over a large device area, we expect a strong influence of the V_{Gg} voltage on the overall resistance. This is confirmed by the much larger resistance values at the charge neutrality conditions of the graphite-gated region. The tilts of the green dashed lines can be speculated as a mutual electrostatic coupling between the graphite and silicon gate.

6.3.3 Filling factors in the quantum Hall regime

At the magnetic field $B = 5.3$ T, in order to determine the operating point where electron edge channels are fully transmitted at the interfaces, without backscattering, nor equilibration, it is necessary to characterize the filling factors ν_{Sg} and ν_{Gg} via the measurements of both the Hall conductance G_{xy} and the longitudinal resistance R_{xx}. These two quantities are represented by the conductance $G_{2,6}$ and resistance $R_{2,3}$ defined in Fig.6.17. The measurements are reported in Fig.6.20, for V_{Sg} and V_{Gg}, within the n-n'-n density quadrant.

The Hall conductance provides information about the filling factor ν_{Sg} in the silicon-gated region. By comparing the measured resistance with the theoretical equations provided in table 6.1, it is possible to identify the regions at integer filling factors in the 2D maps. In particular, in Fig.6.20.a there is an evident horizontal strip of uniform conductance, representing a plateau of at filling factor $\nu_{\mathrm{Sg}} = 2$.

Interestingly, by performing a line cut from this 2D map (Fig.6.21), we can notice the presence of a tiny plateau at filling factor $\nu_{\mathrm{Sg}} = 1$, which indicates that the degeneracy of the electron Landau level N=0 is partially lifted thanks to the high mobility of the device.

Concerning the longitudinal resistance R_{xx} map in Fig.6.20.b, the contoured plateau at almost zero resistance indicates the condition $\nu_{\mathrm{Sg}} = \nu_{\mathrm{Gg}} = 2$, where the carrier density along the Hall bar is almost uniform, and the transitions from one device segment to another do not cause any backscattering.

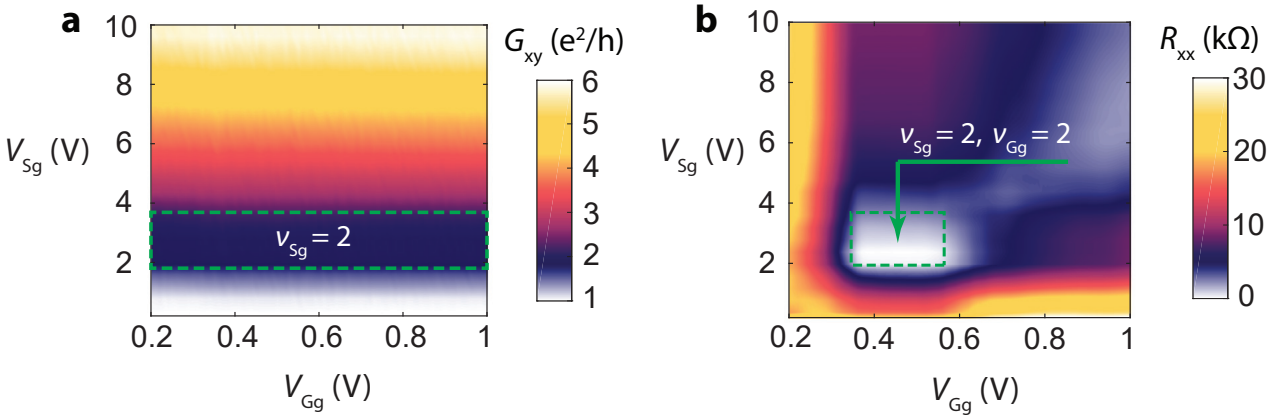

Figure 6.20: (a) Hall conductance map of the graphene junction measured in the silicon backgate region at 5.3 T. The quantum Hall plateau at $\nu_{\mathrm{Sg}} = 2$ is surrounded with a green dashed line. (b) Map of the longitudinal resistance. The extended region at zero resistance inside the green dashed line represents a plateau condition at $\nu_{\mathrm{Sg}} = \nu_{\mathrm{Gg}} = 2$.

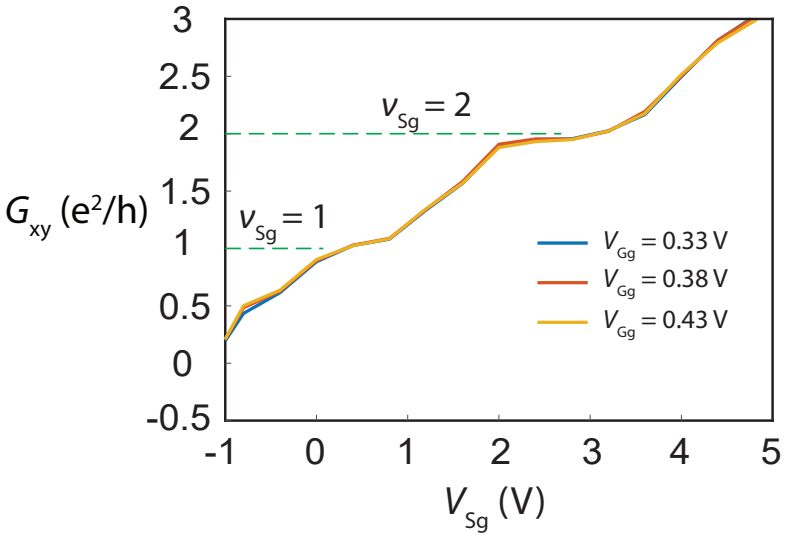

Figure 6.21: Several line-cuts of Fig.6.20.a, highlighting the positions of the plateaus $\nu_{\mathrm{Sg}} = 1$ and $\nu_{\mathrm{Sg}} = 2$.

6.3.4 Scanning gate mapping of backscattering

The SGM imaging of backscattering in the n-p-n junction was performed using the measurement setup of Fig.6.22.a. The longitudinal resistance R_{xx} is recorded in 4-wire configuration by standard lock-in technique at 1.5 K, using an AC voltage excitation $V_{\mathrm{in}} = 100\ \mu$V, at 17 Hz. The tip is positioned at a distance of 200 nm from the sample surface, scanning withing the yellow square in Fig.6.22.a, with a voltage $V_{\mathrm{tip}} = -10$ V. We recorded the backscattering for two different filling conditions in the graphite backgate region, indexed by the arrows inside the resistance plateau at $\nu_{\mathrm{Gg}} = 2$ in Fig.6.22.b. The plot was recorded for a silicon backgate voltage

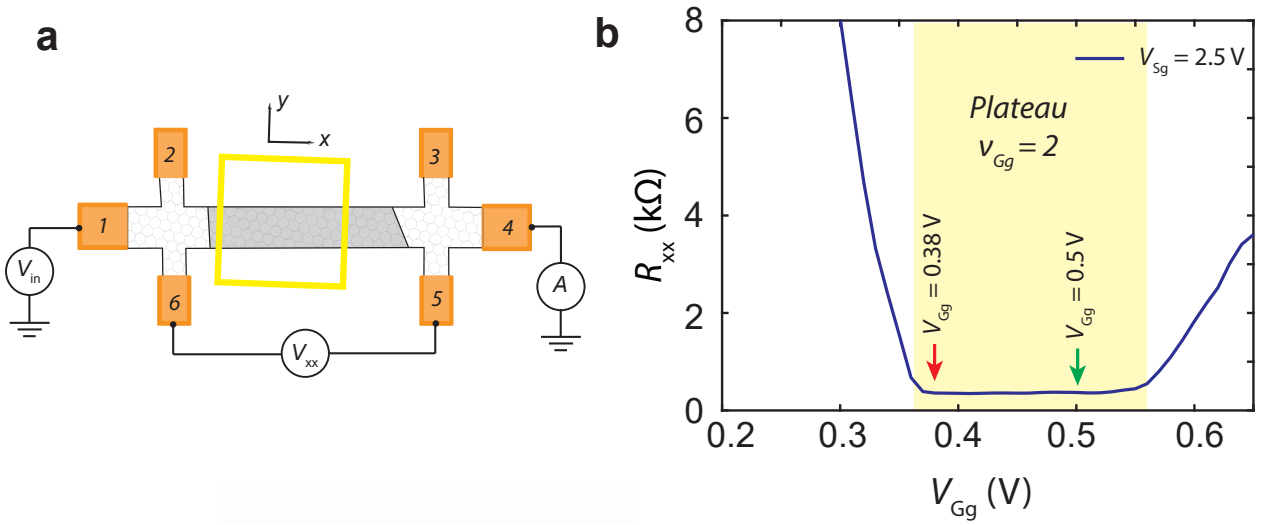

Figure 6.22: (a) Set-up for the 4-wire measurement of the longitudinal resistance R_{xx}. The yellow square of 3x3 μm^2 represents the SGM scan window. (b) Detail of the R_{xx} plateau at $\nu_{\mathrm{Gg}} = 2$, measured with a silicon bottom gate voltage $V_{\mathrm{Sg}} = 2.5$ V (corresponding to a filling $\nu_{\mathrm{Sg}} = 2$). Arrows represent the different voltage values V_{Gg} used for the SGM imaging of backscattering.

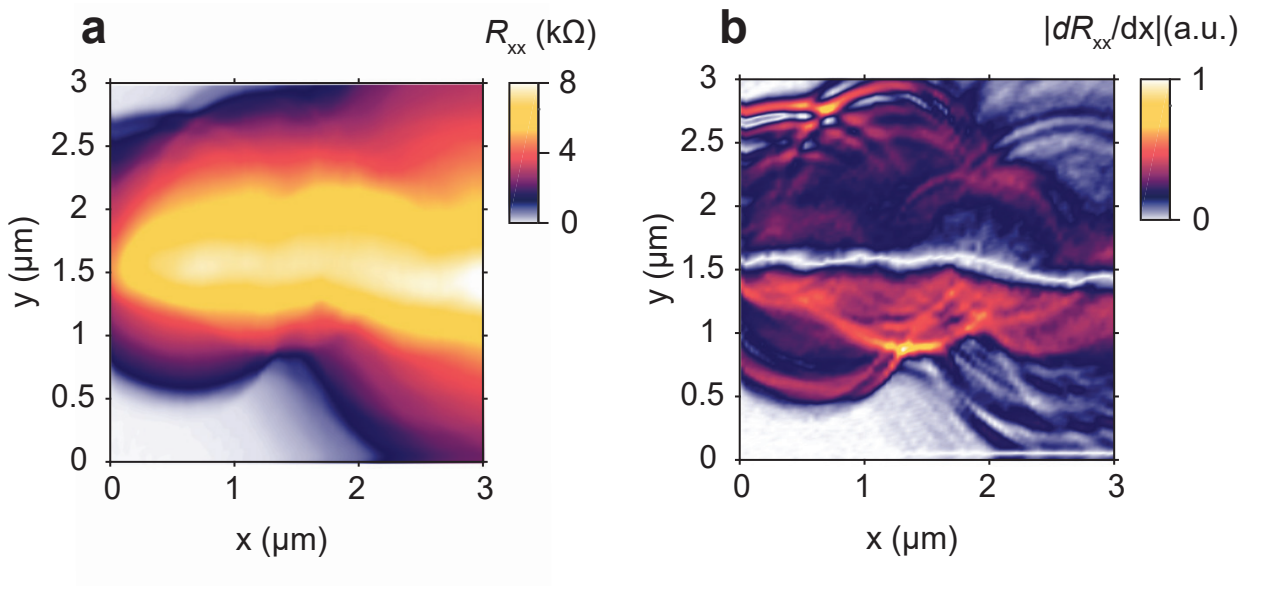

Figure 6.23: (a) SGM map of the longitudinal resistance R_{xx} showing marked signatures of quantum Hall backscattering. This image was recorded for $V_{Sg} = 2.5$ V and $V_{Gg} = 0.38$ V, at $B = 5.3$ T and $T = 1.5$ K. The tip was polarized at $V_{tip} = -10$ V. (b) The derivative of the SGM map reveals well defined arc-structures decorating the backscattering signal.

$V_{Sg} = 2.5$ to have $\nu_{Sg} = 2$ in the outer regions of the junction. The graph however shows that the longitudinal resistance is not perfectly zero in the plateau $\nu_{Gg} = 2$, indicating a residual backscattering in the outer regions. We realized after the SGM experiment that $V_{Sg} = 2.3$ V would have been the best value to reach exactly $\nu_{Sg} = 2$. Since the SGM maps were recorded in the central region only, this additional resistance from the outer regions will not influence the results.

The SGM map recorded at $V_{Gg} = 0.38$ V ($\nu_{Gg} = 1.6$), is reported in Fig.6.23.a. The SGM signal shows evident signatures of backscattering, with deviations from the zero-resistance in the quantum Hall plateau. Its derivative along the x-axis (Fig.6.23.b) allows to appreciate the fine structures composing the SGM map, putting in evidence the intricate arc-shaped pattern typical of AD-mediated backscattering. This backscattering signal closely recalls the pattern observed in [114] and previously discussed in Section 6.2.1 and 6.2.2. This SGM map was recorded in a specific condition, at the very beginning of the quantum Hall plateau $\nu = 2$, in correspondence of a percolation threshold of the Hall bar. In such situation, the bulk localized states of the $N = 0$ Landau level are barely separated from the edge channels, with narrow incompressible states preventing any charge exchange between the edge modes through the bulk. The negative voltage of the tip undermines the already weak topological protection, locally breaking the quantized transport and causing charge exchange between the counterpropagating edge modes. Looking at the resistance maxima in the SGM map, it is possible to infer that the gating action of the tip was not sufficient to generate a complete pinchoff inside the graphite region which would induce about 20 kΩ as seen in 6.20.b.

In order to show the strength of the topological protection against tip-activated percolating paths, I present here a SGM map recorded in the middle of the plateau, far from the percolation threshold of the plateau edge. This SGM map recorded at $V_{Gg} = 0.5$ V ($\nu_{Gg} = 2.2$) is reported in Fig.6.24. As expected, in better quantization condition the backscattering signal is almost completely absent, confirming the improved topological protection inside the device. Only few weak spots in the Hall bar give rise to a small increase of the longitudinal resistance.

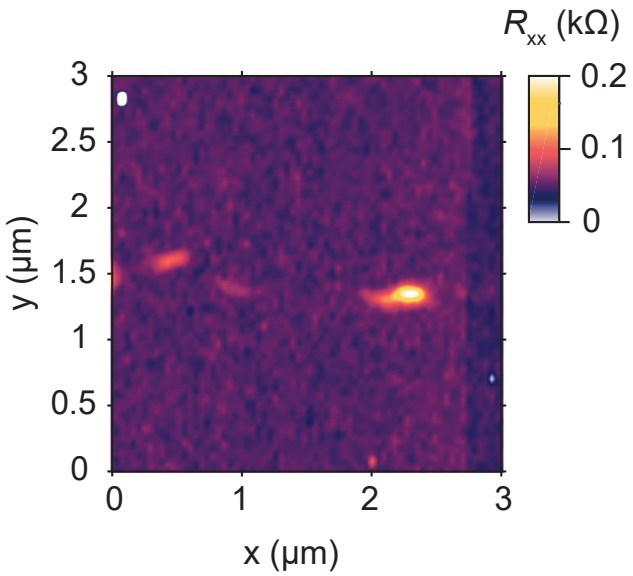

Figure 6.24: SGM map of R_{xx} showing a reduced quantum Hall backscattering at exact quantization. This image was recorded for $V_{\mathrm{Sg}} = 2.5$ V and $V_{\mathrm{Gg}} = 0.5$ V, at $B = 5.3$ T and $T = 1.5$ K. The tip was polarized at $V_{\mathrm{tip}} = -10$ V.

6.4 SGM study of the quantum Hall backscattering

In this section I report the experimental results obtained in a Hall bar fabricated on the same heterostructure as the previous n-p-n junction. The SGM backscattering signals show characteristic arc-shaped resonances witnessing resonant tunneling phenomena associated to an indirect backscattering mechanism involving localized states. The gating action of the tip is used to record a finite-bias spectroscopy diagram in the proximity of the arc-shaped resonances, obtaining marked signatures of Coulomb diamonds confirming the crucial role of charging effects in the percolation process between the chiral edge channels.

6.4.1 The Hall bar device

The schematic of the Hall bar with its measurement set-up is reported in Fig.6.25. In order to investigate the dependence of the backscattering process on the Hall bar width, a graphite backgate is placed under half of the graphene device. The application of a voltage V_{Gg} on the graphite bottom gate can tune the value of filling factor ν_{Gg} in one side of the Hall bar, independently to the device region directly posed over the silicon oxide substrate, which is characterized by a filling factor ν_{Sg}.

The Hall bar has a width of 1 μm, with 5 ohmic contacts (one of them was not connected) allowing for the measurement of the longitudinal resistance R_{xx}. Scanning gate experiments are performed in a VTI cryostat at 1.5 K, with a superconducting coil providing a magnetic field of 5.3 T. SGM maps are obtained at 150 nm and 200 nm from the device surface. The probe is composed of a commercial Pt/Cr metallic tip directly glued on a quartz tuning fork. The tip voltage for the workfunction compensation of the probe is $V_{\mathrm{tip}} = 0.5$ V. The charge neutrality point of the device, setting the separation between the electron and hole side, is at $V_{\mathrm{Sg}}^{\mathrm{CNP}} = -1.2$ V and $V_{\mathrm{Gg}}^{\mathrm{CNP}} = -0.06$ V for the silicon and graphite backagate respectively. The estimated silicon backgate capacitance and graphite backgate capacitance are respectively $C_{\mathrm{Sg}} = 9.35$ nFcm^{-2} and $C_{\mathrm{Gg}} = 86.54$ nFcm^{-2}.

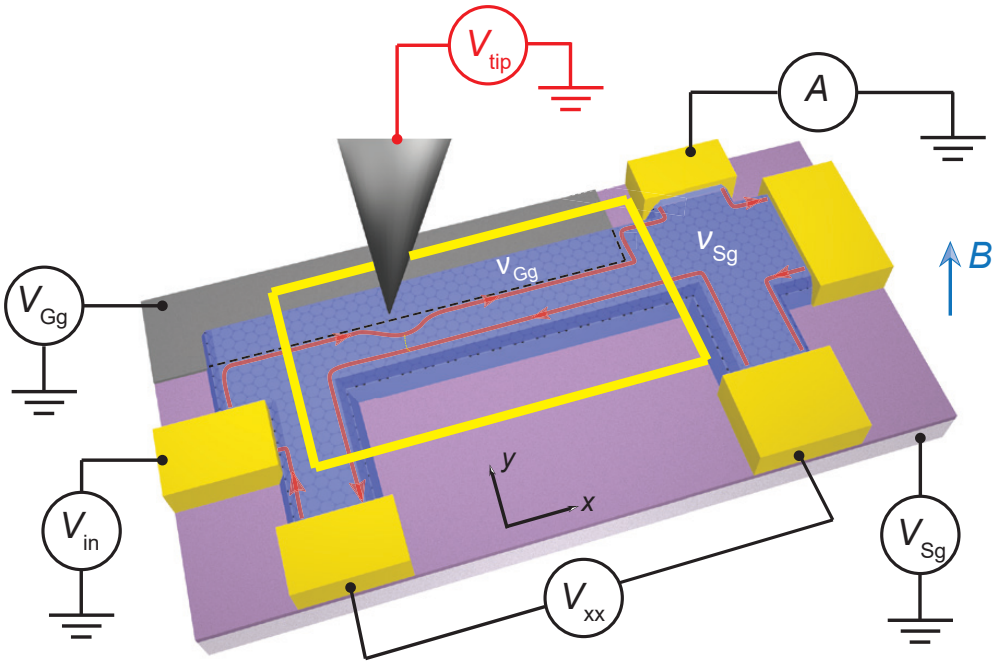

Figure 6.25: Schematic of the Hall bar device with the transport measurement set-up. Half of the graphene heterostructure is deposited over a graphite flake and the other part over a silicon oxide substrate. The SGM tip is scanning within the yellow area, perturbing in space the edge channel positions.

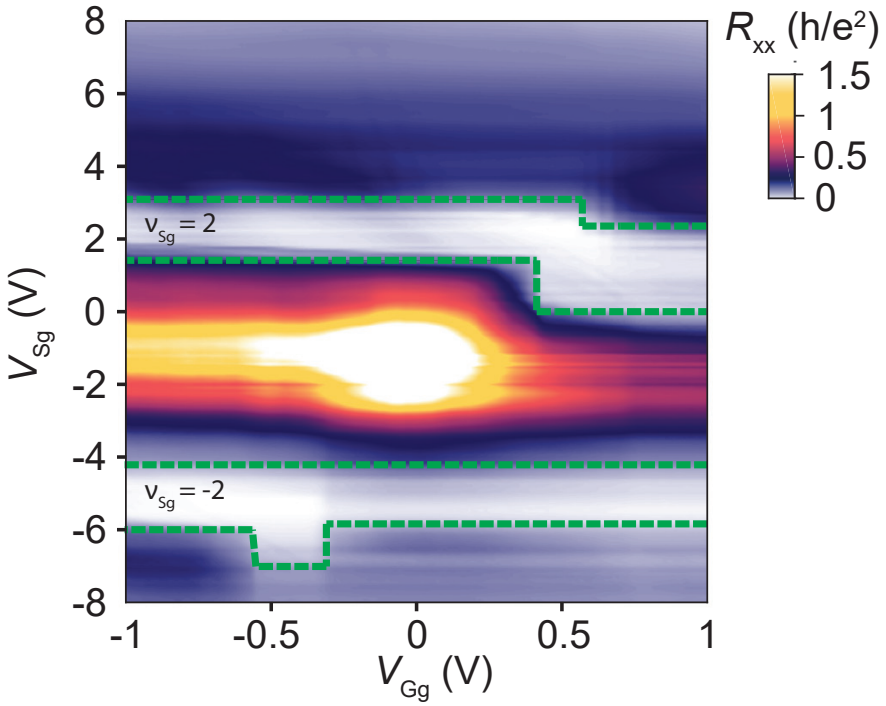

Figure 6.26: Longitudinal resistance map as a function of the graphite voltage V_{Sg} and silicon bottom gate voltage V_{Gg}. In green dashed lines are highlighted the plateaus of zero longitudinal resistance at $\nu_{\mathrm{Sg}} = \pm 2$. Evident variations in the plateaus broadness confirm the dependency of the edge mode coupling with respect the filling factor on the graphite side.

The electrostatic backgate control of the QH edge channels in the Hall bar device is visible in Fig.6.26, showing the colormap of the longitudinal resistance versus V_{Sg} and V_{Gg}. The plateaus of zero resistance at $\nu_{Sg} = \pm 2$ are contoured in the map with green dashed lines. Even if the spatial separation between the ohmic contacts and the graphite gate would suggest an independence of the measured resistance R_{xx} over the voltage V_{Gg}, the assumption seems to be not completely legit by looking at the shapes of the quasi-horizontal plateaus at integer filling $\nu_{Sg} = 2$ and $\nu_{Sg} = -2$. In particular, the width of the plateaus exhibit an enlargement and a shift in the proximity of the isodensity conditions in the Hall bar at $\nu_{Gg} = \pm 2$. This non-trivial behaviour at isodensity can be explained by the increased spatial distance between the counter-propagating edge states, when the density in the graphite-gated region is larger than the density in the silicon-gated region. In this situation, the edge states are not anymore confined in the narrow silicon-gated part of the Hall bar, and therefore less coupled to each other. This increased spatial separation between edge modes should enhance the total width of a quantum Hall plateau.

A specific view on the $\nu_{Sg} = 2$ plateau evolution is reported in Fig.6.27, for graphite gate filling factors: $\nu_{Gg} = -0.57,\ 1.54,\ 1.96,\ 2.38$. The evident modification of the plateaus shape shows that the backscattering in the Hall bar is strongly affected by the graphite gate voltage. In the inset of the figure, the backscattering signal at $V_{Sg} = 2.4$ V shows a weak dependence with respect to the graphite gate voltage, indicating the optimal quantization condition $\nu_{Sg} = 2$ in the silicon-gated region. The coloured arrows are pointing the different values of V_{Gg} employed in the line-cuts.

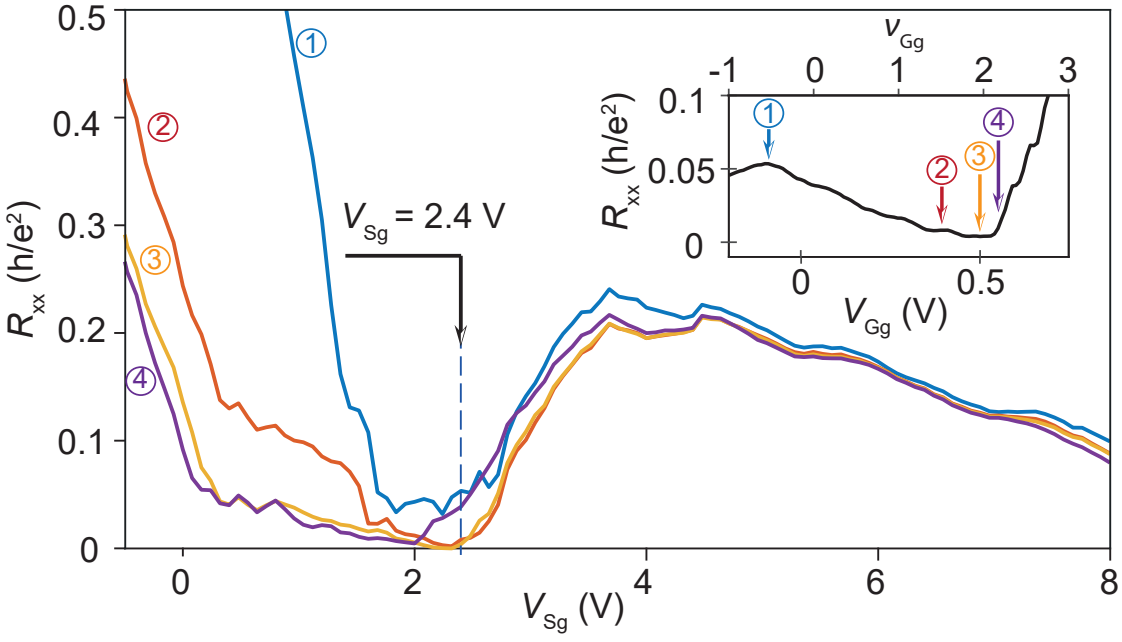

Figure 6.27: (a) Different plateaus of longitudinal resistance R_{xx} at $\nu_{Sg} = 2$. Plateaus were recorded at the graphite gate filling factor $\nu_{Gg} = -0.57,\ 1.54,\ 1.96,\ 2.38$. The labelled arrows in the inset are pointing the different values of V_{Gg} employed in the line-cuts. Evident modifications in the plateau shapes, suggests the existence of intrinsic weak backscattering in the Hall bar influenced by the graphite voltage. The inset shows the graphite voltage dependence of the resistance R_{xx} at the voltage $V_{Sg} = 2.4$ V ($\nu_{Sg} \approx 2$).

6.4.2 Imaging backscattering

Figure 6.28 displays the series of SGM maps recorded with $V_{\text{tip}} = -10$ V at 150nm from the device surface. The silicon backgate voltage is fixed at $V_{\text{Sg}} = 2.4$ V in order to guarantee the filling factor $\nu_{\text{Sg}} \approx 2$. Maps are measured at different graphite backgate voltages, inducing the same filling factor values as above.

The maps are characterized by a series of lobes and arc structures of high resistance, showing marked similarities with the previous SGM map of Fig.6.23.a. The presence of faint arc resonances in the maps are characteristic signatures of single-charge transfer between the counter-propagating edge modes. Interestingly, backscattering events in the device shows evident reduction when the filling factor in the graphite region approaches values close to $\nu_{\text{Gg}} = 2$.

An explanation for the backscattering reduction can be deduced from the illustration of the electron-type Landau level $N = 0$ in Fig.6.29 (details were explained previously for Fig.6.14). When the edge states are confined in the silicon backgate region (Fig.6.29.a), the invasive electrostatic action of the tip repels the upper channel, inducing a strong backscattering signal in the measurements. If the filling factor in the graphite region gradually increases (Fig.6.28.b), the action of the tip becomes less invasive and the previous direct backscattering can change into an indirect backscattering via a localized state. When the Hall bar is at uniform filling factor at $\nu = 2$ (Fig.6.28.c), the tip is no more able to generate backscattering.

The gradual displacement of the backscattering signal toward the interior of the Hall bar contrasts with the patterns observed in Ref. [107] and discussed in Section 6.2.3. In this work, the authors observed ring-shaped resonances decorating the edges of a macroscopic Hall

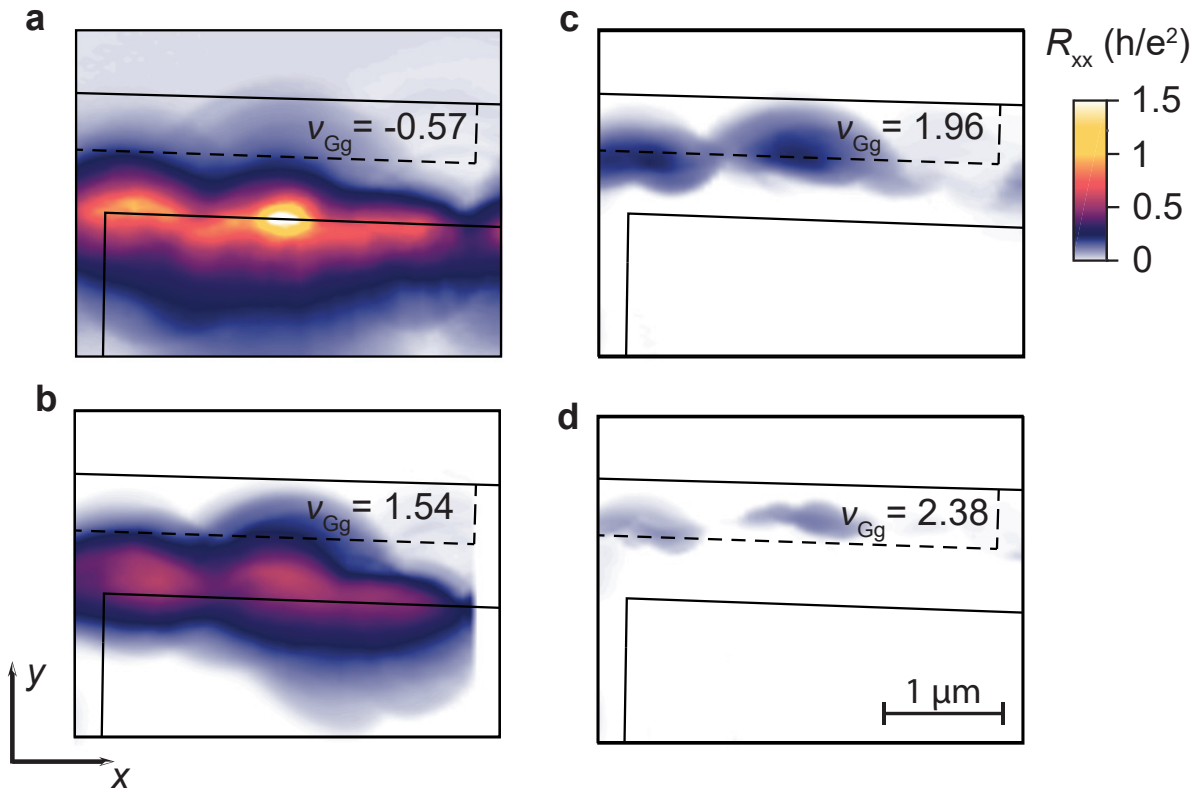

Figure 6.28: SGM maps of the backscattering events in the Hall bar with graphite filling factors $\nu_{\text{Gg}} = -0.57,\ 1.54,\ 1.96,\ 2.38$. The silicon backgate voltage is fixed at $V_{\text{Sg}} = 2.4$ V ($\nu_{\text{Sg}} \approx 2$). All the maps were recorded at 150 nm from the device surface, with a tip voltage tip $V_{\text{tip}} = -10$ V, in the area indicated in Fig.6.25.

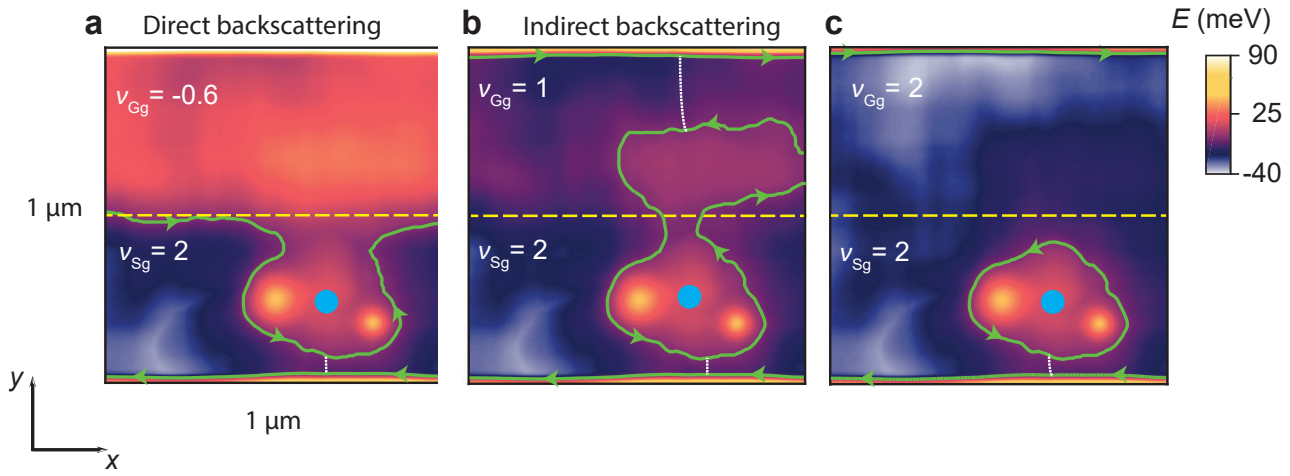

Figure 6.29: Simulated energy of the electron Landau level $N = 0$ showing the influence of the tip potential on the circulating edge channels for different filling conditions of the graphite bottom gate region ν_{Gg}. (a) The tip potential causes a direct backscattering process between the counterpropagating edge states (green lines). (b) Representation of an indirect backscattering process when the upper edge channel is at the very top of the Hall bar. (c) In the exactly quantized condition, when both $\nu_{\mathrm{Gg}} = \nu_{\mathrm{Sg}} = 2$, tip-induced backscattering is topologically prevented.

bar. These features were interpreted as disorder-induced backscattering between upstream and downstream modes flowing together along the sample edges as a result of charge accumulation. Here, this effect is not observed, indicating a better homogeneity of the carrier density in our samples.

The precise position of the backscattering signal with respect to the sample edge in Fig.6.28.a however deserves a discussion. The longitudinal resistance is maximum when the tip is located above the sample edge whereas one would have expected it to be centered with respect to the silicon-gated region around which the $N = 0$ edge channels are flowing at $\nu_{\mathrm{Sg}} = 2$ (incompressible). A first possible explanation could be related to an asymmetric tip-induced potential if the graphite-gate region is in a compressible hole state at $\nu_{\mathrm{Gg}} = -0.57$, thus screening the tip potential, as compared to the incompressible region below the Hall bar which does not screen at all. In case the graphite-gated region is also incompressible due to the opening of a $\nu = 0$ interaction-induced gap [155], the graphite gate itself can be at the origin of the screening since it is very close to the surface. A second possible explanation could result from the asymmetry of the confining potential for the edge channels flowing (i) along the sharp sample edge defined by etching and (ii) along the smooth electrostatically-defined interface between the silicon- and graphite-gated regions.

6.4.3 Scanning gate spectroscopies

I present here two SGM maps performed at opposite tip voltages, for a tip height of 200nm from the device surface. The silicon backgate voltage is fixed in the middle of the plateau, at $V_{\mathrm{Sg}} = 2.3$ V ($\nu_{\mathrm{Sg}} = 2$), while the graphite voltage is $V_{\mathrm{Gg}} = 0.3$ V ($\nu_{\mathrm{Gg}} = 1.12$). The SGM maps reported in Fig.6.30.(a,b) were measured with a tip voltage of $V_{\mathrm{tip}} = -8$ V and $V_{\mathrm{tip}} = 2$ V respectively. Both maps present non-zero background resistance, confirming the presence of intrinsic backscattering in the Hall bar in the absence of the tip. Figure 6.30.a shows the

characteristic SGM backscattering signal for a negative tip voltage inducing electron depletion. Figure 6.30.b, recorded at positive tip voltage, also reveals spatial variations of the longitudinal resistance, although the tip is now inducing electron accumulation, and therefore is not repelling electrostatically the edge states. In this last case, the above described mechanism of tip-enhanced backscattering does not apply, and should instead involve charge transfer by equilibration between edge channels belonging to different Landau levels. Fig.6.7 gives an example of such a backscattering mechanism between the counter-propagating $N = 0$ edge channels through localized states of the $N = 1$ Landau level. A related tip-induced equilibration process has been observed by SGM on graphene in Ref. [19], but in a different regime of equilibration with a reversed polarity under the tip. Interestingly, the here reported SGM maps are decorated with evident rings of resonances that can be attributed to Coulomb blockade mechanisms in localized states, as discussed below.

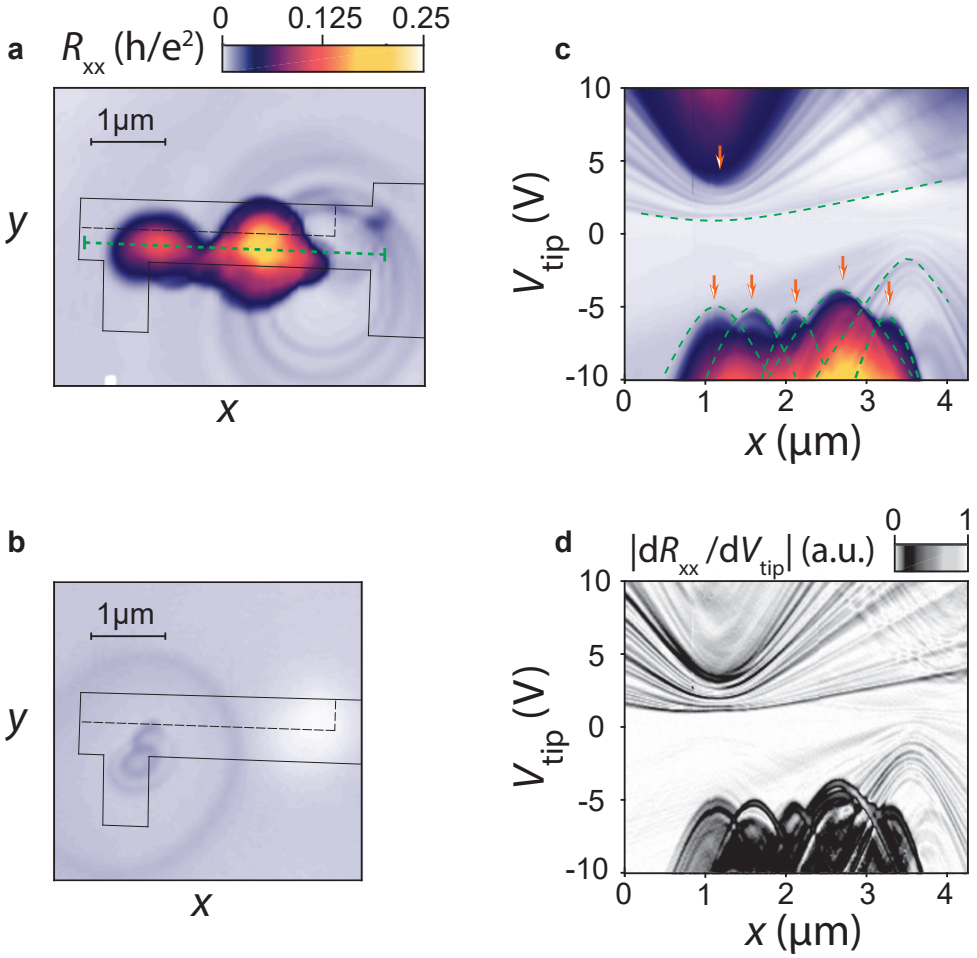

Figure 6.30: (a-b) SGM maps measured with the tip at 200 nm from the device surface, with tip voltage $V_{\text{tip}} = -8$ V and $V_{\text{tip}} = 2$ V respectively (same colour scale). Rings of Coulomb resonances can be spotted in both maps. (c-d) V_{tip} spectroscopy, recorded for $V_{\text{Sg}} = 2.3$ V and $V_{\text{Gg}} = 0.3$V, along the green dashed line in (a). Backscattering is induced for both positive and negative tip voltages. The arrows in (c) are spotting the main backscattering points in the Hall bar. The derivative of the signal (d) shows fine-structure, drawing hyperbolic lines at constant electrostatic tip-induced potential at the backscattering points. Hyperbolic fitting curves are plotted with green dashed lines and rely on the model of the electrostatic influence of an unscreened tip potential on a 2DEG.

V_{tip} spectroscopy: More information on the backscattering can be obtained with a single line spectroscopy as reported in Fig.6.30.c. The V_{tip} spectroscopy was performed along the green line marked in Fig.6.30.a, measuring the backscattering signal at different tip voltages. Figure 6.30.c shows the gradual formation of the backscattering signal at both positive and negative voltages.

While the backscattering for negative values of V_{tip} can be understood within the previous picture of a tip potential repelling the edge states within the same Landau level, and tunnelling through quantum antidots of the $N = 0$ Landau level, the backscattering signal manifesting at positive voltages requires a different explanation since the already fully occupied $N = 0$ Landau level cannot induce backscattering when even more attracted by the tip potential. A possible mechanism could be the intervention of tunnelling processes via bulk quantum dots of the next Landau level $N = 1$, lowered at the Fermi level by the attracting tip potential, such that these dots can participate to the percolation path of the $N = 0$ counter-propagating edge channels as depicted in Fig.6.7. However, this tunnelling has to develop through an incompressible strip between the Landau levels $N = 0$ et $N = 1$, which are separated in energy by a quite large cyclotron gap (about 76 meV). The proximity of the observed features with one of the two voltage probes may also play a role, but no specific mechanism could be identified.

By looking at the derivative of the spectroscopy in fig. 6.30.d, each backscattering point displays short scale modulations drawing a series of nested hyperbolic lines of constant tip-induced electrostatic potential, giving rise to a series of discrete spectra. These successive resonances at a given point may be attributed to level quantization and/or Coulomb blockade in a localized state around an antidot of the disorder potential. The hyperbolic fittings are reported in Fig.6.30.c according to the model of an unscreened potential :

$$\Delta V_{\text{antidot}} = \frac{\alpha V_{\text{tip}}}{\sqrt{x^2 + y^2 + H^2}} = \text{constant} \Rightarrow \beta V_{\text{tip}}^2 - x^2 = y^2 + H^2 = \text{constant}$$

V_{Sg} spectroscopy: In order to identify the precise locations of the backscattering events at the origin of the longitudinal resistance increase in transport curves, SGM single-line spectroscopies have been performed for a continuous set of silicon backgate voltages (and fixed tip voltages). A zoom of the R_{xx} colorplot in absence of the tip is reported in Fig.6.31.a, showing the plateau at $\nu_{Sg} = 2$, around the voltage value $V_{Gg} = 0.3V$ ($\nu_{Gg} = 1.12$). The plateau derivative of Fig.6.31.d shows the existence of marked horizontal lines, related to the onset of additional backscattering paths.

In the single-line spectroscopy of Fig.6.31.b is reported the tip-mediated backscattering in the band at $\nu_{Sg} = 2$ along the scan line, using a tip voltage $V_{tip} = -8$ V. The bottom of the band displays a series of distortions that reflects the unscreened spatial extension of the electrostatic potential induced by the tip. These distortions were fitted with a series of Lorentzian curves, each one representing the space modulation of single resonance participating in the backscattering. The derivative map in Fig.6.31.e put in evidence the individual Lorentzian behaviours, as part of the small-scale modulations in the spectroscopy. Each Lorentzian resonance enters inside the resistance plateau region, under the repulsive influence of the tip, causing a consequent increase on the longitudinal resistance.

As opposed to the lines at the lower edge of the plateau which come from backscattering paths in the $N = 0$ Landau level, the distortion of the upper edge of the plateau in Fig.6.31.b results from states of the $N = 1$ Landau level. The upward energy shift created by the negative tip voltage on the Landau levels, prevents the $N = 1$ Landau level to participate in the backscattering signal in the quantized plateau. This electrostatic action of the tip is indicated by the Lorentzian red line, enlarging vertically the extension of the plateau.

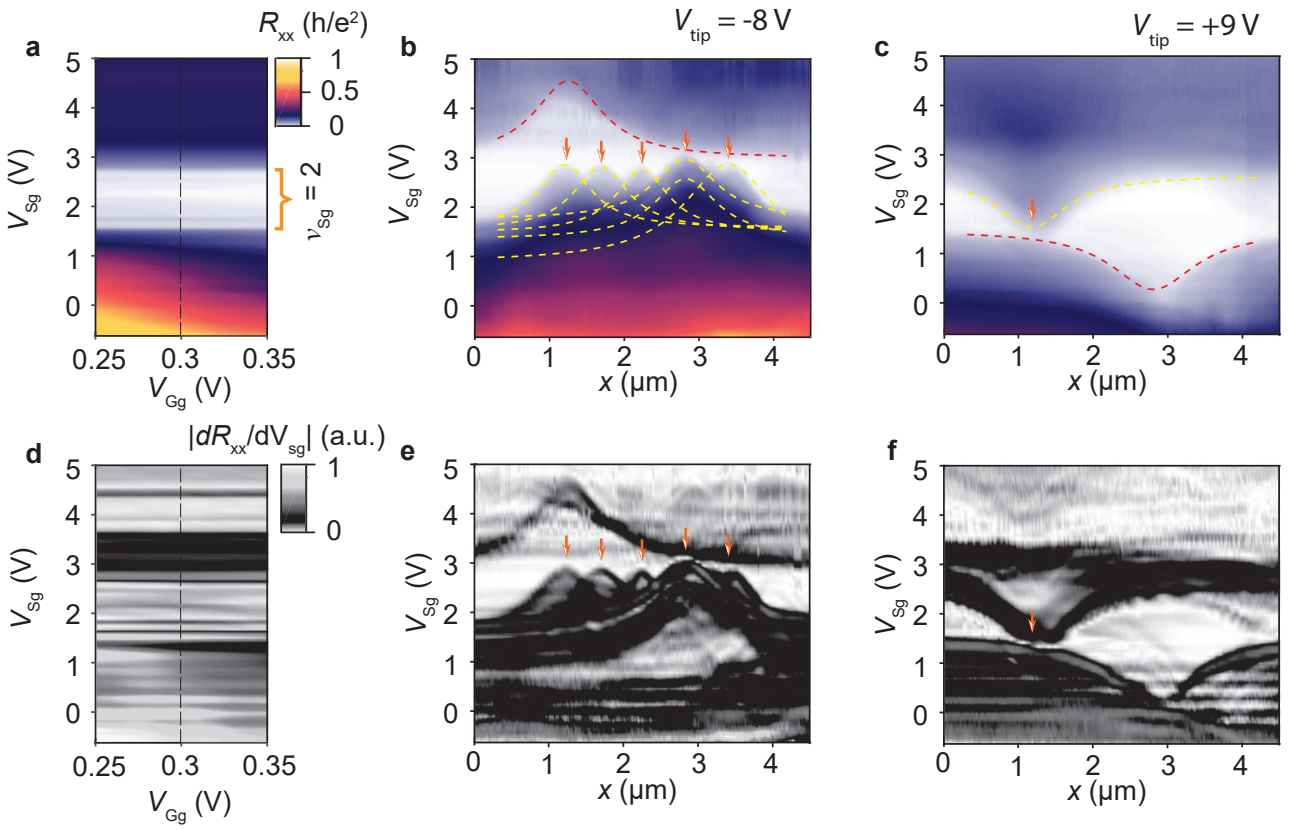

Figure 6.31: (a) Detail of the plateau $\nu_{Sg} = 2$ around the graphite gate voltage $V_{Gg} = 0.3V$ ($\nu_{Gg} = 1.12$). The bottom graph (d) shows its derivative $|dR_{xx}/dV_{Sg}|$. (b,c) Single-line spectroscopies versus silicon gate voltage, recorded along the same line as in Fig.6.30 and for the same graphite gate voltage $V_{Gg} = 0.3$ V. The colour scale is the same as in (a). (b) The tip voltage is set at $V_{tip} = -8V$. The individual backscattering events are highlighted by a sequence of fitted Lorentzian curves decorating the upper and lower band of the plateau. Arrows are indexing the main Lorentzian peaks, which spatially coincide with the arrows reported in Fig.6.30.c. The average FWHM of the Lorentzian curves is $0.5\mu m$. The bottom graph (e) shows the derivative $|dR_{xx}/dV_{Sg}|$ of the spectroscopy. (c) Single-line spectroscopy at fixed $V_{tip} = 9V$. The bottom graph (f) shows its derivative.

Figure 6.31.c represents the spectroscopy performed at positive tip voltage $V_{tip} = 9V$. The polarity inversion on the tip changes the spatial evolution of the backscattering lines. The tip is now inducing a downward energy shift of the Landau levels, such that the participation of antidot states, of the $N = 0$ Landau level, to the the backscattering is prevented by the tip potential. This effect is reflected in the shape of the plateau lower edge, which increases vertically the plateau width, following the red dashed Lorentzian fit.

The yellow line of Fig.6.31.c, entering inside the plateau at the upper edge, is centred at the same location as the backscattering signal observed at positive voltage in Fig.6.30.c. The most reliable explanation of this feature is a tip-enhanced tunneling processes between the edge states, via bulk quantum dots of the upper Landau level $N = 1$. The electrostatics of the tip can facilitate the bulk percolation via the upper localized states, with the occurrence of inter-Landau level tunneling through narrow incompressible regions.

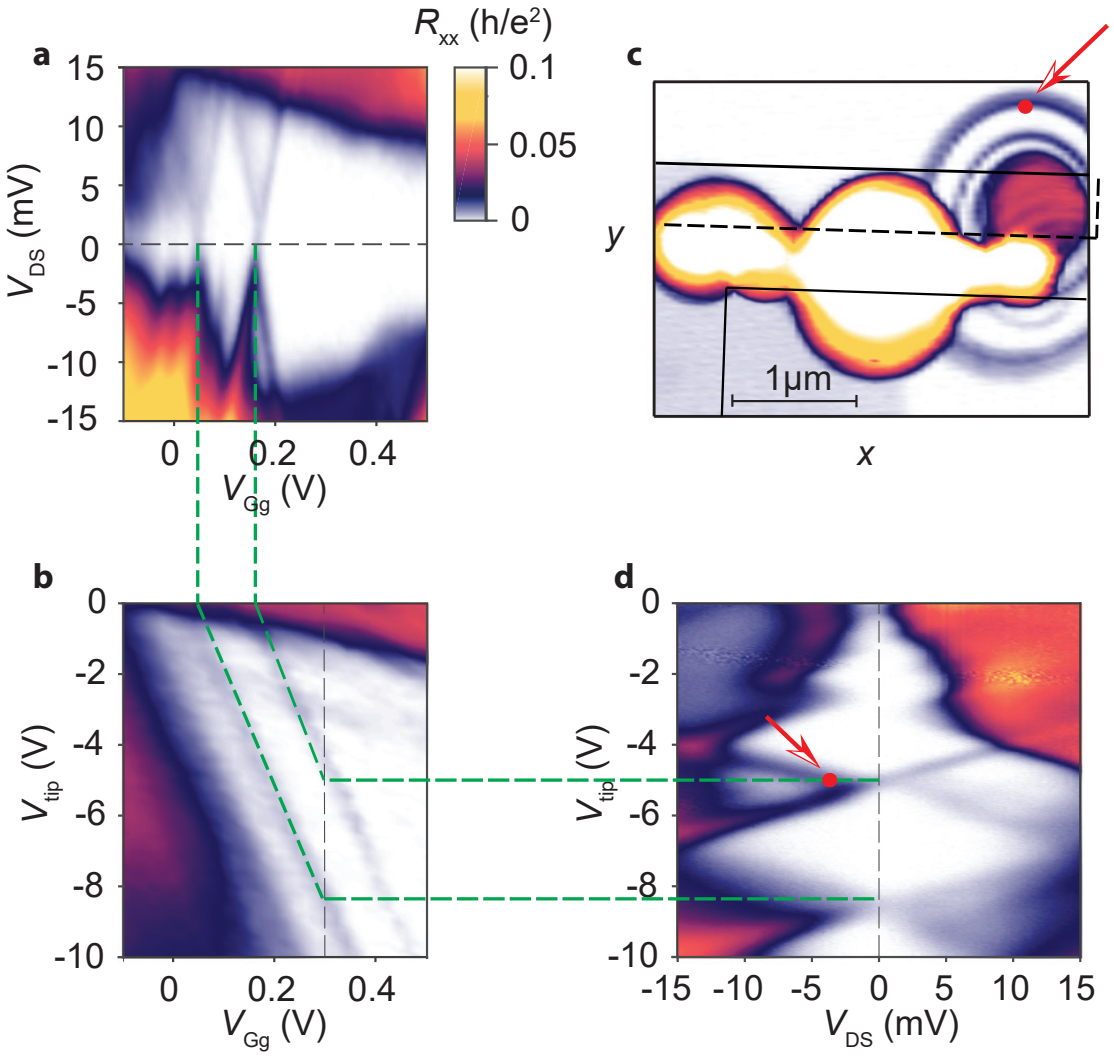

Figure 6.32: (a) Stability diagram of the longitudinal resistance versus graphite backgate voltage. The zero-bias peaks of a Coulomb diamond are evidenced with green dashed lines. (b) Map of the V_{Gg} and V_{tip} capacitive coupling performed with the tip at the position of the red marker in (c). (c) Out-of-equilibrium SGM map performed with $V_{\mathrm{DS}} = -4mV$ and a tip voltage $V_{\mathrm{tip}} = -5V$ at 200nm from the device surface. The graphite backgate voltage is $V_{\mathrm{Gg}} = 0.3V$ ($\nu_{\mathrm{Gg}} = 1.12$) and the silicon backgate voltage $V_{\mathrm{Sg}} = 2.4V$ ($\nu_{\mathrm{Sg}} \approx 2$). (d) Local stability diagram with the tip at the position of the red marker in (c). Coulomb diamonds confirm the relevance of the Coulomb blockade mechanism in the ring-shaped SGM signatures of backscattering.

6.4.4 Coulomb blockade backscattering

The relevance of the Coulomb blockade mechanism in our Hall bar is shown by the stability diagram of Fig.6.32.a, recorded versus graphite backgate voltage, at fixed $V_{\mathrm{Sg}} = 2.4$ V ($\nu_{\mathrm{Sg}} = 2$) and in the absence of the tip. In the diagram, the quantum Hall plateau of zero longitudinal resistance is decorated by a series of Coulomb diamonds.

In order to identify the location of the antidot at the origin of the Coulomb resonances with the SGM technique, in Fig.6.32.c is presented the out-of-equilibrium SGM map recorded at finite source-drain bias $V_{\mathrm{DS}} = -4$ mV and a tip voltage $V_{\mathrm{tip}} = -5$ V, at 200 nm from the device surface. The graphite backgate voltage is $V_{\mathrm{Gg}} = 0.3$ V ($\nu_{\mathrm{Gg}} = 1.12$) and the silicon backgate voltage $V_{\mathrm{Sg}} = 2.4$ V ($\nu_{\mathrm{Sg}} = 2$). From the map stands out a series of high-contrast rings encircling an uniform circular region of backscattering. These rings represent Coulomb blockade resonances in the backscattering process, enhanced by the out-of-equilibrium condition.

Figure 6.32.b shows the relative capacitive coupling of the Coulomb blockade antidot identified in Fig.6.32.a with respect to the tip and graphite voltages, measured with the tip positioned at the red marker of Fig.6.32.c, right over one resonance. The pair of Coulomb peaks, highlighted by two green dashed lines, belong to a diamond observed in Fig.6.32.a and follow a slope of constant electrostatic potential at the position of the antidot.

Figure 6.32.d is the stability diagram gated by the tip, still at the position of the red marker in Fig.6.32.c. The stability diagram unravels evident Coulomb diamond structures, confirming the presence of single-charge transfer through an antidot located at the center of the rings.

It is worth to underline that by following the green dashed lines traced in the whole Fig.6.32, it is possible to make a cross analysis between the complete set of data. We can therefore experimentally relate the spatial origin of the Coulomb peaks observed during transport measurement in Fig.6.32.a with the Coulomb peaks of Fig.6.32.d, which are related to the rings of the SGM map in Fig.6.32.c. This is a strong experimental proof of the relevance of the Coulomb blockade mechanism in the generation of arc-shaped signatures in the SGM maps of backscattering, and more generally in the percolation process of the quantum Hall effect.

Conclusion

In the quantum Hall regime, the crossing of the Landau levels with the Fermi level gives rise to one dimensional edge channels, as well as localized states in the bulk around dots and antidots of the disorder potential.

In this chapter, I explained the phenomenon of quantum Hall backscattering, which affects prominently mesoscopic devices when the percolation length becomes larger than the physical separation between the counter-propagating edge states, even at integer filling factor.

Scanning gate microscopy has been employed to investigate the backscattering mechanism in Hall bar devices. The negative voltage applied to the tip allows to induce non-trivial backscattering events between electron-like edge channels, with the inclusion of percolation paths via antidots in the bulk. With this technique, I therefore characterized the backscattering process in a graphene n-p-n junction and in a Hall bar, obtaining backscattering maps decorated with arc-shaped modulations which are characteristic of charge resonances through a percolative state gated by the tip.

Unexpected backscattering events between electron-type edge channels have been observed at positive tip voltage, which can be explained via the intervention of quantum dots of the upper Landau level.

I finally discussed on a set of experimental data which demonstrate the relevance of the

Coulomb blockade mechanism in the generation of arc-shaped signatures in the SGM maps of backscattering, and more generally in the quantum Hall percolation process.

Conclusions and perspectives

In this PhD work, we successfully fabricated different high-mobility graphene heterostructures, and investigated the electronic transport in the ballistic regime for the study of electron optical lensing effects, and in the quantum Hall regime for the analysis of the quantum Hall topological protection in graphene. A scanning gate microscope (SGM) was used to bring local informations on these physical phenomena.

Scanning gate microscopy in graphene p-n junctions

The first part of this thesis was dedicated to the study of encapsulated graphene p-n junctions for electron optics, where charge carriers can experience negative refraction, with the establishment of a focal point related to the Veselago lensing mechanism. The electrically polarized tip of a SGM was employed to harvest spatially-resolved informations on the transport inside the p-n junctions.

Graphene p-n junctions were fabricated with specific source regions equipped with a pinhole collimator for the control of the collimation of an injected electron beam in the active region of the device. A pristine graphite flake was employed as a bottom gate for the creation of a quasi-ideal electrostatic interface. The SGM technique allowed to image the transmission (refraction) and back reflection currents inside the junctions, obtaining signatures that were interpreted with the help of semi-classical ray tracing simulations. This last algorithm has been extensively used to reverse-engineer the SGM signatures, showing the possibility to image electron caustics due to Veselago lensing and branching generated by charge impurities.

The imaging of a spatially controlled focal point, confirmed that encapsulated graphene is an excellent candidate for electron optical devices. Nevertheless, more research work needs to be done in order to push the limits of the observed lensing effect, improving the device decoupling from the substrate impurities, and obtaining eventually more resolved pictures of electron caustics.

The study of back reflection signals via SGM, revealed the presence of unexpected tunnelling processes of charge carriers at the p-n interface, activated by the electrostatic action of the tip. Although our explanation based on a semi-classical analysis may be correct, it would be important to study this phenomenon with other analytical and numerical tools. The possibility to switch on/off reflection processes with an external gate can be very interesting for a novel generation of electron optical devices, that would no longer need sharp electrostatic interfaces.

It would be interesting to perform SGM experiments under a small perpendicular magnetic field in order to bend the trajectories and probe the refraction of the collimated beam at non-zero incident angles. The limitation imposed by the total internal reflection in smooth junctions should motivate the fabrication of devices with thinner backgate insulators and patterned graphite gates.

Imaging quantum Hall backscattering in graphene

The second part of the thesis was related to the SGM mapping of quantum Hall backscattering inside high-mobility graphene Hall bars. The aim was to probe and characterize the microscopic mechanism that causes the failure of the celebrated topological protection of the quantum Hall quantization condition in mesoscopic samples.

The negatively polarized tip allowed the observation of non-trivial backscattering between electron-like edge channels, mediated via antidots in the bulk. The backscattering maps in both the n-p-n and side-gated Hall bars, were characterized by arc-shaped modulations similar to the one observed in Ref. [114]. Backscattering events between electron-type edge channels were also recorded at positive tip voltage, and interpreted as backscattering processes mediated via quantum dots of the upper Landau level. The stability diagrams performed on the Hall bar allowed to demonstrate the Coulomb blockade single-electron mechanism in the generation of arc-shaped signatures in the SGM maps, and more generally in the percolation process of the quantum Hall effect.

Still it is important to clarify the apparent shift in the position of the SGM signal with respect to the physical device position. This last point shall be investigated both numerically, with a proper self-consistent quantum-electrostatic solver, and experimentally on specifically designed Hall bar devices.

Differently from Ref. [107], the SGM maps presented in this thesis did not show the presence of antidot poisoning of the quantum Hall effect along the etched edges of the heterostructures. Still it is not possible to give a specific explanation to this different behavior, which remains an open debate related to the subtle arrangement of impurities in encapsulated graphene devices.

Thanks to a better knowledge of the backscattering mechanisms in mesoscopic Hall bars and a better control of their SGM imaging, it would now be interesting to investigate in details the quantum Hall regime where electron interactions lift the degeneracy of the Landau levels. Imaging the backscattering of broken-symmetry edge states would provide useful information on the robustness of their quantization in transport experiments.

Appendix A

Graphene edge states on physical edges

A pristine graphene crystal display physical edges which are given from a combination of zigzag and armchair edges. An example of graphene lattice with idealized zigzag and armchairs edges is presented in Fig.A.1.a. Whether under a magnetic field or not, the wave function in

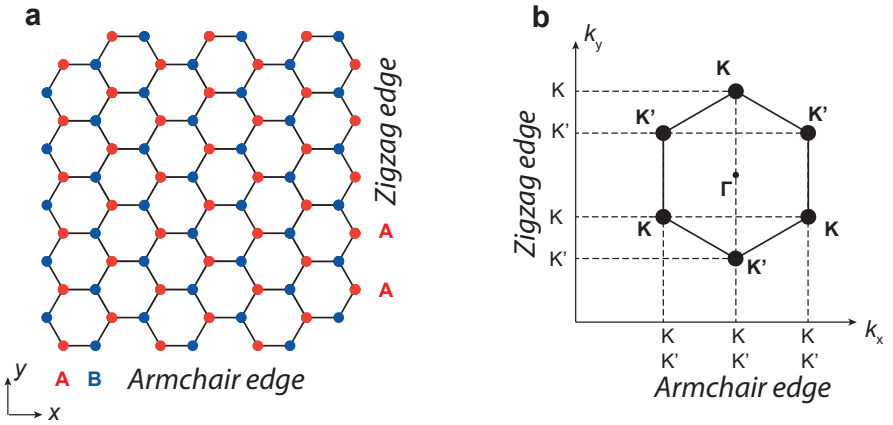

Figure A.1: (a) Graphene honeycomb lattice displaying both armchair and zigzag edges. The A and B sublattices are marked in red and blue respectively. (b) First Brillouin zone in graphene. For the armchair edge, the two valleys K and K' are admixed. Adapted from [33].

graphene $\Psi = (\psi_{\mathrm{A}},\ \psi_{\mathrm{B}})$ is required to vanish at the very edge of a graphene ribbon. This requirement is essentially a boundary condition, which discriminates the typology of edges involved. In the case of a zigzag right edge like in Fig.A.1.a, atoms belong to the same A sublattice, and therefore the bispinor component ψ_{A} has to vanish on the A sites

$$\psi_{\mathrm{A}}(\mathbf{r})|_{\mathrm{edge}} = 0. \tag{A.1}$$

In the case of armchair edges, the wave function must vanish on both A and B sites

$$\psi_{\mathrm{A}}(\mathbf{r})|_{\mathrm{edge}} = \psi_{\mathrm{B}}(\mathbf{r})|_{\mathrm{edge}} = 0. \tag{A.2}$$

In the reciprocal space (Fig.A.1.b), it is interesting to remark that the projection of the Dirac points, on the k_{x} axis (representing the armchair boundary) lead to the condition $K_{\mathrm{x}} = K_{\mathrm{x}}^{'}$, meaning that the two valleys are admixed. On the contrary, along the k_{y} axis (representing the zigzag boundary) the projected valleys are separated and not admixed.

Brey and Fertig in 2006 employed these last boundary conditions for the tight-binding calculation of the graphene energy spectrum in the quantum Hall regime [21], for both armchair

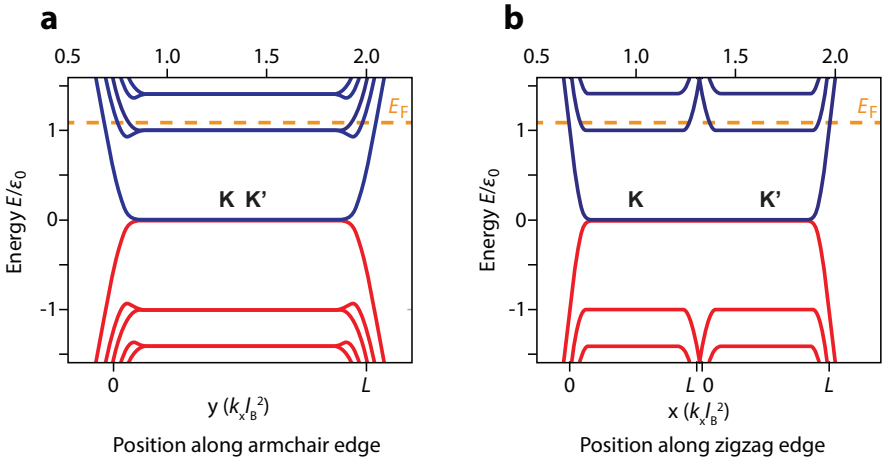

Figure A.2: Graphene edge spectra for a graphene ribbon of width L, under a strong magnetic field $B = 100$ T. (a) Tight-binding spectrum for a graphene ribbon having armchair edges. (b) Calculated spectrum for a zigzag ribbon. In the armchair and zigzag case, the amount of dispersing edge modes at integer filling factor is an odd number. Adapted from [21].

and zigzag edges. The calculated edge dispersions are reported in Fig.A.2. Similarly to the Halperin's picture, Landau levels are flat in the bulk, and disperse toward the edges of the sample. For both armchair and zigzag edges, the number of edge modes which cross the Fermi level at integer filling factor $\nu = N$ is $2(2N + 1)$.

In Fig.A.2, the tight-binding spectra are represented as a function of the space position, within a graphene ribbon of widths L, via the k-vector components as prescribed from the position-momentum relations:

$$y = k_{\mathrm{x}} l_{\mathrm{B}}^2 \tag{A.3}$$

$$x = k_{\mathrm{y}} l_{\mathrm{B}}^2 \tag{A.4}$$

These last relations lock the guiding centers evolutions of the edge states to the momentum components in the orthogonal directions [45].

For the zigzag edges (Fig.A.2.b), the double valleys are not admixed, and therefore each energy spectrum is treated separately. For each valley, the zeroth Landau level disperses from one side of the sample, but not on the other side since it is dispersionless. The dispersing side represents the current-carrying eigenstate.

In the armchair case (Fig.A.2.a), there is only one unique spectrum, since the valleys are admixed. In the bulk the spectrum lines are valley-degenerate. This degeneracy is lifted at both the edges, obtaining thus two dispersing current-carrying branches, one of them being non monotonous.

As it is possible to notice so far, the presence of two valleys further complicates the description of the edge modes formation. The Halperin's picture for conventional 2DEG is not enough to fully understand the roles of the **K** and **K′** valleys in the creation of current-carrying edge states, and suited boundary conditions of wave-function vanishing for the A and B sublattices are required in order to formally understand all the edge states contributions on the transport signatures in the quantum Hall effect.

However, we can usually neglect these differences between zigzag and armchair crystalline orientations, since they both give similar transport signatures. Moreover, this approximation is further justified for realistic graphene crystals, since their physical edges are mainly composed by a combination of zigzag and armchair orientations.

Bibliography

[1] Adam, S., E. H. Hwang, V. M. Galitski, and S. Das Sarma. 2007. A self-consistent theory for graphene transport, *Proceedings of the National Academy of Sciences*, 104(47), 18392–18397, URL http://dx.doi.org/10.1073/pnas.0704772104. (Cited on page 98.)

[2] Aidala, K., R. Parrott, T. Kramer, E. Heller, R. Westervelt, M. Hanson, and A. Gossard. 2007. Imaging magnetic focusing of coherent electron waves, *Nature Physics*, 3(7), 464–468, URL http://dx.doi.org/10.1038/nphys628. (Cited on pages 38 and 39.)

[3] Aidala, K.E., R.E. Parrott, E.J. Heller, and R.M. Westervelt. 2006. Imaging electrons in a magnetic field, *Physica E: Low-dimensional Systems and Nanostructures*, 34(1), 409–412, URL https://www.sciencedirect.com/science/article/pii/S1386947706001214. (Cited on page 38.)

[4] Allain, P.E. and N.J. Fuchs. 2011. Klein tunneling in graphene: optics with massless electrons, *The European Physical Journal B*, 83, 301–317, URL http://dx.doi.org/10.1140/epjb/e2011-20351-3. (Cited on pages 7, 8, 9, 11, and 13.)

[5] Amet, F., J. R. Williams, K. Watanabe, T. Taniguchi, and D. Goldhaber-Gordon. 2014. Selective equilibration of spin-polarized quantum hall edge states in graphene, *Phys. Rev. Lett.*, 112(19), 196601, URL http://dx.doi.org/10.1103/PhysRevLett.112.196601. (Cited on page 125.)

[6] Aragón-Muñoz, L., G. Chacón-Acosta, and H. Hernandez-Hernandez. 2020. Effective quantum tunneling from semiclassical momentous approach, *International journal of modern physics B*, 34(29), 2050271, URL http://dx.doi.org/10.1142/S0217979220502719. (Cited on page 56.)

[7] Barnard, A., A. Hughes, A. Sharpe, K. Watanabe, T. Taniguchi, and D. Goldhaber-Gordon. 2017. Absorptive pinhole collimators for ballistic dirac fermions in graphene, *Nature Communications*, 8(1), URL http://dx.doi.org/10.1038/ncomms15418. (Cited on pages 57, 58, and 59.)

[8] Bassani, F., L. Gerald, and W. Peter. 2005. Encyclopedia of condensed matter physics, *Academic Press*, 3, 447, URL https://www.semanticscholar.org/paper/Encyclopedia-of-Condensed-Matter-Physics-Bassani-Liedl/7f196cc89a12c74ed24da487dbd1e0f23ea97872. (Cited on pages 114 and 115.)

[9] Baumgartner, A., T. Ihn, K. Ensslin, K. Maranowski, and A. C. Gossard. 2007. Quantum hall effect transition in scanning gate experiments, *Phys. Rev. B*, 76, 085316, URL https://link.aps.org/doi/10.1103/PhysRevB.76.085316. (Cited on page 120.)

[10] Beenakker, C.W.J. and H. van Houten. 1991. Quantum transport in semiconductor nanostructures, *Solid State Physics*, 1–228, URL http://dx.doi.org/10.1016/S0081-1947(08)60091-0. (Cited on pages 57 and 58.)

[11] Bøggild, P., J. Caridad, C. Stampfer, G. Calogero, N. Papior, and M. Brandbyge. 2017. A two-dimensional dirac fermion microscope, *Nature Communications*, 8(1), URL http://dx.doi.org/10.1038/ncomms15783. (Cited on pages 1, 3, and 57.)

[12] Bhandari, S., M. Kreidel, A. Kelser, G. Lee, K. Watanabe, T. Taniguchi, P. Kim, and R.M. Westervelt. 2020. Imaging the flow of holes from a collimating contact in graphene, *Semiconductor Science and Technology*, 35(9), URL https://doi.org/10.1088/1361-6641/aba08d. (Cited on pages 59, 60, and 86.)

[13] Bhandari, S., G. Lee, P. Kim, and R. Westervelt. 2017. Analysis of scanned probe images for magnetic focusing in graphene, *Journal of Electronic Materials*, 46(7), 3837–3841, URL http://dx.doi.org/10.1007/s11664-017-5350-y. (Cited on page 42.)

[14] Bhandari, S., G. Lee, A. Klales, K. Watanabe, T. Taniguchi, E. Heller, P. Kim, and R. M. Westervelt. 2016. Orbits of electrons in graphene, *Nano Letters*, 16(3), 1690–1694, URL http://dx.doi.org/10.1021/acs.nanolett.5b04609. (Cited on pages 41, 42, 79, and 86.)

[15] Bhandari, S., G. Lee, K. Watanabe, T. Taniguchi, E. Heller, P. Kim, and R. M. Westervelt. 2018. Imaging electron flow from collimating contacts in graphene, *2D Materials*, 5, URL https://doi.org/10.1088/2053-1583/aab38a. (Cited on pages 59, 60, 79, and 86.)

[16] Bhandari, S., A. Lin, and R. Westervelt. 2017. Investigating the transition region in scanned probe images of the cyclotron orbit in graphene, *Journal of Nanoelectronics and Optoelectronics*, 12(9), 952–955, URL https://www.ingentaconnect.com/content/asp/jno/2017/00000012/00000009/art00014. (Cited on page 42.)

[17] Bhandari, S. and R. Westervelt. 2017. Imaging electron motion in graphene, *Semiconductor Science and Technology*, 32(2), 024001, URL http://dx.doi.org/10.1088/1361-6641/32/2/024001. (Cited on page 42.)

[18] Bondesan, Roberto. 2012. Edge states and supersymmetric sigma models, *PhD thesis, Université Paris 6*. (Cited on pages 114 and 115.)

[19] Bours, L., S. Guiducci, A. Mrenca, B. Szafran, J.C. Maan, and S. Heun. 2017. Manipulating quantum hall edge channels in graphene through scanning gate microscopy, *Phys. Rev. B*, 96, 195423, URL https://link.aps.org/doi/10.1103/PhysRevB.96.195423. (Cited on pages 120, 127, and 136.)

[20] Braem, B.A., C Gold, S. Hennel, M. Röösli, M Berl, W Dietsche, W Wegscheider, K Ensslin, and T. Ihn. 2018. Stable branched electron flow, *New Journal of Physics*, 20(7), 073015, URL https://doi.org/10.1088/1367-2630/aad068. (Cited on pages 34 and 35.)

[21] Brey, L. and H. A. Fertig. 2006. Edge states and the quantized hall effect in graphene, *Physical Review B*, 73(19), URL http://dx.doi.org/10.1103/PhysRevB.73.195408. (Cited on pages 108, 145, and 146.)

[22] Brun, B., F. Martins, S. Faniel, B. Hackens, G. Bachelier, A. Cavanna, C. Ulysse, A. Ouerghi, U. Gennser, D. Mailly, S. Huant, V. Bayot, M. Sanquer, and H. Sellier. 2014. Wigner and kondo physics in quantum point contacts revealed by scanning gate microscopy, *Nature communications*, 5, 4290, URL https://www.nature.com/articles/ncomms5290. (Cited on page 34.)

[23] Brun, B., N. Moreau, S. Somanchi, V.H. Nguyen, A. Mreńca-Kolasińska, K. Watanabe, T Taniguchi, J.C. Charlier, C. Stampfer, and B. Hackens. 2020. Optimizing dirac fermions quasi-confinement by potential smoothness engineering, *2D Materials*, 7(2), 025037, URL https://doi.org/10.1088/2053-1583/ab734e. (Cited on page 32.)

[24] Brun, B., N. Moreau, S. Somanchi, V.H. Nguyen, K. Watanabe, T. Taniguchi, J.C. Charlier, C. Stampfer, and B. Hackens. 2019. Imaging dirac fermions flow through a circular veselago lens, *Phys. Rev. B*, 100, 041401, URL https://link.aps.org/doi/10.1103/PhysRevB.100.041401. (Cited on pages 16, 32, and 86.)

[25] Büttiker, M. 1988. Absence of backscattering in the quantum hall effect in multiprobe conductors, *Phys. Rev. B*, 38, 9375–9389, URL https://link.aps.org/doi/10.1103/PhysRevB.38.9375. (Cited on page 108.)

[26] Castro Neto, A.H., F. Guinea, N.M.R. Peres, K.S. Novoselov, and A.K. Geim. 2009. The electronic properties of graphene, *Reviews of Modern Physics*, 81(1), 109–162, URL http://dx.doi.org/10.1103/RevModPhys.81.109. (Cited on pages 2, 4, and 14.)

[27] Chalker, J.T. and P. D. Coddington. 1988. Percolation, quantum tunnelling and the integer hall effect, *Journal of Physics C: Solid State Physics*, 21(14), 2665–2679, URL https://doi.org/10.1088/0022-3719/21/14/008. (Cited on pages 113 and 114.)

[28] Cheianov, V.V. and V. Fal'ko. 2006. Selective transmission of dirac electrons and ballistic magnetoresistance of $n-p$ junctions in graphene, *Phys. Rev. B*, 74, 041403, URL https://link.aps.org/doi/10.1103/PhysRevB.74.041403. (Cited on page 11.)

[29] Cheianov, V.V., V. Fal'ko, and B.L. Altshuler. 2007. The focusing of electron flow and a veselago lens in graphene p-n junctions, *Science*, 315(5816), 1252, URL https://science.sciencemag.org/content/315/5816/1252. (Cited on page 11.)

[30] Chen, S., Z. Han, MM. Elahi, K. M. Habib, L. Wang, B. Wen, Y. Gao, T. Taniguchi, K. Watanabe, J. Hone, A. W. Ghosh, and C.R. Dean. 2016. Electron optics with p-n junctions in ballistic graphene, *Science*, 353(6307), 1522–1525, URL http://dx.doi.org/10.1126/science.aaf5481. (Cited on pages 11 and 19.)

[31] Chklovskii, D.B., B.I. Shklovskii, and L.I. Glazman. 1992. Electrostatics of edge channels, *Phys. Rev. B*, 46, 4026–4034, URL https://link.aps.org/doi/10.1103/PhysRevB.46.4026. (Cited on pages 109, 110, and 111.)

[32] Chua, C., M. Connolly, A. Lartsev, T. Yager, S. Lara-Avila, S. Kubatkin, S. Kopylov, V. Falko, R. Yakimova, and R. Pearce. 2014. Quantum hall effect and quantum point contact in bilayer-patched epitaxial graphene, *Nano Letters*, 14(6), 3369–3373, URL http://dx.doi.org/10.1021/nl5008757. (Cited on page 120.)

[33] Coissard, Alexis. 2021. Visualizing quantum Hall edge channels in graphene, *PhD thesis, Université Grenoble Alpes*. (Cited on pages 67, 106, and 145.)

[34] Connolly, M.R., R.K. Puddy, D. Logoteta, P. Marconcini, M. Roy, J.P. Griffiths, G.A. C. Jones, P.A. Maksym, M. Macucci, and C.G. Smith. 2012. Unraveling quantum Hall breakdown in bilayer graphene with scanning gate microscopy, *Nano Letters*, 12(11), 5448–5454, URL http://dx.doi.org/10.1021/nl3015395. (Cited on page 120.)

[35] Cooper, N.R. and J.T. Chalker. 1993. Coulomb interactions and the integer quantum hall effect: Screening and transport, *Phys. Rev. B*, 48, 4530–4544, URL https://link.aps.org/doi/10.1103/PhysRevB.48.4530. (Cited on page 114.)

[36] Couto, N.J.G., D. Costanzo, S. Engels, D. Ki, K. Watanabe, T. Taniguchi, C.h Stampfer, F. Guinea, and A.F. Morpurgo. 2014. Random strain fluctuations as dominant disorder source for high-quality on-substrate graphene devices, *Physical Review X*, 4(4), URL http://dx.doi.org/10.1103/PhysRevX.4.041019. (Cited on page 124.)

[37] Crook, R., C.G. Smith, C.H.W. Barnes, M.Y. Simmons, and D.A. Ritchie. 2000. Imaging diffraction-limited electronic collimation from a non-equilibrium one-dimensional ballistic constriction, *Journal of Physics: Condensed Matter*, 12(8), L167–L172, URL https://doi.org/10.1088/0953-8984/12/8/102. (Cited on page 36.)

[38] Crook, R., C.G. Smith, C.H.W. Barnes, M.Y. Simmons, and D.A. Ritchie. 2000. Imaging electron and conduction-band-hole trajectories through one and two series constrictions, *Physica E: Low-dimensional Systems and Nanostructures*, 6(1), 234–237, URL https://doi.org/10.1016/S1386-9477(99)00117-4. (Cited on pages 36, 37, and 38.)

[39] Crook, R., C.G. Smith, M.Y. Simmons, and D.A. Ritchie. 2000. Imaging cyclotron orbits and scattering sites in a high-mobility two-dimensional electron gas, *Phys. Rev. B*, 62, 5174–5178, URL https://link.aps.org/doi/10.1103/PhysRevB.62.5174. (Cited on pages 36, 37, and 38.)

[40] Cserti, J., A. Pályi, and C. Péterfalvi. 2007. Caustics due to a negative refractive index in circular graphene $p-n$ junctions, *Phys. Rev. Lett.*, 99, 246801, URL https://link.aps.org/doi/10.1103/PhysRevLett.99.246801. (Cited on page 15.)

[41] Cui, Y.T., B. Wen, E.Y. Ma, G. Diankov, Z. Han, F. Amet, T. Taniguchi, K. Watanabe, D. Goldhaber-Gordon, C.R. Dean, and Z.H Shen. 2016. Unconventional correlation between quantum hall transport quantization and bulk state filling in gated graphene devices, *Phys. Rev. Lett.*, 117(18), URL http://dx.doi.org/10.1103/PhysRevLett.117.186601. (Cited on page 111.)

[42] Datta, S. 1995. *Electronic Transport in Mesoscopic Systems*, Cambridge University Press, URL https://doi.org/10.1017/CBO9780511805776. (Cited on page 106.)

[43] Davisson, C. and L.H. Germer. 1927. Diffraction of electrons by a crystal of nickel, *Phys. Rev.*, 30, 705–740, URL https://link.aps.org/doi/10.1103/PhysRev.30.705. (Cited on pages 1 and 3.)

[44] Dean, C.R., A.F. Young, I. Meric, C. Lee, L. Wang, S. Sorgenfrei, K. Watanabe, T. Taniguchi, P. Kim, K.L. Shepard, and J. Hone. 2010. Boron nitride substrates for high-quality graphene electronics, *Nature Nano.*, 5, 722–726, URL http://dx.doi.org/10.1038/nnano.2010.172. (Cited on page 64.)

[45] Delplace, P. and G. Montambaux. 2010. WKB analysis of edge states in graphene in a strong magnetic field, *Phys. Rev. B*, 82, 205412, URL http://dx.doi.org/10.1103/PhysRevB.82.20541. (Cited on page 146.)

[46] Dewdney, C. and B.J. Hiley. 1982. A quantum potential description of one-dimensional time-dependent scattering from square barriers and square wells, *Foundations of Physics*, 12(1), URL https://doi.org/10.1007/BF00726873. (Cited on page 56.)

[47] Dodoo-Amoo, N.A., K. Saeed, L.H. Li, E.H. Linfield, A.G. Davies, and A.G. Cunningham. 2013. The quantum percolation model of the scaling theory of the quantum hall effect: a unifying model for plateau-to-plateau transitions, *Journal of Physics: Conference Series*, 456, 012007, URL https://doi.org/10.1088/1742-6596/456/1/012007. (Cited on pages 112 and 113.)

[48] Don Cross. 2013. Fundamentals of ray tracing, URL http://cosinekitty.com/raytrace/raytrace_ebook.pdf. (Cited on page 46.)

[49] Dürig, U., H. Steinauer, and N. Blanc. 1997. Dynamic force microscopy by means of the phase-controlled oscillator method, *Journal of Applied Physics*, 82, 3641–3651, URL https://doi.org/10.1063/1.365726. (Cited on page 24.)

[50] Ekinci, K. and M. Roukes. 2005. Nanoelectromechanical systems, *Review of Scientific Instruments*, 76, 061101, URL https://doi.org/10.1063/1.1927327. (Cited on page 23.)

[51] Ferrari, A. and *et al.* 2015. Science and technology roadmap for graphene related two-dimensional crystals and hybrid systems, *Nanoscale*, 7, 4598–4810, URL https://doi.org/10.1039/C4NR01600A. (Cited on page 8.)

[52] Ford, C.J.B., P.J. Simpson, I. Zailer, D.R. Mace, M. Yosefin, M. Pepper, D.A. Ritchie, J.E.F. Frost, M.P. Grimshaw, and G.A.C. Jones. 1994. Charging and double-frequency aharonov-bohm effects in an open system, *Phys. Rev. B*, 49, 17456–17459, URL https://link.aps.org/doi/10.1103/PhysRevB.49.17456. (Cited on page 120.)

[53] Fratus, K.R., R.A. Jalabert, and D. Weinmann. 2019. Energy stability of branching in the scanning gate response of two-dimensional electron gases with smooth disorder, *Phys. Rev. B*, 100, 155435, URL https://link.aps.org/doi/10.1103/PhysRevB.100.155435. (Cited on pages 36 and 103.)

[54] Garcia, A., M. Konig, D. Goldhaber-Gordon, and K. Todd. 2013. Scanning gate microscopy of localized states in wide graphene constrictions, *Phys. Rev. B*, 87, 085446, URL https://link.aps.org/doi/10.1103/PhysRevB.87.085446. (Cited on page 64.)

[55] GmbH, Nanonis. 2005. Piezoelectric quartz tuning forks for scanning probe microscopy. (Cited on page 23.)

[56] Goerbig, M.O. 2011. Electronic properties of graphene in a strong magnetic field, *Rev. Mod. Phys.*, 83, 1193–1243, URL http://dx.doi.org/10.1103/RevModPhys.83.1193. (Cited on pages 7 and 106.)

[57] Goldman, V. and B. Su. 1995. Resonant tunneling in the quantum hall regime: Measurement of fractional charge, *Science (New York, N.Y.)*, 267, 1010–2, URL https://science.sciencemag.org/content/267/5200/1010. (Cited on page 120.)

[58] Groth, C.W., M Wimmer, A.R. Akhmerov, and X. Waintal. 2014. Kwant: a software package for quantum transport, *New Journal of Physics*, 16(6), 063065, URL https://doi.org/10.1088/1367-2630/16/6/063065. (Cited on page 32.)

[59] Grushina, A.L., D. Ki, and A. Morpurgo. 2013. A ballistic pn junction in suspended graphene with split bottom gates, *AIP*, (102), 223102, URL https://doi.org/10.1063/1.4807888. (Cited on page 75.)

[60] Gutiérrez, C., D. Walkup, F. Ghahari, C. Lewandowski, J. Rodriguez-Nieva, K. Watanabe, T. Taniguchi, N. Levitov, L.and Zhitenev, and J. Stroscio. 2018. Interaction driven quantum hall wedding cake-like structures in graphene quantum dots, *Science*, 361, 789–794, URL http://dx.doi.org/10.1126/science.aar2014. (Cited on page 111.)

[61] Hackens, B., F. Martins, S. Faniel, C.A. Dutu, H. Sellier, S. Huant, M. Pala, L. Desplanque, X. Wallart, and V. Bayot. 2010. Imaging coulomb islands in a quantum hall interferometer, *Nature Communications*, 1(1), URL https://doi.org/10.1038/ncomms1038. (Cited on page 120.)

[62] Halperin, B.I. 1982. Quantized hall conductance, current-carrying edge states, and the existence of extended states in a two-dimensional disordered potential, *Phys. Rev. B*, 25, 2185–2190, URL https://link.aps.org/doi/10.1103/PhysRevB.25.2185. (Cited on page 107.)

[63] Hannay, N.B., T. H. Geballe, B. T. Matthias, K. Andres, P. Schmidt, and D. MacNair. 1965. Superconductivity in graphitic compounds, *Phys. Rev. Lett.*, 14, 225–226, URL https://link.aps.org/doi/10.1103/PhysRevLett.14.225. (Cited on page 2.)

[64] Heinisch, R.L., F.X. Bronold, and H. Fehske. 2013. Mie scattering analog in graphene: Lensing, particle confinement, and depletion of klein tunneling, *Phys. Rev. B*, 87, 155409, URL https://link.aps.org/doi/10.1103/PhysRevB.87.155409. (Cited on page 15.)

[65] Heller, E.J. 2018. The semiclassical way to dynamics and spectroscopy, URL https://doi.org/10.23943/9781400890293. (Cited on pages 16 and 100.)

[66] Heller, E.J. and S. Scot. 2003. Branching and fringing in microstructure electron flow, *International Journal of Modern Physics B*, 17, URL https://doi.org/10.1142/S0217979203021964. (Cited on pages 32 and 103.)

[67] Huard, B., J. A. Sulpizio, N. Stander, K. Todd, B. Yang, and D. Goldhaber-Gordon. 2007. Transport measurements across a tunable potential barrier in graphene, *Phys. Rev. Lett.*, 98, 236803, URL https://link.aps.org/doi/10.1103/PhysRevLett.98.236803. (Cited on pages 7 and 75.)

[68] Hunt, B., J. D. Sanchez-Yamagishi, A. F. Young, M. Yankowitz, B. J. LeRoy, K. Watanabe, T. Taniguchi, P. Moon, M. Koshino, P. Jarillo-Herrero, and R. C. Ashoori. 2013. Massive Dirac Fermions and Hofstadter Butterfly in a van der Waals Heterostructure, *Science*, 340(6139), 1427–1430, URL http://dx.doi.org/10.1126/science.1237240. (Cited on page 64.)

[69] Hwang, E.H., S. Adam, and S. Das Sarma. 2007. Carrier Transport in Two-Dimensional Graphene Layers, *Phys. Rev. B*, 98, 186806, URL http://dx.doi.org/10.1103/PhysRevLett.98.186806. (Cited on page 64.)

[70] Ihn, T. 2009. *Semiconductor Nanostructures: Quantum States and Electronic Transport*, Oxford University Press, URL https://oxford.universitypressscholarship.com/view/10.1093/acprof:oso/9780199534425.001.0001/acprof-9780199534425. (Cited on page 58.)

[71] Ilani, S., J. Martin, E. Teitelbaum, J. Smet, D. Mahalu, V. Umansky, and A. Yacoby. 2004. The microscopic nature of localization in the quantum hall effect, *Nature*, 427, 328–32, URL http://dx.doi.org/10.1038/nature02230. (Cited on pages 115 and 116.)

[72] Inh, T. 2004. Electronic quantum transport in mesoscopic semiconductor structures, *Springer*, URL https://www.springer.com/gp/book/9780387400969. (Cited on pages 22, 23, 24, and 26.)

[73] Inh, T. 2009. Semiconductor nanostructures: Quantum states and electronic transport, *Oxford University Press*, URL https://oxford.universitypressscholarship.com/view/10.1093/acprof:oso/9780199534425.001.0001/acprof-9780199534425. (Cited on page 106.)

[74] Ishigami, M, J. H. Chen, W.G. Cullen, M.S. Fuhrer, and E. D. Williams. 2007. Atomic Structure of Graphene on SiO_2 , *Nano Lett.*, 7, 1643–1648, URL http://dx.doi.org/10.1021/nl070613a. (Cited on page 64.)

[75] J. Bricmont. 2016. *Making sense of quantum mechanics*, Springer, URL https://www.springer.com/gp/book/9783319258874. (Cited on page 32.)

[76] Jiang, Y, J. Mao, D. Moldovan, M.R. Masir, G. Li, K. Watanabe, T. Taniguchi, F. M. Peeters, and E.Y. Andrei. 2017. Tuning a circular p–n junction in graphene from quantum confinement to optical guiding, *Nature Nanotechnology*, 12, 1045, URL http://dx.doi.org/10.1038/nnano.2017.181. (Cited on page 16.)

[77] Jura, M., M. Topinka, L. Urban, Ali Yazdani, H. Shtrikman, L. Pfeiffer, K. West, and David Goldhaber-Gordon. 2007. Unexpected features of branched flow through high-mobility two-dimensional electron gases, *Nature Physics*, 3, 841, URL http://dx.doi.org/10.1038/nphys756. (Cited on page 100.)

[78] Kaplan, L. 2002. Statistics of branched flow in a weak correlated random potential, *Phys. Rev. Lett.*, 89, 184103, URL https://link.aps.org/doi/10.1103/PhysRevLett.89.184103. (Cited on page 100.)

[79] Katsnelon, M., K. Novoselov, and A. Geim. 2006. Chiral tunnelling and the Klein paradox in graphene, *Nature Phys*, 2, 620–625, URL http://dx.doi.org/10.1038/nphys384. (Cited on page 14.)

[80] Kim, S., J. Schwenk, D. Walkup, Y. Zeng, F Ghahari, S.T. Le, M. Slot, J. Berwanger, S. Blankenship, K Watanabe, T. Taniguchi, F. Giessibl, N. Zhitenev, C. Dean, and J. Stroscio. 2020. Edge channels of broken-symmetry quantum hall states in graphene probed by atomic force microscopy, *arXiv*, URL https://arxiv.org/abs/2006.10730. (Cited on page 111.)

[81] Klein, O. 1929. Die Reflexion von Elektronen an einem Potentialsprung nach der relativistichen Dynamik von Dirac, *Z. Physik*, 53, 157, URL https://link.springer.com/article/10.1007/BF01339716. (Cited on page 7.)

[82] Klitzing, K.V., G. Dorda, and M. Pepper. 1980. New method for high-accuracy determination of the fine-structure constant based on quantized hall resistance, *Phys. Rev. Lett.*, 45, 494–497, URL https://doi.org/10.1103/PhysRevLett.45.494. (Cited on page 118.)

[83] Kozikov, A., C. Rossler, T. Ihn, K. Ensslin, C. Reichl, and W. Wegscheider. 2012. Interference of electrons in backscattering through a quantum point contact, *New Journal of Physics*, 15, URL https://iopscience.iop.org/article/10.1088/1367-2630/15/1/013056. (Cited on page 34.)

[84] LaGasse, S. and C. Cress. 2020. Unveiling electron optics in two-dimensional materials by nonlocal resistance mapping, *Nano Letters*, 20, URL https://doi.org/10.1021/acs.nanolett.0c02443. (Cited on page 90.)

[85] Landau, L.D. and E.M Lifshitz. 1980. Statistical physics, URL https://doi.org/10.1021/ed015p550.2. (Cited on page 2.)

[86] Lee, G.H., G.H. Park, and Lee H. J. 2015. Observation of negative refraction of dirac fermions in graphene, *Nature Physics.*, 11, 925, URL url={http://dx.doi.org/10.1038/nphys3460},. (Cited on pages 11, 17, and 18.)

[87] LeRoy, B.J. 2003. Imaging coherent electron flow, *Journal of Physics: Condensed Matter*, 15(50), R1835–R1863, URL https://doi.org/10.1088/0953-8984/15/50/r02. (Cited on pages 33 and 34.)

[88] LeRoy, B.J. 2003. Imaging coherent electron flow through semiconductor nanostructures, *PhD thesis, Harvard*. (Cited on page 33.)

[89] LeRoy, B.J., A.C. Bleszynski, M.A. Topinka, R.M. Westervelt, S.E.J. Shaw, E.J. Heller, K.D. Maranowski, and A.C. Gossard. 2003. Imaging coherent electron wave flow in a two-dimensional electron gas, *Physica E: Low-dimensional Systems and Nanostructures*, 12, 678–683. (Cited on page 33.)

[90] LeRoy, B.J., M. Topinka, R. Westervelt, K. Maranowski, and A. Gossard. 2002. Imaging electron density in a two-dimensional electron gas, *Applied Physics Letters*, 80, 4431–4433. (Cited on page 33.)

[91] LeRoy, B.J., M.A. Topinka, A.C. Bleszynski, R.M. Westervelt, S.E.J. Shaw, E.J. Heller, K.D. Maranowski, and A.C. Gossard. 2003. Imaging coherent electron flow in a two-dimensional electron gas, *Applied Surface Science*, 210(1), 134–139, URL https://www.sciencedirect.com/science/article/pii/S0169433202014939. 5th International Conference on non-contact AFM in Montreal, Canada. (Cited on page 33.)

[92] Libisch, F., T. Hisch, R. Glattauer, L.A. Chizhova, and J. Burgdörfer. 2017. Veselago lens and klein collimator in disordered graphene, *Journal of Physics: Condensed Matter*, 29(11), 114002, URL https://doi.org/10.1088/1361-648x/aa565e. (Cited on page 13.)

[93] Lier, K. and R.R. Gerhardts. 1994. Self-consistent calculations of edge channels in laterally confined two-dimensional electron systems, *Phys. Rev. B*, 50, 7757–7767, URL https://link.aps.org/doi/10.1103/PhysRevB.50.7757. (Cited on page 110.)

[94] Liu, B. and E.J. Heller. 2013. Stability of branched flow from a quantum point contact, *Phys. Rev. Lett.*, 111, 236804, URL https://link.aps.org/doi/10.1103/PhysRevLett.111.236804. (Cited on page 36.)

[95] Liu, M., C. Gorini, and K. Richter. 2017. Creating and steering highly directional electron beams in graphene, *Phys. Rev. Lett.*, 118, 066801, URL https://link.aps.org/doi/10.1103/PhysRevLett.118.066801. (Cited on page 57.)

[96] Low, T., S. Hong, J. Appenzeller, S. Datta, and M.S. Lundstrom. 2009. Conductance asymmetry of graphene p-n junction, *IEEE Transactions on Electron Devices*, 56(6), 1292–1299, URL https://ieeexplore.ieee.org/document/4895330. (Cited on page 76.)

[97] Marguerite, A., J. Birkbeck, A. Aharon-Steinberg, D. Halbertal, K. Bagani, I. Marcus, Myasoedov Y., A. K. Geim, D. J. Perello, and E. Zeldov. 2019. Imaging work and dissipation in the quantum Hall state in graphene, *Nature*, 575, 628–633, URL https://doi.org/10.1038/s41586-019-1704-3. (Cited on pages 111 and 120.)

[98] Martin, J., N. Akerman, G. Ulbricht, T. Lohmann, K. Klitzing, J. Smet, and Amir Yacoby. 2009. The nature of localization in graphene under quantum hall conditions, *Nature Phys.*, 5, URL https://doi.org/10.1038/nphys1344. (Cited on pages 115 and 116.)

[99] Martin, J., N. Akerman, G. Ulbricht, T. Lohmann, J. H. Smet, K. von Klitzing, and A. Yacoby. 2007. Observation of electron–hole puddles in graphene using a scanning single-electron transistor, *Nature Physics*, 4(2), 144–148, URL http://dx.doi.org/10.1038/nphys781. (Cited on page 100.)

[100] Martin, J., S. Ilani, B. Verdene, J. Smet, V. Umansky, D. Mahalu, D. Schuh, G. Abstreiter, and A. Yacoby. 2004. Localization of fractionally charged quasi-particles, *Science (New York, N.Y.)*, 305, 980–3, URL http://dx.doi.org/10.1103/PhysRevLett.125.227701. (Cited on page 116.)

[101] Martin, S.C., S. Samaddar, B. Sacépé, A. Kimouche, J. Coraux, F. Fuchs, B. Grévin, H. Courtois, and C. B. Winkelmann. 2015. Disorder and screening in decoupled graphene on a metallic substrate, *Physical Review B*, 91(4), URL http://dx.doi.org/10.1103/PhysRevB.91.041406. (Cited on page 100.)

[102] Martins, F., S. Faniel, B. Rosenow, M.G. Pala, H. Sellier, S. Huant, L. Desplanque, X. Wallart, V. Bayot, and B. Hackens. 2013. Scanning gate spectroscopy of transport across a quantum hall nano-island, *New Journal of Physics*, 15(1), 013049, URL http://dx.doi.org/10.1088/1367-2630/15/1/013049. (Cited on page 120.)

[103] Martins, F., S. Faniel, B. Rosenow, H. Sellier, S. Huant, M.G. Pala, L. Desplanque, X. Wallart, V. Bayot, and B. Hackens. 2013. Coherent tunnelling across a quantum point contact in the quantum hall regime, *Scientific Reports*, 3(1), URL http://dx.doi.org/10.1038/srep01416. (Cited on page 120.)

[104] Mattheakis, M., G.P. Tsironis, and E. Kaxiras. 2018. Emergence and dynamical properties of stochastic branching in the electronic flows of disordered dirac solids, *EPL*, 122(2), 27003, URL https://doi.org/10.1209/0295-5075/122/27003. (Cited on pages 84 and 100.)

[105] Mayorov, A.S., R.V. Gorbachev, S.V. Morozov, L. Britnell, R. Jalil, L.A. Ponomarenko, P. Blake, K.S. Novoselov, K. Watanabe, and T. Taniguchi. 2011. Micrometer-scale ballistic transport in encapsulated graphene at room temperature, *Nano Letters*, 11(6), 2396–2399, URL http://dx.doi.org/10.1021/nl200758b. (Cited on page 65.)

[106] Metzger, J.J., R. Fleischmann, and T. Geisel. 2010. Universal statistics of branched flows, *Phys. Rev. Lett.*, 105, 020601, URL https://link.aps.org/doi/10.1103/PhysRevLett.105.020601. (Cited on page 100.)

[107] Moreau, N., S. Brun, B.and Somanchi, K. Watanabe, T. Taniguchi, C. Stampfer, and B. Hackens. 2020. Upstream modes and antidots poison graphene quantum hall effect, *ArXiv*, URL https://arxiv.org/abs/2010.12499. (Cited on pages 111, 120, 123, 124, 134, and 144.)

[108] Mrenca, A., K. Kolasinski, and B. Szafran. 2015. Conductance response of graphene nanoribbons and quantum point contacts in scanning gate measurements, *Semiconductor Science and Technology*, 30(8), 085003, URL https://doi.org/10.1088/0268-1242/30/8/085003. (Cited on page 86.)

[109] Mrenca, A., K. Kolasinski, and B. Szafran. 2017. Imaging backscattering in graphene quantum point contacts, *Phys. Rev. B*, 96, 165310, URL https://link.aps.org/doi/10.1103/PhysRevB.96.165310. (Cited on page 86.)

[110] Mrenca, A., K. Kolasinski, B. Szafran, S. Heun, and B. Szafran. 2016. Aharonov-Bohm interferometer based on $n-p$ junctions in graphene nanoribbons, *Phys. Rev. B*, 93, 125411, URL https://link.aps.org/doi/10.1103/PhysRevB.93.125411. (Cited on page 86.)

[111] Novoselov, K.S., A. K. Geim, S. V. Morozov, D. Jiang, M. I. Katsnelson, I. V. Grigorieva, S. V. Dubonos, and A. A. Firsov. 2005. Two-dimensional gas of massless Dirac fermions in graphene, *Nature*, 438, 197–200, URL https://doi.org/10.1038/nature04233. (Cited on pages 2, 64, 118, and 119.)

[112] Onodera, M., K. Watanabe, M. Isayama, M. Arai, S. Masubuchi, R. Moriya, T. Taniguchi, and T. Machida. 2019. Carbon-rich domain in hexagonal boron nitride: carrier mobility degradation and anomalous bending of landau fan diagram in adjacent graphene, *Nano Letters*, 19, URL https://doi.org/10.1021/acs.nanolett.9b02879. (Cited on page 124.)

[113] Ozyilmaz, B., P. Jarillo-Herrero, D. Efetov, D. A. Abanin, L. S. Levitov, and P. Kim. 2007. Electronic transport and quantum hall effect in bipolar graphene p-n-p junctions, *Phys. Rev. Lett.*, 99, 166804, URL https://link.aps.org/doi/10.1103/PhysRevLett.99.166804. (Cited on pages 125 and 127.)

[114] Paradiso, N., S. Heun, S. Roddaro, G. Biasiol, L. Sorba, D. Venturelli, F. Taddei, V. Giovannetti, and F. Beltram. 2012. Imaging backscattering through impurity-induced antidots in quantum hall constrictions, *Physical Review B*, 86, 085326, URL https://link.aps.org/doi/10.1103/PhysRevB.86.085326. (Cited on pages 2, 4, 120, 121, 122, 123, 130, and 144.)

[115] Paradiso, N., S. Heun, S. Roddaro, L.N. Pfeiffer, K.W. West, L. Sorba, G. Biasiol, and F. Beltram. 2010. Selective control of edge-channel trajectories by scanning gate microscopy, *Physica E: Low-dimensional Systems and Nanostructures*, 42(4), 1038–1041, URL https://www.sciencedirect.com/science/article/pii/S1386947709005827. (Cited on page 34.)

[116] Paradiso, N., S. Heun, S. Roddaro, D. Venturelli, F. Taddei, V. Giovannetti, R. Fazio, G. Biasiol, L. Sorba, and F. Beltram. 2011. Spatially resolved analysis of edge-channel equilibration in quantum hall circuits, *Phys. Rev. B*, 83, 155305, URL https://link.aps.org/doi/10.1103/PhysRevB.83.155305. (Cited on page 120.)

[117] Paredes-Rocha, E., Y. Betancur-Ocampo, N. Szpak, and T. Stegmann. 2020. Gradient-index electron optics in graphene pn junctions, *arXiv, cond-mat.mes-hall*, URL https://arxiv.org/abs/2009.05535. (Cited on pages 13, 15, and 16.)

[118] Pascher, N., C. Rössler, T. Ihn, K. Ensslin, C. Reichl, and W. Wegscheider. 2014. Imaging the conductance of integer and fractional quantum hall edge states, *Phys. Rev. X*, 4, 011014, URL https://link.aps.org/doi/10.1103/PhysRevX.4.011014. (Cited on page 120.)

[119] Patsyk, A., U. Sivan, M. Segev, and M. Bandres. 2020. Observation of branched flow of light, *Nature*, 583, 60–65, URL https://doi.org/10.1038/s41586-020-2376-8. (Cited on page 103.)

[120] Peirls, R.E. 1934. Remarks on transition temperatures, *Helv. Phys. Acta*, 7, 81, URL https://doi.org/10.1142/9789812795779_0014. (Cited on page 2.)

[121] Pendry, J.B. 2000. Negative refraction makes a perfect lens, *Phys. Rev. Lett.*, 85, 3966–3969, URL https://link.aps.org/doi/10.1103/PhysRevLett.85.3966. (Cited on page 14.)

[122] Ryndyk, D.A. 2016. Theory of quantum transport at nanoscale, URL https://www.springer.com/gp/book/9783319240862. (Cited on page 59.)

[123] Sajjad, R., C. Polanco, and A. Ghosh. 2013. Atomistic deconstruction of current flow in graphene based hetero-junctions, *Journal of Computational Electronics*, 12, URL https://doi.org/10.1007/s10825-013-0459-6. (Cited on page 75.)

[124] Samaddar, S., I. Yudhistira, S. Adam, H. Courtois, and C. B. Winkelmann. 2016. Charge puddles in graphene near the dirac point, *Phys. Rev. Lett.*, 116, 126804, URL https://link.aps.org/doi/10.1103/PhysRevLett.116.126804. (Cited on page 98.)

[125] Sellier, H., B. Hackens, M. Pala, F. Martins, S. Baltazar, X. Wallart, L. Desplanque, V. Bayot, and S. Huant. 2011. On the imaging of electron transport in semiconductor quantum structures by scanning-gate microscopy: Successes and limitations, *Semiconductor Science and Technology*, 35, URL https://doi.org/10.1088/0268-1242/26/6/064008. (Cited on page 22.)

[126] Shankar, R. 1994. *Principles of quantum mechanics*, Springer. (Cited on page 4.)

[127] Shaw, S.E.J. 2002. Propagation in smooth random potentials, *PhD thesis, Harvard*. (Cited on page 33.)

[128] Shon, N.H. and T. Ando. 1998. Quantum transport in two-dimensional graphite system, *J. Phys. Soc. Jpn.*, 67, 2421, URL https://doi.org/10.1143/JPSJ.67.2421. (Cited on page 7.)

[129] Silvestrov, P.G. and K.B. Efetov. 2008. Charge accumulation at the boundaries of a graphene strip induced by a gate voltage: Electrostatic approach, *Phys. Rev. B*, 77(155436), 1–5, URL https://link.aps.org/doi/10.1103/PhysRevB.77.155436. (Cited on page 111.)

[130] Sim, H.S., M. Kataoka, and C.J.B. Ford. 2008. Electron interactions in an antidot in the integer quantum hall regime, *Physics Reports*, 456(4), 127–165, URL https://doi.org/10.1016/j.physrep.2007.11.001. (Cited on pages 120 and 122.)

[131] Sivan, U., M. Heiblum, C. P. Umbach, and H. Shtrikman. 1990. Electrostatic electron lens in the ballistic regime, *Phys. Rev. B*, 41, 7937–7940, URL https://link.aps.org/doi/10.1103/PhysRevB.41.7937. (Cited on pages 1 and 3.)

[132] Slevin, K. and T. Ohtsuki. 2009. Critical exponent for the quantum hall transition, *Phys. Rev. B*, 80, 041304, URL https://link.aps.org/doi/10.1103/PhysRevB.80.041304. (Cited on page 112.)

[133] Steinacher, R., A.A. Kozikov, C. Rössler, C. Reichl, W. Wegscheider, K. Ensslin, and T. Ihn. 2016. Scanning gate imaging in confined geometries, *Phys. Rev. B*, 93, 085303, URL https://link.aps.org/doi/10.1103/PhysRevB.93.085303. (Cited on page 34.)

[134] Steinacher, R., C. Pöltl, T. Krähenmann, A. Hofmann, C. Reichl, W. Zwerger, W. Wegscheider, R. A. Jalabert, K. Ensslin, D. Weinmann, and T. Ihn. 2018. Scanning gate experiments: From strongly to weakly invasive probes, *Phys. Rev. B*, 98, 075426, URL https://link.aps.org/doi/10.1103/PhysRevB.98.075426. (Cited on pages 39, 40, and 85.)

[135] Takumi, M., M. Shigenori, and M. Norikatsu. 2008. Mechanical q-factor measurement of a quartz oscillator at cryogenic temperature, *Applied Physics Express*, 1, URL https://doi.org/10.1143/apex.1.077002. (Cited on page 24.)

[136] Taychatanapat, T., K. Watanabe, T. Taniguchi, and P. Jarillo-Herrero. 2013. Electrically tunable transverse magnetic focusing in graphene, *Nature Physics*, 9(4), 225–229, URL http://dx.doi.org/10.1038/nphys2549. (Cited on page 65.)

[137] Timp, G., A. M. Chang, P. Mankiewich, R. Behringer, J. E. Cunningham, T. Y. Chang, and R. E. Howard. 1987. Quantum transport in an electron-wave guide, *Phys. Rev. Lett.*, 59, 732–735. (Cited on page 120.)

[138] Tomimatsu, T., K. Hashimoto, S. Taninaka, S. Nomura, and Y. Hirayama. 2020. Probing the breakdown of topological protection: Filling-factor-dependent evolution of robust quantum hall incompressible phases, *Phys. Rev. Research*, 2, 013128, URL https://link.aps.org/doi/10.1103/PhysRevResearch.2.013128. (Cited on page 120.)

[139] Topinka, M.A. 2002. Imaging coherent electron wave flow through 2d electron gas nanostructures, *PhD thesis, Harvard*. (Cited on page 33.)

[140] Topinka, M.A., B.J. LeRoy, S.E. Shaw, E.J. Heller, R. Westervelt, K.D. Maranowski, and A.C. Gossard. 2000. Imaging coherent electron flow from a quantum point contact, *Science*, 289, 2323–6. (Cited on page 33.)

[141] Topinka, M.A., B.J. LeRoy, R. Westervelt, S. Shaw, R. Fleischmann, E.J. Heller, K. Maranowski, and A.C. Gossard. 2001. Coherent branched flow in a two-dimensional electron gas, *Nature*, 410, 183–6, URL https://doi.org/10.1038/35065553. (Cited on pages 33, 34, 85, and 100.)

[142] Topinka, M.A., B.J. LeRoy, R.M. Westervelt, K.D. Maranowski, and A.C. Gossard. 2002. Imaging coherent electron wave flow in a two-dimensional electron gas, 12, 678–683, URL https://doi.org/10.1016/S1386-9477(01)00375-7. (Cited on page 33.)

[143] Topinka, M.A., R. Westervelt, and E. Heller. 2003. Imaging electron flow, *Physics Today*, 56, 47–52, URL https://doi.org/10.1063/1.1650228. (Cited on page 33.)

[144] Trugman, S.A. 1983. Localization, percolation, and the quantum hall effect, *Phys. Rev. B*, 27, 7539–7546, URL https://link.aps.org/doi/10.1103/PhysRevB.27.7539. (Cited on page 114.)

[145] Veselago, V.G. 1968. The electrodynamics of substances with simultaneously negative values of ϵ and μ, *Soviet Physics Uspekhi*, 10(4), 509–514, URL https://doi.org/10.1070/PU1968v010n04ABEH003699. (Cited on page 14.)

[146] Wallace, P.R. 1947. The band theory of graphite, *Phys. Rev.*, 71, 622–634, URL https://link.aps.org/doi/10.1103/PhysRev.71.622. (Cited on page 2.)

[147] Wang, L., I. Meric, P. Y. Huang, Q. Gao, Y. Gao, H. Tran, T. Taniguchi, K. Watanabe, L. M. Campos, D. A. Muller, J. Guo, P. Kim, J. Hone, K. L. Shepard, and C. R. Dean. 2013. One-dimensional electrical contact to a two-dimensional material, *Science*, 342(6158), 614–617, URL https://doi.org/10.1126/science.1244358. (Cited on pages 64, 65, and 72.)

[148] Weis, J. and K. von Klitzing. 2011. Metrology and microscopic picture of the integer quantum hall effect, *Philosophical transactions. Series A, Mathematical, physical, and engineering sciences*, 369, 3954–3974, URL https://doi.org/10.1098/rsta.2011.0198. (Cited on page 119.)

[149] Westervelt, R.M., M.A. Topinka, B.J. LeRoy, A.C. Bleszynski, S.E.J. Shaw, E.J. Heller, K.D. Maranowski, and A.C. Gossard. 2003. Imaging coherent electron flow in a two-dimensional electron gas, *Physica E: Low-Dimensional Systems and Nanostructures*, 18, 138–140, URL https://doi.org/10.1016/S1386-9477(02)01050-0. (Cited on page 33.)

[150] Wilmart, Q., S. Berrada, D. Torrin, V. Nguyen, G. Fève, J. Berroir, P. Dollfus, and B. Plaçais. 2014. A klein-tunneling transistor with ballistic graphene, *2D Materials*, 1, 011006, URL http://dx.doi.org/10.1088/2053-1583/1/1/011006. (Cited on page 79.)

[151] Woodside, M.T., C. Vale, P.L. McEuen, C. Kadow, K.D. Maranowski, and A.C. Gossard. 2001. Imaging interedge-state scattering centers in the quantum hall regime, *Phys. Rev. B*, 64, 041310, URL https://link.aps.org/doi/10.1103/PhysRevB.64.041310. (Cited on page 120.)

[152] Wu, J.S. and M. M. Fogler. 2014. Scattering of two-dimensional massless dirac electrons by a circular potential barrier, *Phys. Rev. B*, 90, 235402, URL https://link.aps.org/doi/10.1103/PhysRevB.90.235402. (Cited on pages 15 and 16.)

[153] Yankowitz, M., Q. Ma, P. Jarillo-Herrero, and B. LeRoy. 2019. van der waals heterostructures combining graphene and hexagonal boron nitride, *Nature Reviews Physics*, 1, 1, URL https://www.nature.com/articles/s42254-018-0016-0. (Cited on page 65.)

[154] Yeazell, J. and T. Uzer. 2000. The physics and chemistry of wave packets, URL https://books.google.ca/books/about/The_Physics_and_Chemistry_of_Wave_Packet.html?id=_sScnHz1kfsC&redir_esc=y&hl=en. (Cited on page 32.)

[155] Young, A.F., C. R Dean, L. Wang, H. Ren, P. Cadden-Zimansky, K. Watanabe, T. Taniguchi, J. Hone, K. L. Shepard, and P. Kim. 2012. Spin and valley quantum hall ferromagnetism in graphene, *Nature Physics*, 8, 550–556, URL https://doi.org/10.1038/nphys2307. (Cited on page 135.)

[156] Zhang, Y., V. W. Brar, C. Girit, A. Zettl, and M.F. Crommie. 2009. Origin of spatial charge inhomogeneity in graphene, *Nature Physics*, 5(10), 722–726, URL http://dx.doi.org/10.1038/nphys1365. (Cited on page 100.)

[157] Zhang, Y., Y. W. Tan, H. L. Stormer, and P. Kim. 2005. Experimental observation of the quantum Hall effect and Berry's phase in graphene, *Phys. Rev. B.*, 438, 201–204, URL https://doi.org/10.1038/nature04235. (Cited on page 64.)

[158] Zhao, Y., W. Jonathan, F. Natterer, J. Rodriguez-Nieva, K. Lewandowski, C. Watanabe, T. Taniguchi, L. Levitov, N. Zhitenev, and A. Stroscio. 2015. Creating and probing electron whispering-gallery modes in graphene, *Science*, 348, 672–675, URL https://doi.org/10.1126/science.aaa7469. (Cited on page 16.)

[159] Zhou, X., A. Kerelsky, M. M. Elahi, D. Wang, K. M. M. Habib, R. N. Sajjad, P. Agnihotri, J. U. Lee, A. W. Ghosh, F. M. Ross, and A. N. Pasupathy. 2019. Atomic-scale characterization of graphene p–n junctions for electron-optical applications, *ACS Nano*, 13(2), 2558–2566, URL https://doi.org/10.1021/acsnano.8b09575. (Cited on page 13.)

[160] Zimmermann, Katrin. 2016. Quantum point contact in high mobility graphene, *PhD thesis, Université Grenoble Alpes*.